Large Stroke Electrostatic Pump for an Electrocaloric Micro-Cooler

Submitted in partial fulfillment of the requirements for

the degree of

Doctor of Philosophy

In

ELECTRICAL AND COMPUTER ENGINEERING

Jinsheng Gao

B.S., Electrical and Computer and Engineering, Nankai University, Tianjin
M.S., Electrical and Computer and Engineering, Northeastern University, Boston

Carnegie Mellon University
Pittsburgh, PA

August, 2015

Acknowledgments

I would like to express my sincere appreciation and gratitude to my advisor Professor Gary K. Fedder for supporting me and guiding me in the last five years. His professional expertise and invaluable guidance inspired me to pursue truth and quality research. He sets an example of excellence as a researcher and mentor.

I would like to thank Prof. James A. Bain, Prof. Peter. J Gilgunn, Prof. Alan J.H. McGaughey and Prof. Shi-Chune Yao for serving on my dissertation committee, and for offering their suggestions and helpful advice on my research and thesis.

I would also like to extend my appreciation to my project collaborators: Suresh Santhanam, Dr. Dongzhi Guo and Ying-Ju Yu for their assistance and instructions for my research. Equal thanks also go to other members in ACM group for the many helpful discussions, including Andrew Slippey, Taylor Maxwell, David Wolf & Chris Peters at Active Cooling Technology, Inc., and Matthew Moran at Isotherm Technologies LLC.

It's both fun and rewarding to work with a group of top talents at CMU. I would like to acknowledge professors, staffs, graduate students and friends for their support and help all the time: Prof. Tamal Mukherjee, Prof. Gianluca Piazza, Prof. Yi Luo, Dr. Yang Zhang, Dr. Congzhong Guo, Dr. Pengfei Li, Dr. Dylan Fang, Dr. Kristen Dorsey, Dr. Nathan Lazarus, Dr. Yunchuan Kong, Dr. Yixuan Chen, Dr. Jeronimo Segovia-Fernandez, Dr. Cristian Cassella, Dr. Siddhartha Gohosh, Erdinc Tatar, Lionel Wong, Xiao Chuan Ong, Sean Yen, Jinglin Xu, Mary Beth Galanko, Mats Forssell, Metin Guney, Naser Naserifar, Lisha Shi, Changting Xu, Xiaolan Zhou, Chenyang Wu, Mohamed Mahmoud, Ming Xu, Abhishek Sharma, Enes Calayir , Baoan Liu, Wei Gong.

A special thanks to my family. Words could not express how grateful I am for all of the support and sacrifices that you've made on my behalf.

Finally, this work was supported by the Defense Advanced Research Projects Agency (DARPA) and the U.S. Army Aviation and Missile Research, Development, and Engineering Center (AMRDEC) under Grant No. W31P4Q-10-1-0015.

Abstract

The increasing integration density of electronic components in systems where very high speed and/or power are essential leads to a desire for miniature active cooling technologies. An active micro-cooler that pumps working fluid past an electrocaloric regenerator has potential to realize such a high cooling performance. However, such a micro-cooler requires two key new components – an electrostatic micro-pump subsystem and the electrocaloric regenerator – that are the primary subject of this thesis. The micro-pump system drives the working fluid back and forth through the regenerator. The electrocaloric regenerator provides storage and release of heat under the application and removal of an electric field. Through synchronization of the electrical and mechanical cycling, heat can be extracted from the cold side and released to the hot side to achieve cooling.

A 10 mm-long by 2 mm-wide by 100 μm-deep silicon micro-pump with an electrostatically actuated snap-in action enables a large displacement volume (1 μL). Each pump chamber element comprises an approximately 11 μm-thick polydimethylsiloxane (PDMS) diaphragm with an embedded thin-film aluminum electrode suspended over a silicon chamber that acts as a 3D shaped counter electrode to enable electrostatic "zipper" operation. Both single-pump prototypes and dual-pump test systems confirmed operation predicted by finite-element simulation.

The need for compliant diaphragms in the micro-pump motivated development of a fabrication, release and transfer process for large area (> 5 cm diameter), ultra-thin (1 μm to 20 μm) PDMS membranes having embedded metal mesh electrodes with critical dimensions

down to 2 μm. Experimental bulge testing of the ultra-thin PDMS films indicates that Young's modulus at 1 μm thickness is increased ten-fold over mm-scale PDMS.

A modified grayscale photolithography and silicon etch process enables more grayscale levels than prior approaches, resulting in a smooth etched 3D silicon surface for the micro-pump counter electrode. The combination of the thin PDMS diaphragm and the spline-shaped silicon substrate significantly reduces electrostatic actuation voltage. A maximum snap-in displacement of 100 μm occurs as low as 100 V (dependent on the exact chamber electrode shape), corresponding to a displacement volume of ~1 μL/stroke. This ultra-large stroke PDMS micro-pump opens a promising route for designing and fabricating large electrostatic stroke actuators and soft electronics devices.

Experimental characterization of P(VDF-TrFE-CFE) terpolymer layers using infrared imaging resulted in measurement of an adiabatic temperature change of 5.2°C at an electric field of 90 V/μm, with the material performance acting stable over a long testing period. A prototype regenerator established the feasibility to assemble terpolymer layers interspersed with microfabricated epoxy spacers in order to form microchannels for the working fluid to pass. These results suggest that this polymer is a promising material for micro-scale cooling application.

Multi-physics finite element simulations indicate cooling performance of a 15°C temperature drop with 5 W/cm^2 heat rejection and a coefficient of performance (*COP*) of 4 at 150 V/μm electric field across the electrocaloric regenerator at a 10 Hz operating frequency. One full prototype micro-cooler, comprising two micro-pumps and the electrocaloric regenerator, was

assembled into a 3D-printed package; however, it was not functionally tested due to its fragility. Further micro-cooler system-level development is left as potential future work.

Table of Contents

List of Figures x

List of Tables xvi

Chapter 1 Introduction 1

1.1 Background and Motivation 1

1.2 Electrocaloric Cooling 5

1.3 Electrocaloric Micro-Cooler 9

1.3.1 Design Concept 9

1.3.2 Cooling Mechanism 11

1.4 Thesis Overview 12

1.5 Thesis Contribution 15

Chapter 2 Fabrication, Transfer and Material Characterization of Ultra-Thin PDMS Membrane 18

2.1 Introduction 18

2.2 Fabrication of Ultra-Thin PDMS Films 20

2.2.1 Normal PDMS Films of Different Thicknesses (50 μm - 500 μm) with C_4F_8 Polymer Releasing Layer 21

2.2.2 Thin PDMS Films of Different Thicknesses (1 μm - 50 μm) with Gelatin Sacrificial Layer 22

2.2.3 Thin Multi-Layer Films (11 μm) with Cr/Au/Cr Electrodes and C_4F_8 Polymer Release Layer 23

2.2.4 Thin Multi-Layer Films of Different Thicknesses (2 μm - 50 μm) with Cr/Al/Cr Electrodes with Gelatin Sacrificial Layer 25

2.2.5 Thin PDMS Films of Different Thicknesses (2 μm - 50 μm) with Reactive-Ion Etch 31

2.3 Release and Transfer of Ultra-Thin PDMS Film 34

2.3.1 Release and Transfer Thin PDMS Film with Heat Release Tape 34

2.3.2 Release and Transfer Large Area Ultra-Thin PDMS Film with Gelatin Sacrificial Layer 36

2.4 Characterization of Mechanical Properties of Ultra-Thin PDMS Films 38

2.4.1 Experimental Setup 39

2.4.2 Theoretical Model and Finite Element Simulations 42

2.4.3 Results and Discussion 47

2.5 Summary and Conclusion 54

Chapter 3 Modified Grayscale Photolithography with Over Exposed Resist and Timed, Diluted Development 56

3.1 Introduction 56

3.2 Grayscale Photolithography 56

3.3 Modified Grayscale Photolithography Process 60

3.3.1 The Grayscale Mask Design 60

3.3.2 Modified Grayscale Photolithography Process and its calibration 61
3.3.3 Modified Grayscale Photolithography model 64
3.4 Changing Parameters 66
3.4.1 Changing Development Time 66
3.4.2 Changing Developer Dilution Ratio 68
3.4.3 Changing Exposure Time 71
3.5 Deep Reactive Ion Etching 72
3.6 Further Discussion 76
3.7 Summary and Conclusion 86
Chapter 4 Electrostatic Actuated Micro-Pump 88
4.1 Introduction 88
4.2 Design Concept 91
4.3 Finite Element Simulation of Micro-Pump 92
4.4 Fabrication of Micro-Pump 101
4.4.1 Ultra-thin PDMS Diaphragm with Embedded Metal Electrodes 101
4.4.2 Curled Silicon Substrate Fabricated by Modified Grayscale Photolithography 103
4.4.3 Micro-Pump Assembly 107
4.5 Actuation Tests of Micro-Pump 109
4.6 Summary and Conclusion 121
Chapter 5 Electrocaloric Regenerator Sub-Assembly 122
5.1 Introduction 122
5.2 Design Concept 122
5.3 Fabrication of EC Regenerator 124
5.3.1 EC Terpolymer Film 124
5.3.2 SU-8 Spacer 127
5.3.3 EC Regenerator Assembly 129
5.4 Thermal and Electrical Tests of EC Terpolymer 130
5.4.1 Experimental Setup 131
5.4.2 Measured Results and the Adiabatic Temperature Change 133
5.4.3 Effect of Stage Temperature and Operating Frequency 137
5.4.4 EC Terpolymer Stability 139
5.4.5 Breakdown of EC Terpolymer 140
5.5 Structural Tests of EC Terpolymer 142
5.6 Electrical Tests of EC Regenerator 145
5.7 Summary and Conclusion 147

Chapter 6 Micro-Cooler Assembly 148
6.1 Introduction 148
6.2 Finite Element Simulation of Micro-Cooler 149
6.2.1 Computation Setup 151
6.2.2 Results and Discussion 152
6.3 Assembly of Micro-Cooler 156
6.4 Summary and Conclusion 160
Chapter 7 Summary and Future Work 162
7.1 Thesis Conclusion 162
7.2 Future Work 164
Appendix 167
Appendix 1. Process Flows and Recipes 167
Appendix 2. FEA Simulation Settings 177
Appendix 3. Scripts and Codes 185
References 195

List of Figures

Figure 1.1 A schematic of the TMT programs (MACE, TGP, ACM, NTI and NJTT) and the task areas in a representative device [3]. 3
Figure 1.2. The tradeoffs in cooling systems related to heat lift, temperature drop, and efficiency, where $COP = 30\% \frac{T_H - T_C}{T_C} = \frac{P_{cooling}}{P_{input}}$ 4
Figure 1.3. Active cooling technology (a) Typical thermoelectric module [9]. (b) Stirling engine micro-cooler[11] 5
Figure 1.4. Conceptual demonstration of the mechanism of the electrocaloric effect. 6
Figure 1.5 Design and setup of a solid-state refrigerator based on the electrocaloric effect (Jia and Ju [13]). 8
Figure 1.6 Schematic of the prototype of a solid-state electrocaloric cooler (Gu et al.[24]), which includes two 0.25 mm thick 24-layer EC module and four 0.5 mm thick regenerators. 8
Figure 1.7. Model (made in SolidWorks 3D, Dassault Systèmes SolidWorks Corporation, Waltham, MA) for the electrocaloric refrigeration system. 10
Figure 1.8. The thermodynamic refrigeration cycle of a fluid element based on the EC effect. 12
Figure 2.1. Thickness of PDMS as a function of spin speed (30 s at maximum speed for polymer and 150 s at maximum speed for gelatin). 21
Figure 2.2 Thickness of PDMS as a function of mix ratio with Hexane. The solution is spun at 6000 rpm for 150 s. 23
Figure 2.3. The process flow for the fabrication of PDMS film with Cr/Au/Cr electrode embedded. 24
Figure 2.4. The optical microscope picture of a fabricated PDMS film with three-layer sandwich structure. The metal mesh line embedded in the PDMS is 2μm wide in layout. (a) six connected diaphragms with bonding pads. (b) zoom in picture for one diaphragm. (c) zoom in picture for serpentine mesh. 25
Figure 2.5 Process flow of PDMS membranes with embedded electrodes: (a) sequentially spin-cast gelatin sacrificial layer, spin-cast first PDMS layer, and evaporate Cr/Al/Cr layers on the handle substrate, (b) pattern metals, (c) spin-cast second PDMS layer. 26
Figure 2.6 Optical microscope photos of a fabricated membrane: (a) wide-angle view of diaphragm with bonding pad for micro-pump application, (b) non-patterned area (bonding pad) showing wrinkles, (c) and (d) serpentine mesh patterned area (diaphragm) showing no wrinkles. 27
Figure 2.7 comparison among (a) Al sputtering on PDMS/Si substrate, (b) Al sputtered on PDMS/gelatin/Si substrate and (c) Al evaporated on PDMS/gelatin/Si substrate. 28
Figure 2.8 (a) Normal lithography on metal/PDMS/gelatin multi-layers. (b) Lithography on metal/PDMS/gelatin multi-layers with thicker gelatin edges. (3) Lithography results from (b). The patterns are blurred. 29
Figure 2.9 (a) Sample is diced after evaporation. Some of corner dies without high gelatin edge can still be used (b) Final results after lithography and pattern for each die. The close up view for the diaphragm mesh is shown in Figure 2.6. 30
Figure 2.10 (a) Process flow for Al deposited and patterned on the plain PDMS as a hard mask to define the PDMS. (b) Ethed PDMS films. 32
Figure 2.11 . The process flow for molding PDMS mask. 33

Figure 2.12 (a) PDMS etching in RIE system with molded PDMS as a shadow mask. (not scaled) (b) Final etching results for the bonding pad. The winkles can be seen in the figure because the bonding pad is not patterned as mesh. 33
Figure 2.13. The optical microscope picture showing a PDMS film with embedded electrode hanging over a fabricated Si chamber. 34
Figure 2.14. The process flow for the transferring of ultra-thin PDMS film onto the fabricated Si chamber with heat release tape assistance. 35
Figure 2.15: Process flow for transfer and release of PDMS diaphragm. (a) Si device substrate with through hole and microfluidic channels. (b) Bonding of membrane and handle substrate to device substrate. (c) Release of handle substrate. (d) Completed membrane over through hole. 36
Figure 2.16: Release and transfer of large area (> 5 cm diameter) PDMS layer by using gelatin sacrificial layer and aluminum ring. (a) Si substrate with gelatin sacrificial layer and 1 μm PDMS layer. (b) Al ring is attached on the PDMS with vacuum grease. (c) Release the substrate. 37
Figure 2.17 (a) Released 10 μm thick 5cm large PDMS ultra-thin film. (b) Released 1 μm thick 5cm large PDMS ultra-thin film. 38
Figure 2.18: Illustration of the setup for characterizing PDMS membrane stiffness. 40
Figure 2.19: A deformed PDMS membrane under different pressures. The diameter of membrane is 2 mm and the thickness is 56 μm. 41
Figure 2.20 (a) PDMS's effective Young's modulus is also measured by the nanoindentation. (b) The tip of the probe is is a Berkovich tip, which has a half angle, θ, of 65.35 degrees. 41
Figure 2.21: (a) Illustration of inflated circular PDMS membrane with its coordinates in an axisymmetric cross section view of half of the membrane. 45
Figure 2.22. Theoretical calculations of deformed PDMS shapes. a = 1 mm, h_0 = 56 μm. 46
Figure 2.23: Example of a 2D axisymmetric FEA simulation of membrane displacement. a = 1 mm, h_0 = 56 μm, P = 7 kPa. 46
Figure 2.24 FEA simulation for nanoindentation. The 2D axis-symmetric simulations are examined instead of 3D to reduce the complexity. The membrane in the example is 12 μm thick and force applied is 70 μN. 47
Figure 2.25: An example of deflections of inflated plain PDMS membranes with increasing pressure comparing experimental measurements, fitted calculation of the theoretical model, and finite element simulations. The membrane diameter is 2 mm. 48
Figure 2.26: The effective Young's modulus of plain PDMS, PDMS after metal evaporation, and PDMS after RIE ashing, as extracted from membrane bulge tests. 49
Figure 2.27: The extracted effective Young's modulus of 120 μm-thick PDMS films for different mixing ratio of the pre-polymer gel and cross linker. 51
Figure 2.28: Summary of strain stress relationships of PDMS based on the extracted parameter C_1 and effective Young's modulus. The effective Young's modulus equals to the initial slope of each curve. "10 μm after plasma" is short for 11 μm thick film after 1 μm surface plasma etching. "11μm after evap" is short for 11 μm thick film after surface metal evaporation. 52
Figure 2.29: Comparison of simulation and experimental results of nanoindentation on a plasma etched 12 μm-thick PDMS film. 53
Figure 2.30: Color data points: the extracted effective Young's modulus of PDMS films from nanoindentation measurements. Grey data points: data from Figure 2.26 as comparison. 54
Figure 3.1 Three key steps to grayscale lithography: (1) grayscale mask design, (2) & (3) grayscale lithography, and (4) & (5) dry anisotropic etching. 58

Figure 3.2. (a) 8μm×8μm subpattern, 64 levels grayscale mask design. The numbers represent the sequence of opaque pixels. (b) Three grayscale examples. 61
Figure 3.3. (a)Measured thickness of developed photoresist vs. dose after traditional grayscale lithography. (b) Solid line: Measured thickness of developed photoresist. Dash line: Fitting line as exponential curve. 63
Figure 3.4. The transmission ratio vs. length on grayscale mask designed for cubic function shape based on the calibration in section 3.3 67
Figure 3.5. Developed photoresist thickness for different development times. The exposure time is 500s. The developers diluted as 1: 2.7 (developer: water). 67
Figure 3.6. Optical images of developed photoresist. The periodic structures are intentionally designed to help prevent adhesion of PDMS to the silicon during pump actuation. The dash line indicates the direction of the scan. 68
Figure 3.7 Development rate vs different exposure times for different developer concentrations. 70
Figure 3.8 Developed photoresist thickness for different developer dilution ratios. The exposure time is 380s. 70
Figure 3.9. Development rate for different developer concentration under 100% transmission ratio. 71
Figure 3.10. Developed photoresist thickness for different exposure times. The developing time is 380 s. 72
Figure 3.11 Transferring photoresist profiles into silicon profiles. 74
Figure 3.12 Measured Si height after DRIE. The profile is designed as a cubic function shape. 75
Figure 3.13 SEM picture of a 150 μm deep Si pump base. The profile shows a smooth cubic function shape. The channels are open by backside DIRE for the microcooling system application. 76
Figure 3.14. Patterns on grayscale mask near 50% transmission ratio (a) before modification and (b) after modification. The numbers correspond to n. 77
Figure 3.15. Examples of the effect on the profiles from the parameters a and b. (a) effect of parameter a: b is fixed as 0.16, and a has three different values: 0.4, 0.5, 0.6. (b) effect of parameter b: a is fixed as 0.5, and a has three different values:0.1, 0.16, 0.5. 79
Figure 3.16. Different shapes for different parameter a and b. 80
Figure 3.17. Transmission ratio vs. length for six different profiles. 81
Figure 3.18. New measured development rate for different developer concentration under 100% transmission ratio. 83
Figure 3.19. New measured thickness of developed photoresist vs UV light dose. Blue line: The developer dilution is ratio 1:2.7, and the development rate is 0.3 μm/min. Red line: The developer dilution is ratio 1:3.4, and the development rate is 0.06 μm/min. Grey line: Data in Figure 3.3 for comparison. The developer dilution is ratio 1:2.7, and the development rate is 0.06 μm/min. 84
Figure 3.20. Measured developed resist height and the theoretical predication based on Figure 3.19 for different profiles. The values of a and b are the original values. 85
Figure 4.1. Electrostatically actuated, dual-diaphragm micro-pump system developed by Honeywell Laboratories. [72] 89
Figure 4.2. Illustration and cross section for large stroke electrostatic micro-pump. The pump comprises a compliant PDMS diaphragm and a smoothly shaped Si chamber. 91
Figure 4.3 A simple demonstration of customized contact force. The fixed-fixed beam is 2 mm long and 11 μm thick, and the gap is 50 μm. The linear model is applied to the beam and the Young's modulus is fixed as 2 MPa. The moving mesh is set for both of the beam and the gap. When 30 V electrical field is applied on the beam, the beam snaps in on the substrate and stopped by the contact force. 93

Figure 4.4 Example of the multi-physics finite element simulation for a 2D half cross section of the pump to overcome the computational complexity. In this example, a = 0.5, and b = 0.16. The color in fluid par represents velocity and color in diaphragm part represents displacement. 94
Figure 4.5. Static simulation results for minimum required snap-in voltage for different chamber shape. 95
Figure 4.6. Examples of the multiphysics simulation for (a) single element and (b) stacked double elements. The color map indicates the pressure in the liquid flow. 98
Figure 4.7. Results of the displacement and pressure drop for the multiphysics simulation for (b) single element and (c) stacked double elements under (a) applied voltage. In (b) and (c): Red and green: diaphragm displacement; Blue: pressure drop. 99
Figure 4.8. Maximum operating frequency for particular applied voltage. Simulations include single stacked cooling element with and without regenerator, and back to back stacked double cooling elements with and without regenerator 100
Figure 4.9. Maximum pressure drop for particular applied voltage for single stacked cooling element and back to back stacked elements with regenerator. 100
Figure 4.10. Fabricated large stroke electrostatic actuated PDMS-on-Si micro-pump. (a) Assembled micro-pump (b) and (c) Fabricated diaphragm hanging over the chamber. (d) Fabricated bonding pad. 102
Figure 4.11. Process flow for shaped Si substrate electrode fabrication 103
Figure 4.12 Measured Si height after DRIE. The profile is designed as a cubic function shape. 105
Figure 4.13 Fabricated 100 μm deep curved Si substrate (a) Optical picture of developed photoresist. (b) Full part. (c) Front side SEM of the shaped Si electrode.(d) back side SEM of Si channels. 106
Figure 4.14 Process flow for micro-pump assembly. After bonding, the assembled device is then dipped in 40°C warm water to dissolve gelatin to release the pump. The polypropylene prevents the diaphragm sticking on the Si electrode when drying. 107
Figure 4.15 Test bed setup for micro-pump electrostatic actuation. 110
Figure 4.16. Optical images of pump actuation (a) and (b) diaphragm is operated in the air. (c) and (d) diaphragm and pump is operated with filling with the HT-70. 111
Figure 4.17. Measured vs. simulated displacement of the center of the pump diaphragm and the corresponding displaced volume. 112
Figure 4.18. Variation of a and b and the corresponding maximum size change in the profile. (a) b is set to be 0.16, and a varies from 0.4 to 0.6. (b) a is set to be 0.5, and b varies from 0.07 to 0.5 113
Figure 4.19. Different shapes for different values of a and b. 114
Figure 4.20. Diaphragm displacement vs applied for changing value of a while keeping b as the value of 0.15. 115
Figure 4.21. Diaphragm displacement vs applied for changing value of b while keeping a as the value of 0.5. 115
Figure 4.22. Sensitivity of profile height changes from (a) parameter a and (b) parameter b for snap-in voltage 116
Figure 4.23. Fabricated Si chamber with a = 0.58, b = 0.17. 117
Figure 4.24. Measurement and simulation results for different chamber shapes of micro-pumps. Blue dots: Simulation; and red dots: measurements. 118
Figure 4.25. Illustration and cross section for double micro-pump element. (a)Top view of diaphragm. (b) Top, bottom, and cross section view of chamber. (c) Cross section of assembly element. 119
Figure 4.26. Fabricated double pump element. 120

Figure 4.27. The double pump system is operated by electrostatic actuation in the air. When the voltage is applied on one of the pump, the diaphragm of that pump is completely snapped in on the chamber, squeezing the air through the channels to the other pump, and pushing the other pump's diaphragm up. 120
Figure 5.1. (a) Solid model for electrocaloric regenerator. The 1 cm x 2.5 mm x 580 µm regenerator includes 8 layers of electrocaloric polymer and 10 SU-8 spacers. (b) A-A' cross section of the electrocaloric regenerator. (c) B-B' cross section of the electrocaloric regenerator. 123
Figure 5.2. (a) Shadow masks for fabricate the EC terpolymer. The masks have 1.2 cm by 2mm rectangular holes. The small circular holes are designed for alignment during the cutting and assembly. (b) Cross section for EC terpolymer setup. The front side mask is used for front side sputtering, and back side mask is used for back side sputtering 125
Figure 5.3. Fabricated electrocaloric films with gold electrodes on both sides. The film is suspended on the cylindrical aluminum frame. 126
Figure 5.4. Customized cutter for cutting EC terpolymer. 126
Figure 5.5. Process flow for SU-8 spacer fabrication. The spacers are fabricated by patterning two layers of SU-8 subsequently. 127
Figure 5.6. Fabricated SU-8 spacer and its illustration of 3D model 128
Figure 5.7. Cross section of assembled EC regenerator. 129
Figure 5.8. Assembled EC regenerator in the 3D printed package. 130
Figure 5.9. Test bed setup for the thermal and electrical test for the EC materials. 132
Figure 5.10 (a) Example of a trapezoidal electric field applied to the EC sample and the measured current. The ramp time of the electric field is 1.2 s and its maximum amplitude is 67 V/µm. (b) and (c) Infrascope-measured temperature and images at different time in a cycle and the temperature as a function of time. The temperature changes abruptly when the electric field is ramping up and down (event 2 and event 4, respectively). 134
Figure 5.11 Measured cooling temperature as a function of the electric field at different voltage ramp times. The stage temperature is 25 ˚C for all measurements. 135
Figure 5.12 The comparison between the measured data and the computational result at an electric field of 90 V/µm. The details of definitions and calculations can be found in [26]. 136
Figure 5.13 Adiabatic temperature change vs. electric field and comparison to literature results. 136
Figure 5.14 Measured cooling temperature at different stage temperatures. The ramp time of the voltage is 0.8 s. 137
Figure 5.15 (a) Measured minimum temperature as a function of the operating frequency for an electric field of 73 V/ µm. (b) Measured temperature change when switching off the electric field with the operating frequency. A ramp time of 0.8 s is fixed at different frequencies for a fair comparison. The stage temperature is 25˚C. The inset is a plot of measured temperature when the operating frequency is 0.3 Hz and the electric field amplitude is 73 V/µm. ΔT is the temperature change when switching off the electric field. 138
Figure 5.16 Temperature history of a sample for 30 minutes at a stage temperature of 25°C. The ramp time of the voltage is 0.8 s. The frequency is 0.2 Hz and the electric field amplitude is 54 V/µm. Gaps in the data are due to limitations of the infrascope. The electric field was modulated at all times. 140
Figure 5.17. Leakage current at applied voltage (a) 54V/µm and (b) 88 V/µm. When 88 V/µm voltage is applied, the P(VDF-TrFE-CFE) terpolymer starts to breakdown usually after dozens of cycles. 141
Figure 5.18 3D images of polymer after breakdown collected by optical profilometry. The picture shows the uneven surface of terpolymer and the through hole caused by breakdown. 142
Figure 5.19 Illustration for XRD peaks generation and calculation of d-spacing in crystals. 143

Figure 5.20. XRD data for an 11 μm-thick P(VDF-TrFE-CFE) terpolymer film with different voltages at a temperature of 25˚C. The ferroelectric phase peak gradually grows and the relaxor ferroelectric phase peak reduces with the increase of the electric field. 144
Figure 5.21 Leakage current measurement for the assembled regenerator with 500 V, 0.8 s ramp pulse applied. 146
Figure 6.1 Solid-model view of the EC cooler element. The two diaphragm actuators are driven electro-statically. The EC module, which includes multiple terpolymer layers, is located between two diaphragm actuators. The fluid flow is within the plane of the wafer (Courtesy of Andrew Slippey, Advanced Cooling Technologies, Inc.). 148
Figure 6.2. (Dash line) Timing of a micro-pump diaphragm actuation and (solid line) voltage applied on electrocaloric regenerator. 149
Figure 6.3 2D computational region of the EC cooling device coupled with multiple physics phenomena. 151
Figure 6.4 Temperature contours at different time when the diaphragm is driven electrostatically at an operating frequency of 5 Hz. (a) t = 1 s (b) t = 1.05 s (c) t = 1.1 s (d) t = 1.15 s. 152
Figure 6.5 The volume variations of hot and cold chambers and the electric filed applied to EC materials. 153
Figure 6.6 The volume variations of hot and cold chambers, corresponding to the driven voltage of hot and cold diaphragms. 154
Figure 6.7 Comparisons of (a) the cooling power density and (b) pressure drop in a frequency range of 1 to 10 Hz between the thermal modeling results [26] and multiphysics modeling results. 155
Figure 6.8. (a) Cross section of assembly for single element for thermal performance evaluation using external mechanical pumps. (b) Envisioned assembly for micro-cooler with stacked push-pull elements. 156
Figure 6.9 Micro-cooler assembly process flow. (1) 3D-printed package. (2) Place two chambers upside down in the package. (3) Attach bottom PDMS sealing layer on the bottom of two chambers. (4) Take two chambers with PDMS layer out of package. (5) Drop liquid PDMS in the package (center and four corners). (6) Put chambers back in the package. (7) Place SU-8 spacer in the package. (8) Drop liquid PDMS to fix SU-8 spacer. (9) Place EC polymer on the SU-8 spacer. (10) Use liquid PDMS to fix the EC polymer. Repeat (7) and (10). (11) Connect the wires. (12) Attach the top sealing PDMS layer with feeding holes. (13) Drop liquid PDMS and silicone rubber to seal the chambers except for the feeding holes. (14) Inject liquid into the chamber through the feeding holes. (15) Seal the feeding holes with liquid PDMS. (16) Attach lid. 158
Figure 6.10 (a) Assembled micro-cooler after working fluid injection, but before the lid is attached. (b)After lid is attached. 159
Figure 6.11 Assembled micro-cooler after testing tube is attached. The cooler is ready to test with external pump. 160

List of Tables

Table 1.1 Summary of EC materials and their performances 7
Table 3.1. The parameters of deep reactive ion etching 75
Table 4.1 Material properties of heat transfer fluid HT-70 96
Table 5.1 Capacitance measurements for individual EC layer and assembled regenerator 146

Chapter 1 Introduction

1.1 Background and Motivation

The integration density of electronic components and subsystems today leads to an increasing demand on thermal engineering and cooling technologies. Cooling approaches for power electronics need to reject large amounts of heat and sustain only a modest temperature drop. According to the international technology roadmap for semiconductors, the average power density from future processing chips will be at least 25 W/cm^2 [1]. Novel cooling technologies with a high efficiency are also attractive due to the requirement of thermal management. The coefficient of performance (*COP*) of a cooler, is defined as the ratio of heat removal to the input work [2]. The Carnot coefficient of performance, COP_C, which represents the maximum theoretical efficiency possible between constant temperature hot (T_H) and cold (T_C) sources, is

$$COP_C = T_C / (T_H - T_C). \tag{1.1}$$

In recent years, the Defense Advanced Research Projects Agency (DARPA) has invested extensively to improve thermal management technologies (TMT) [3] and enhance the cooling capacity and efficiency for electronics systems. As shown in Fig. 1.1 [3], the DARPA TMT program (2008-2013) includes five subprograms: Microtechnologies for Air-Cooled Exchangers (MACE), Thermal Ground Plane (TGP), Nano-Thermal Interfaces (NTI), Near Junction Thermal Transport (NJTT) and Active Cooling Modules (ACM). Each subprogram is corresponding to a specific task area according to the thermal resistance chain in Figure 1.1. The MACE program is to develop new technologies to improve the performance of heat sinks by decreasing the thermal resistance. The TGP program is to achieve superior heat conduction (10 kW/(m·K) to

20 kW/(m·K)) by incorporating nanostructured material for thin two-phase chambers at high g-load (10 g to 20 g) operational conditions, while replacing the traditional heat spreader. The goal of the NTI program is to reduce the thermal resistance of the interface layers that exist in many places from the electronic device to air by using novel materials and nanostructures. The fourth program, NJTT, pursued a 3x enhancement in RF power output by providing localized thermal management within 100 μm of the electronic junction. The primary goal of the ACM program is developing and demonstrating active cooling of electronics based on novel materials and thermodynamic cycles, to provide about 10 ˚C to 25 ˚C of cooling with a cooling power density of 25 W/cm^2 and a coefficient of performance (*COP*) of 2 in the centimeter scale [3]. An efficient active cooling module with a high performance could enable low-temperature operation of the device, including operation below ambient temperature, and allow larger power utilization margins in electronic devices. Figure 1.2 shows the tradeoffs in cooling systems related to cooling load, $P_{cooling}$, temperature drop, $\Delta T = T_H - T_C$, and efficiency, represented by *COP*. The *COP* in this calculation is defined as

$$COP = 30\% \frac{T_H - T_C}{T_C} = \frac{P_{cooling}}{P_{input}} \tag{1.2}$$

where P_{input} is the required input power.

Thermoelectric coolers, shown in Figure 1.3(a), are the most common refrigeration devices used active cooling for chip and board level electronics [4, 5, 6, 7]. Thermoelectric coolers operate by the Peltier effect. In these devices, the electrodes are typically made of a metal with excellent electrical conductivity. The semiconductor material between the electrodes creates two junctions between dissimilar materials, which, in turn, creates a pair of thermocouple voltages. When applied to the electrodes, these voltages force electrical current through the

semiconductor and heat flows in the direction of the charge carriers [8, 9]. However, thermoelectric energy conversion has low efficiency resulting in significant power requirements and waste heat generation. Significant challenges [10] exist in the design and fabrication of thermoelectric materials that can meet the large cooling power and high cooling efficiency requirements.

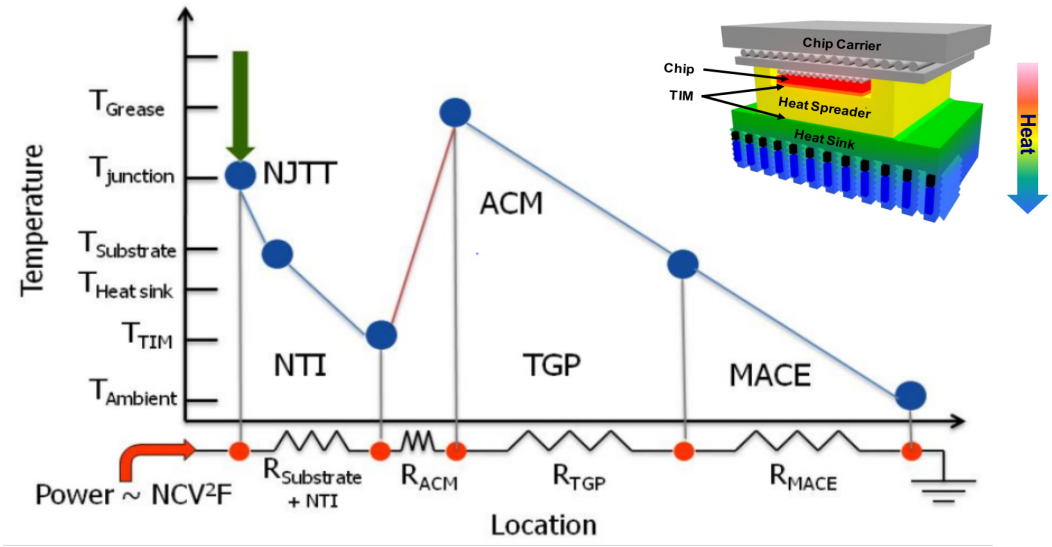

Figure 1.1 A schematic of the TMT programs (MACE, TGP, ACM, NTI and NJTT) and the task areas in a representative device [3].

The Stirling cooler microsystem is another option. The traditional mechanical Stirling cooler uses two pistons to transfer the working fluid back and forth between hot and cold chambers that are separated by a regenerator. The heat is released from the hot chamber during the compression process and absorbed from the cold chamber during the expansion process. The Stirling micro-cooler addresses frictional loss issues by replacing conventional pistons and the associated linkages with electrostatically driven diaphragms. The Moran concept [11, 12] used 1 cm to 2 cm diameter silicon diaphragms with vertical electrostatic comb drives to move the

working gas through a layered metal/polymer regenerator, as illustrated in Figure 1.3. The substantial heat loss from the hot side to the cold side is challenging to minimize. However, the weakness in the Stirling microcooler approach is the inability of micro-actuation approaches to achieve the high differential pressure required to approach the large heat lift.

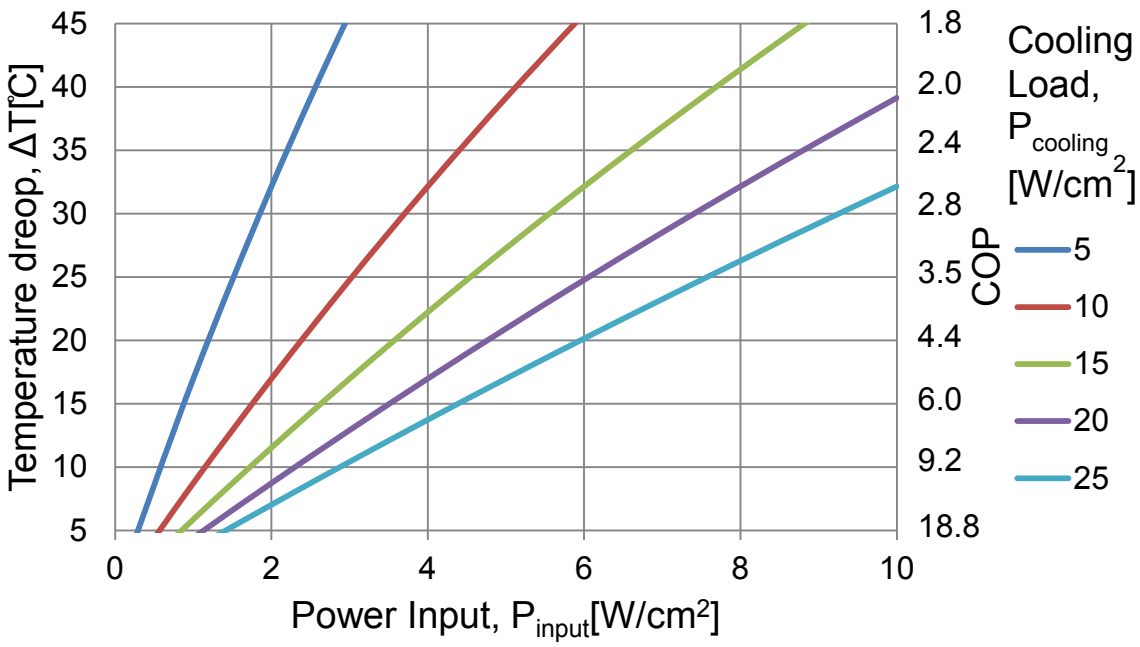

Figure 1.2. The tradeoffs in cooling systems related to heat lift, temperature drop, and efficiency, where $COP = 30\% \frac{T_H - T_C}{T_C} = \frac{P_{cooling}}{P_{input}}$

In this work, alternative options, active refrigeration devices based on electrocaloric (EC) materials, are investigated to realize a high cooling performance in the centimeter scale. The design concept, the analysis methodology, fabrication process, testing approach and results provide a valuable insight of this active cooling technology and build the foundation for further exploration.

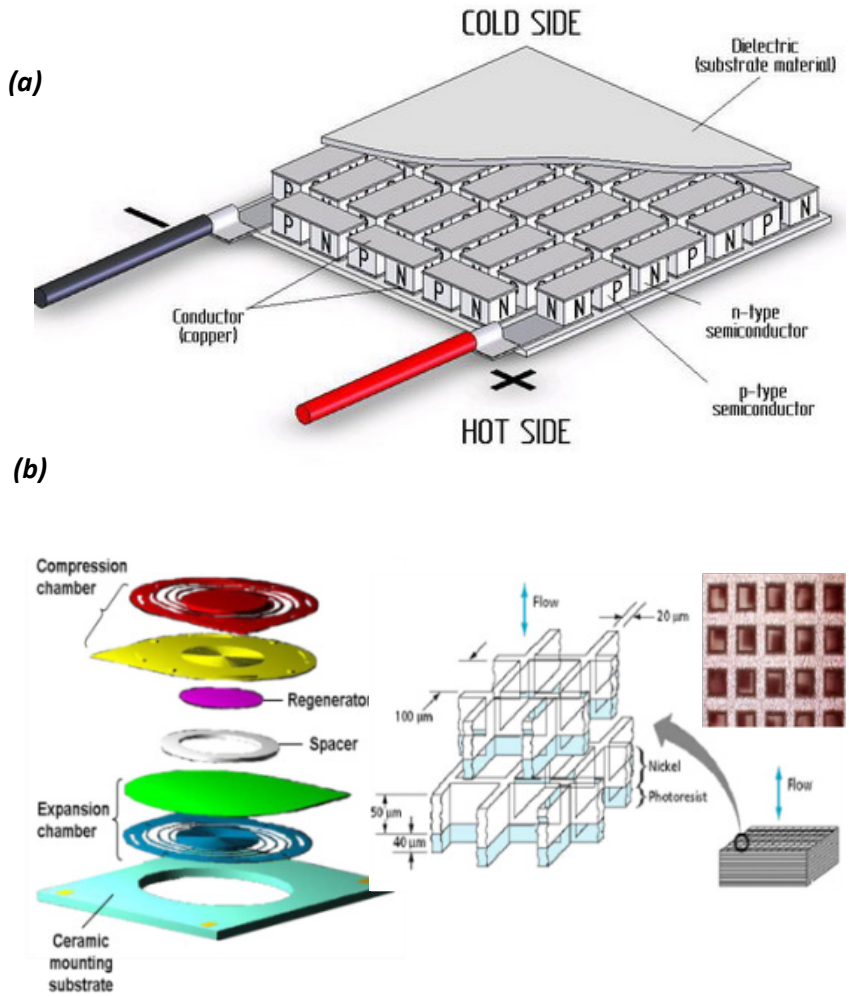

Figure 1.3. Active cooling technology (a) Typical thermoelectric module [9]. (b) Stirling engine micro-cooler[11]

1.2 Electrocaloric Cooling

In recent years, electrocaloric (EC) cooling [13] has attracted interest as a new approach that may satisfy requirements of advanced cooling modules due to its high efficiency. The electrocaloric effect is a phenomenon in which reversible temperature and entropy changes of a material due to changes in polarization appear under the application and removal of an electric

field. As shown in Figure 1.4, applying the electric field to an isolated material orients the poles and reduces the entropy associated with polarization. This process happens so fast (on the order of milliseconds [14]) that the system can be considered adiabatic. The temperature of the material is increased, as required by the entropy decrease. Conversely, removing the electric field disorders the dipoles, increases the entropy, and cools the material. This phenomenon can be described thermaodymatically by

$$\dot{Q} = \rho T \left(\frac{\partial S}{\partial E}\right)_T \frac{\partial E}{\partial t}, \tag{1.3}$$

where $\dot{Q}$ is the heat source term generated by the EC effect of the material, ρ is the density, T is the temperature, S is the entropy and E is the applied electric field.

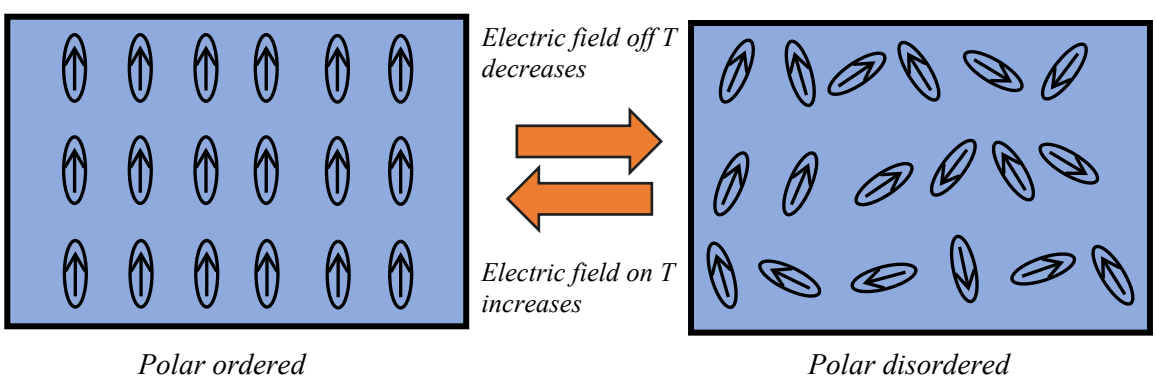

Figure 1.4. Conceptual demonstration of the mechanism of the electrocaloric effect.

Although the EC effect was first reported by Kobeco and Kurtschatov in 1930 [15], potential applications have been limited by the relatively low entropy and temperature changes for most ferroelectric materials. Recently, materials with a giant electrocaloric effect have been

reported [16, 17]. Some EC materials and their performances are listed in Table 5.1. These discoveries suggest practical applications in cooling devices. Jia and Ju [18] proposed a design of a solid-state refrigeration system based on the EC effect where an EC material is dynamically moved by a motorized z-stage between a heat source and a heat sink, as shown in Figure 1.5. A 1 K temperature drop was observed in their experimental testing at a frequency of 0.3 Hz. Reduction of the thermal contact resistances at the interfaces between the EC material and the heat source/sink (which are periodically brought into and out of contact) is challenging in this design. The overall cooling performance is limited by the poor performance of the electrocaloric material $BaTiO_3$.

Table 1.1 Summary of EC materials and their performances

Year	Material	Reference temperature T_0(˚C)	Electric field ΔE(V/μm)	ΔT (K)	$\Delta T / \Delta E$ [(K· μm)/V]
1963[19]	Rochelle Salt	22.2	0.14	0.0036	0.0257
1977[20]	$SrTiO_3$	269	0.542	1	1.85
1981[21]	$Pb_{0.99}Nb_{0.02}(Zr_{0.75}$-$Sn_{0.20}Ti_{0.05})O_3$	161	3	2.6	0.867
2006[16]	$PbZr_{0.95}Ti_{0.05}O_3$	226	48	12	0.25
2010[22]	P(VDF-TrFE)	80	209	12	0.0574
2011[23]	P(VDF-TrFE-CFE)	30	150	15.7	0.105

Gu et al. [24, 25] reported a chip scale solid-state electrocaloric oscillatory refrigeration device based on the high energy electron irradiated poly (vinylidene fluoridetrifluoroethylene) 68/32 mol% (ei-copolymer [24]). The prototype cooling device achieved more than 6 K

temperature span between the hot and cold sides, as shown in Figure 1.6. However, the cyclic motion of regenerators in the refrigerator was realized by a step motor, which is not compact and does not satisfy the size requirement for the chip scale cooling. The cooler performance is also limited by the friction loss and the thermal conduction between EC modules and regenerators in this design.

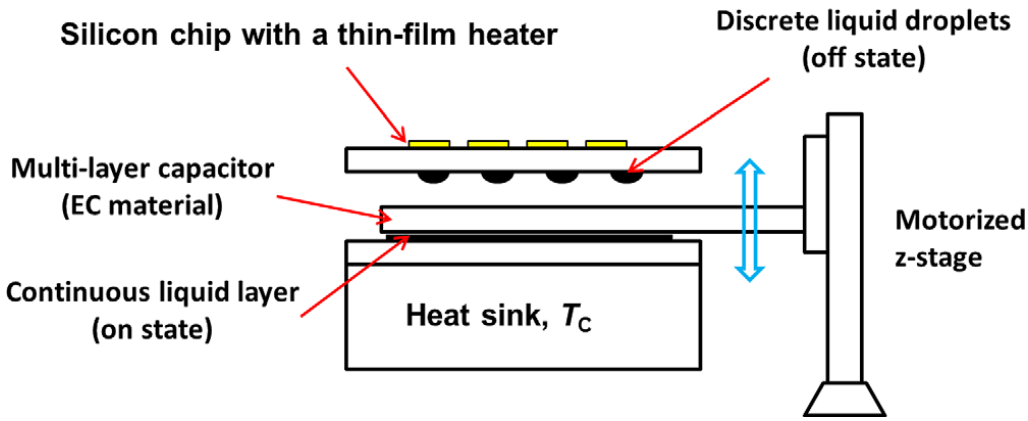

Figure 1.5 Design and setup of a solid-state refrigerator based on the electrocaloric effect (Jia and Ju [13]).

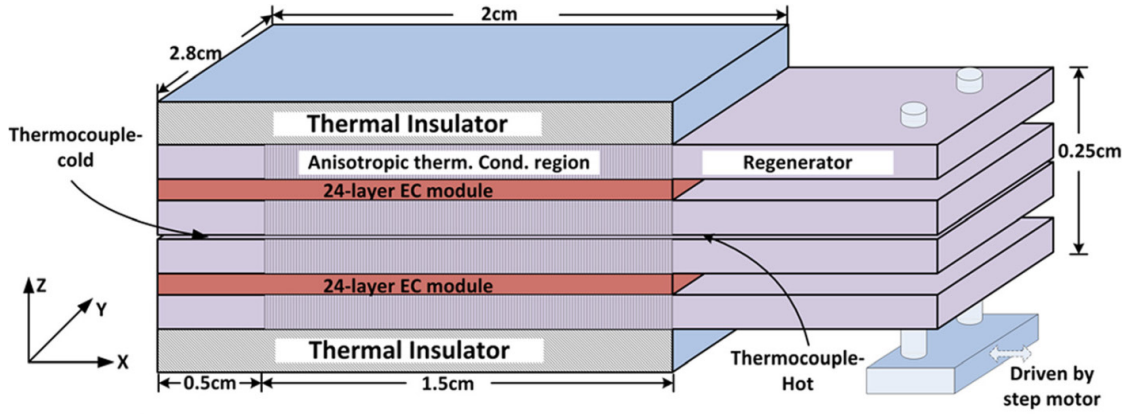

Figure 1.6 Schematic of the prototype of a solid-state electrocaloric cooler (Gu et al.[24]), which includes two 0.25 mm thick 24-layer EC module and four 0.5 mm thick regenerators.

In this thesis, P(VDF-TrFE-CFE) terpolymer, poly(vinylidene fluoride-trifluoroethylene-chlorofluoroethylene), is chosen as the EC material for the cooling components. It has a large electrocaloric effect while operating near room temperature, as tableted in Table 1.1. It has demonstrated an adiabatic temperature change of 7 K under a change of electric field of 100 MV/m over a broad temperature range around room temperature (280 K ~ 320 K) [23].

1.3 Electrocaloric Micro-Cooler

1.3.1 Design Concept

In this thesis, a refrigeration system is designed and fabricated and partially tested based on the electrocaloric effect of P(VDF-TrFE-CFE) terpolymer. In the design, shown in Figure 1.7, the proposed prototype cooling element is 1 cm long, 7 mm wide, and has a thickness of 300 μm. The system includes two key components: electrostatic micro-pumps and an electrocaloric regenerator. In the regenerator, electrocaloric terpolymer material is located between the two chambers to act as a "regenerator" that stores and releases thermal energy depending upon the electrical control signal. The micro-pumps drive the working fluid back and forth to carry the thermal energy through the regenerator. Through synchronization of the electrical and mechanical cycling, the heat is extracted from the cold side and released to the hot side to achieve cooling.

Each micro pump is a chamber composing a silicon cavity covered by a diaphragm. The 2 mm-wide, 11 μm-thick diaphragm is made of polydimethylsiloxane (PDMS) layers embedded with aluminum thin-film electrodes. The thin diaphragm creates a highly compliant membrane which is driven electrostatically. The silicon cavity has a rectangular 2 mm by 1 cm area and is

shaped in depth to have a spline cross section. The silicon enables efficient heat transfer between the fluid and the heat source/sink to improve the performance of the cooling element. The "zipping" shaped substrate reduces the pull-in voltage required to actuate the diaphragms. Channels are built at the outlet of the chambers to guide the fluid and improve the heat transfer between the fluid and heat sink/source. More details of micro-pumps are discussed in Chapter 4.

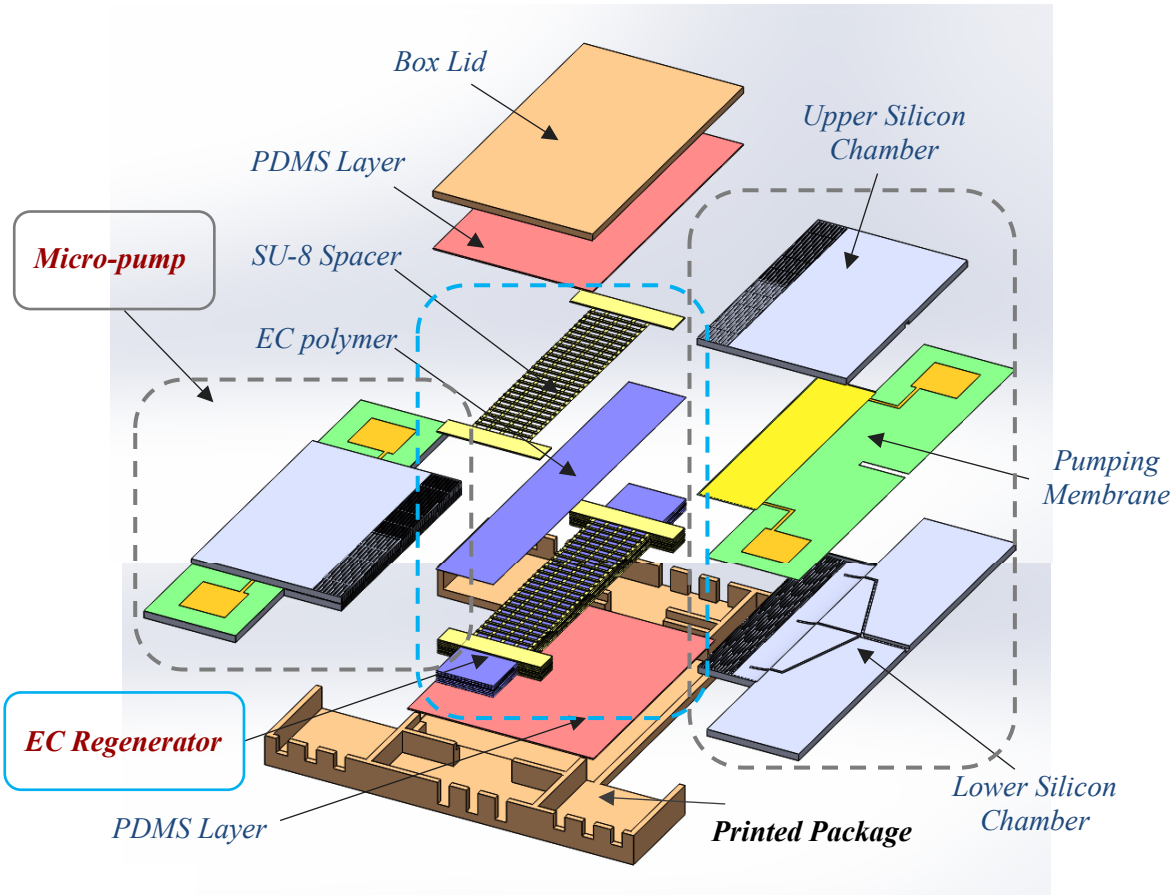

Figure 1.7. Model (made in SolidWorks 3D, Dassault Systèmes SolidWorks Corporation, Waltham, MA) for the electrocaloric refrigeration system.

The regenerator comprises the electrocaloric terpolymer layers interleaved with spacers patterned from SU-8 photodefinable epoxy (MicroChem Corp., Westborough, MA). The

terpolymer provides reversible temperature under the application and removal of an electric field. Spacers are placed between the terpolymer layers to form channels to allow the passage of heat transfer fluid, while maintaining low thermal conductivity between the chambers to thermally isolate the hot and cold sides. More details of electrocaloric regenerator are discussed in Chapter 5. The 3D printed package and PDMS layers enclose the entire element to implement fluid sealing, structural support and electrical connection to the electrocaloric layers. In operation, heat transfer working fluid flows back and forth between the chambers past the electrocaloric regenerator. The in-plane design offers efficient thermal isolation by enabling the EC module between the two diaphragm actuators.

1.3.2 Cooling Mechanism

The EC-based thermodynamic refrigeration process in the cooler design, as illustrated schematically in Figure 1.8, includes four steps: (A) Heat absorption: the fluid absorbs heat from the cold side chamber region; (B) Polarization: the EC material temperature is increased by applying the electric field and the fluid absorbs heat from the EC material as it flows from the cold side to the hot side; (C) Heat rejection: the heat carried by the fluid is rejected to the hot side chamber region; (D) Depolarization: the fluid moves from the hot side to the cold side and releases heat to the EC material while the electric field is turned off simultaneously to lower the EC temperature. Through periodic cycling, net heat is extracted from the cold fluid chamber and released to the hot chamber, and the fluid reaches its lowest temperature in the cold side. The design and analysis details of EC cooler operation is not within the scope of this thesis and it can be found in [26].

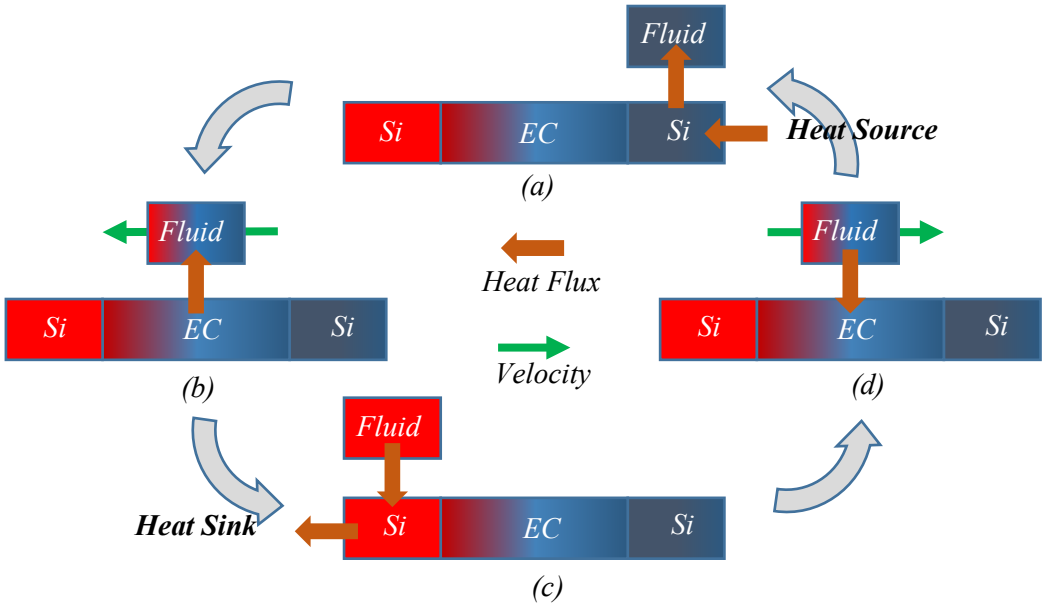

Figure 1.8. The thermodynamic refrigeration cycle of a fluid element based on the EC effect.

1.4 Thesis Overview

In this thesis, an active refrigerating system in millimeter scale based on electrocaloric materials and MEMS techniques, are designed and investigated to be expected to realize a high cooling performance. The thesis mainly focuses on the design, analysis, fabrication and test of the large stroke electrostatic actuated PDMS-on-silicon micro-pump for the electrocaloric micro-cooler.

Chapter 1 introduces the background of active cooling technology and the motivation of the thesis. It also gives a brief introduction of the configuration of the electrocaloric micro-refrigerating system. As mentioned in section 1.3, the refrigeration system mainly includes two key components: the electrostatic micro-pump and the electrocaloric regenerator. These two

parts are designed and fabricated separately and then assembled together. The electrostatic micro-pump is the major contribution of this thesis.

The electrostatic micro-pump consists of a moving electrode and a substrate electrode. The moving electrode is made of ultra-thin PDMS membrane with embedded metal mesh, and the substrate electrode is made of 3D shaped silicon. Prior to discuss the details of micro-pump, Chapter 2 introduces the fabrication of the ultra-thin PDMS membrane, the characterization of its mechanical properties, and its transfer to the silicon cavity. Fabrication of ultra-thin (1 μm to 20 μm thickness) PDMS films is enabled with a hexane dilution process and an underlying gelatin release layer. The release and transfer of these films over large areas (> 5 cm) allows measurement of the thickness-dependent (1 μm to 500 μm thickness) and process-dependent (metal evaporation and subsequent reactive ion etch patterning on PDMS) mechanical properties of ultra-thin PDMS membranes. This is the groundwork for designing and fabricating the moving electrode of the micro-pump.

Chapter 3 introduces a modified grayscale lithographic method that enables a wide range of grayscale levels resulting in a smooth etched silicon curved surface for the substrate electrode of the micro-pump. The spun photoresist is overexposed through a grayscale mask, and then immersed in a timed etch in over dilute developer resulting in robust control of the designed resist shape through the weak development. Different dilution ratio and developing time also give flexibility for creating different heights and profiles of the photoresist to account for the undesired variations in traditional grayscale lithography process without redesign of the masks.

The design, simulation, fabrication and actuation tests of large stroke electrostatic micro-pump are presented in Chapter 4. The thin PDMS moving electrode creates a highly compliant

diaphragm. The curved spline-shaped silicon substrate significantly reduces electrostatic actuation voltage. Combining the effects of the compliant diaphragm and the "zipper" electrode gap, an ultra-large (100 μm) diaphragm displacement is achieved, giving a displacement volume of 1 μL/stroke and a pumping rate of 60 μL/min at 1 Hz..

Chapter 5 discusses the electrocaloric regenerator, the second key component of the refrigerating system. The design concept and fabrication of electrocaloric regenerator are introduced first, and then the thermal, electrical and structural tests of electrocaloric P(VDF-TrFE-CFE) terpolymer are investigated. All results suggest that this polymer is a promising material for micro-scale cooling application.

Assembly of the micro-pumps and the electrocaloric regenerator to create the micro-cooler is the topic of Chapter 6. The multi-physics finite element simulations including heat transfer are examined for the full system level. The assembly process and preliminary tests are then discussed.

Chapter 7 gives the summary of the thesis and future work for the electrocaloric micro-cooler.

The thesis is part of a larger collaborative effort on a DARPA ACM program involving graduate students Dongzhi Guo (thermal modeling & analysis, electrocaloric materials testing), Ying-Ju Yu (electrocaloric materials molecular dynamics modeling and fabrication) in the mechanical engineering department, and Andrew Slippey (test bed setup and thermal performance testing) at Advanced Cooling Technologies, Inc. (ACT) in Lancaster, PA. Their collaborative contributions are attributed in various parts of this prospectus.

1.5 Thesis Contribution

The contributions of this thesis will be as follows:

1. A first prototype micro-cooling system is designed, built and tested based on the electrocaloric effect and MEMS techniques. The system can achieve 15°C temperature drop with 5 W/cm^2 cooling power flux and *COP* equals to 4 at 150 V/μm electrical field and 10 Hz operating frequency according to the simulations [27]. The device provides a feasibility test of the scaling of the EC cooling principle and may enlighten other researchers to explore more possibility for fulfill the requirement for today's increasing demand of electronics cooling. (Jinsheng Gao's contribution: electrostatic micro-pump modeling and fabrication; Dongzhi Guo's contribution: thermodynamic system simulations; Jinsheng Gao and Dongzhi Guo's joint contribution: EC material performance testing; Ying-Ju Yu's contribution: EC material fabrication and printed box development)
2. A large stroke electrostatically actuated micro-pump is designed with a snap-in action to enable an ultra large volume displacement (1 μL) for a MEMS-based system [28]. Each pump chamber element comprises a compliant PDMS diaphragm over a 3D shaped silicon electrode that enables electrostatic "zipper" operation. The electrostatic micro-pump demonstrates to drive a heat transfer fluid. The pump features an ultra-large stroke (100 μm), whose design and fabrication can inform that of other large electrostatic stroke actuators.
3. A gray-scale lithographic process flow with silicon deep-reactive-ion-etching is refined for fabrication of a smoother curved Si structure compared to traditional grayscale lithography due to the approach enabling more grayscale levels (5 times more UV dosage range compared to traditional grayscale lithography). This modified grayscale process with a timed, dilute development enables the creation of more predictable and smoother (RMS: 0.05 μm to 0.1 μm

compared to 0.4 μm to 0.5 μm for traditional grayscale lithography [29]) 2.5D microstructures compared to traditional grayscale photolithography.

4. Fabrication of ultra-thin (1 μm to 20 μm thickness) polydimethylsiloxane (PDMS) films is enabled with a hexane dilution process and an underlying gelatin release layer [30]. Ultra-thin (down to 2 μm thickness) PDMS membranes with embedded meander metal electrodes having 2 μm lines and spaces are fabricated. Two layers of electrodes are embedded to enable push-pull actuation pump behavior with an approximate 1 μm-thick PDMS electrode spacer layer. Patterning multi-layer metallic thin films with such small resolution directly onto thin elastomeric substrates leads an improvement for fabricating microelectrodes and interconnects for soft electronics.
5. Release and transfer of large areas of ultra-thin PDMS films, particularly with small feature size embedded electrodes [30], opens a promising route for fabricating new compliant MEMS and electronic devices. PDMS films down to 1 μm thickness and up to 5 cm in diameter are successfully fabricated and released for the first time [31].
6. The release and transfer of these films over large areas allows measurement of the thickness-dependent and process-dependent mechanical properties of ultra-thin PDMS membranes [31]. The mechanical properties of PDMS films thinner than 20 μm is reported for the first time. The effective Young's modulus of 1 μm-thick PDMS, measured by bulge testing, is approximately 10 times larger than that of the bulk material. Metal evaporation and subsequent reactive ion etch patterning on PDMS increases its Young's modulus due to the increase the cross-link formation and hardening of the surface. The results are meaningful in design and fabrication of soft electronics, microsensors, microvalves, and micropumps.

7. Multi-physics finite element analysis (FEA) is performed for the electrostatic actuated pumps as well as the full micro-cooling system. The simulations combine heat transfer, solid nonlinear mechanics, mechanical contact, electrostatic force, laminar fluid flow, and moving mesh conditions. The success of combining many physics in one FEA may benefit for other complex system simulations. (Jinsheng Gao's contribution: micro-pump simulations; Dongzhi Guo's contribution: thermal dynamics simulation)
8. An infrascope measurement on electrocaloric thin films is demonstrated as a convenient and effective method to measure the dynamic thermal response of the electrocaloric material to electrical signals [32]. (Dongzhi Guo: joint testing of EC films)
9. The X-ray diffraction measurements on P(VDF-TrFE-CFE) terpolymer film with different electrical fields are performed for the first time [32]. The ferroelectric phase peak gradually grows and the relaxor ferroelectric phase peak reduces with the increase of the electric field. These experimental results successfully demonstrate the structural transformation of P(VDF-TrFE-CFE) terpolymer. (Dongzhi Guo: joint XRD testing)

Chapter 2 Fabrication, Transfer and Material Characterization of Ultra-Thin PDMS Membrane

2.1 Introduction

The micro-cooling system mainly includes two active components: an electrostatic micro-pump and an electrocaloric regenerator. The two components are designed and fabricated separately and then assembled together. The electrostatic micro-pump consists of a moving electrode and a fixed substrate electrode. The moving electrode is made from an ultra-thin polydimethylsiloxane (PDMS) layer with meandered metal interconnect to create a highly compliant diaphragm. In this chapter, fabrication and transfer of ultra-thin PDMS membranes along with characterization of their mechanical properties are discussed. This represents the groundwork for designing and fabricating the moving electrode of the micro-pump.

Polydimethylsiloxane has been widely used in flexible electronics, optics and biomedical research due to its excellent biocompatibility, physical properties and fabrication flexibility [33]. It is adopted in a wide range of applications such as large-area conformable displays [34] and stretchable integrated circuits [35]. In addition, due to their elastic properties, PDMS structures can function as active mechanical components in MEMS devices [36]. Significant research efforts have been made to develop MEMS actuators made of PDMS not only because they are low-cost and lightweight but also due to their large actuation strain and potential medical applications. Takao et al. reports a MEMS microvalve with PDMS diaphragm for integrated

blood tests [37], and Jeong et al. reports a peristaltic PDMS micropump for a μTAS application [38].

Due to its low Young's modulus and relatively high adhesion to handle substrates, fabrication of ultra-thin free-standing films (below 20 μm) in PDMS is difficult. As a result, mechanical properties of PDMS below 20 μm thickness are not reported. Further, patterning micron-scale electrode sizes (below 10 μm) is challenging due to poor microfabrication compatibility. Traditional patterning techniques on PDMS include transfer printing and shadow masking. Those techniques limit the minimum patterned feature size to about 100 μm. In literature reports on PDMS film transfer to date, the thickness of PDMS is generally in the mm range [39]. Moreover, in the design and modeling of microactuators, the Young's modulus of PDMS is commonly considered a constant with same value as the bulk material. However, as PDMS membranes become thinner, the resulting material properties change [40]. Also, the additional fabrication steps needed to build these actuators, such as metal deposition, lithography, and reactive ion etching on PDMS, can alter its Young's modulus. Many researchers have reported stress-strain data for PDMS at the millimeter and centimeter scale by using nano-indentation [41], by stretching tensile test structures [42,43], and by inflating membranes with differential pressure [44]. It is hypothesized that thinner films form stronger cross-linked networks of polymer chains [40], resulting in the Young's modulus of PDMS increasing with decreasing thickness. Gerratt et al. [45] reported on characterization of 20 μm-thick, 6 μm-wide PDMS springs that fit within tensile-test structures made in a silicon-on-insulator MEMS process. The work, performed with the fixed size, quantified PDMS properties that change with processing parameters.

In this chapter, fabrication of ultra-thin (1 μm to 20 μm thickness) PDMS films is enabled with a hexane dilution process and an underlying gelatin release layer. This can release and transfer greater than 3" diameter, 1 μm-thick PDMS diaphragms. This technique enables investigation of the mechanical properties of ultra-thin membranes as a function of thickness with or without changes caused by the effects of metal deposition and patterning. The effective Young's modulus of PDMS membranes of various thicknesses down to 1 μm, as well as the influence of metal deposition and patterning are measured.

Both the fabrication of the ultra-thin PDMS diaphragm and characterization of its mechanical properties are critical for the micro-pump design. In order to achieve large stroke, ultra-thin PDMS with embedded metal electrodes are needed to create a highly compliant membrane as the diaphragm of the micro-pump actuator. Transferring the ultra-thin PDMS diaphragm to the silicon fixed electrode and cavity, as well as predicting diaphragm stiffness as a function of thickness are essential for the micro-pump design, as detailed in the next chapter.

2.2 Fabrication of Ultra-Thin PDMS Films

Four types of PDMS films are designed and fabricated for characterizing their mechanical properties and validating their performance in the micro-pump. Films include: (1) normal PDMS films of different thicknesses (50 μm to 500 μm), (2) thin and ultra-thin PDMS films of different thicknesses (1 μm to 50 μm), (3) thin and ultra-thin PDMS films of different thicknesses (2 μm to 50 μm) with evaporated metal patterned and then embedded within PDMS, and (4) thin and ultra-thin PDMS films of different thicknesses (2 μm to 50 μm) etched in a reactive-ion etching system.

Two types of release layer for the transfer process are developed: (1) a C_4F_8 polymer

anti-adhesion layer for lift-off release process (with heat release tape assistance), and (2) a gelatin sacrificial layer for a dissolving release process.

2.2.1 Normal PDMS Films of Different Thicknesses (50 µm - 500 µm) with C_4F_8 Polymer Sacrificial Release Layer

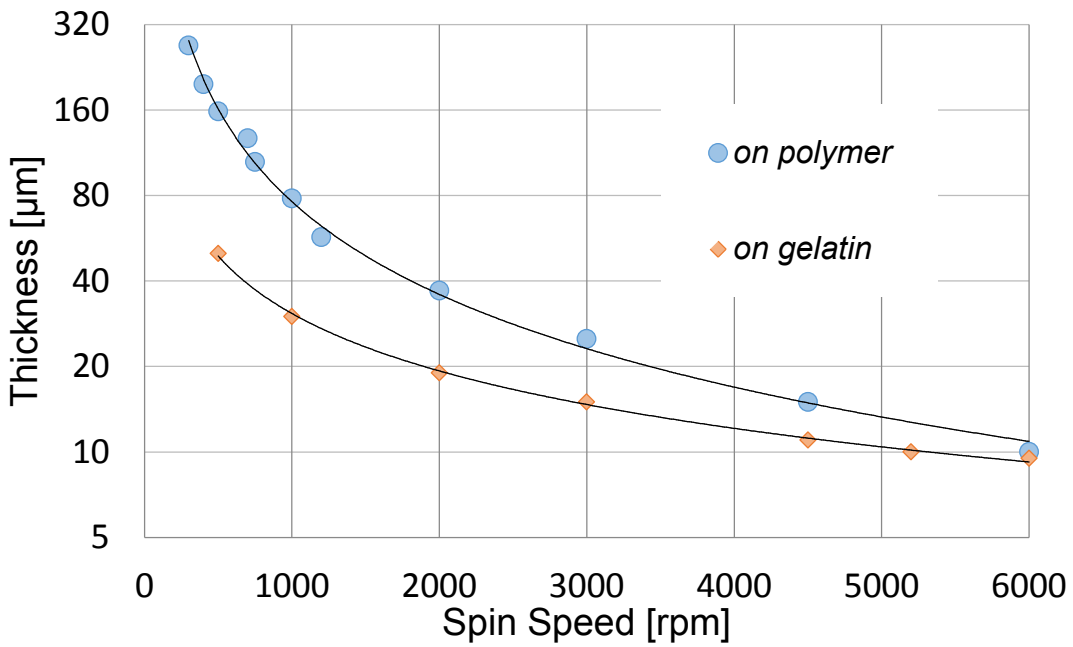

Figure 2.1. Thickness of PDMS as a function of spin speed (30 s at maximum speed for polymer and 150 s at maximum speed for gelatin).

A 100 nm-thick anti-adhesion polymer film deposited from a C_4F_8 precursor in an inductively coupled plasma (ICP) tool (SPTS Technologies; Newport, UK) is used as a release layer to peel off PDMS films over 50 µm thick PDMS (Sylgard 184, Dow Corning; Midland, MI) is created by mixing pre-polymer gel and the cross linker in a 10:1 (w/w) ratio [46]. To fabricate membranes with different thicknesses, the thickness as a function of spin speed for PDMS on polymer release layers are characterized. PDMS spun on the C_4F_8 polymer starts at 500 rpm for 6 s, accelerated to full target speed for 30 s, and then decelerated at 170 rpm/s^2. The thickness on

C_4F_8 polymer release layers versus spin speed curves are shown in Figure 2.1. The samples are then cured for 12 h in an oven at 70°C.

2.2.2 Thin PDMS Films of Different Thicknesses (1 μm - 50 μm) with Gelatin Sacrificial Layer

Gelatin powder (250 bloom, Modernist Pantry) is first dissolved in warm water (10 wt%). The solution is spun on a silicon handle substrate at 1000 rpm for 2 min with infrared heating applied simultaneously to prevent the gelatin from hardening, and then baked in a 40°C oven to form a 2 μm-thick sacrificial gelatin layer. Later, this layer will be dissolved in water to release ultra-thin PDMS membranes under 50 μm thick. The C_4F_8 polymer technique is easier than the gelatin release; however films under 50 μm thick have low yield using the polymer technique, motivating the need for parallel development of the gelatin release technique. (The details are discussed in Section 2.3.)

To fabricate membranes with different thicknesses, the thickness as a function of spin speed for PDMS on gelatin are characterized. The film is spun on gelatin at 500 rpm for 30 s, accelerated to half of the target speed for 30 s, spun at full target speed for 150 s, and then decelerated slowly at 170 rpm/s^2. The thickness versus spin speed curves are shown in Figure 3. However, due to the speed limitation of the spinner (≤ 6000 rpm), the films' thicknesses are constrained to be thicker than 10 μm. To achieve thinner films, the PDMS solution is created by first mixing pre-polymer gel and the cross linker in a 10:1 (w/w) ratio and then diluted with hexane (ACS grade, Fisher Scientific) with different mixing ratio. The mixture is spun at 6000 rpm for 150 s to create ultra-thin PDMS films. The thickness versus diluted ratio curves are shown in Figure 2.2.

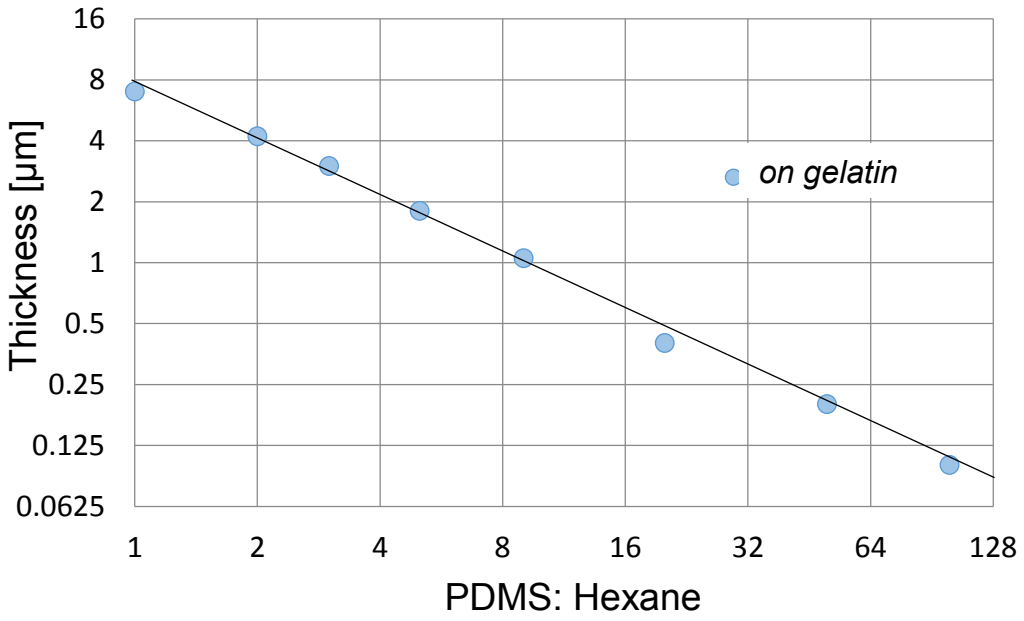

Figure 2.2 Thickness of PDMS as a function of mix ratio with Hexane. The solution is spun at 6000 rpm for 150 s.

2.2.3 Thin Multi-Layer Films (11 µm) with Cr/Au/Cr Electrodes and C_4F_8 Polymer Sacrificial Release Layer

PDMS films with Cr/Au/Cr electrodes are made with three sequential thin-film layers, 1 µm PDMS, 0.2 µm Cr/Au/Cr, 10 µm PDMS, following the process flow in Figure 2.3. A completed film with embedded metal electrodes, shown in Figure 2.4, serves as the actuator diaphragm in the micro-pump. In this release process, the C_4F_8 polymer film is deposit on the substrate (Surface Technology System (SPTS), Newport, Wales (UK); power: 600 W; pressure: 10m T; C_4F_8 flow: 85 sccm; deposition time: 1 min) and acts as an anti-adhesion layer for eventual lift-off release of the completed PDMS diaphragm. The Cr/Au/Cr metal layers are then sputtered (Perkin Elmer, Waltham, MA; power: 50 W; pressure: 5 mT; flow: 20 sccm; deposition time: 12 s/ 300 s/ 12 s) on the first PDMS layer, and are ion milled (Commonwealth Scientific

Corp., Alexandria, VA; voltage: 500 V; current 40 mA; pressure: 1e-4 T; angle: 22.5 ºC; etching time: 20 min) in a serpentine mesh pattern to prevent buckling and breakage that may be caused by intrinsic or actuation stresses [47]. Flood exposure is performed after the regular lithography for final photoresist (AZ P4210; AZ Electronic Materials, Merck KGaA, Darmstadt, Germany) removal by AZ developer after patterning, since PDMS can be swelled by acetone. Low temperature treatments (<70°C) and slow temperature ramping rates are applied in the process steps to prevent potential metal cracking within PDMS films on the Si substrate due to different temperature expansion coefficients. The details of process flow and recipes can be found in Appendix 1.

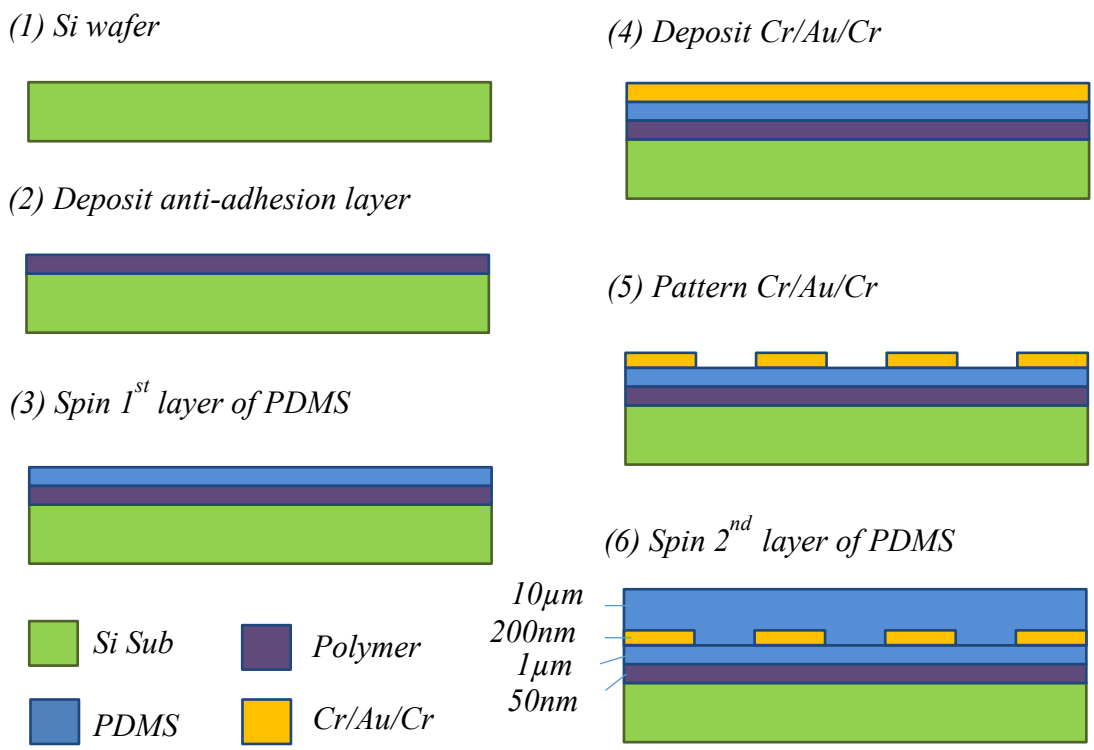

Figure 2.3. The process flow for the fabrication of PDMS film with Cr/Au/Cr electrode embedded.

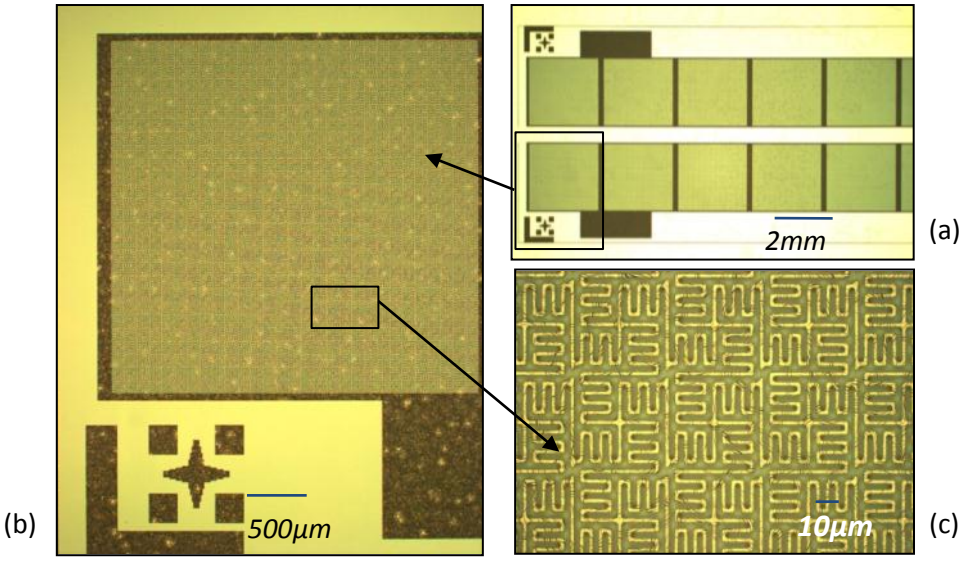

Figure 2.4. The optical microscope picture of a fabricated PDMS film with three-layer sandwich structure. The metal mesh line embedded in the PDMS is 2µm wide in layout. (a) six connected diaphragms with bonding pads. (b) zoom in picture for one diaphragm. (c) zoom in picture for serpentine mesh.

2.2.4 Thin Multi-Layer Films of Different Thicknesses (2 µm - 50 µm) with Cr/Al/Cr Electrodes with Gelatin Sacrificial Layer

Figure 2.5 illustrates the process flow for embedding Cr/Al/Cr metal electrodes into thin PDMS layers over the gelatin sacrificial layer. For creating the PDMS membrane with embedded metal electrodes, Cr/Al/Cr metal layers (5 nm/200 nm/5 nm) are evaporated (Ultek (Perkin-Elmer) E-Beam Evaporator; voltage: 6 kV; deposition rate 1 Å/s) on the gelatin surface, and wet etched in a serpentine mesh pattern to prevent buckling and breakage [47]. A second layer of 1 µm-thick PDMS is spun and cured to seal the metal layer. Stress, which leads to the wrinkles seen in Figure 2.6(b), is induced during evaporation due to the different thermal expansion

coefficient values of the gelatin, PDMS and metals. However, the wrinkles are not evident after the metal is patterned into repeating serpentine lines.

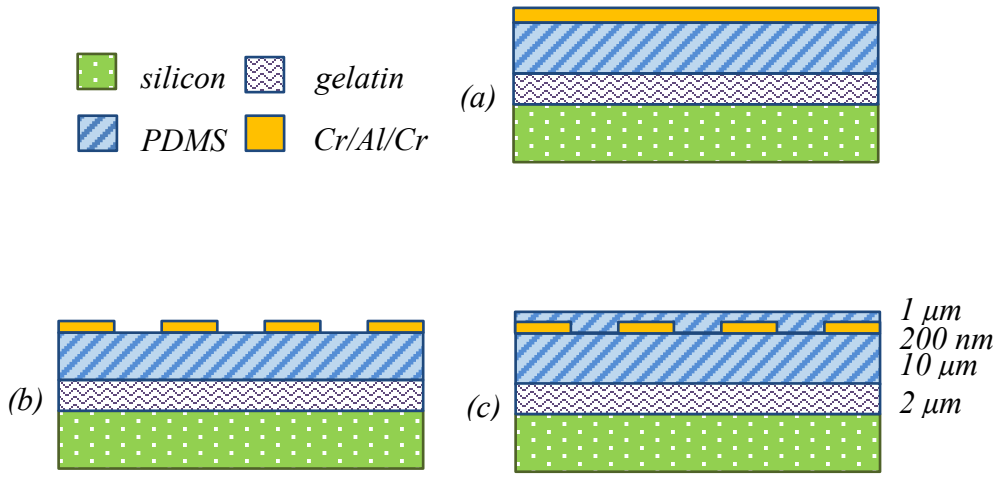

Figure 2.5 Process flow of PDMS membranes with embedded electrodes: (a) sequentially spin-cast gelatin sacrificial layer, spin-cast first PDMS layer, and evaporate Cr/Al/Cr layers on the handle substrate, (b) pattern metals, (c) spin-cast second PDMS layer.

Al deposition by sputtering on the multi-layer stacks is also investigated. Figure 2.7 shows the comparison among Al sputtering on a PDMS/Si substrate, Al sputtering on a PDMS/gelatin/Si substrate, and Al evaporated on a PDMS/gelatin/Si substrate. Cracks appear on the Al sputtered on the gelatin. The sputtering occurs at higher processing temperature compared to evaporation, resulting in larger temperature expansion mismatch with the gelatin. The temperature-induced expansion during the Al evaporation on gelatin creates the wrinkles but it is not large enough to crack the Al films.

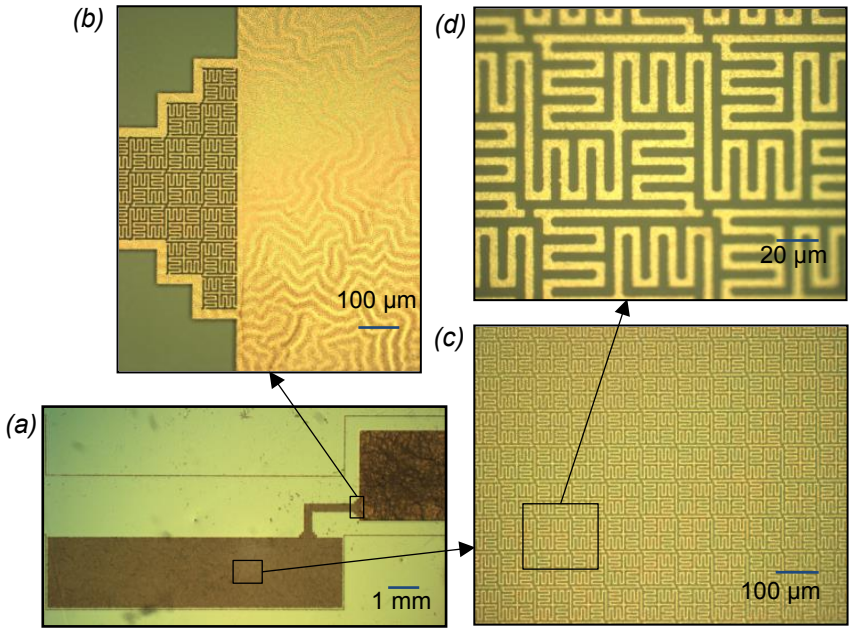

Figure 2.6 Optical microscope photos of a fabricated membrane: (a) wide-angle view of diaphragm with bonding pad for micro-pump application, (b) non-patterned area (bonding pad) showing wrinkles, (c) and (d) serpentine mesh patterned area (diaphragm) showing no wrinkles.

When gelatin is spun on the Si substrate, thicker gelatin films form on the edge of the Si substrate due to its viscosity properties. This has a huge impact for the following contact lithography for the metal layer. The gap between the mask and sample due to the thicker gelatin edge will cause diffraction of UV light resulting in a blurring pattern after exposure, shown in Figure 2.8. To solve this problem, the sample is spun and covered by the photoresist after evaporation, and then it is flood exposed. Then the sample is diced into 2.5 cm by 4 cm dies and thicker edges are discarded. The lithography can be done successfully on each die (smallest feature down to 2 µm). The final results are shown in Figure 2.9.

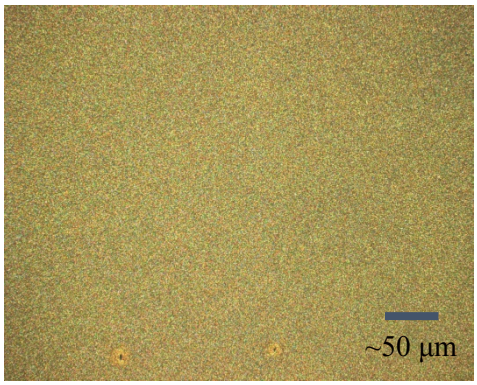

(a) Al (100 nm) sputtering on PDMS/Si

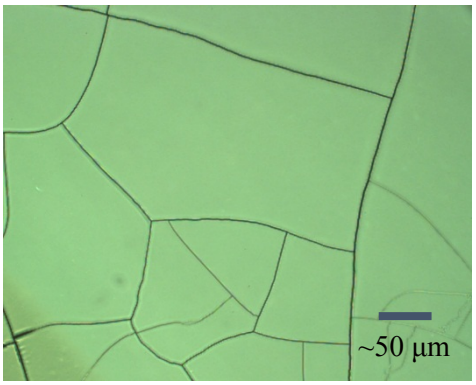

(b) Al (100 nm) sputtering on PDMS/gelatin/Si

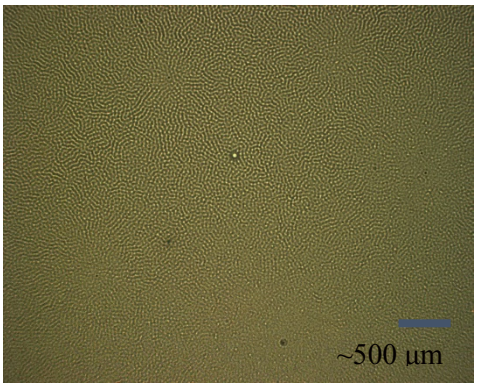

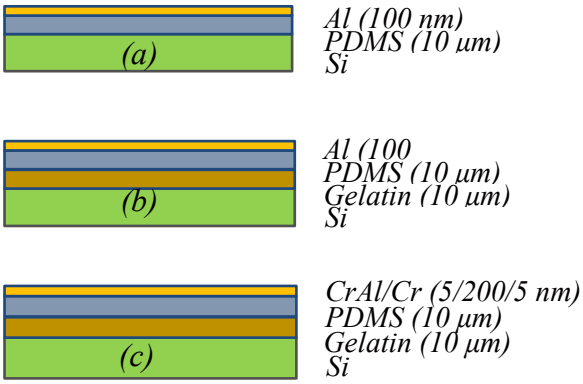

(c) Cr/Al/Cr (5 nm/200 nm/5 nm) evaporated on PDMS/gelatin/Si

Figure 2.7 comparison among (a) Al sputtering on PDMS/Si substrate, (b) Al sputtered on PDMS/gelatin/Si substrate and (c) Al evaporated on PDMS/gelatin/Si substrate.

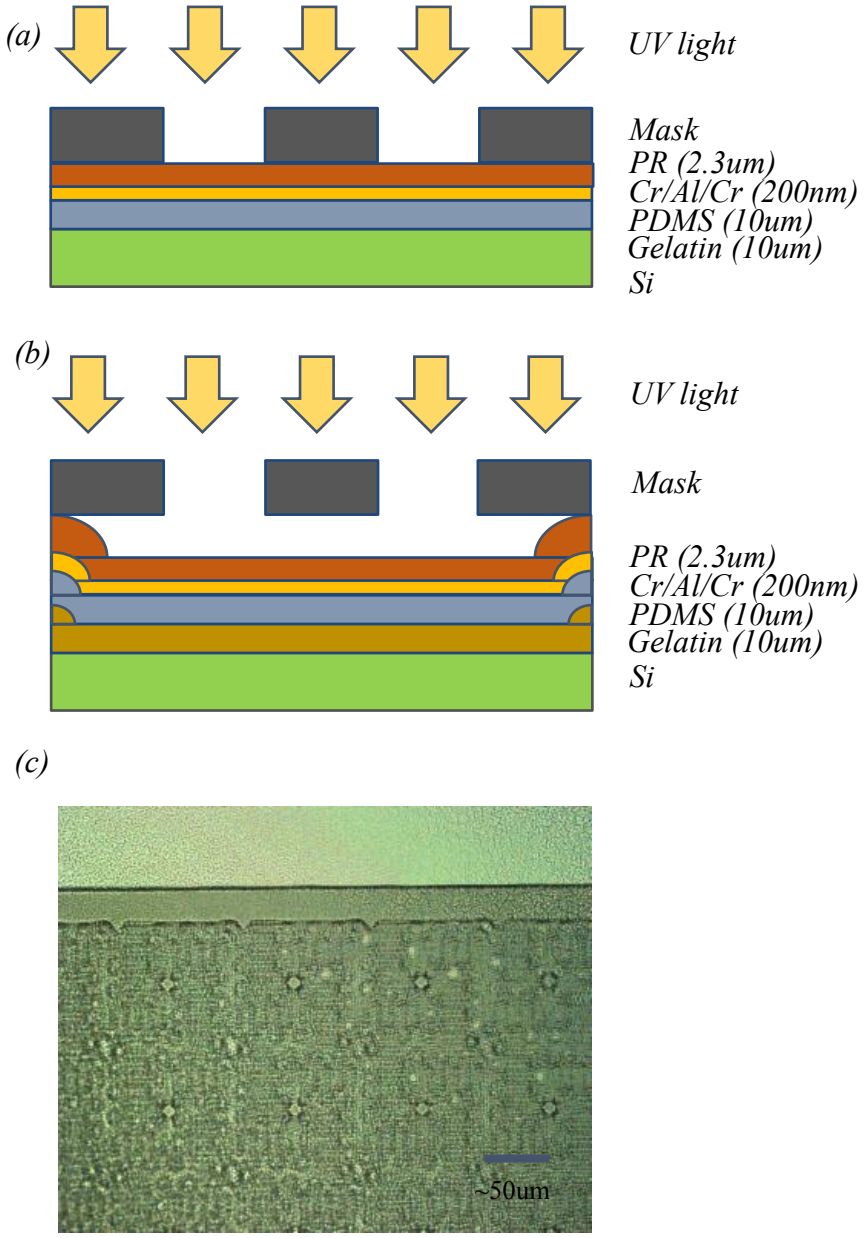

Figure 2.8 (a) Normal lithography on metal/PDMS/gelatin multi-layers. (b) Lithography on metal/PDMS/gelatin multi-layers with thicker gelatin edges. (3) Lithography results from (b). The patterns are blurred.

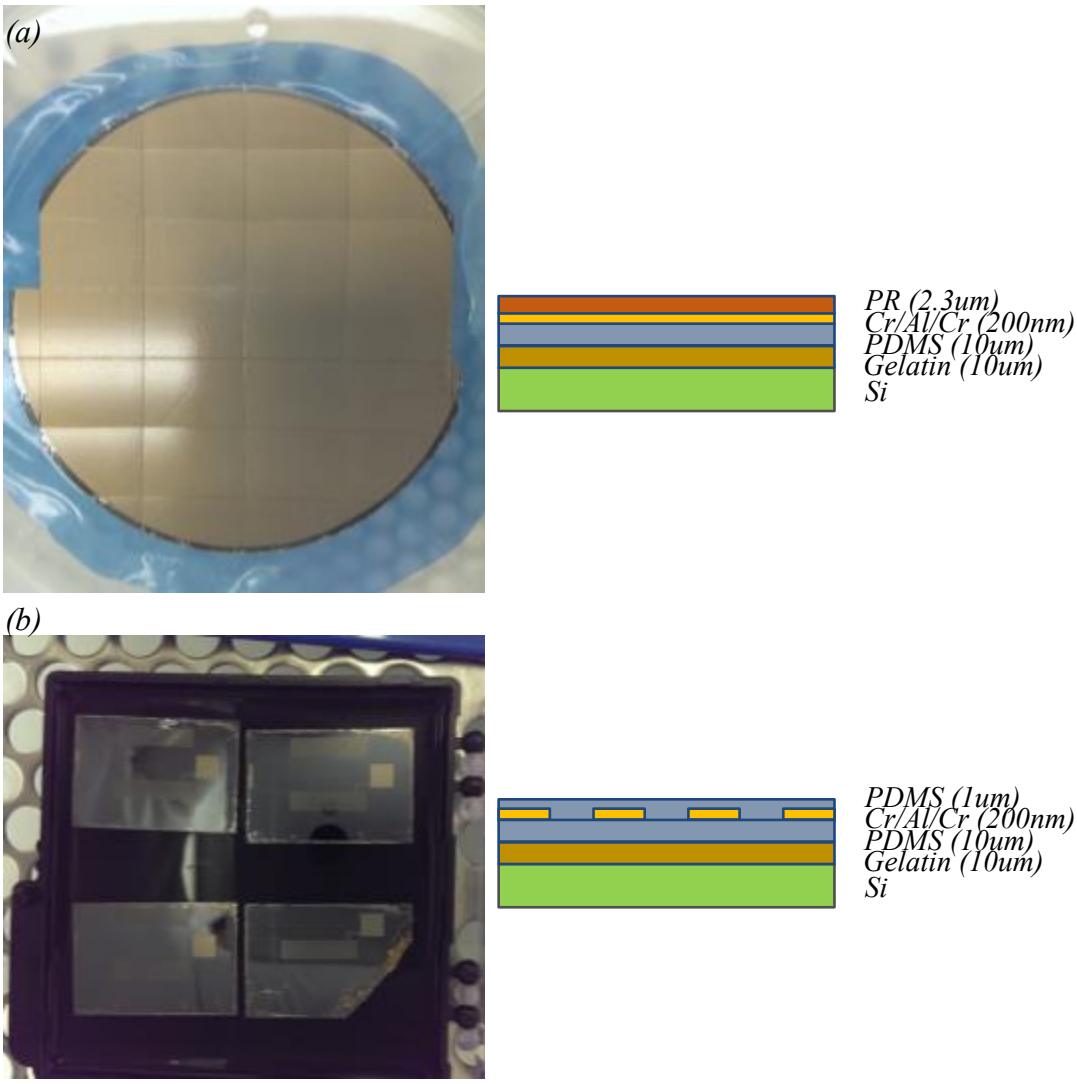

Figure 2.9 (a) Sample is diced after evaporation. Some of corner dies without high gelatin edge can still be used (b) Final results after lithography and pattern for each die. The close up view for the diaphragm mesh is shown in Figure 2.6.

2.2.5 Thin PDMS Films of Different Thicknesses (2 μm - 50 μm) with Reactive-Ion Etch

Select PDMS samples were etched in a reactive-ion etch system (Trion Phantom III RIE etcher, Trion Technology, Clearwater, FL; pressure: 60 mT, CF_4 flow: 30 sccm, O_2 flow: 10 sccm, forward power: 100 W). A 200 nm Al mask is deposited (CVC Connexion Sputtering System, CVC, Inc., Rochester, NY; power: 250 W; pressure: 5 mT; flow: 20 sccm; deposition time: 666 s) and patterned (wet etching) on the plain PDMS as a hard mask to define the PDMS. The process flow is shown in Figure 2.10 (a). The etch rate is measured as 0.25 μm/min. The pictures of etched PDMS films are shown in Figure 2.10 (b).

The above method is not compatible with PDMS membranes with an embedded Al electrode because the last step (wet Al etching) will attack the electrode as well. An 1/16 inch aluminum shadow mask was machined in a first attempt pattern the PDMS, but it was found the plasma and CF_4/O_2 plasma reaction extends into the gap between shadow mask and sample substrate due to the incomplete contact between them. This plasma damages the undesirable etching areas. An alternative approach is a 1 mm PDMS mask is that molded and coated with thin C_4F_8 layer on the bottom side to avoid PDMS-PDMS sticking during the etching process. The process flow is shown in Figure 2.11. The compliant property of the PDMS mask ensures the excellent contact between mask and the sample, which prevents the plasma attack under the mask. This RIE process enables direct patterning of PDMS and creates contact cuts in the PDMS to access the embedded metal for the 2 mm by 2 mm bonding pads of micro-pump, shown in Figure 2.12.

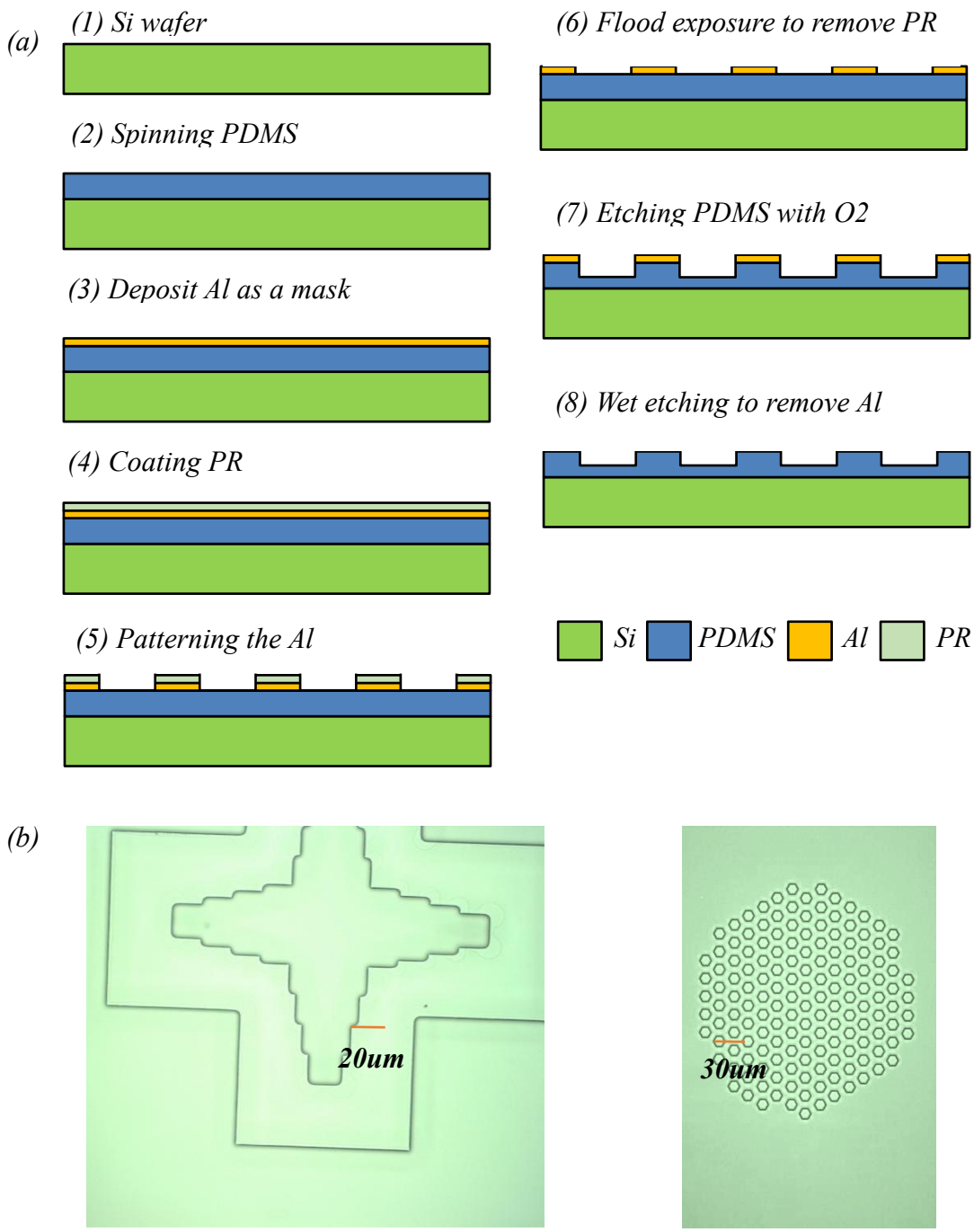

Figure 2.10 (a) Process flow for Al deposited and patterned on the plain PDMS as a hard mask to define the PDMS. (b) Ethed PDMS films.

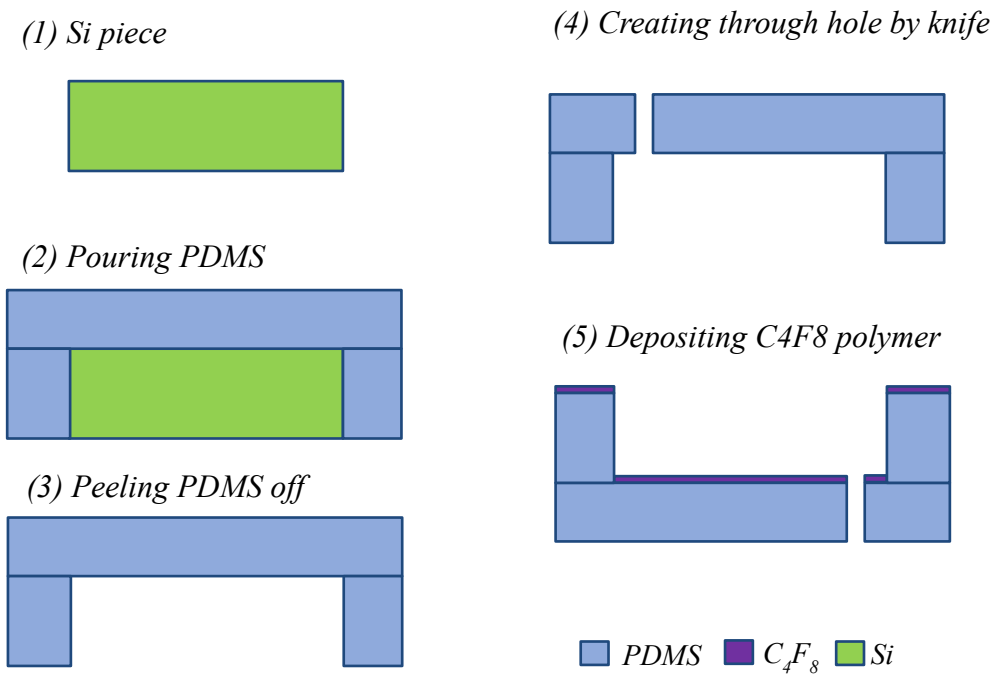

Figure 2.11 . The process flow for molding PDMS mask.

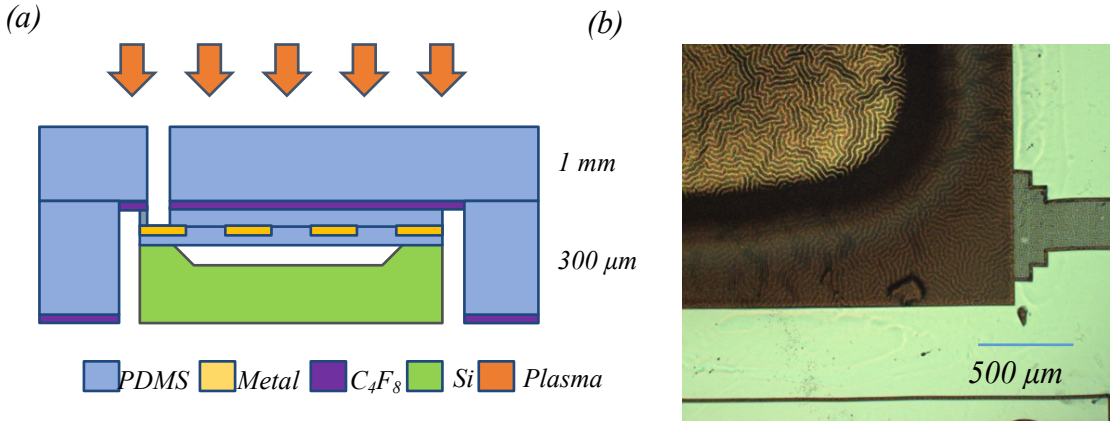

Figure 2.12 (a) PDMS etching in RIE system with molded PDMS as a shadow mask. (not scaled) (b) Final etching results for the bonding pad. The winkles can be seen in the figure because the bonding pad is not patterned as mesh.

2.3 Release and Transfer of Ultra-Thin PDMS Film

2.3.1 Release and Transfer Thin PDMS Film with Heat Release Tape

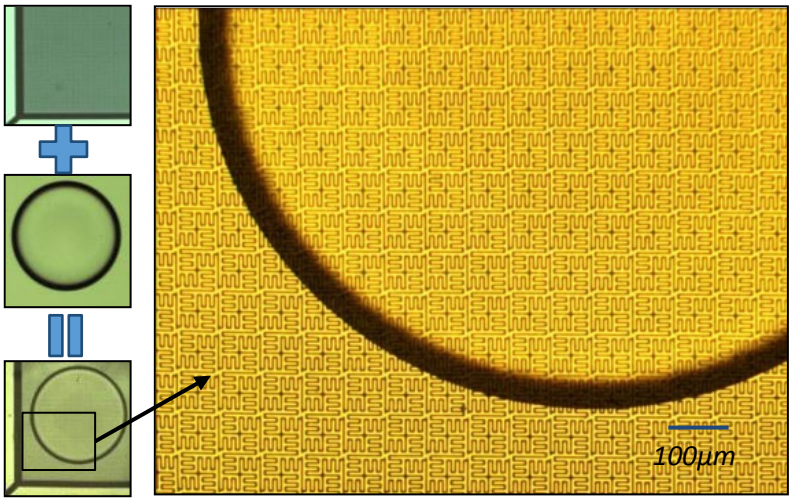

Figure 2.13. The optical microscope picture showing a PDMS film with embedded electrode hanging over a fabricated Si chamber.

A silicon chamber is formed by deep reactive-ion etching (DRIE) in the SPTS system and acts as the counter electrode for the diaphragm. The PDMS film is released and transferred onto the chamber by a lift-off process (Figure 2.14). 150°C Heat release tape (HRT) (Nitto Denko Corp., Osaka, Japan) is attached to the fabricated PDMS film, which is then peeled from the Si substrate. Both the peeled-off film and fabricated chamber are treated in O_2 plasma for 30 s to activate the PDMS to increase adhesion. The two parts are aligned and placed into contact using a device bonder (Besi/Laurier M9, BE Semiconductor Industries N.V., Duiven, The Netherlands). The heat release tape is then removed at 150°C. The final assembled miniature pump is shown is Figure 2.13. The optical microscope picture shows the PDMS film with embedded electrodes hanging over the Si chamber. The above transfer procedure works reliably for devices around

1 mm in size and PDMS thicker than 10 μm, but the thermal expansion mismatch of the PDMS and heat release tape leads to buckled diaphragms and torn films for larger areas and thinner films.

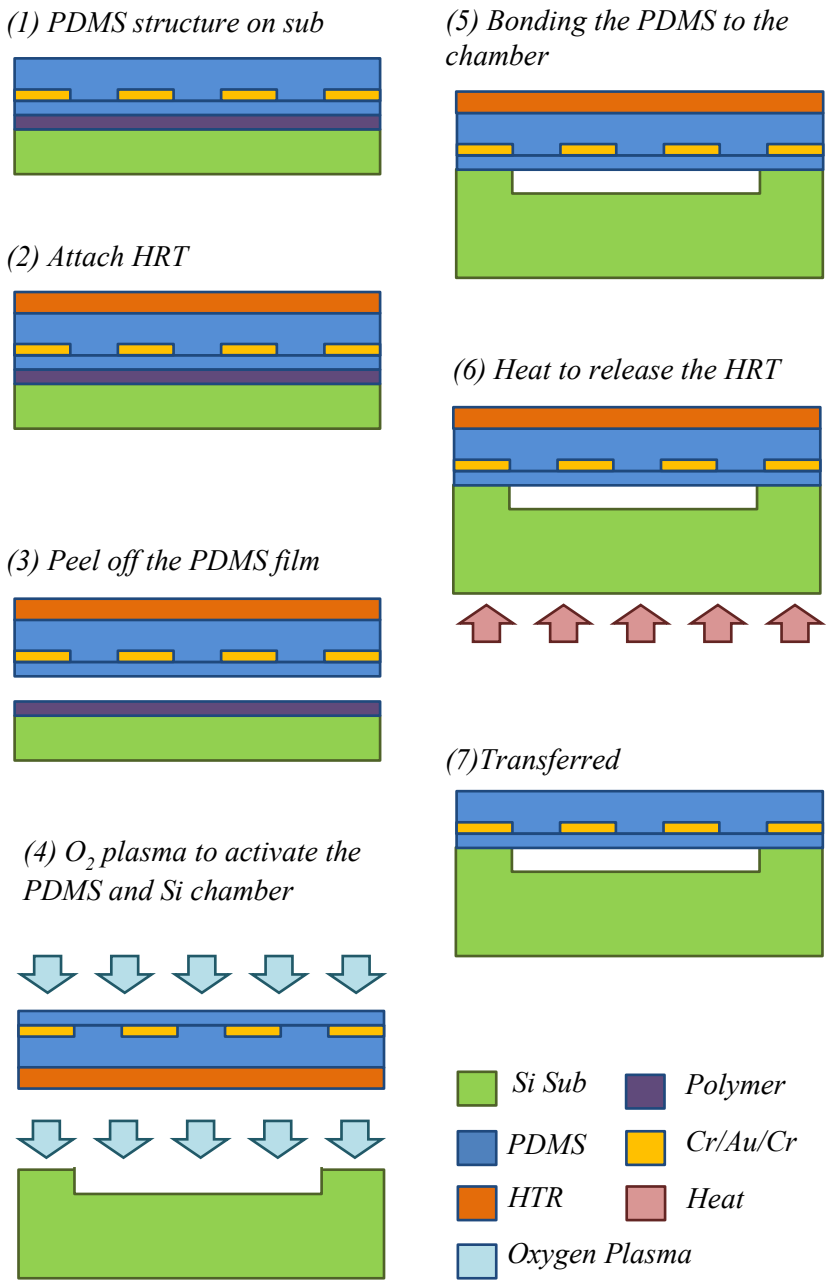

Figure 2.14. The process flow for the transferring of ultra-thin PDMS film onto the fabricated Si chamber with heat release tape assistance.

2.3.2 Release and Transfer Large Area Ultra-Thin PDMS Film with Gelatin Sacrificial Layer

An alternative way for releasing the PDMS film by using gelatin as a sacrificial layer enables PDMS transfer for much larger areas. The gelatin was chosen as a release layer due to its low processing temperature and high water solubility.

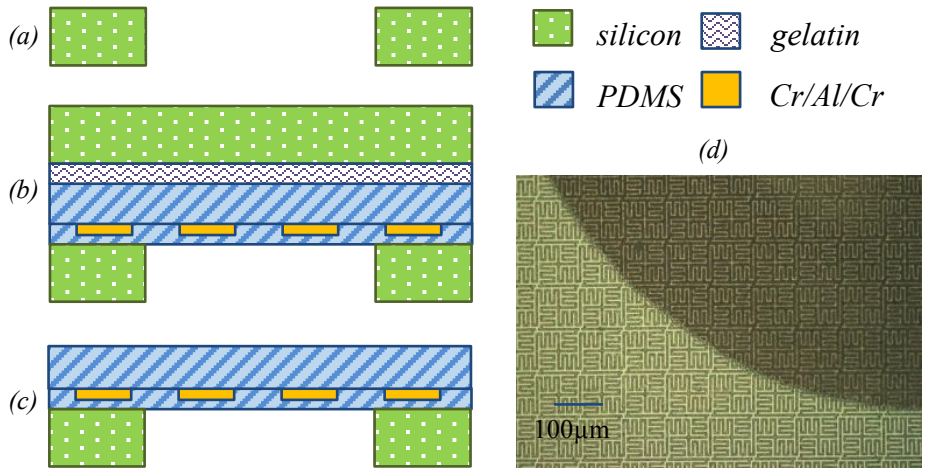

Figure 2.15: Process flow for transfer and release of PDMS diaphragm. (a) Si device substrate with through hole and microfluidic channels. (b) Bonding of membrane and handle substrate to device substrate. (c) Release of handle substrate. (d) Completed membrane over through hole.

The process flow for transfer of the PDMS diaphragm on the Si chamber is shown in Figure 2.15. After 30 s O_2 plasma surface activation treatment of the PDMS diaphragm and of the Si chamber to increase adhesion, the two components are aligned and bonded using a device bonder (Besi/Laurier M9). The assembled device is then dipped in 40°C warm water. The gelatin

layer dissolves after about 2 hours, releasing the PDMS layer. The sample is then dried in an oven at 40°C for 30 min. The final released sample is shown is Figure 2.15 (d).

This process enables the release and transfer for large area ultra-thin PDMS films. Shown in Figure 2.15 and Figure 2.16, a large (>5cm) diameter, uniform 10 μm-thick and 1 μm-thick PDMS film, respectively, were successfully released from the substrate after attaching to an aluminum release ring coated with vacuum grease. Dissolution of the gelatin for such a large area takes about 20 hours in 40°C water.

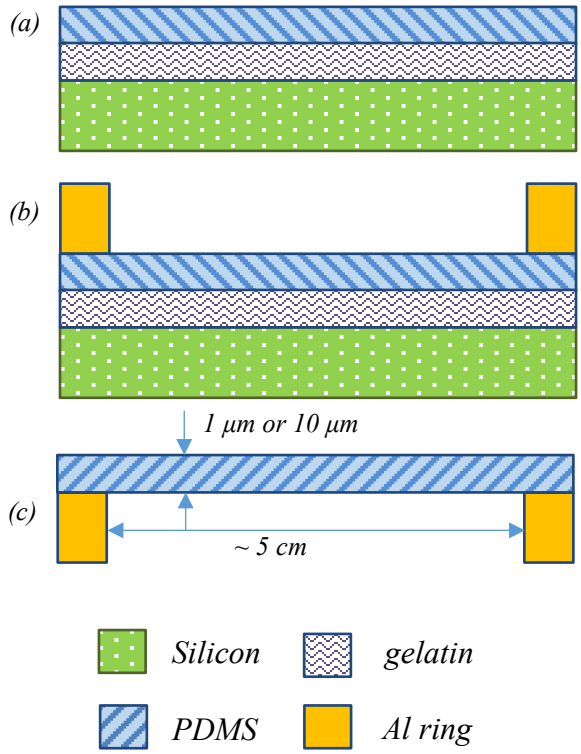

Figure 2.16: Release and transfer of large area (> 5 cm diameter) PDMS layer by using gelatin sacrificial layer and aluminum ring. (a) Si substrate with gelatin sacrificial layer and 1 μm PDMS layer. (b) Al ring is attached on the PDMS with vacuum grease. (c) Release the substrate.

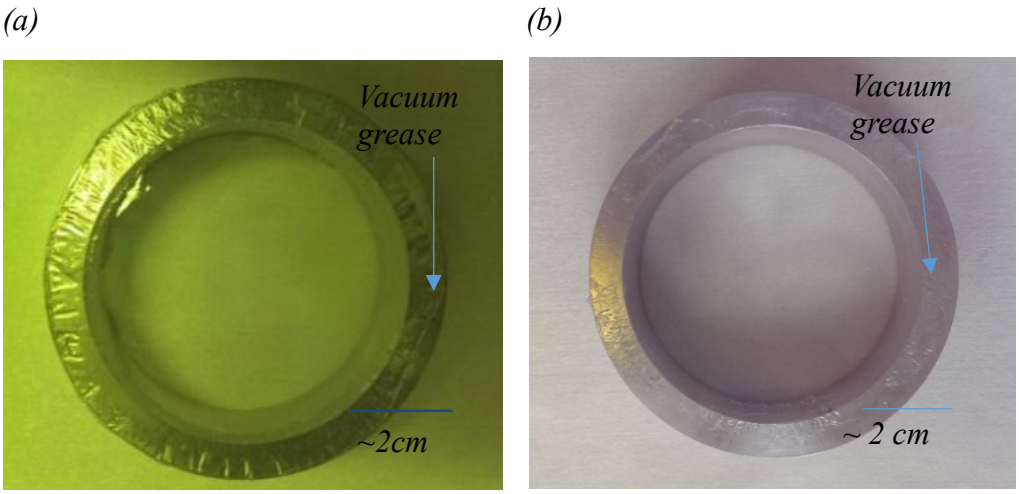

Figure 2.17 (a) Released 10 μm thick 5cm large PDMS ultra-thin film. (b) Released 1 μm thick 5cm large PDMS ultra-thin film.

The release and transfer of ultra-thin (down to 1 μm) large area (larger than 5 cm) PDMS films, particularly with small feature size (down to 2 μm) embedded electrodes, opens a promising route for fabricating new compliant MEMS and electronic devices.

2.4 Characterization of Mechanical Properties of Ultra-Thin PDMS Films

Commonly, in the design and modeling of actuators made of PDMS, the Young's modulus of PDMS is considered a constant with same value as the bulk material. However, as PDMS membranes become thinner, the resulting material properties change [40]. Also, other fabrication steps needed to build these actuators, such as metal deposition, lithography, reactive ion etching on PDMS, can also change its mechanical properties. In this section, experimental results on the effective Young's modulus of PDMS membranes of various thicknesses, as well as

the influence of various fabrication process steps is reported. Predicting the stiffness of the diaphragm as a function of thickness is critical for developing the micro-pump actuator in the next chapter.

2.4.1 Experimental Setup

All four types of PDMS discussed in previous section are tested for their mechanical properties. A silicon test device substrate is micromachined with a circular through hole and microfluidic feed lines on its top surface by deep reactive-ion etching (DRIE) in the SPTS ICP tool. The PDMS film on the handle substrate is transferred onto the device substrate by using the gelatin dissolution transfer method introduced in the previous section.

The mechanical strength is measured by inflating clamped circular PDMS membranes with differential pressure. As shown Figure 2.18, the experimental setup includes a pressure source, pressure measurement setup, and side image acquisition. The cylindrical air cavity on the backside of the PDMS membrane is connected through the silicon microfluidic feed lines to a bulk PDMS manifold, which connects to polyethylene tubes on the front side to both the pressure source and the pressure sensor. The backside of the sample is bonded to another bulk PDMS layer to seal the air cavity. A constant pressure is applied to cause the membrane to deform. The pressure source is provided by a gas-tight syringe (Hamilton GASTIGHT syringe, 1700 series, 0.5 mL; Hamilton Laboratory Products, Reno, NV), and pressure is measured by a differential pressure sensor (OMEGA PX409 series, range 0-7000 Pa; Omega Engineering, Inc., Stamford, CT). The cross-sectional images of the inflated PDMS membrane are obtained by a CCD camera (IDS LX series, Baumer Ltd., Southington, CT). The sample is placed on a six degree-of-freedom (DOF) stage to adjust the view and focus of the camera. The maximum deflection with

pressure is extracted from the images. A series of side images of deformed PDMS membrane at three different pressure values is shown in Figure 2.19. In this example, the diameter of the circular hole on the Si substrate is 2 mm and the thickness of the PDMS is 56 µm. The shooting angle is slightly tilted to the front side of the camera to increase the clarity and sharpness of image due to the better reflection of light on the transparent PDMS. The tilt correction is taken into account when extracting the membrane deflections. A dot of silver paste is placed in the center of the diaphragm to allow for the easier measurement of the center deflection.

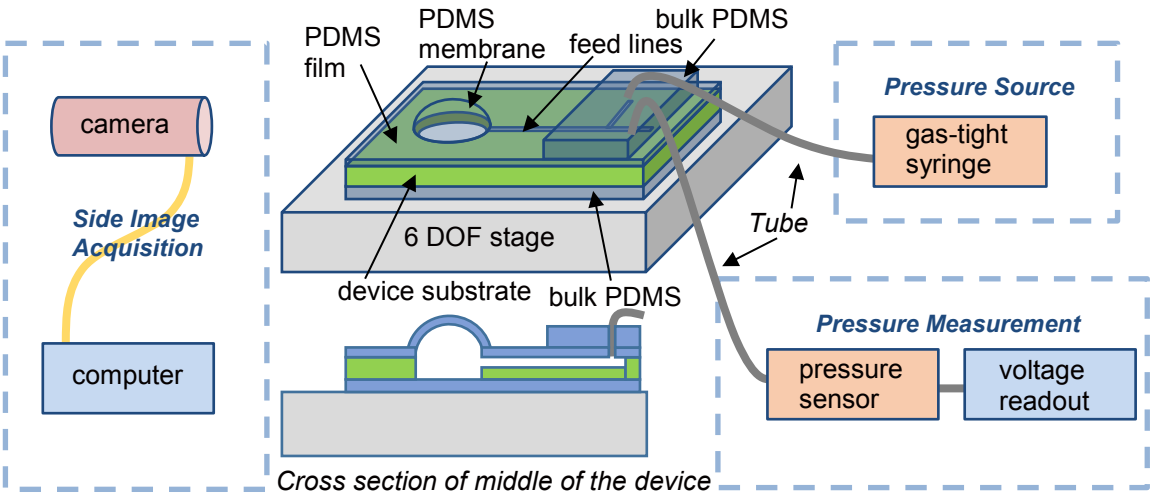

Figure 2.18: Illustration of the setup for characterizing PDMS membrane stiffness.

The effective Young's modulus of different types of PDMS membranes are also measured by using a nanoindenter (Hysitron TI 900 TriboIndenter; Hysitron, Inc., Minneapolis, MN). The tip installed on the probe is a Berkovich tip, which has a half angle of 65.35 degrees [48] (shown in Figure 2.20). The PDMS membranes are transferred to a silicon substrate etched with a circular through hole. During the indentation, the tip indents the center of the membranes, and the displacements of the tip along with the force applied on the tip are recorded.

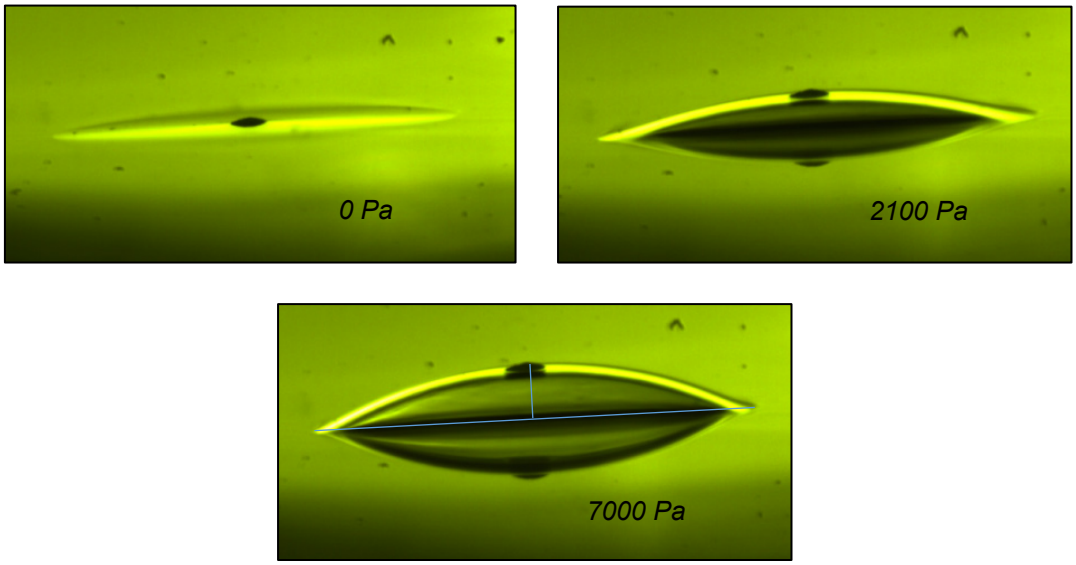

Figure 2.19: A deformed PDMS membrane under different pressures. The diameter of membrane is 2 mm and the thickness is 56 μm.

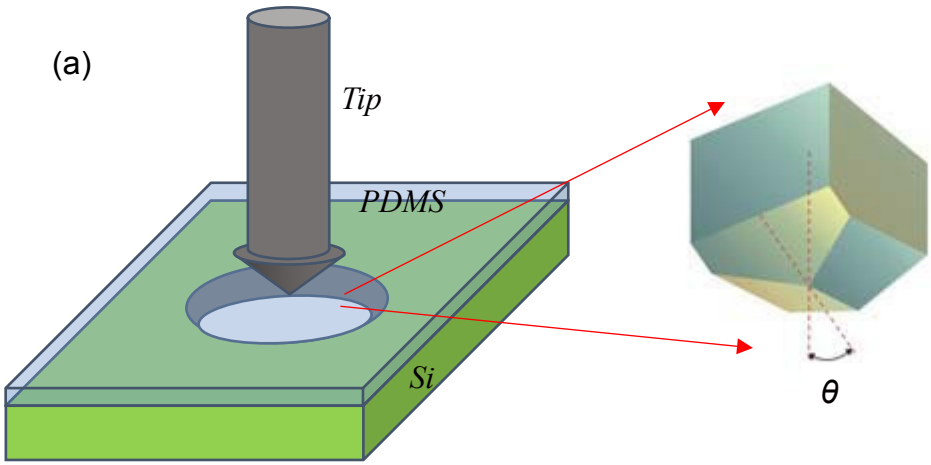

Figure 2.20 (a) PDMS's effective Young's modulus is also measured by the nanoindentation. (b) The tip of the probe is is a Berkovich tip, which has a half angle, θ, of 65.35 degrees.

2.4.2 Theoretical Model and Finite Element Simulations

Linear elastic models do not accurately describe the rubber-like behavior. Hyperelasticity [49] is a type of constitutive model for stretchable material, where the stress-strain relationship derives from a strain energy density function:

$$\mathbf{S} = \frac{\partial W}{\partial \mathbf{E}} \tag{2.1}$$

where **S** is the second Piola–Kirchhoff stress and **E** is the Lagrangian Green strain, and W is the strain energy density.

The Mooney–Rivlin solid model [50, 51] is a hyperelastic material model where the strain energy density function is a linear combination of two invariants of the left Cauchy–Green deformation tensor.

$$W = C_1\left(J^{-\frac{2}{3}} I_1 - 3\right) + C_2\left(J^{-\frac{4}{3}} I_2 - 3\right) \tag{2.2}$$

where C_1 and C_2 are empirically determined material constants; I_1 and I_2 are the first and the second invariant of the unimodular component of the left Cauchy–Green deformation tensor and

$$J = \det(\mathbf{F}) \tag{2.3}$$

where **F** is the deformation gradient, defined as

$$F_{ij} = \frac{\partial x_i}{\partial X_j} \tag{2.4}$$

where $\boldsymbol{x}$ is the deformed vector and $\boldsymbol{X}$ is the reference vector.

The constants C_1 and C_2 are determined by the fitting predicted stress from the above equations to experimental data.

Based on Rivlin's original paper [51] and J. Selby et al. [52], a more specific theoretical model is built for inflation of a clamped circular incompressible hyperelastic membrane with uniform pressure. Compared to the FEA model, this model dramatically simplified the calculation. Consider a thin planar circular PDMS membrane with radius a, and uniform thickness h_0, in its zero stress state. The PDMS is clamped to the Si substrate, forming a freestanding membrane over the hole. The cylindrical coordinates (r, φ, $z = 0$) define the position of a material particle in the membrane before inflation, where φ is the angle around the z-axis. The inflation gauge pressure $p(r)$, will carry a material particle at point Q to the point Q' in the deformed state, defined by the coordinates (ρ, φ, ζ) (Figure 2.21 (a)). The meridional, circumferential, and normal directions to the membrane surface are denoted by the subscripts 1, 2, and 3, respectively. The other nomenclature is: ξ is the arc length of the membrane (constant φ) from the membrane pole (*i.e.*, center) Q_0 to Q; θ is declination angle from the ζ axis; κ_1 and κ_2 are the membrane curvatures; λ_1 and λ_1 are the stretch ratios and T_1 and T_2 are the stress resultants.

Through combinations, rearrangements, and derivatives of basic relationships from differential geometry associated with the deformed membrane configuration, the seven first-order differential equations describing the membrane are

$$\frac{d\rho}{dr} = \lambda_1 \cos\theta \tag{2.5}$$

$$\frac{d\zeta}{dr} = -\lambda_1 \sin\theta \tag{2.6}$$

$$\frac{d\theta}{dr} = \kappa_1 \lambda_1 \tag{2.7}$$

$$\frac{d\kappa_1}{dr} = -\frac{1}{T_1}\left(\frac{dT_1}{dr}\kappa_1 + \frac{d\kappa_2}{dr}T_2 + \frac{dT_2}{dr}\kappa_2\right) \tag{2.8}$$

$$\frac{d\kappa_2}{dr} = \frac{1}{r\lambda_2}\frac{d\rho}{dr}\left(\kappa_1 - \kappa_2\right) \tag{2.9}$$

$$\frac{d\lambda_1}{dr} = \frac{1}{\lambda_2\left(\lambda_1^4\lambda_2^2 + 3\right)}\left(\frac{\lambda_1^4\lambda_2^4}{2h_0\left(C_1 + C_2\right)}\frac{dT_1}{dr} + \lambda_1\frac{d\lambda_2}{dr}\left(\lambda_1^4\lambda_2^2 - 3\right)\right) \tag{2.10}$$

$$\frac{d\lambda_2}{dr} = \frac{1}{r}\left(\frac{d\rho}{dr} - \lambda_2\right) \tag{2.11}$$

The boundary conditions are satisfied as $\rho = 0$, $\theta = 0$, $\lambda_1 = \lambda_2$, $\kappa_1 = \kappa_2$, $\kappa_1 T_1 + \kappa_2 T_2 = p$ at $r = 0$ and $\zeta = 0$, $\lambda_2 = 1$ at $r = a$. Due to the simplification of the model, the value of θ at $r = 1$ is not constrained to 90°. This constraint would lead divergent numerical results when transferring the boundary conditions from $r = a$ to $r = 0$.

The above equations are solved for the seven variables ρ, ζ, θ, λ_1, λ_2, κ_1 and κ_2 as a function of r. The calculation is achieved by aid of symbolic manipulation computer software (Mathematica, Wolfram Research, Champaign, IL). Due to the incompressive property of PDMS, C_2 is assumed to be zero in the calculation, and the effective Young's modulus of PDMS is [51]

$$E_{eff} = 6\,(C_1 + C_2) \approx 6\,C_1 \tag{2.12}$$

which is found as the initial slope of the stress-strain curve. One example of the theoretical model results (Figure 2.21 (b)) shows a set of inflated membrane deflection under different pressure conditions.

In addition to the theoretical model discussed above, finite element analysis (FEA) (COMSOL Multiphysics 4.3; Burlington, MA) is used to simulate the inflated PDMS membrane

deflection. The Mooney-Rivlin model is chosen in the solid mechanics module in COMSOL for calculating the deformation behavior of the PDMS membrane. One example simulation result is shown in Figure 2.23.

Simulations of the nanoindentation are also performed in COMSOL Multiphysics. The 2D axis-symmetric simulations are examined instead of 3D to reduce the complexity. The angle of the tip is simplified as 70 degree. The Mooney-Rivlin model is applied to the PDMS membrane, and the contact model is used between the PDMS and the tip. One of simulation examples are shown in Figure 2.24.

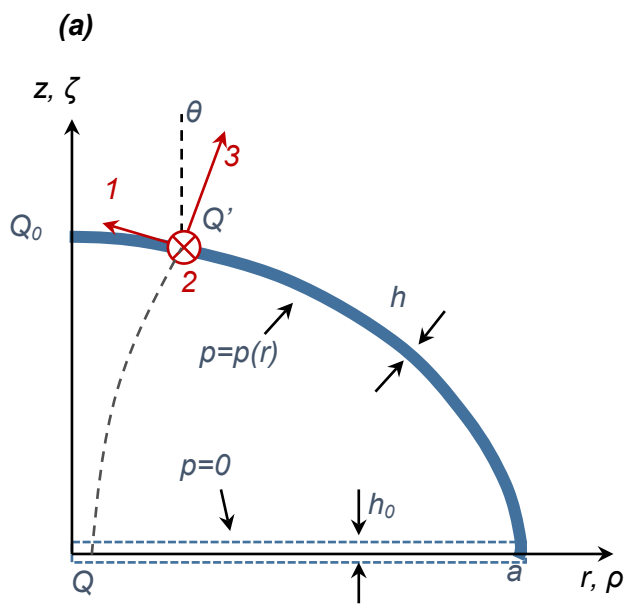

Figure 2.21: (a) Illustration of inflated circular PDMS membrane with its coordinates in an axisymmetric cross section view of half of the membrane.

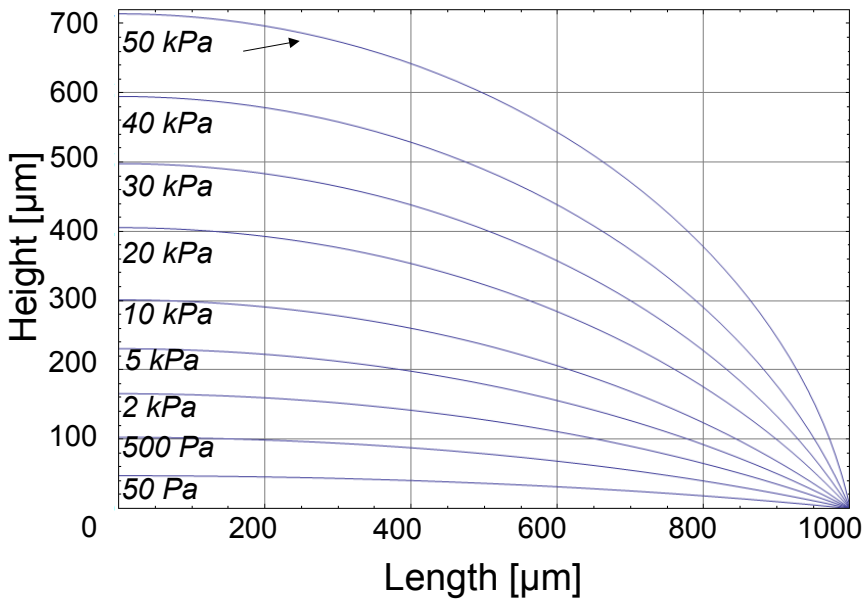

Figure 2.22. Theoretical calculations of deformed PDMS shapes. a = 1 mm, h_0 = 56 µm.

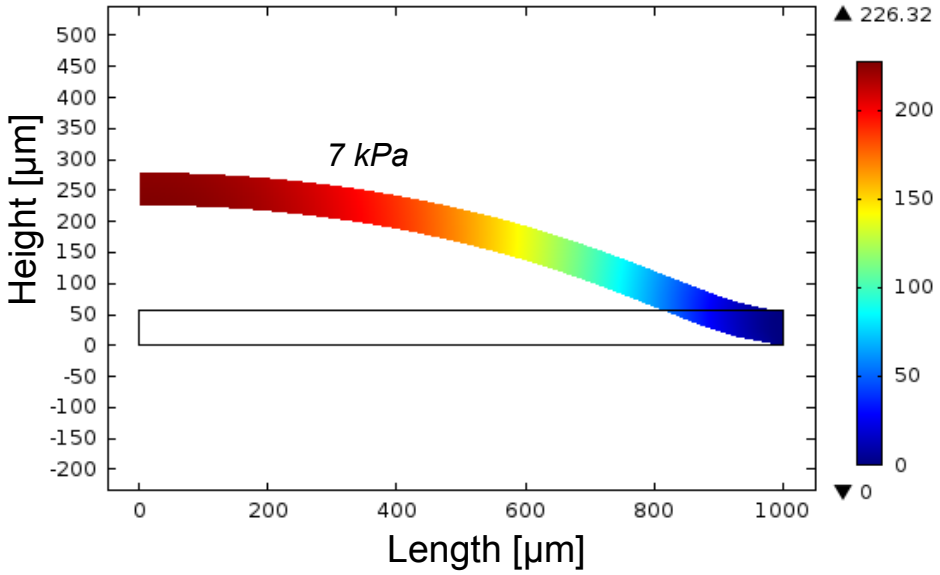

Figure 2.23: Example of a 2D axisymmetric FEA simulation of membrane displacement. a = 1 mm, h_0 = 56 µm, P = 7 kPa.

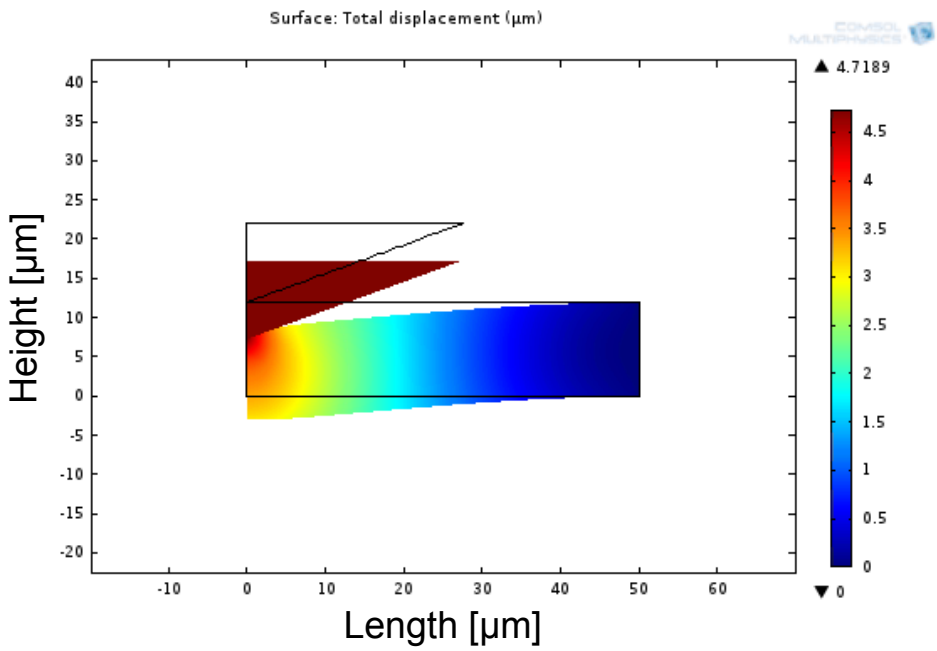

Figure 2.24 FEA simulation for nanoindentation. The 2D axis-symmetric simulations are examined instead of 3D to reduce the complexity. The membrane in the example is 12 μm thick and force applied is 70 μN.

2.4.3 Results and Discussion

Figure 2.25 is an example of the center displacements of plain PDMS membranes with increasing pressure from experimental measurements, from fitted calculation of the theoretical model, and from FEA simulations. The diameter of the membrane in the example is 2 mm and the thickness of the PDMS is 56 μm (10:1 (w/w) mixing ratio), 10 μm (10:1) and 120 μm (30:1) respectively. The Mooney-Rivlin parameter $C1$ and effective Young's modulus are extracted using the FEA simulations from the experimental measurements by the least squares method. The theoretical model uses these material parameter values to verify the FEA simulations. The theoretical, FEA and measured results match to within 10%. However, when the ratio of thickness to the radius of the membrane is greater than 1/10, the results from the theoretical

model become inaccurate and deviate from the FEA simulation results. This is because such relatively thick membranes cannot be simply modeled as thin shell structures. The results from Figure 2.25 also show the hyperelastic behavior at low stretch where the change in the displacement becomes smaller as pressure increases.

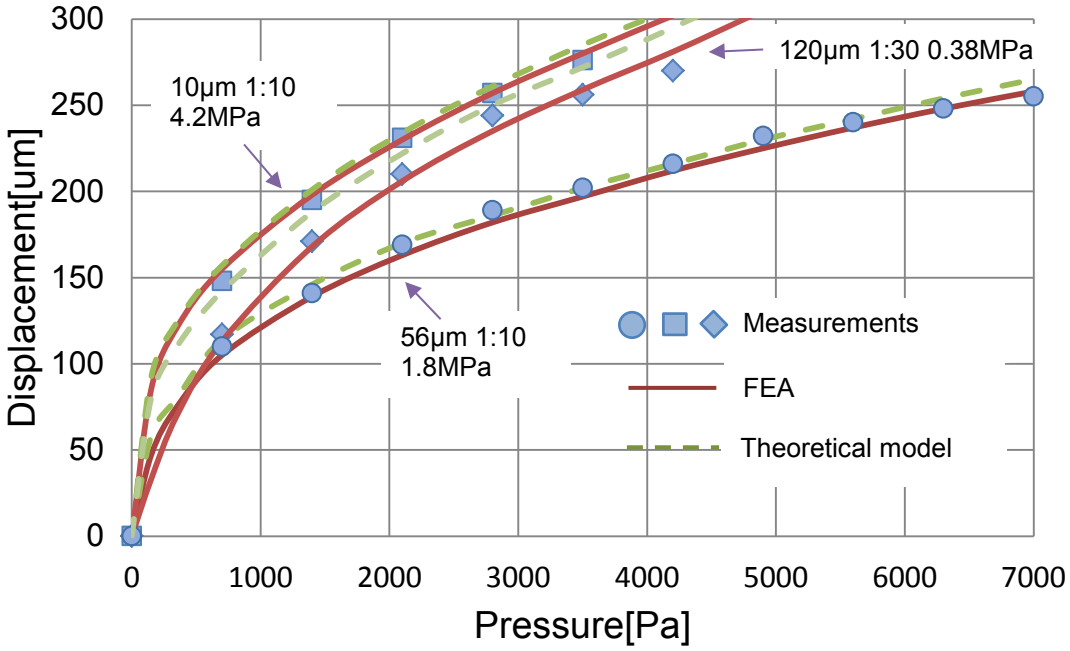

Figure 2.25: An example of deflections of inflated plain PDMS membranes with increasing pressure comparing experimental measurements, fitted calculation of the theoretical model, and finite element simulations. The membrane diameter is 2 mm.

Figure 2.26 shows the results of effective Young's modulus extracted by FEA least-square fit to the measurements of PDMS membranes with different thicknesses. At least three samples are tested for each thickness. The standard deviations are also showed as error bars. The trend clearly shows that the stiffness increases when the membrane becomes thinner. The

Young's modulus of 1 μm PDMS films (9 MPa) is 10 times larger than 500 μm films (0.9 MPa). It is believed that this is due to the thinner films forming stronger cross-linked networks of polymer chains in PDMS. These polymer chains are small with a diameter of about 0.7 nm, and they normally form random coils with dimensions in the range of about 10 nm [53]. It is suggested that the straight chains are desired to form stronger cross linked networks, and they could be stretched in the PDMS due to the spin coating process [40]. Random coiled polymer chains in PDMS solutions are subjected to shear forces due to the relative motion between the spinning wafer substrate and the viscous PDMS mixture. Higher angular velocities are required to achieve thinner PDMS membranes. The resultant increased shear stress acts on the membranes to create a greater fraction of straight polymer chains, resulting in stiffer PDMS membranes.

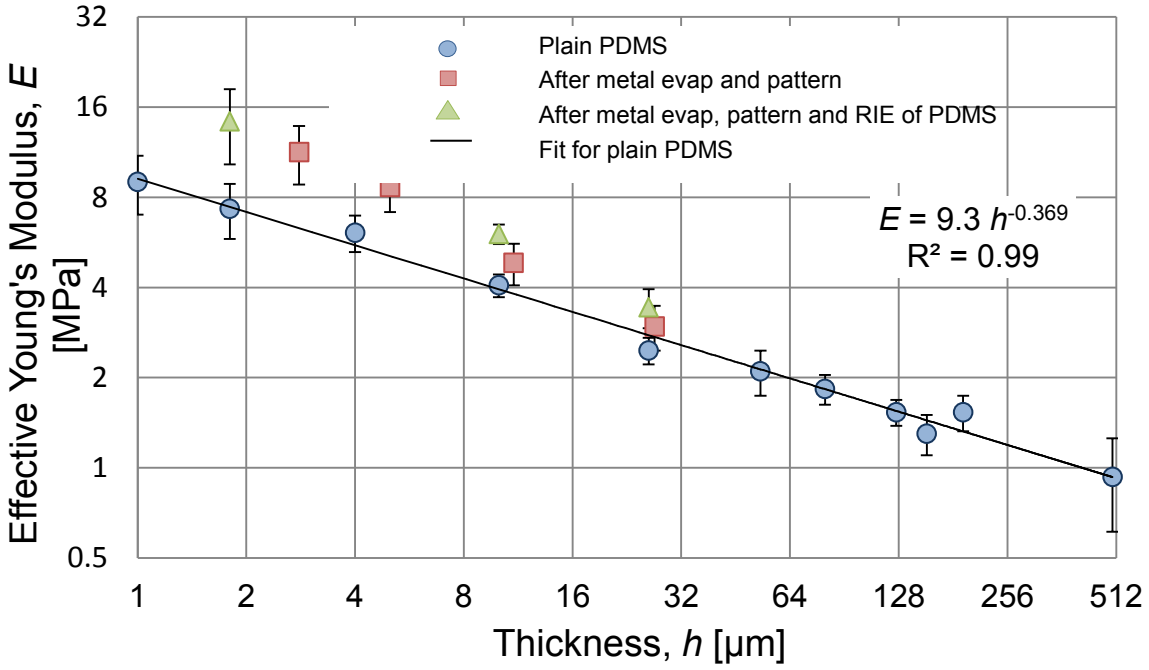

Figure 2.26: The effective Young's modulus of plain PDMS, PDMS after metal evaporation, and PDMS after RIE ashing, as extracted from membrane bulge tests.

Both the metal exposed to evaporation and RIE ashing of PDMS increase the membrane stiffness. The effect of the 1 μm sealing PDMS layer that is not exposed is taken account into consideration based on the data from plain PDMS measurements. The effective Young's modulus of 10 μm-thick films increases about 15% to 40% after Al evaporation and wet etch removal. As seen in Figure 2.6, wrinkles are formed due to TCE mismatch from heating of surface, even at very slow e-beam deposition rates (1Å/s). The wrinkle wave has periodicities about 30 μm and depth about 0.5 μm. Some other papers report this phenomenon, such as [54], but they claim the wrinkles remain after metal removal. These wrinkles disappear after either Al removal or Al patterning in our process; however, it is believed that the heating modifies the top portion of the PDMS, increases the formation of crosslinks [54,55], and results in an increase in effective Young's modulus.

After RIE of PDMS, the effective Young's modulus of 10 μm-thick films increases another 10% to 30% and the films' appearance changes from transparent to translucent. Ion bombardment from the O_2 plasma is found to harden the surface of PDMS, because the O_2 plasma converts a small portion of the surface of PDMS to SiO_x oxygen-rich material [56]. This effect also helps explain why post-processing on PDMS has greater influence on thinner films, leading to larger increases in their effective Young's modulus. Further increase of plasma power from the 100 W value reported here will enhance the etching rate of 0.25 μm/min, but will cause deeper hardened areas on the PDMS leading to stiffer films. Such high power plasmas can also crack the PDMS films.

The mechanical strength of PDMS is also heavily dependent on other preparation processes, such as the mixing ratio of the pre-polymer gel with the cross linker, along with

curing temperature and curing time. Figure 2.27 shows the effective Young's modulus for 120 µm-thick PDMS with different mixing ratios. At least three samples are tested for each ratio and the standard deviations are showed as error bars. Higher curing temperatures produce lower Young's modulus of PDMS. The 70°C, 12 h cure gives approximately 1 MPa effective Young's modulus for the near-bulk PDMS with 10:1 mixing ratio. These results match the trend reported in [57].

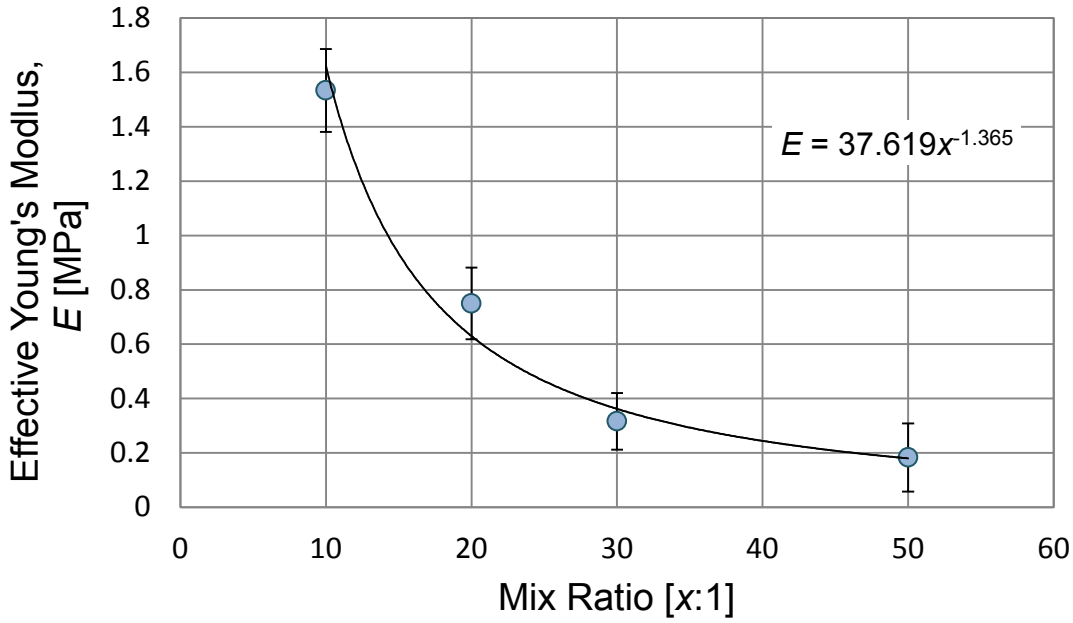

Figure 2.27: The extracted effective Young's modulus of 120 µm-thick PDMS films for different mixing ratio of the pre-polymer gel and cross linker.

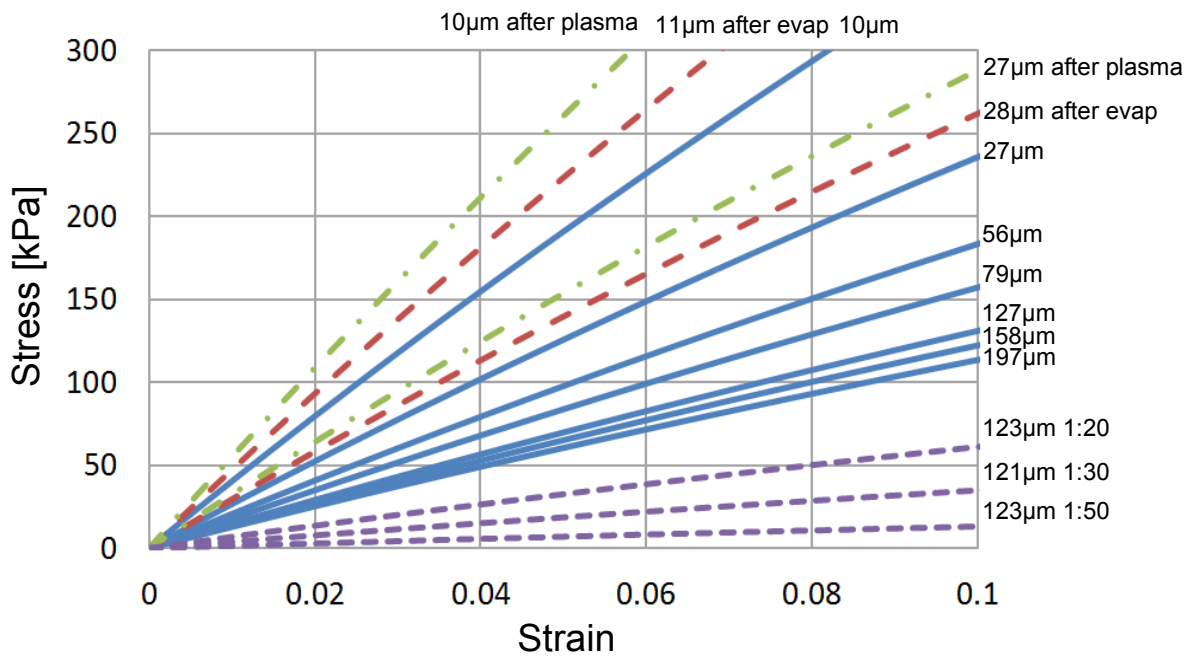

Figure 2.28: Summary of strain stress relationships of PDMS based on the extracted parameter C_1 and effective Young's modulus. The effective Young's modulus equals to the initial slope of each curve. "10 μm after plasma" is short for 11 μm thick film after 1 μm surface plasma etching. "11μm after evap" is short for 11 μm thick film after surface metal evaporation.

Figure 2.28 gives the summary of mechanical properties of different types of PDMS. Strain-stress curves of PDMS are simulated based on the extracted Mooney-Rivlin parameter C_1 and effective Young's modulus from experiments. The curves bend slightly, which matches the feature of Mooney-Rivlin model at low strain. The effective Young's modulus equals to the initial slope of the curve.

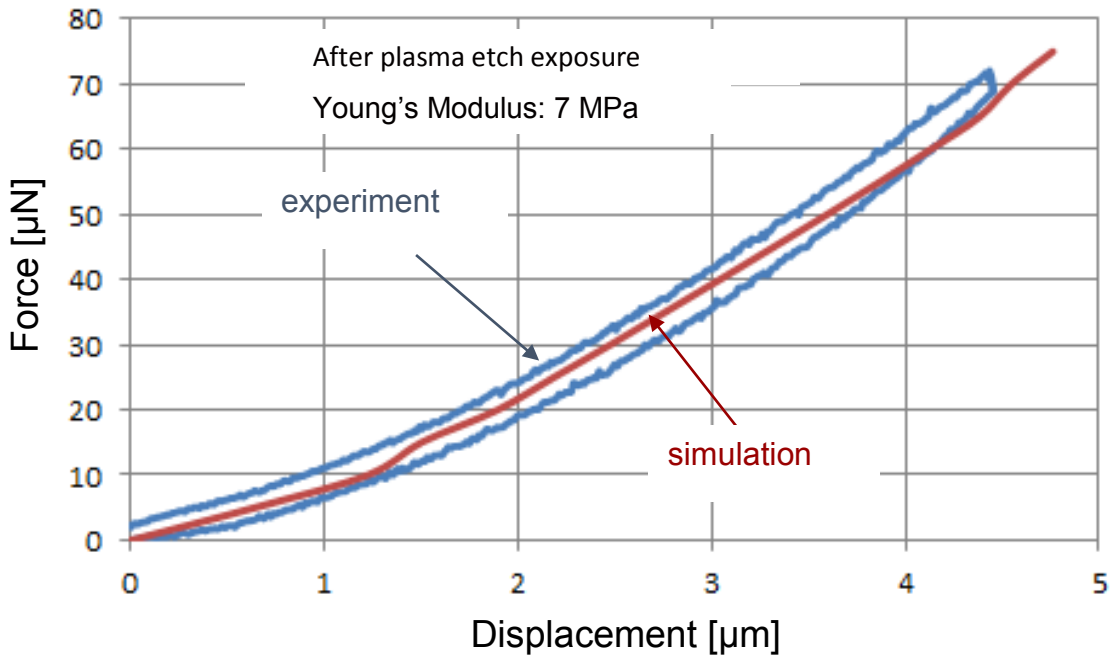

Figure 2.29: Comparison of simulation and experimental results of nanoindentation on a plasma etched 12 μm-thick PDMS film.

The results from the nanoindenter tests are shown in Figure 2.29 and Figure 2.30. Figure 2.29 gives an example of experimental measurements compared to the simulations. By adjusting the C_1 values of PDMS in the simulation to match the experimental results, the effective Young's modulus can be extracted. The extracted measurement data of effective Young's modulus are shown in Figure 2.30. They match the trend (within 35%) of results extracted from the clamped PDMS membranes except 500 μm-thick film. Because 500 μm-thick film is too thick, during the nanoindentation, the probe mainly compresses the PDMS instead of moving it. Therefore the measurement result is believed to be inaccurate.

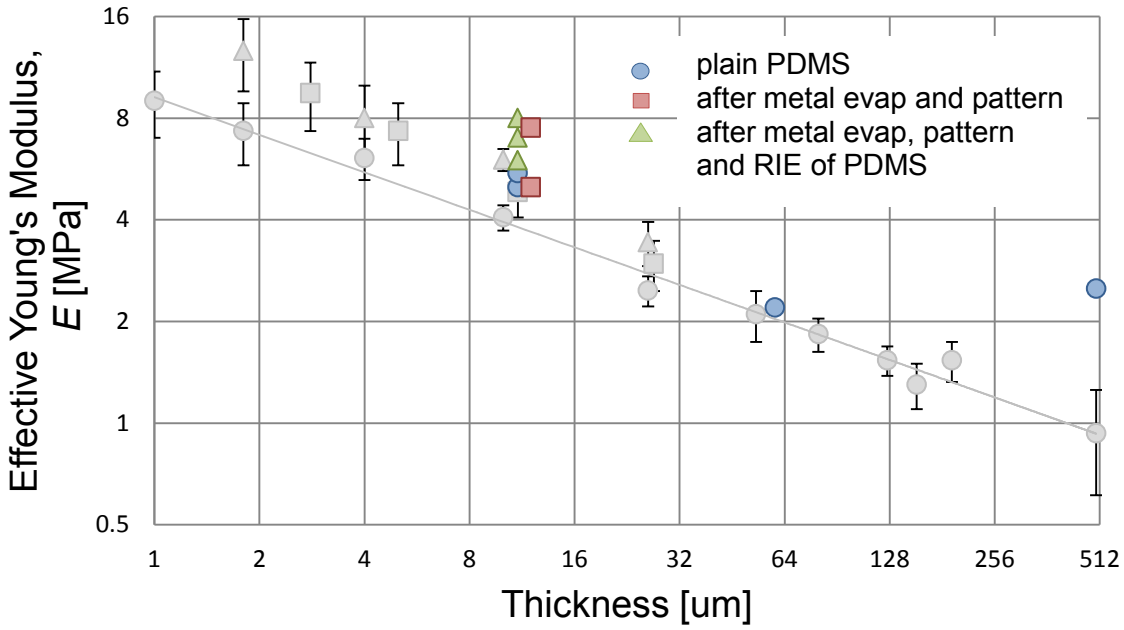

Figure 2.30: Color data points: the extracted effective Young's modulus of PDMS films from nanoindentation measurements. Grey data points: data from Figure 2.26 as comparison.

2.5 Summary and Conclusion

The membrane transfer and release method enables the manufacture of ultra-thin PDMS films having thicknesses down to at least 1 μm. The effective Young's modulus, E, follows a consistent power law

$$E = 9.3h^{-0.369} \qquad (2.13)$$

as a function of PDMS thickness, h, (where E is in units of MPa and h is in μm) having a value of 9 MPa for 1 μm-thick films, which is ten times that of bulk PDMS (0.9 MPa). It is believed the trend is due to the shear stress during the fabrication, which makes thinner films forming

stronger cross-linked networks of polymer chains in PDMS. From the trend, it is expected that Young's modulus will become even larger for film thicknesses below 1 μm. Additional fabrication, such as metal evaporation and reactive ion etching increases PDMS stiffness by 20 to 70% due to enhancement of cross links and hardening of the surface, and this effect is greater when films become thinner. The fabrication and transfer of ultra-thin PDMS thin films with or without embedded electrodes opens a promising route for creating the micro-pump in next chapter and possibly for other soft electronics devices. The characterization of mechanical properties for these very thin films is meaningful for designing and modeling the micro-pump and other MEMS elastomer actuators.

Chapter 3 Modified Grayscale Photolithography with Over Exposed Resist and Timed, Diluted Development

3.1 Introduction

The counter electrode of the micro-pump is a shaped silicon substrate. The spline-shaped substrate significantly reduces electrostatic actuation voltage compared to a regular trench shape. The shape is refined in its smoothness by a modified grayscale lithography method that is detailed in this chapter. This modified grayscale lithography method enables more grayscale levels resulting in a smoother three-dimensional Si structure compared to the traditional grayscale lithography method.

3.2 Grayscale Photolithography

Micro-electromechanical systems (MEMS) technologies can greatly benefit from three-dimensional microstructures. However, MEMS fabrication technologies originate from the mature processes developed for silicon integrated circuit (IC) fabrication, so the traditional patterning technology such as photolithography normally only produces two-dimensional or planar structures. Therefore, the ability to develop 3D microstructures has been explored by many researchers. Previous technologies include multiple direct writing steps, multiple photolithography steps, or other process run on customized equipment, such as micro-stereolithography and laser-enhanced etching [58, 59, 60, 61].

Grayscale lithographic technology enables the development of arbitrary 3D microstructures in various materials [62, 63, 64]. In contrast to traditional binary lithography, grayscale photolithography can achieve different depths of photoresist by applying variable exposure doses specified through a layout design. A mask with different gray levels transmit varying amounts of light. Different regions of the photoresist underneath the mask therefore receive different dosages. When developed, these varying dosages result in the corresponding inverse thicknesses of resist, thus creating 2.5D microstructures. This 2.5D resist pattern can be either transferred into a substrate via anisotropic dry etching [65] or used directly as the structural material.

There are three key steps to grayscale lithography as shown in Figure 3.1: (a) grayscale mask design, (b) grayscale lithography and (c) dry anisotropic etching. Steps (a) and (b) yield a precisely designed 3D profile in a photoresist layer by modulating the intensity incident on the resist surface. Step (c) allows the 3D profile in the resist to be transferred into the underlying substrate by dry anisotropic etching. A variety of applications have taken advantage of this new design capability, such as encapsulated microfluidic channels [66], photonic crystals [67], Fresnel lenses [29] and micro-turbomachinery [65].

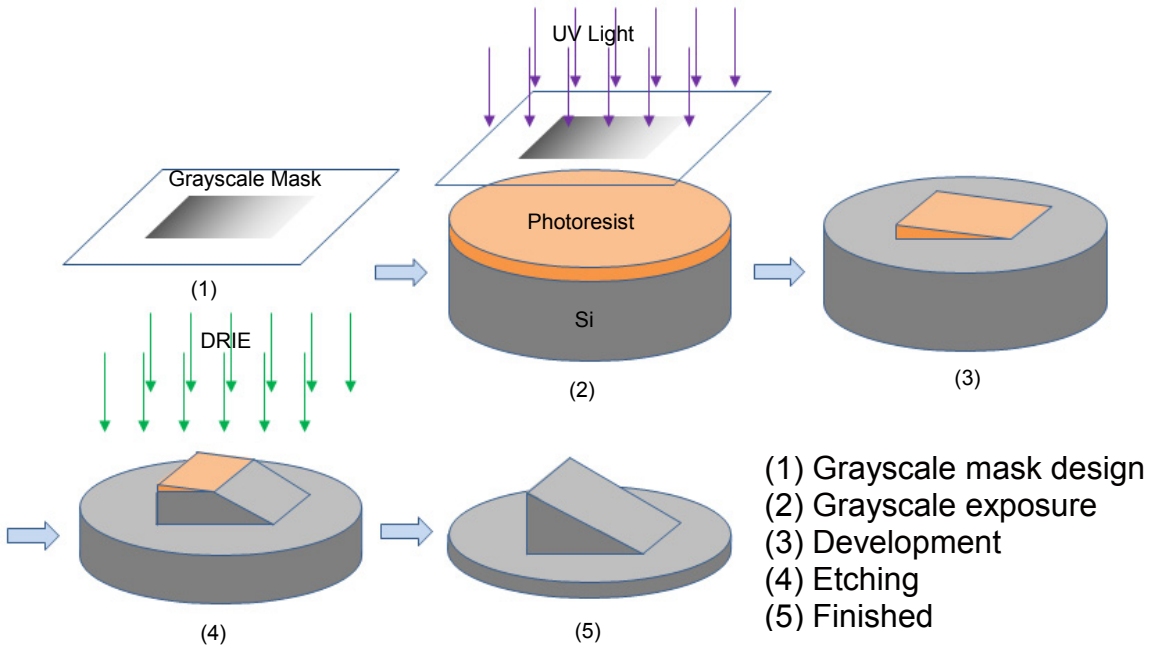

Figure 3.1 Three key steps to grayscale lithography: (1) grayscale mask design, (2) & (3) grayscale lithography, and (4) & (5) dry anisotropic etching.

Traditional grayscale lithography techniques have several drawbacks. (1) Unlike normal masks, grayscale mask design involves pixel sizes and spacing that are intentionally designed to be below the resolution limit of the exposure system, allowing the diffraction of UV light. The mask typically uses a set of subresolution opaque pixels and a fixed center-to-center spacing. The different grey levels are created by varying the sizes of the pixels. These grayscale masks need high resolution mask writers capable of submicrometer size features, resulting in high mask costs. (2) Only a finite number of pixel/spacing sizes can be realized due to the mask writer's capability, thus limiting the number of possible gray levels. After development, this results in discrete steps and therefore increases the roughness of the resist surface. (3) During the development process, normal developer concentrations are used to remove the exposed resist.

However, unlike normal photolithography that has a binary transition between clear and dark regions, grayscale lithography ideally involves a series of very small discrete steps to create a smooth transition. Therefore, standard developing processes may create jagged surfaces because of fast development [68]. (4) Calibration is very critical for traditional grayscale lithography. To achieve desired shapes after dry etching, complicated and time consuming calibrations are necessary [69]. However, even the best calibration can only give an average estimate in grayscale lithography because presuming that each processing step is perfectly repeatable is unrealistic. These steps include exposure dosage, environmental temperature and humidity, and concentrations or conditions of the photoresist and developer. In addition, because the selectivity of etching materials and resist in the subsequent dry etching step controls height and slope of etched profiles, any variation in the behavior of the dry etching tool will contribute to the fluctuation. In addition, regular maintenance of dry etching tools sometimes changes their etching characteristics dramatically. (5) In some cases, designers need a series of structures with different heights but sharing the same profile shape. This is very common in parametric design. To achieve this goal, either a group of grayscale masks are needed to create the different heights separately, which is costly and painstaking, or the selectivity from the dry etching tool needs to be finely tuned, which is extremely challenging. The end of result of the drawbacks discussed above is a relatively unpredictable nature of the shape created in the substrate after processing.

The goal of this chapter is to report on the development of a modified grayscale photolithography process that enables more grayscale levels resulting in a smoother and predictable etched substrate using normal mask writers and aligners. The modified process involves overexposure of the photoresist and timed development in dilute developer. The weak developer gives robust control of the desired shapes and smooth photoresist surfaces. Different

dilution ratios and developing times also give flexibility for creating different heights and profiles of the resist to overcome the undesired variations in traditional grayscale lithography without redesigning the masks. This modified grayscale process enables the creation of more predictable and smoother 3D microstructures. It is the key process for fabricating the shaped substrate electrode for the micro-pump.

3.3 Modified Grayscale Photolithography Process

3.3.1 The Grayscale Mask Design

The grayscale lithography discussed in this paper utilizes optical masks (Figure 3.2) patterned with 1μm pixels, which can be fabricated using a regular laser mask writer. The grayscale levels are achieved by alteration of the configuration of an 8μm×8μm subpattern, instead of varying the pixel sizes and spacings, resulting in changes in the intensity of transmitted UV light. Each different intensity level determines a gray level, with a total of 64 levels. The dosage absorbed by the photoresist is proportional to the percentage of light transmitted through the mask. By calculating the number of opaque elements n in the 8μm×8μm subpattern, we can determine the transmission percentage of UV light. The relationship between the transmission ratio, β, and the gray level, n, on the mask is

$$\beta = \frac{A_c}{A_t} = 1 - \frac{n}{64} \tag{3.1}$$

where A_c is the clear area of the subpattern, A_t is the total area of the subpattern and n is the pixel number in the subpattern (i.e., the gray level) .

(a)

1	49	13	61	4	52	16	64
33	17	45	29	36	20	48	32
9	57	5	53	12	60	8	56
41	25	37	21	44	28	40	24
3	51	15	63	2	50	14	62
35	19	47	31	34	18	46	30
11	59	7	55	10	58	6	54
43	27	39	23	42	26	38	22

8 μm

(b) Three examples:

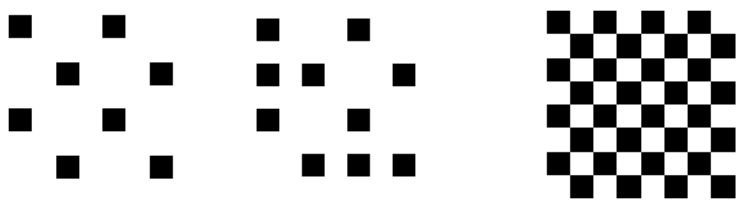

$n = 8, \beta = 87.5\%$ $n = 10, \beta = 15.6\%$ $n = 32, \beta = 50\%$

Figure 3.2. (a) 8μm×8μm subpattern, 64 levels grayscale mask design. The numbers represent the sequence of opaque pixels. (b) Three grayscale examples.

3.3.2 Modified Grayscale Photolithography Process and its Calibration

A calibration mask is fabricated to demonstrate the basic differences between conventional grayscale lithography and the modified grayscale process. The calibration mask is also responsible for extracting the initial fitting parameters for the resist development model. A

Karl Suss MA6 aligner (λ=320nm, resolution ~ 1μm; SUSS MicroTec AG, Garching, Germany) and AZ4210 photoresist are used for the lithography process. The transmission ratio in the calibration mask is designed to increase linearly with position on the mask. The AZ4210 photoresist is spun on an HMDS coated Si substrate at 2000 rpm to create a 3 μm thick layer. The wafer is soft baked at 95°C for 2 min. Normal exposure time using the MA6 aligner for this thickness resist is 120 s. The sample is over exposed for 380 s at 5 mW/cm^2 intensity under proximity mode. The gap between the sample and the grayscale mask is set to be 150 μm to diffract the UV light. The sample is then soaked horizontally in AZ developer that is over diluted with water (AZ developer to water: 1:2.7). No agitation is used during development. As soon as the 3 μm resist located in the 100% UV transmission regions is dissolved, the development is stopped. This process takes 50 min. It offers the robust control of the designed resist shape through this long and weak development. For example, if the development time is off the set time by ±1 min, the results only vary 2% of the target with predicated depth. The wafer is removed from the developer, rinsed very slowly in DI water, and dried with nitrogen. The developed resist profile (Figure 3.3) is then measured by a P-15 profilometer (KLA Tencor Corp., Milpitas, CA).

For comparison, traditional grayscale lithography is also performed using the same mask. 3 μm AZ4210 photoresist is exposed for 380 s at 5 mW/cm^2 intensity under approximation mode. The developer used is AZ developer diluted 1:1 with water and the development time is 60 s. Unlike the modified process, this development is the same as normal development, and the time is based on the complete dissolution of the 100% exposed resist across the whole wafer. The remaining resist thickness versus transmission ratio is also shown in Figure 3.3.

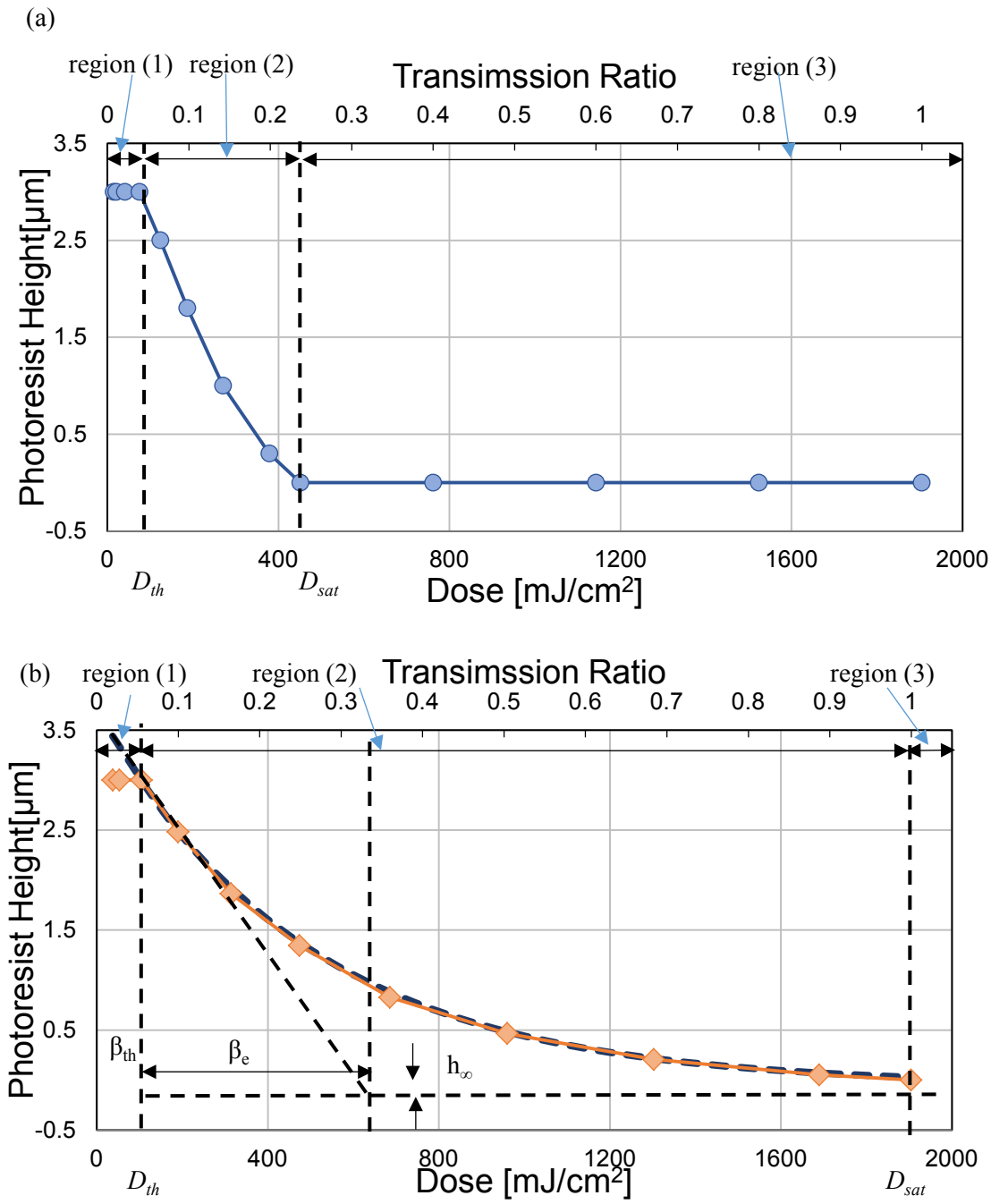

Figure 3.3. (a)Measured thickness of developed photoresist vs. dose after traditional grayscale lithography. (b) Solid line: Measured thickness of developed photoresist. Dash line: Fitting line as exponential curve.

The traditional resist curve typically has three regions: (1) low exposure where almost all of the resist remains; (2) the transition region between low and high exposure; and (3) high exposure, where all of the resist is removed;. It is well known that positive resist requires a minimum dosage (D_0) to initiate photochemistry and begin to break the cross link. Similarly, a clearance dosage (D_{100}) is required to completely break the cross link throughout the resist's thickness [70]. In region (1), the sample that receives exposures below a threshold dosage D_{th} will not be attacked during development. In region (2) the photoresist that receives exposures greater than a saturation dosage D_{sat} will completely dissolve during development. For the intermediate region (3), where the dose is between the D_{th} and D_{sat}, the image will partially developed, which is the applicable area for grayscale lithography. For the traditional lithography, the range of the dose in the region (2) is quite narrow (~90 to 450 mJ/cm^2) compared to the full range, resulting in low resolution and few unique gray levels in grayscale mask design. On the other hand, the modified lithography process facilitates usage of most of the dosage range (~100 to 1800 mJ/cm^2), and the slow development guarantees robust control of the photoresist profiles.

3.3.3 Modified Grayscale Photolithography model

Due to the exponential nature of the exposure dose absorption, the measured remaining thickness of resist after development h are fit to an exponential equation of the form:

$$h = ae^{-\beta/\beta_e} + h_\infty \tag{3.2}$$

where β_e is a fitting parameter representing the transmission ratio corresponding to thickness of the resist reaching $1/e$ of its original height. Substituting the boundary conditions:

$$0 = ae^{-1/\beta_e} + h_\infty \tag{3.3}$$

$$h_0 = ae^{-\beta_{th}/\beta_e} + h_\infty \tag{3.4}$$

where h_0 is the initial height of the resist, and β_{th} is the transmission ratio corresponding the minimum threshold dosage, D_{th}. The coefficients a and h_∞ are

$$a = \frac{h_0}{e^{-\beta_{th}/\beta_e} - e^{-1/\beta_e}} \tag{3.5}$$

$$h_\infty = \frac{-h_0 e^{-1/\beta_e}}{e^{-\beta_{th}/\beta_e} - e^{-1/\beta_e}} = \frac{h_0}{1 - e^{(1-\beta_{th})/\beta_e}} \ . \tag{3.6}$$

The revised fitting equation becomes

$$h = h_0 \frac{1 - e^{(1-\beta)/\beta_e}}{1 - e^{(1-\beta_{th})/\beta_e}} \quad . \tag{3.7}$$

The set of fitting parameters are h_0, β_{th} and β_e.

The measured thickness of the photoresist after grayscale lithography along with the least square fitting line is shown in the Figure 3.3. The fitting parameter β_e equals 27.4% for h_0 = 3 μm and β_{th} = 5.5%. h_∞ is calculated to be −0.098 μm. Grayscale optical masks were designed and fabricated (Photo Sciences, Inc., St. Torrance, CA) to produce cubic function spline shaped structures in positive photoresist for characterization of the profile based on these initial characterization results. The same mask is also used to create various spline shapes utilizing different exposure doses, different diluted ratio developers and different developing times to explore their effects on the modified grayscale lithography process. The spline shape is chosen here because both a range of thickness and gradients of the resist can be tested in the process. The ultimate application goal is creating a smooth cubic function shaped silicon electrode for a

micro-pump, allowing for electrostatic zippered actuation to avoid problems with a large starting electrode gap.

3.4 Changing Parameters

3.4.1 Changing Development Time

The first experiment involves the study of photoresist profiles with increasing development time, as shown in Figure 3.3. The grayscale mask is designed based on the calibration represented in the previous section. The transmission ratio is shown in Figure 3.4. The exposure time is fixed as 500 s and AZ developer is mixed with water in the ratio 1: 2.7 (developer: water). The developed resist profiles are measured by a KLA Tencor P-15 profilometer.

The experiments show that developing rate is approximately constant over time for each particular position on the pattern for a given exposure dose, i.e. developing rate is not a function of time or depth. This approximation of a development rate independent of resist depth leads to simplification of the development model. The profile in Figure 3.5 requires 50 min development time to remove the 3 μm thick photoresist in the center of the pattern where the transmission ratio of grayscale mask is 100%. The corresponding maximum development rate is 60 nm/min for 1:2.7 diluted AZ developer. This maximum depth can be controlled by varying development time in diluted developer. It can compensate for variations from other steps in the lithography process, such as conditions of the photoresists and developers, as well as the selectivity of dry etching tools. By adjusting the development time, calibration is performed to account for the current conditions of resist, developer and etching tool. This approach achieves an accurate resist

profile without redesign and refabrication of grayscale masks. Structures with the same shape but with different heights may be made by only changing the development time without creating another mask.

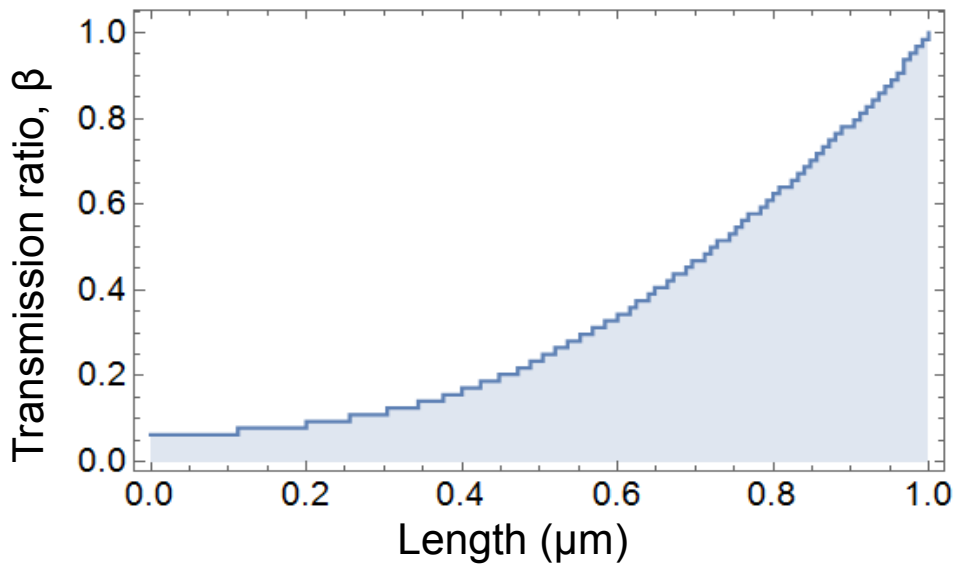

Figure 3.4. The transmission ratio vs. length on grayscale mask designed for cubic function shape based on the calibration in section 3.3

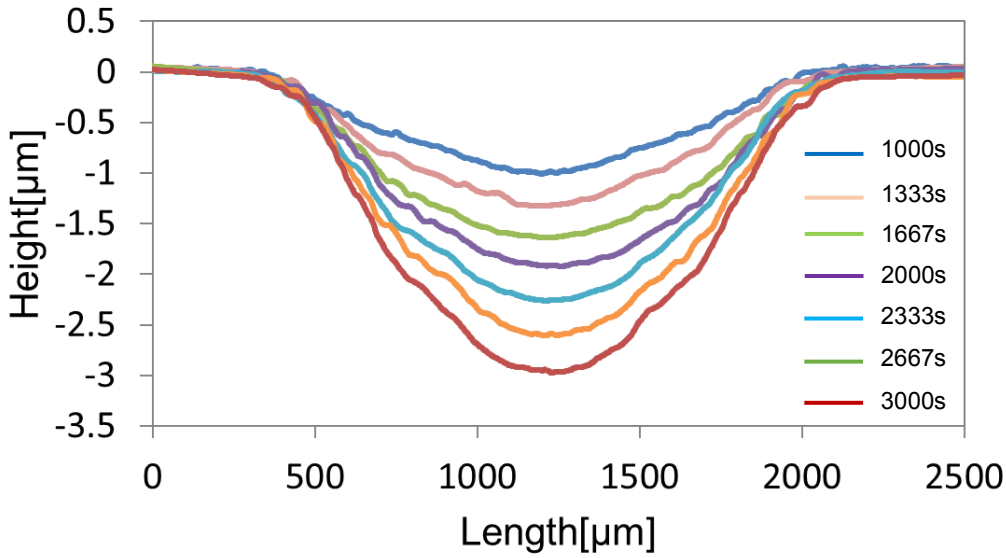

Figure 3.5. Developed photoresist thickness for different development times. The exposure time is 500s. The developers diluted as 1: 2.7 (developer: water).

The optical images of the developed resist are shown in Figure 3.6. The 25 μm periodic structures in the *x* direction are intentionally designed to prevent adhesion during the electrostatic miniature pump actuation.

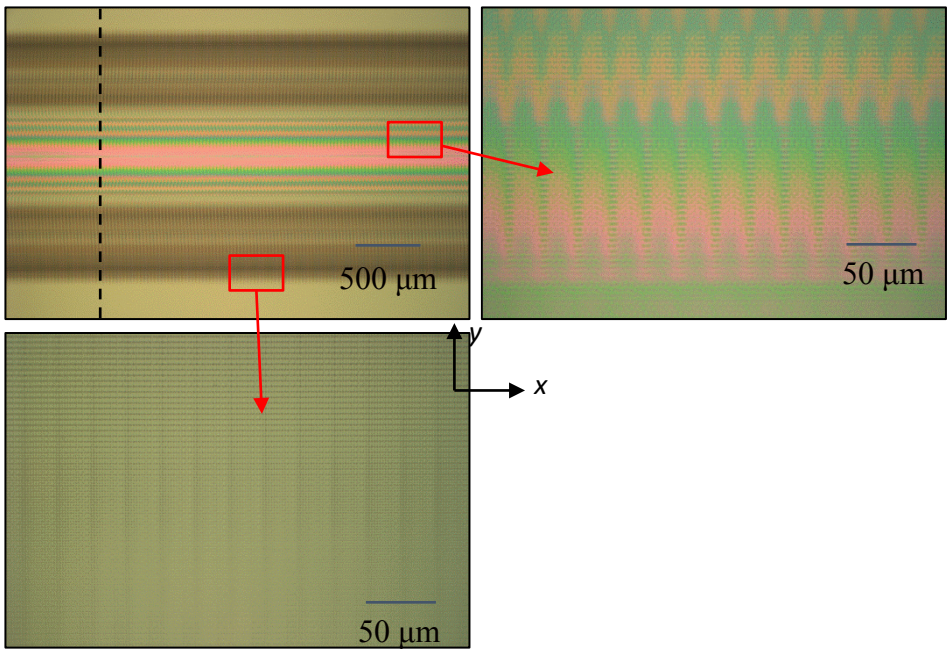

Figure 3.6. Optical images of developed photoresist. The periodic structures are intentionally designed to help prevent adhesion of PDMS to the silicon during pump actuation. The dash line indicates the direction of the scan.

3.4.2 Changing Developer Dilution Ratio

Figure 3.7 provides the development rate versus exposure dose on the grayscale mask using different developer concentrations. The development rates are nonlinear with exposure dose. For less dilute developer, such as a 1:2 ratio, the development rate saturates quickly after

reaching 100 s exposure time, Use of 1:2 developer results in a narrow range of applicable dosage and few gray levels.

Results of the effects of developer with different dilution ratios are summarized in Figure 3.8. The figure shows the resist profiles with dilution ratios (AZ developer: water): 1:2, 1:2.5, 1:2.7 and 1:3. The exposure time is fixed at 380 s. The results indicate the development rate decreases dramatically as the dilution ratio increases. The development rate extracted from the experimental results for the region that has 100% transmission ratio on the grayscale mask is shown in the Figure 3.8 and Figure 3.9. The rate is found to be approximately linear to the concentration of developer. The variation in resist shape illustrates the nonlinear response of development rate to different dilutions. It also shows that the greater dilution gives much smoother resist surfaces, which is reasonable since weaker developer etches the resist much more slowly, resulting in more uniform and smoother development. This enables the improvement in the quality of the resist profile compared to traditional grayscale lithography. However, the disadvantage of highly diluted developer is very long development times. The ratio of 2.7:1 is chosen to produce high quality resist surfaces while keeping development time to a minimum.

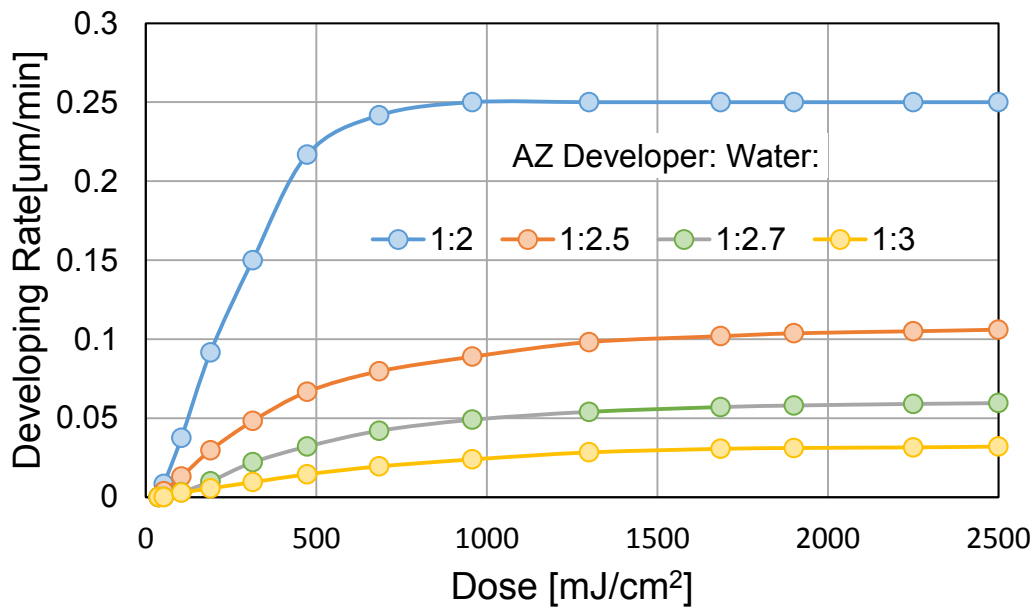

Figure 3.7 Development rate vs different exposure times for different developer concentrations.

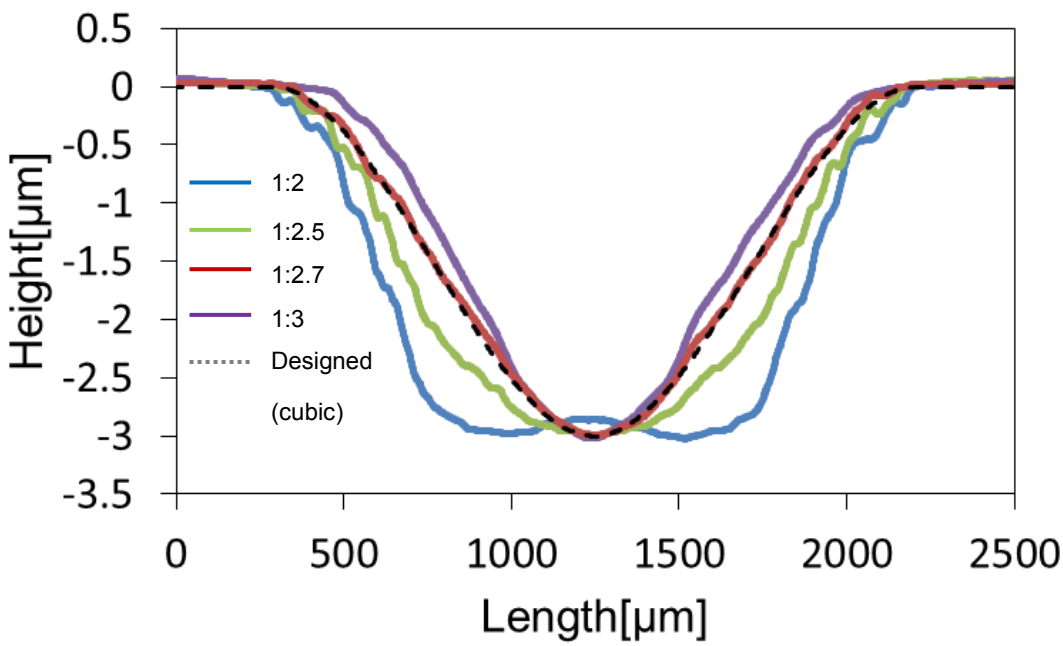

Figure 3.8 Developed photoresist thickness for different developer dilution ratios. The exposure time is 380s.

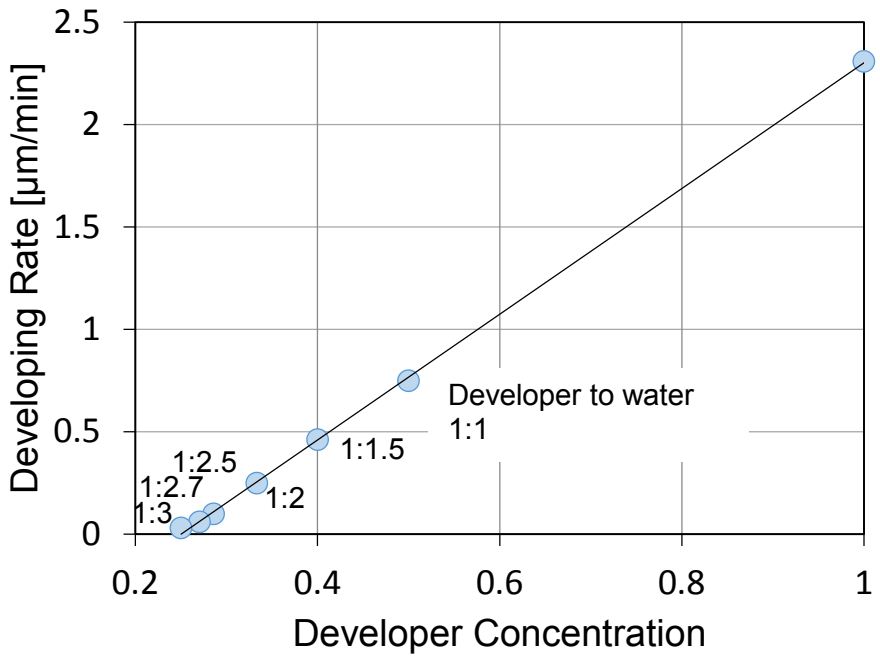

Figure 3.9. Development rate for different developer concentration under 100% transmission ratio.

3.4.3 Changing Exposure Time

In Figure 3.10, results from further separate tests are shown with the developer concentration fixed as 1:2.7 (AZ developer: water), while the exposure time is set at 220 s, 300 s, 380 s and 460 s. The developed profiles are calculated from the rates in Figure 3.9 and shown as dashed lines in Figure 3.10. The experimental data and calculations match within 10%, demonstrating the accuracy of the model for the grayscale lithography. Among these developed profiles, the shape under 380 s exposure and 2.7: 1 diluted development is a cubic function, which matches the characterization performed in Figure 3.5. Small systemic bumps in the photoresist height are indicated in the figure and are discussed in Section 3.6.

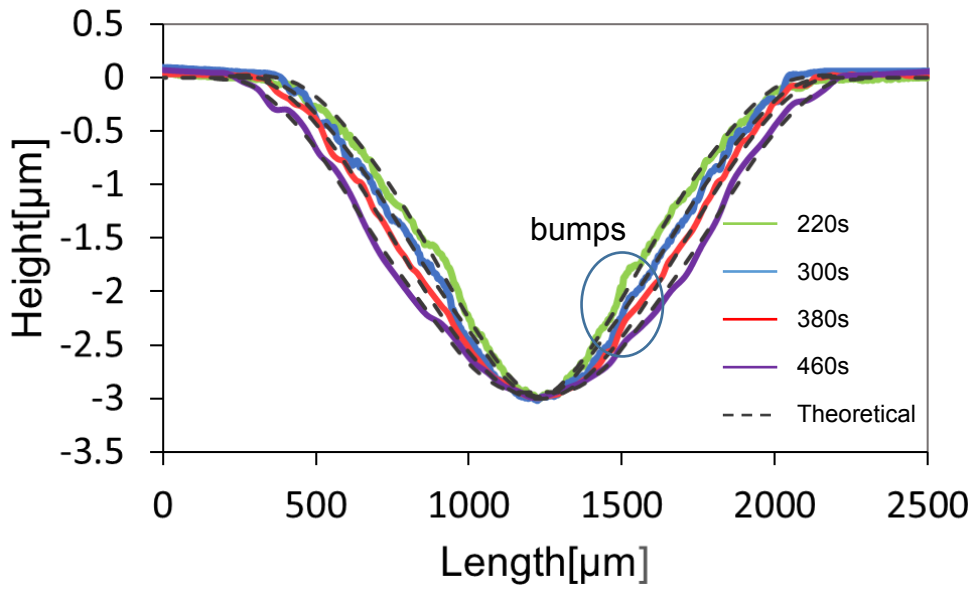

Figure 3.10. Developed photoresist thickness for different exposure times. The developing time is 380 s.

3.5 Deep Reactive Ion Etching

The profile under 380 s exposure and 2.7: 1 diluted development meets the target cubic spline function as a resist mask for subsequent dry etch of the Si shape for the micro-pump application. A cubic function shaped Si surface of 150 μm height is designed as the counter electrode to create the tapered gap for zipper actuation to reduce the pull-in voltage required. The substrate is placed in a Surface Technology System (SPTS) inductively coupled plasma Deep Reactive Ion Etching (DRIE) machine to transfer the cubic function shape from the resist to the silicon. The resulting Si etch depth as a function of different locations on the substrate is

$$d_{Si}(x,y) = R_{Si} t_{Si}(x,y) \tag{3.8}$$

where R_{Si} and t_{Si} are the Si etch rate and etching time, respectively. The photoresist etch depth

$$d_{PR}(x,y) = R_{PR} t_{PR}(x,y) \tag{3.9}$$

where R_{PR} and t_{PR} are the resist etch rate and etch time, respectively. Therefore

$$d_{Si}(x,y) = R_{Si} t_{Si}(x,y) = R_{Si}(t - t_{PR}(x,y)) = R_{Si}\left(t - \frac{d_{PR}(x,y)}{R_{PR}}\right)$$

$$= R_{Si} t - \frac{R_{Si}}{R_{PR}} d_{PR}(x,y) = d_0 - S d_{PR}(x,y) \tag{3.10}$$

where t is the total etch time, d_0 is the Si etch depth if no resist covers before etch, and S is the selectivity in the STS DRIE system:

$$S = \frac{R_{Si}}{R_{PR}} \tag{3.11}$$

The details of the process is shown in Figure 3.11.

The desired depth of the Si micro-pump chamber is 150 μm. The recipe for DRIE is shown in Table 3.1, where settings include the input gas and flow rate, wafer electrode power, RF coil power, chamber pressure, temperature, and the time of etch and passivation steps. The measured Si etching rate is about 2 μm/min, and etching rate of resist is about 0.04 μm/min, resulting in $S = 50$. The total etching time is 75 min. Therefore a 3 μm step of photoresist can be transferred to 150 μm Si step. Additional isotropic etching (3 min; etch rate: 2 μm/min) is applied to the sample after DRIE, using the recipe shown in Table 3.1. The purpose of isotropic etching is to smooth the relatively rough silicon surface created due to discretization in the lithography. The etched Si structures are then measured by profilometer. By changing the development time and the thickness of resist, other different depths of Si structures with the same

shape can be created using the same grayscale mask and same lithography process. One example is a 100 µm deep Si chamber transferred from 2.5 µm resist. The measured profiles for these two depths, shown in Figure 3.12, have the desired cubic function shape, indicated by the dashed lines. The SEM corresponding to the 150 µm deep device is shown in Figure 3.13. The channels on the Si structure are created by using the backside DRIE for the microcooling system application. The channels allow the pumped fluid to pass through.

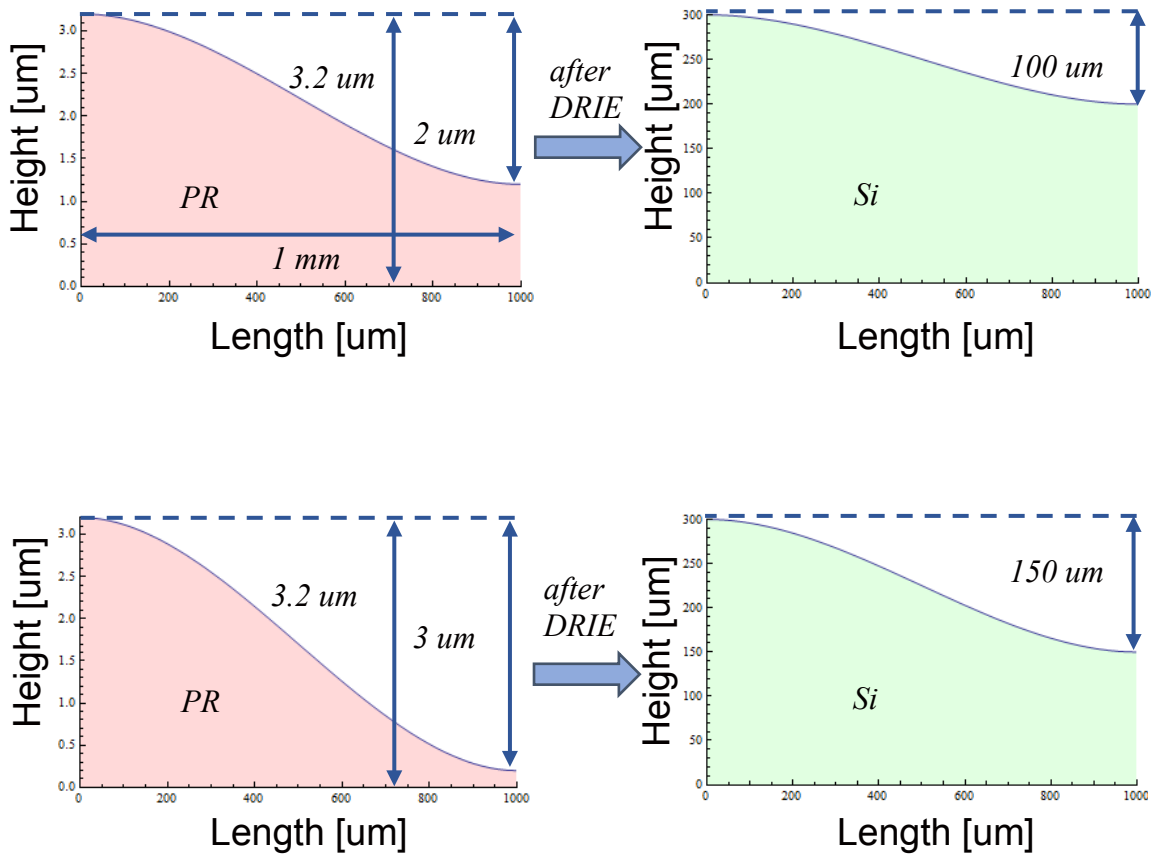

Figure 3.11 Transferring photoresist profiles into silicon profiles.

Table 3.1. The parameters of deep reactive ion etching

Anisotropic etch	Etch	SF_6 flow (sccm)	O_2 flow (sccm)	Cycle time (s)	Pressure (mT)	Coil power (W)	Platen Power (W)	Temperature (ºC)
		130	13	12	20	600	12	19
	Passivation	C_4F_8 flow (sccm)	O_2 flow (sccm)	Cycle time (s)	Pressure (mT)	Coil power (W)	Platen Power (W)	Temperature (ºC)
		85	0	8	10	600	0	19
Isotropic etch	Etch	SF_6 flow (sccm)	O_2 flow (sccm)	Cycle time (s)	Pressure (mT)	Coil power (W)	Platen Power (W)	Temperature (ºC)
		130	0	n/a	50	600	12	19

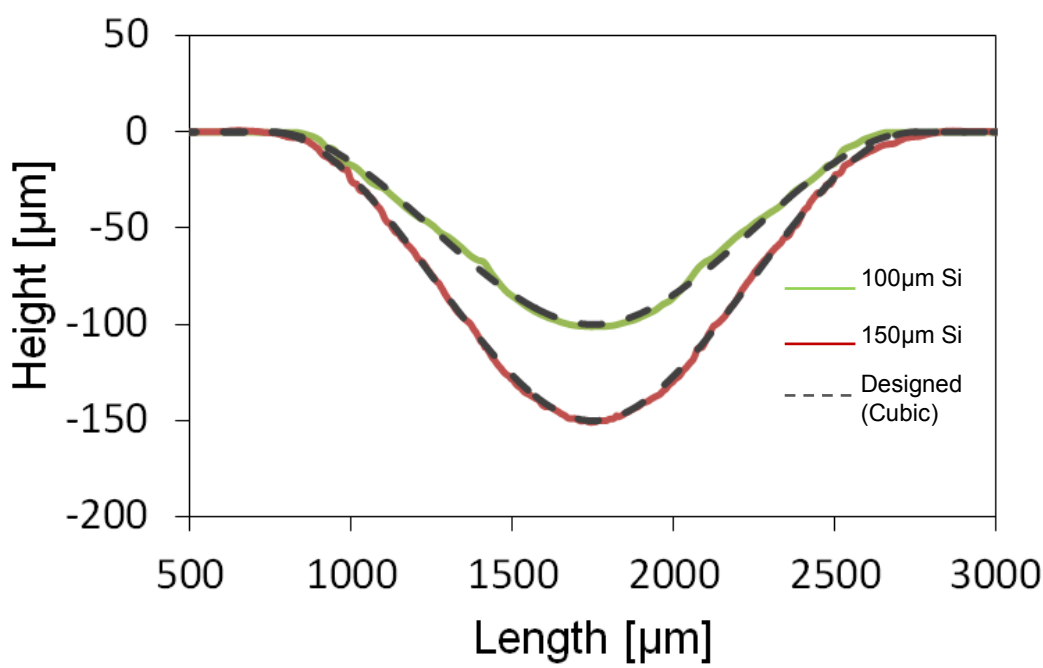

Figure 3.12 Measured Si height after DRIE. The profile is designed as a cubic function shape.

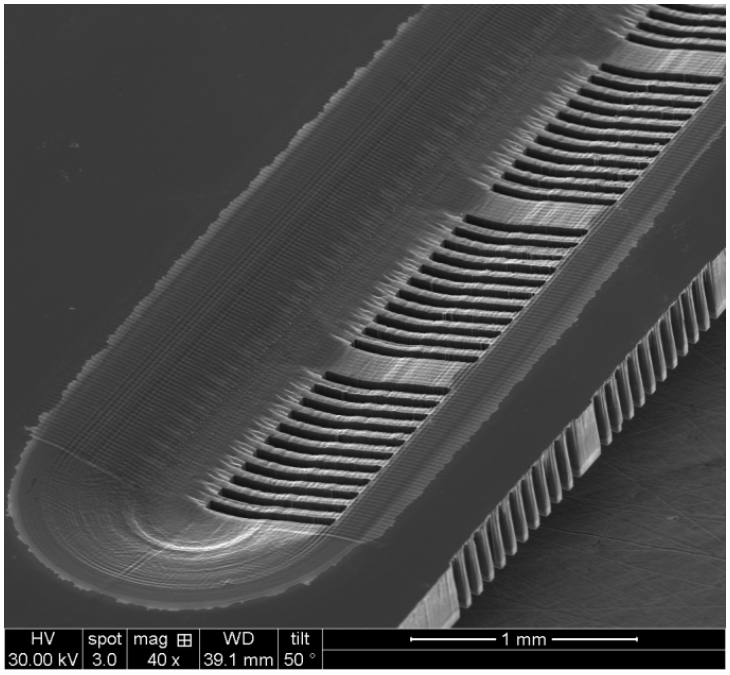

Figure 3.13 SEM picture of a 150 µm deep Si pump base. The profile shows a smooth cubic function shape. The channels are open by backside DIRE for the microcooling system application.

3.6 Further Discussion

In the figures of developed photoresist shown in previous section, bumps appear on some resists and developed profiles deviate from designed shapes. Figure 3.10 shows some examples of the bumps. They are 0.05 µm to 0.1 µm height, and 30 µm to 100 µm long for different profiles under different exposure and developing conditions. The bump position corresponds to the 45% to 55% transmission ratio region on the grayscale mask. Shown in Figure 3.14 (a), these areas mainly include 29 - 35 pixels (out of 64) subpatterns. The reason is not fully understood. It may be due to the inaccurate calibration or the complex UV light reconstruction during the

diffraction near 50% transmission ratio region. The practical solution is to remove some subpatterns. This compensates the average dose in this region resulting in elimination of the systemic cause of the bumps.

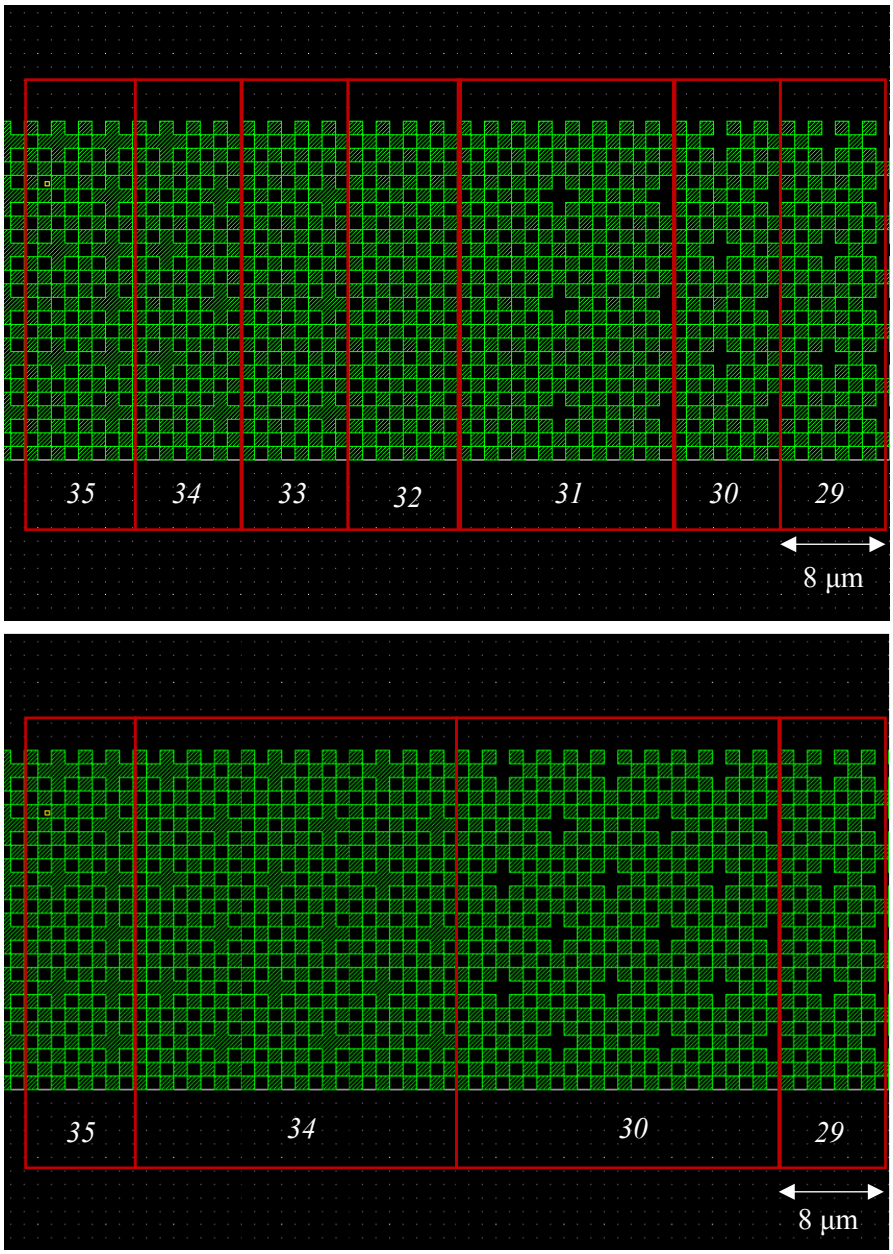

Figure 3.14. Patterns on grayscale mask near 50% transmission ratio (a) before modification and (b) after modification. The numbers correspond to n.

A new grayscale mask is designed and fabricated based on the calibration presented in Section 3.3.2. In the new design, the grayscale subpattern of n=31, 32, and 33 are removed from the mask and replaced by n=30 and 34 subpatterns, shown in Figure 3.14 (b).

In the new grayscale mask, different transmission ratio profiles are included. It is designed to create different photoresist shapes resulting in different shaped Si chamber after DRIE. The purpose is to investigate the effect of different shapes for snap-in behavior of micro-pump's diaphragm, which will be discussed in Chapter 4.

The Fermi-Dirac function is introduced to define the shape of different photoresist due to its excellent diversity for different profiles:

$$f(x,a,b) = \frac{1}{e^{-(x-a)/b} + 1} \tag{3.12}$$

where x is the length of the chamber; parameter a determines the center of turning point of the shape, and parameter b controls the curvature level of the shape. Figure 3.15 shows the examples of the effect on the profiles from the parameters a and b.

The normalized shape profile of the chamber is described as:

$$z(x,a,b) = \frac{f(x,a,b) - f(0,a,b)}{f(1,a,b) - f(0,a,b)} \tag{3.13}$$

Six different photoresist profile are designed (a = 0.5, b = 0.16; a = 0.4, b = 0.3; a = 0.6, b = 0.3; a = 0.6, b = 0.16; a = 0.6, b = 0.5; a = 0.8, b = 0.3). These shapes are shown in Figure 3.16. These designs are based on the micro-pump snap-in voltage simulations. The details are presented in Section 4.3.

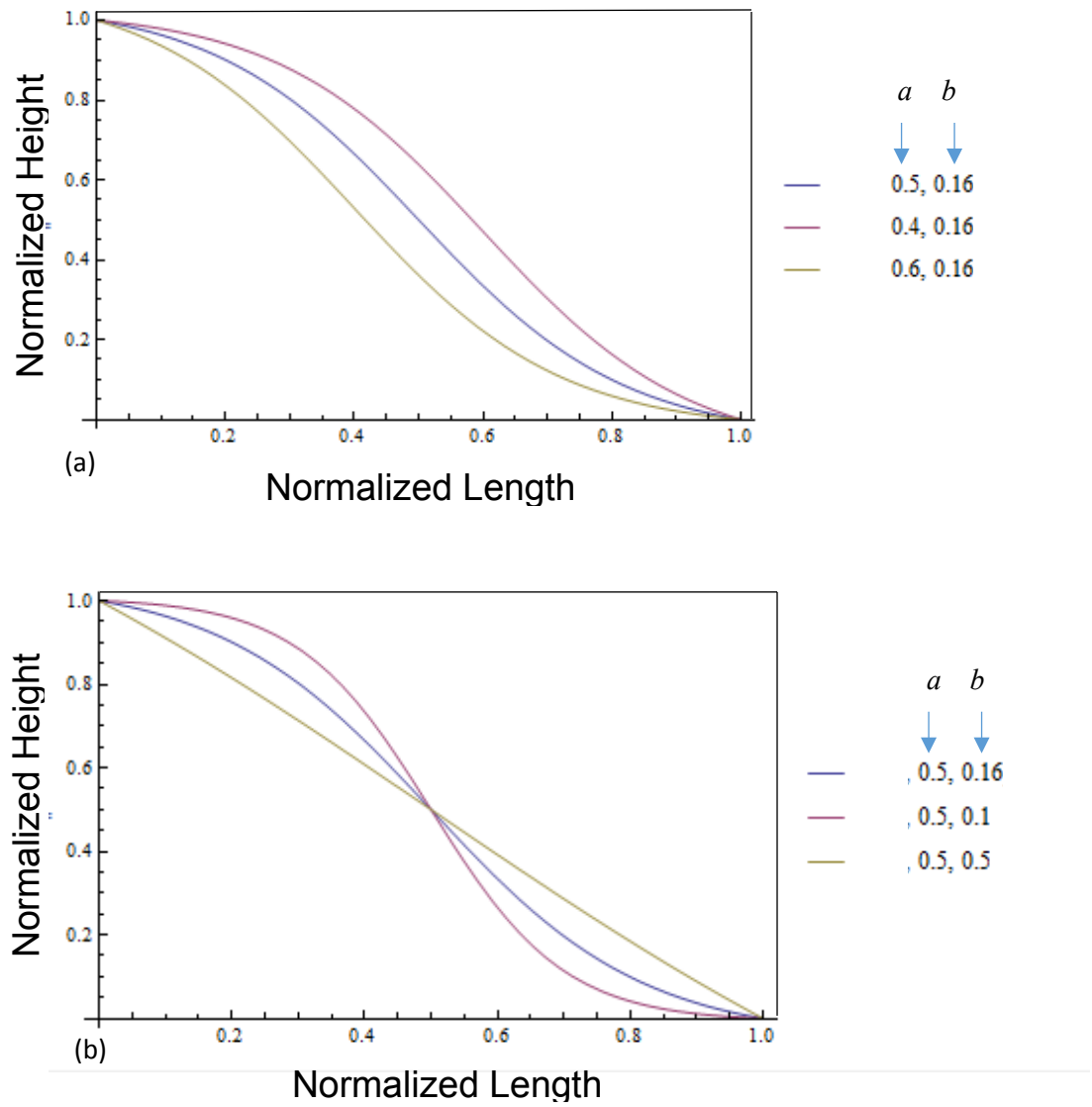

Figure 3.15. Examples of the effect on the profiles from the parameters a and b. (a) effect of parameter a: b is fixed as 0.16, and a has three different values: 0.4, 0.5, 0.6. (b) effect of parameter b: a is fixed as 0.5, and a has three different values:0.1, 0.16, 0.5.

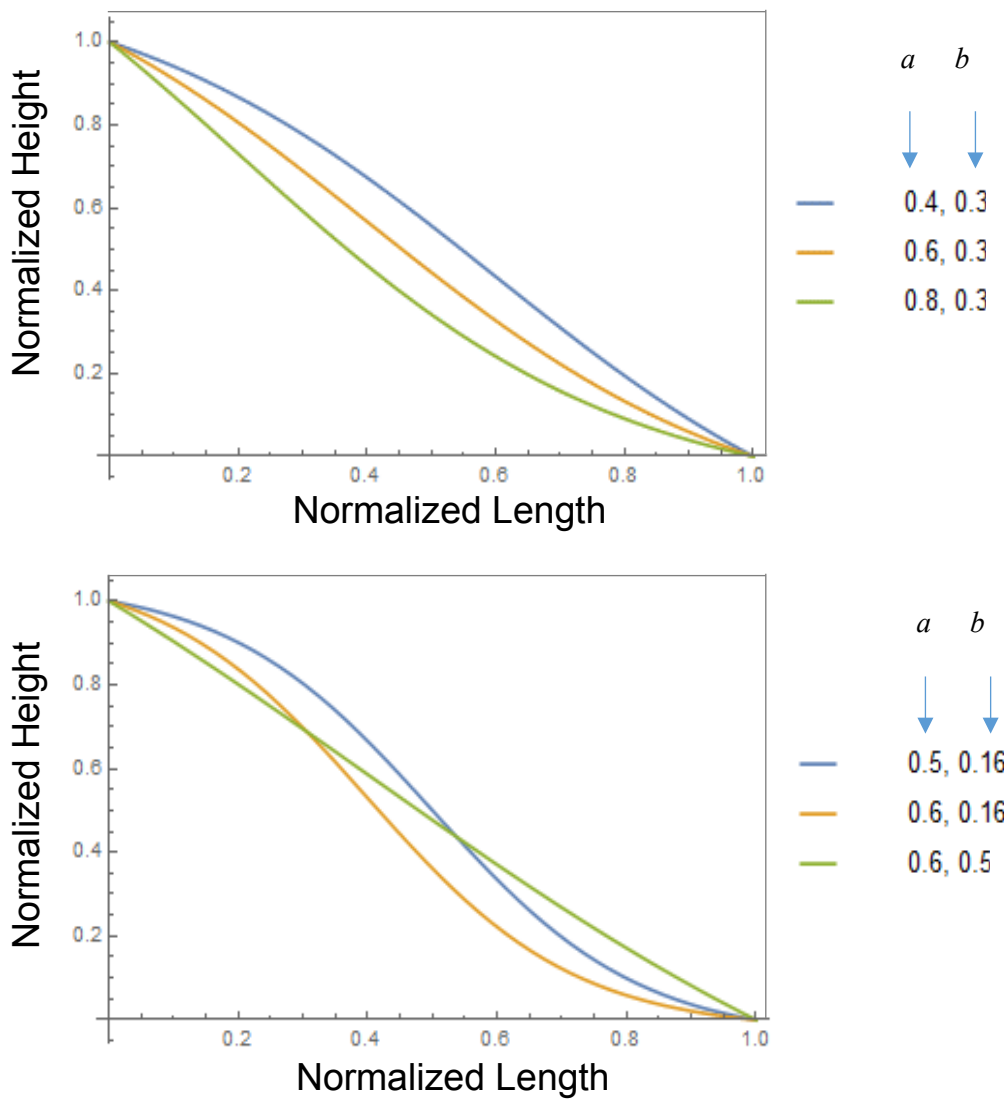

Figure 3.16. Different shapes for different parameter a and b.

Based on the calibration in section 3.3.2, six different transmission ratio profiles can be calculated correspondingly. The calculated transmission profiles on the mask are shown in Figure 3.17.

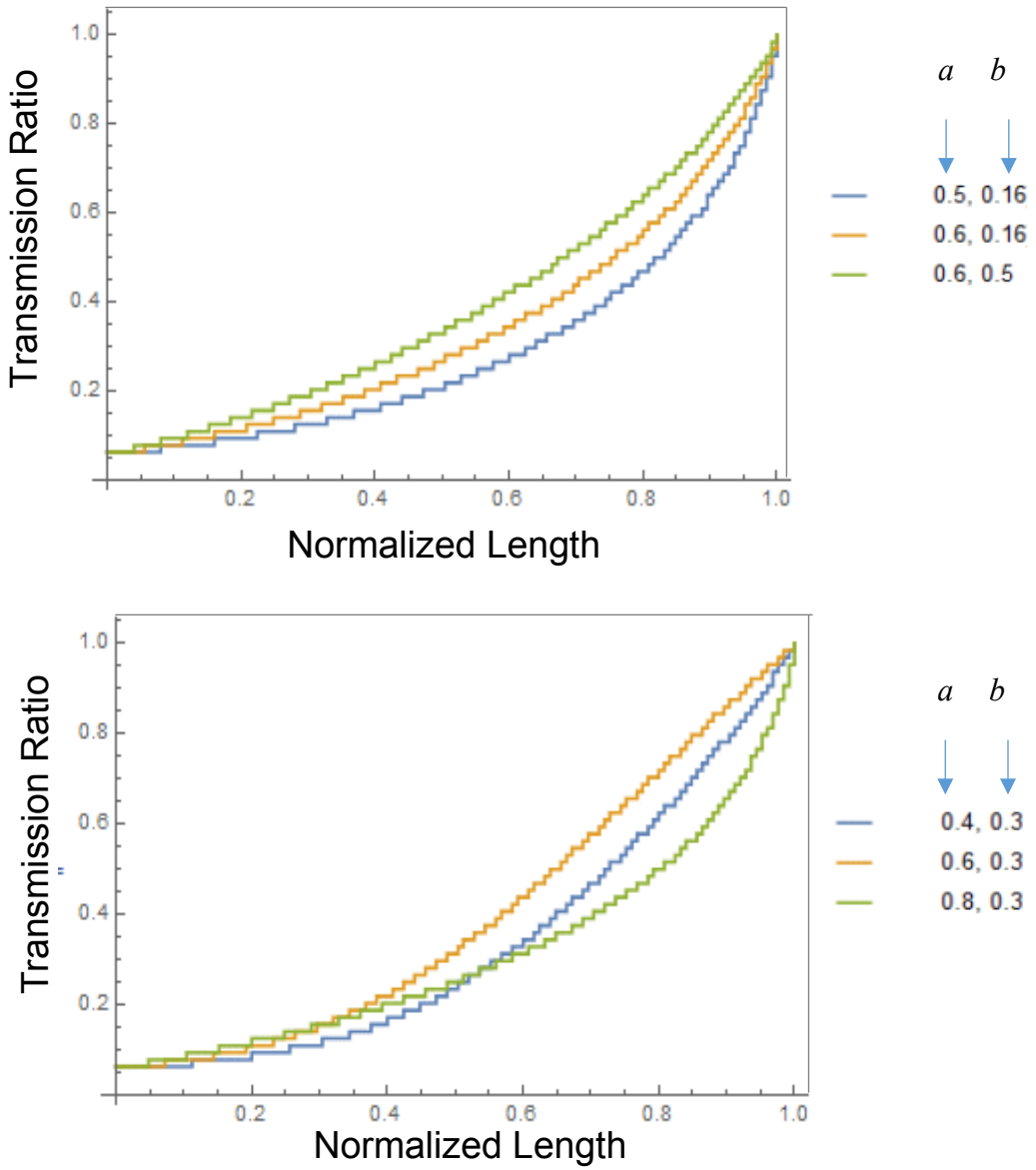

Figure 3.17. Transmission ratio vs. length for six different profiles.

However, the aligner that the grayscale lithography was performed on received maintenance after the calibration. A new ellipsoidal mirror was installed. This changes the dose of the UV output and the beam directivity, resulting in changing the relationship of the UV dose vs developed photoresist height in Figure 3.3. It is also found that the development rates are also different from the ones measured in Figure 3.9 . The reason is not very clear. It is possibly due to

the change of exposure condition because of the new installed ellipsoidal mirror, or because of aging of photoresist, different batch of AZ developer, and the environmental changes in the cleanroom (such as temperature and humidity). The new measured development rates with different dilution ratio for AZ developer are shown in Figure 3.18. The exposure time is set as 380 s, corresponding to UV dose of 1900 mW/cm^2. The new relationships of UV dose vs developed resist height are shown in Figure 3.19. The data from Figure 3.3 is also plotted here for comparison (grey line). In the figure, the blue line shows the result from 1:2.7 dilution ratio. This ratio is same as the data in Figure 3.3 (Shown as grey line in Figure 3.19), but the development rate is much faster (0.3 um/s for 100% transmission ratio: only 0.06 μm/s before), giving a very rough developed surface similar to 1:2 dilution ratio case in Figure 3.8. The red line shows the result from 1:3.4 dilution ratio, with the same measured development rate as the grey line (0.06 μm/s for 100% transmission ratio). In addition, the new relationship shown here is more complex. At low exposure dose (110 to 280 mW/cm^2), the resist height drops more slowly compared to standard exponential curve, so it could not be modeled as an exponential equation as presented in section 3.3.3. This effect needs further investigation.

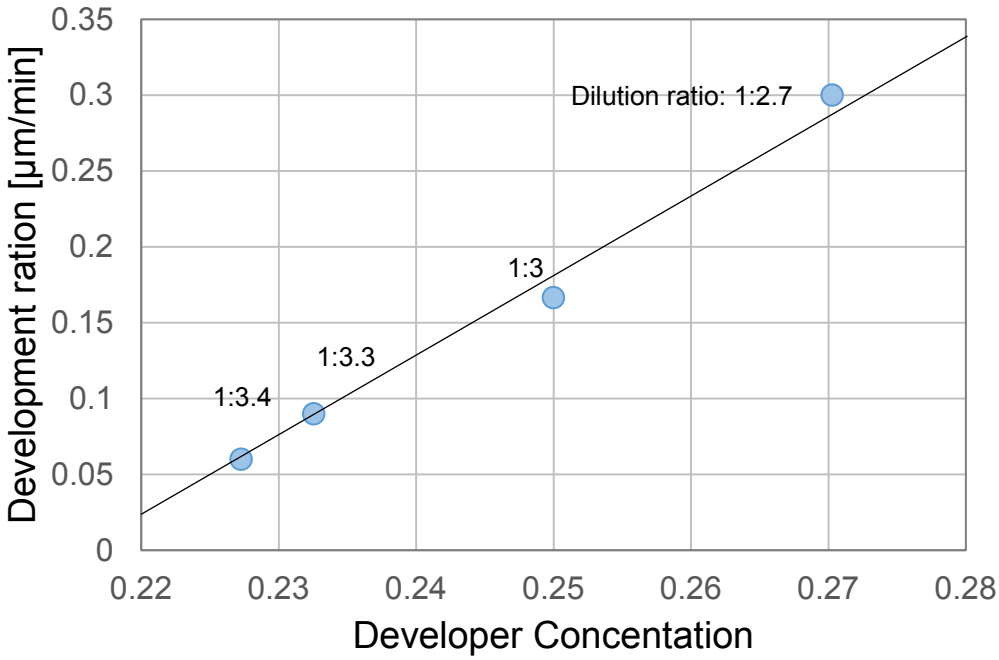

Figure 3.18. New measured development rate for different developer concentration under 100% transmission ratio.

Although the relationship of UV dose vs. developed height is different from the prior calibration, the predication of six different developed photoresist profiles can still be calculated based on Figure 3.20. Figure 3.20 shows the measured results vs. the theoretical predications. They match within 5%, demonstrating the uniformity and stability of the UV light during the exposure.

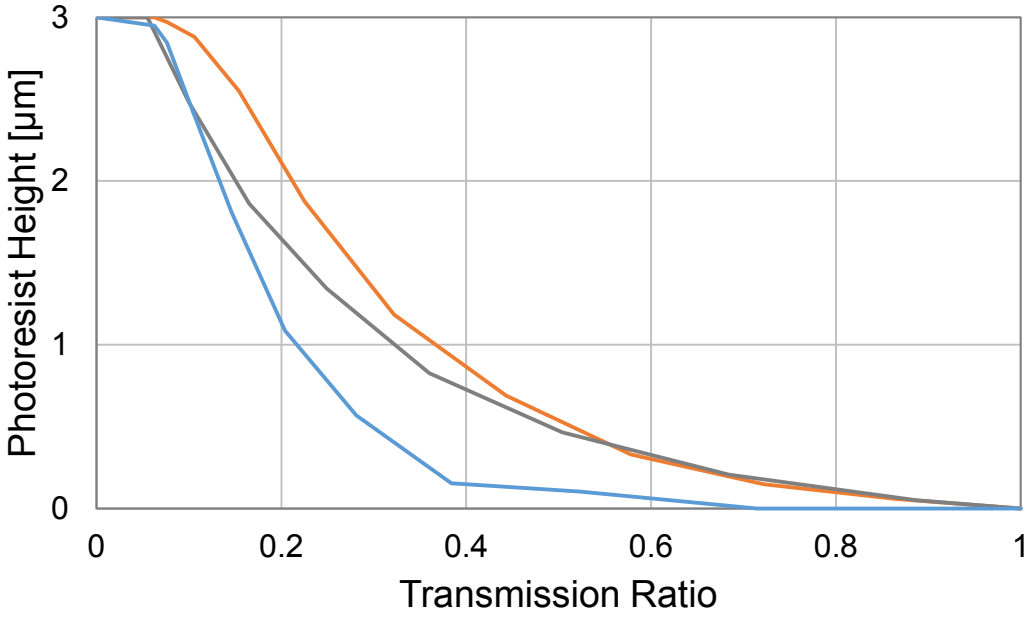

Figure 3.19. New measured thickness of developed photoresist vs UV light dose. Blue line: The developer dilution is ratio 1:2.7, and the development rate is 0.3 µm/min. Red line: The developer dilution is ratio 1:3.4, and the development rate is 0.06 µm/min. Grey line: Data in Figure 3.3 for comparison. The developer dilution is ratio 1:2.7, and the development rate is 0.06 µm/min.

The measured profiles in Figure 3.20 also show the improvement for the bump issue. Although the bumps still exist in some profiles, they are smaller (lower than 0.03 µm height) compared to the ones before the modification of the grayscale mask.

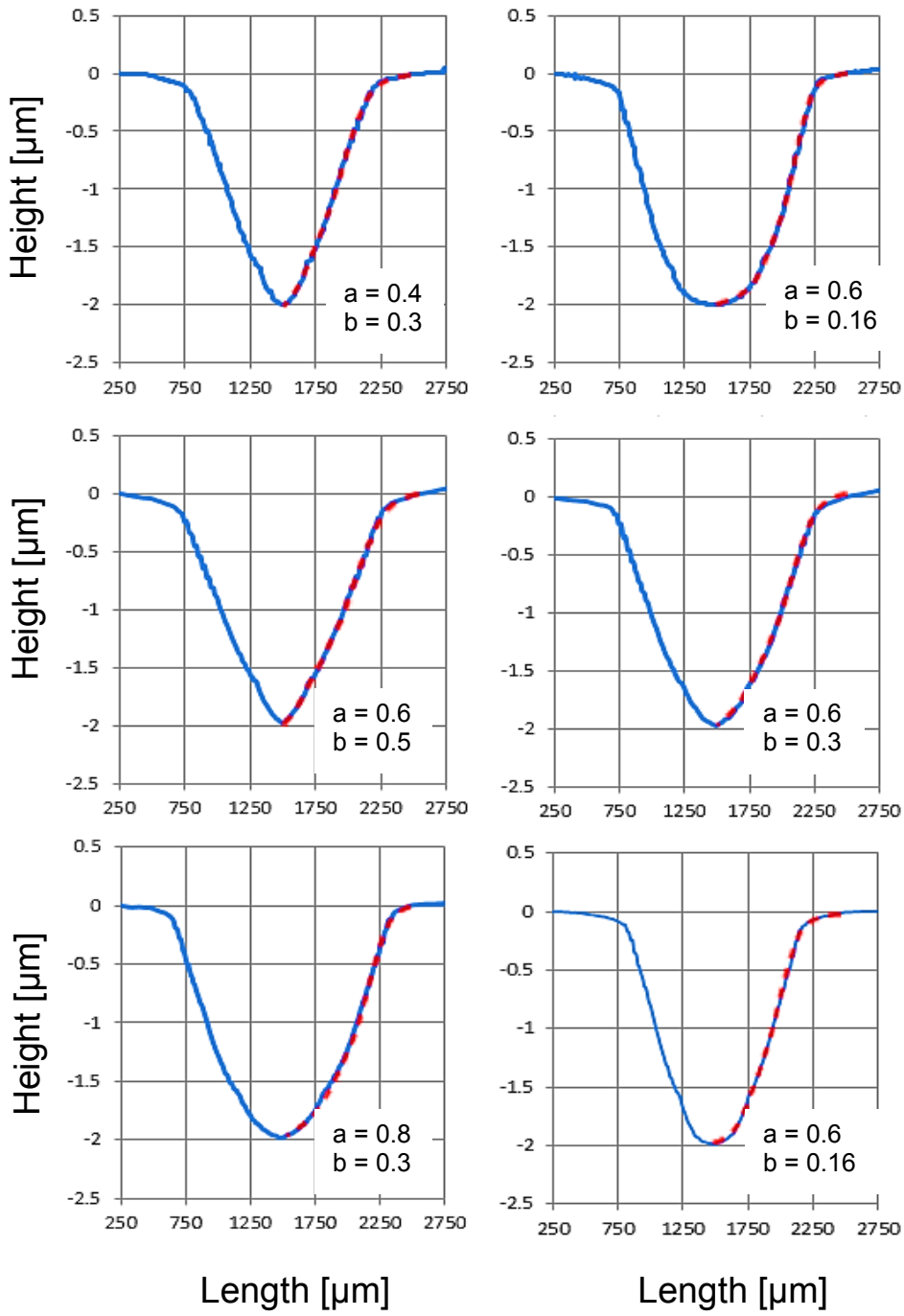

Figure 3.20. Measured developed resist height and the theoretical predication based on Figure 3.19 for different profiles. The values of a and b are the original values.

However, more explorations are needed on this topic in the future, including the reasons of bump formation, the change of relationship of dose vs. developed resist height and change of resist development rate. However, this modified grayscale lithography method still qualifies for the purposes of the micro-pump application. Once the calibration is finished, the results are accurate and stable over a period of time. By adjusting the dilution ratio of developer and development time, it can compensate some small process fluctuation. However, recalibration is needed when large changes occurred from the equipment or the environment. This modified method is still better than the traditional grayscale lithography, because the traditional grayscale lithography suffers the same issues and it is even much more sensitive to the changes mentioned above, and it requires the recalibration for any small change.

3.7 Summary and Conclusion

In summary, a modified grayscale photolithography process is developed, with the following features: (1) grayscale masks are fabricated with regular laser mask writers; (2) The photoresist is overexposed through the grayscale mask; (3) Very dilute AZ developer is used for a timed etch of the resist. Compared to prior lithography, the modified process has the following advantages: (1) it enables the use of almost the entire dosage region, giving more grayscale levels, resulting in a smoother resist profile (RMS: 0.05 μm to 0.1 μm compared to 0.4 μm to 0.5 μm in traditional grayscale lithography [29]). (2) Relatively slow development allows repeatable timed control of the designed photoresist shape. (3) The process can compensate for variations from other steps in the lithography process. (4) Different dilution ratios and development time enables tuning the profiles of the resist. (5) Scaling of the shape height can be accomplished by using the same grayscale mask. This modified grayscale process enables fabrication of the

smooth shaped micro-pump substrate electrode and other predicable 2.5D microstructures in MEMS devices and other systems.

Chapter 4 Electrostatic Actuated Micro-Pump

4.1 Introduction

For achieving the cooling effect in the micro-cooler, two micro-pumps are needed to move the working fluid that transfers heat from the hot chamber and to the cold chamber. In this chapter, the design, simulation, fabrication and actuation tests of a large stroke electrostatic micro-pump that meets the micro-cooler design specification are presented. Based on the thermal analysis of the micro-cooler [26] for achieving a cooling power density of 3 W/cm^2, micro-pump's needs to have >1 μL displacement volume at 10 Hz displacement frequency.

There continues to be great interest in the research and development of micro-pump systems because of increasing demands from chemistry, biology and microelectronics. Pumps provide the driving force to move fluids, which enables transfer, injection, and separation capability in microfluidic systems. For example, biological samples needs be transported through miniature assay systems [71]. In an example relevant to the micro-cooler application, coolant must be interchanged through the heat regenerator [26].

Many researchers have previously developed micro-pumps based on electrostatic [72], piezoelectric [73], electromagnetic [74], and thermal [75] actuation methods. For example, shown in Figure 4.1, an electrostatically actuated, dual-diaphragm pump developed by Honeywell Laboratories [76] achieved a flow rate of 30 ml/min with a power consumption of 8 mW. Micro-pumps might also be built directly into an electronics system to cool transient hot spots, so the fabrication methods and temporal response characteristics may be particularly important. In this chapter, a MEMS-based micro-pump system is designed and fabricated for

moving fluid designed for heat transfer in the electrocaloric cooling system. Electrostatic actuation is chosen here due to its ability to accommodate the large stroke needed to obtain the highest volume displacement of the working fluid and thus the highest heat transfer per cycle. Unlike a Stirling cooler [77, 78], the electrocaloric cooler does not require a pressure cycle to operate, freeing that constraint on the pump design. The pump only needs to operate against the pressure drop across the constrictions formed from the regenerator and pump outlets. This relaxed pressure specification is important as it frees the design space to investigate diaphragm-based pumping systems.

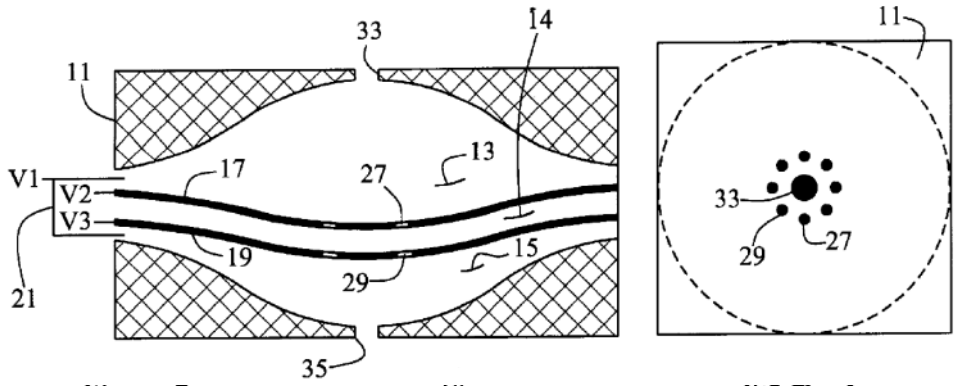

Figure 4.1. Electrostatically actuated, dual-diaphragm micro-pump system developed by Honeywell Laboratories. [76]

In its simplest form, like most other electrostatic actuators, the pump considered in this thesis consists of a moving electrode and a substrate electrode. When an electrical field is applied, the moving electrode is pulled down toward the substrate by the attractive electrostatic force. When the electrical field is removed, the moving electrode returns to its original position due to a restoring force from supporting flexures. It features high compatibility with micromachining technology, low power dissipation, quick response and simple structure. However, most

electrostatic microactuators suffer a major limitation: the electrostatic stroke is small (typically several microns), resulting in low pumping volume in micro-pump applications [79]. This restriction is mainly due to two reasons: (a) most actuation diaphragms are relatively stiff due to relatively thick (>50 μm) elastic materials such as PDMS, or due to relatively stiff (> 100 GPa) materials such as metal or oxides; (b) electrostatic force is proportional to $1/g^2$ where g is the electrode spacing, giving extremely weak force between the diaphragm and a conventional underlying etch pit, that contains substantial fluid displacement volume. For example, the micro-cooler application requires several 1 μL displacement volume, corresponding to a 2 mm x 1 cm pump area with gap greater than > 50 μm. The corresponding electrostatic force would be several hundred nN (for 2 mm x 1 cm area), which is small, leading to only about 10 to 20 μm displacement even for an ultra-thin (10 μm thick) and soft (6 MPa) PDMS diaphragm with large aspect ratio (2 mm / 10 μm = 200).

In this chapter, an electrostatic micro-pump that performs large stroke compared with traditional electrostatic actuators is presented. The moving electrode is made from an ultra-thin (10 μm thick) PDMS layer with meandered metal interconnect to create a highly compliant diaphragm. It is based on the processes to fabricate and transfer ultra-thin PDMS with assistance of gelatin discussed in Chapter 2. A shaped surface for the Si counter electrode is created by modified gray-scale lithography followed by a series of silicon dry etch steps introduced in Chapter 3. The curved 3D shaped silicon electrode allows for an electrostatic zippered actuation to avoid the problem with a large (100 μm deep) starting electrode gap. The combined effects of the compliant diaphragm and the zipping electrodes gap, results in diaphragm displacement greater than 100 μm, giving a displacement volume greater than 1 μL/stroke (for a 20 mm^2 diaphragm area), and a pumping rate of 60 μL/min at 1Hz. High cooling power in the micro-

cooler system can be achieved due to pump's relatively large pumping volume and potential for > 1 Hz pump rate.

4.2 Design Concept

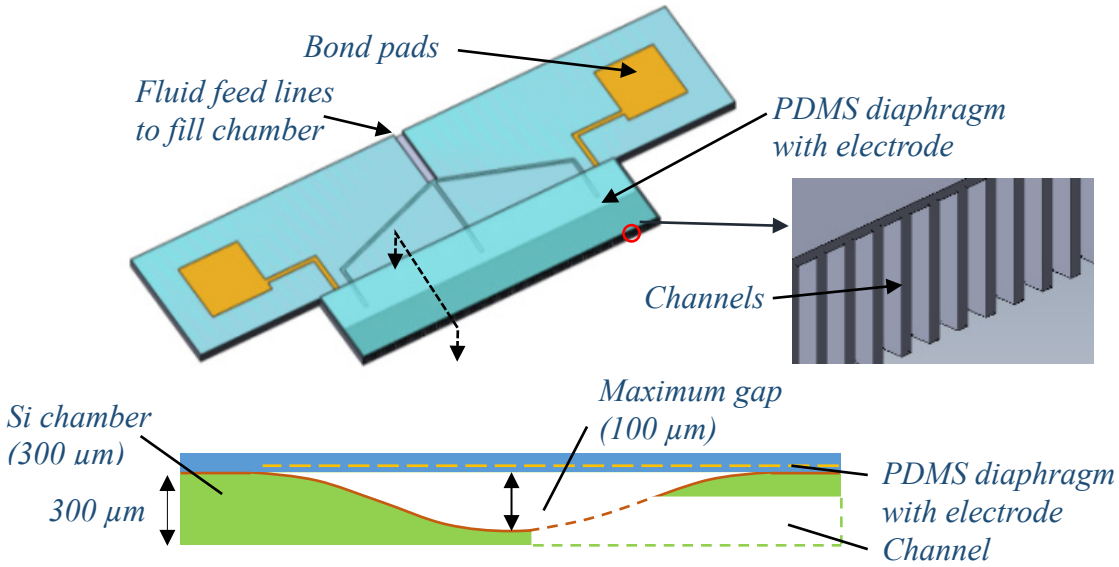

Figure 4.2. Illustration and cross section for large stroke electrostatic micro-pump. The pump comprises a compliant PDMS diaphragm and a smoothly shaped Si chamber.

In the micro cooling system, the micro-pump actuators on either side of electrocaloric terpolymer are designed for moving heat transfer fluid. Figure 4.2 shows the illustration of the cross section of the pump, comprising two key elements, the PDMS diaphragm and the curved 3D-structured Si chamber. The chamber has a width of 2 mm and a length of 1 cm. The diaphragms are made of an 11 µm PDMS layer embedded with metal electrodes (top to bottom: 10 µm PDMS/ 200nm metal/1 µm PDMS). The counter electrode is etched from a 300 µm thick

silicon substrate and created by gray-scale lithography followed by a series of silicon dry etch steps. The choice of silicon for the chamber enables efficient heat transfer between the fluid and heat source/sink to improve the performance of the cooling element. Channels are opened at the outlet of chambers to allow the fluid to pass. The channels and the spacing of the channels are both designed for 50 μm considering the fabrication limitation (aspect ratio dependent etching) and structural robustness.

4.3 Finite Element Simulation of Micro-Pump

The coupled multiphysics used in the COMSOL finite element simulation includes the Mooney Rivlin solid mechanics module, electrostatic module, fluid flow module, porous media module and moving mesh module. The contact force is calculated by adding a customized spring force on the diaphragm after contact:

$$F_c = -k_p g\,, \text{ when } g < 0, \tag{4.1}$$

where F_c is the contact force, k_p is the contact spring constant and g is the gap between diaphragm and substrate. The spring constant is determined by the Young's modulus of the diaphragm and the thickness of the diaphragm between the electrode and the diaphragm's surface. After contact, the distance of the gap becomes negative in the simulation, giving rise to a positive valued normal force acting on the diaphragm. The moving mesh is simulated by using the arbitrary Lagrangian-Eulerian (ALE) moving mesh method. The hyperplastic model (i.e., Mooney-Rivlin model) is chosen in the solid mechanics module for simulating the deformation behavior of the PDMS diaphragm. For improving the simulation's convergence, customized

mapped mesh is applied and fully coupled solver is used in the model. More details can be found in Appendix 2.

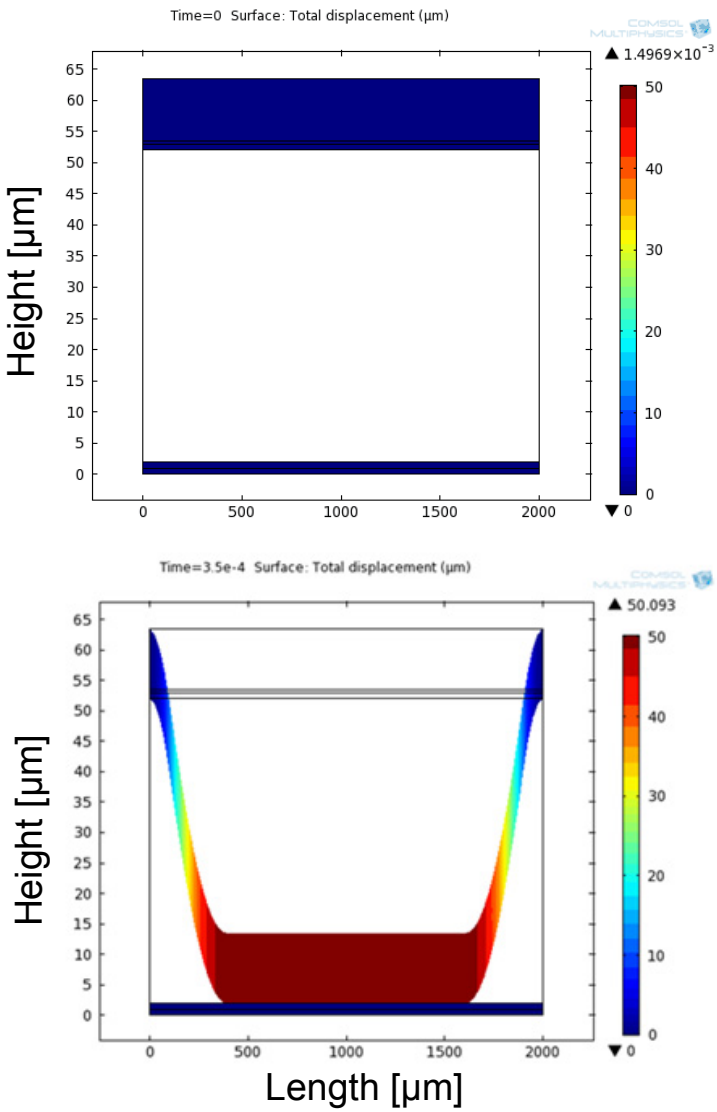

Figure 4.3 A simple demonstration of customized contact force. The fixed-fixed beam is 2 mm long and 11 μm thick, and the gap is 50 μm. The linear model is applied to the beam and the Young's modulus is fixed as 2 MPa. The moving mesh is set for both of the beam and the gap. When 30 V electrical field is applied on the beam, the beam snaps in on the substrate and stopped by the contact force.

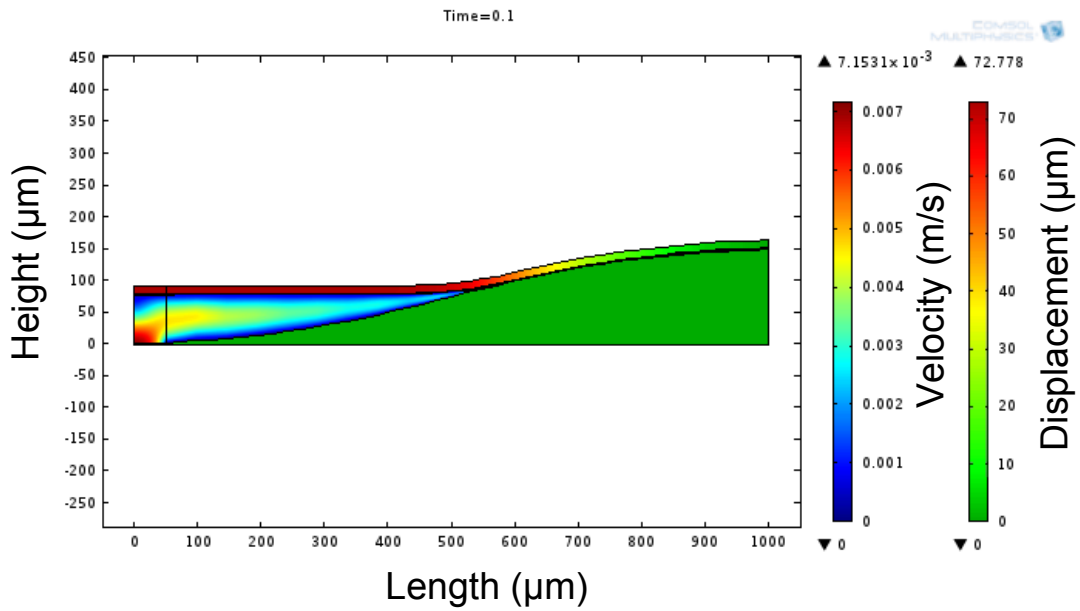

Figure 4.4 Example of the multi-physics finite element simulation for a 2D half cross section of the pump to overcome the computational complexity. In this example, a = 0.5, and b = 0.16. The color in fluid par represents velocity and color in diaphragm part represents displacement.

Figure 4.3 shows a simple demonstration of the customized contact force and moving mesh. The fixed-fixed beam is 2 mm long and 11 μm thick, and the gap is 50 μm. The linear model is applied to the beam and the Young's modulus is fixed as 2 MPa. The moving mesh is set for both of the beam and the gap. When a 30 V electrical field is applied on the beam, the beam snaps in on the substrate and is stopped by the contact force.

Simulations are first performed to investigate the effect of chamber profile for the snap-in voltage. The first simulation is performed as a 2D half cross section of the pump to overcome the computational complexity, shown in Figure 4.4 as an example. A 50 μm outlet is open in the center of the pump (left position of the half pump in the figure). The diaphragm is 13 μm thick and the insulating layer is 1 μm thick. The gap of the chamber is 150 μm deep, and filled with

Galden HT-70 fluorinated heat transfer fluid (Solvay S.A., Brussels, Belgium). The properties of the fluid is shown in Table 5.1. The material constants of PDMS used for the Mooney Rivlin model of PDMS membrane are C_1 = 321 kPa, C_2 = 0 kPa, corresponding to the Young's modulus of 2 MPa. The Fermi-Dirac function that is introduced in Section 3.6., is define the different shape of Si chamber here. Figure 4.5 shows the simulation results for minimum required snap-in voltage for different shapes of chamber profile when parameters *a* and *b* vary.

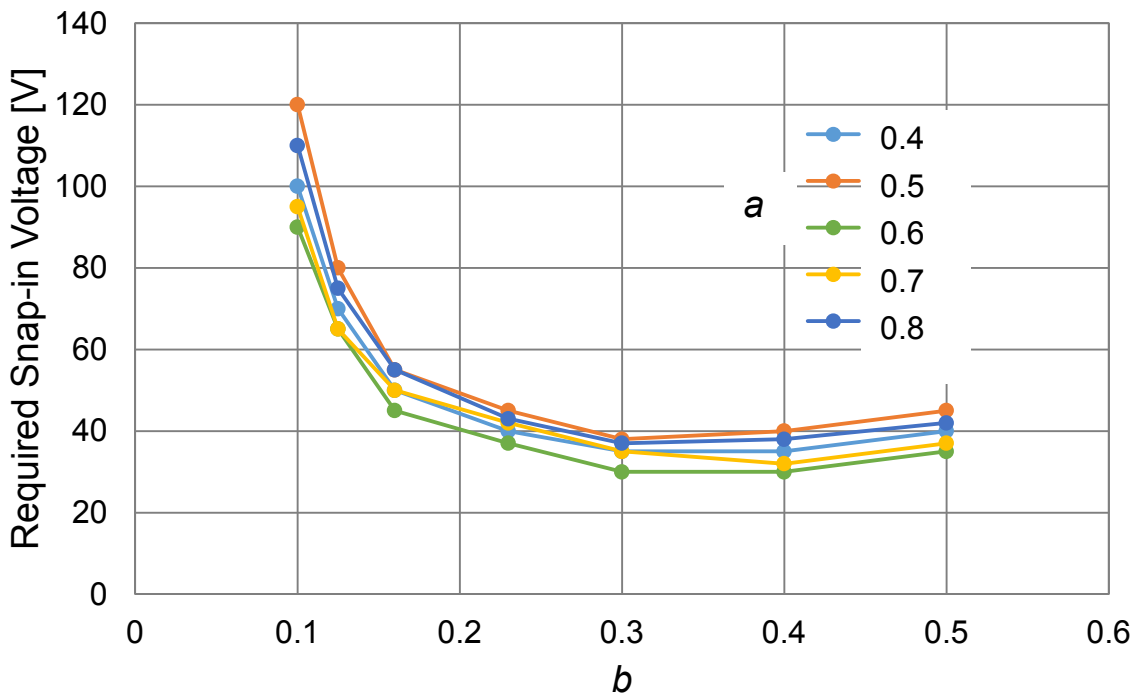

Figure 4.5. Static simulation results for minimum required snap-in voltage for different chamber shape.

Table 4.1 Material properties of heat transfer fluid HT-70

Material	Density, ρ (kg/m^3)	Relative Permittivity, ε	Viscosity, μ (Pa·s)	Thermal conductivity, k (W/(m·K))	Heat capacity, c (J/(kg·K))
HT-70[80]	1680	1.88	8.4×10^{-4}	0.065	970

For simulations of push-pull pump behavior in the micro-cooling system, to overcome the computational complexity brought about by the fine structure in the regenerator, a porous medium model was used as an abstracted model to replace the EC polymer thin layers and spacers that create the channels. The permeability of the porous media is calculated based on Darcy's law:

$$\kappa = \frac{\mu l v}{\Delta p} \tag{4.2}$$

where μ is the porosity; l is the length of the EC module; Δp is the pressure drop crossing the electrocaloric regenerator and v is the velocity of the fluid flow. The ratio of Δp and v is extracted from the thermal/fluid flow simulation [81].

An single-stack cooling element with push-pull pumps is first explored, and then a back-to-back stack of two elements designed for micro-coolers application (described in section 1.3 and depicted in Figure 1.6) are simulated. The thickness of the diphragm is 11 μm, and the chamber depth is 150 μm. The Mooney Rivlin constants are C_1 = 321 kPa, C_2 = 0 kPa, coresponding to Young's modulus of 2 MPa. Figure 4.6 (a) is an example 2D simulation of a

single-stack cooling element while the Figure 4.6 (b) is a simulation of a back-to-back stack of two elements. In, Figure 4.6 (a), two different actuation voltages are applied on two diaphragms (1 and 2) alternatively and the Si chamber (1 and 2) is grounded. When 100 V actuation voltage is turned on, the diphragm starts to snap in from the edge of the cavity to the center gradually. The fluid is pushed through the regenerator that is simulated by porus media, pushing up the diaphragm of the other pump and generating pressure drop. Figure 4.7 (b) shows the results of displacements and pressure drop of the pump under the applied voltage (Figure 4.7 (a)). In Figure 4.6 (b), separate actuation voltages are applied on each of the four Si chambers (3, 4, 5 and 6) while the diaphragms (3 and 4) are grounded (Figure 4.7 (a)). The results of displacements and pressure drop are shown in Figure 4.7 (c). Single-stack element and back-to-back stack of two elements without regenerator pressure drop are also simulated. In the simulations, the porus media module in regenerator area is replaced by normal fluid module (with no-slip boundry condition, i.e. the velocity at wall equals to zero), while the porous media in the channel area remains.

The simulation results in Figure 4.9 show the maximum frequency that the device can be operated and still allow the diaphragm to completely snap-in in during each cycle under the particular applied voltage. Figure 4.9 shows the pressure drop, p, crossing the electrocaloric regenerator under the particular applied voltage. It depends linearly on velocity, v, and thus frequency, f,

$$p = 100 \times f \tag{4.3}$$

where p is in units of Pa and f is in Hz.

In the figure, the results of back-to-back stack of two elements only show two sets of data (50 V and 100 V). Simulations with higher voltage fail to converge in COMSOL Multiphysics due to the complex structures.

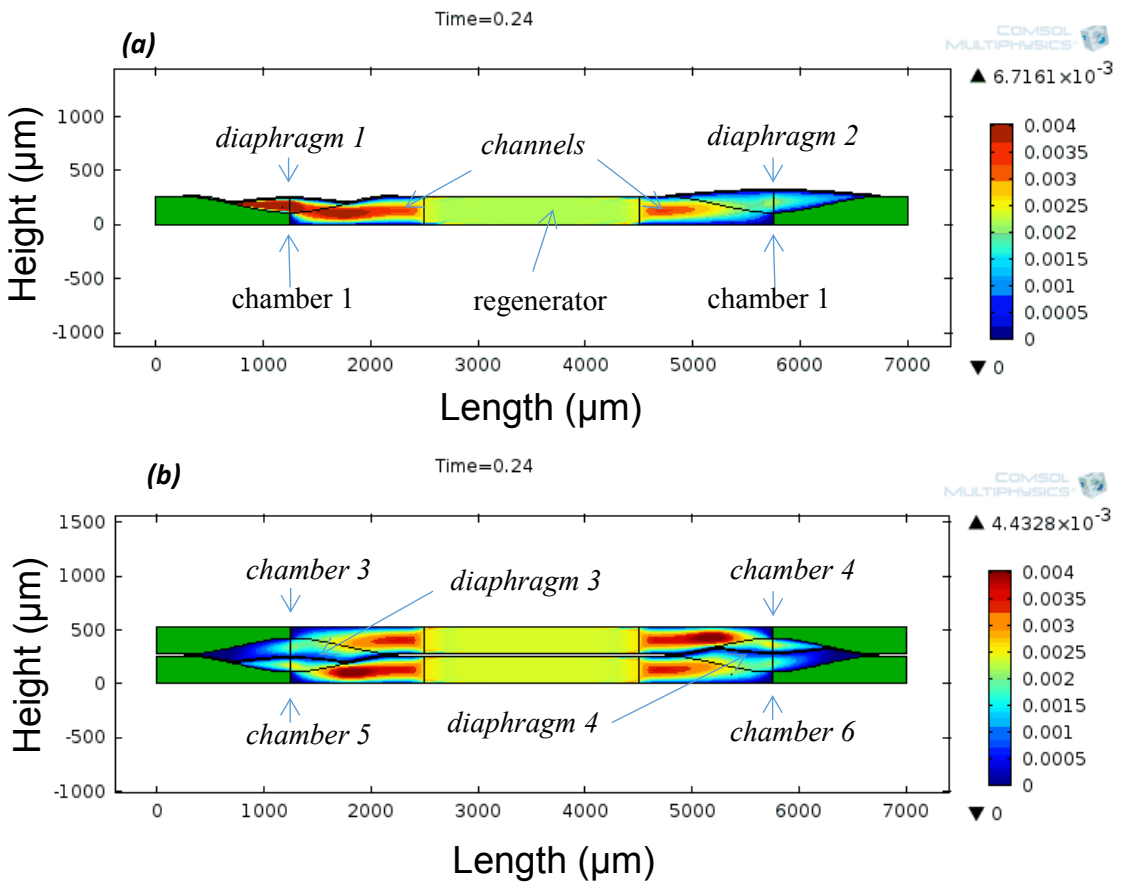

Figure 4.6. Examples of the multiphysics simulation for (a) single element and (b) stacked double elements. The color map indicates the pressure in the liquid flow.

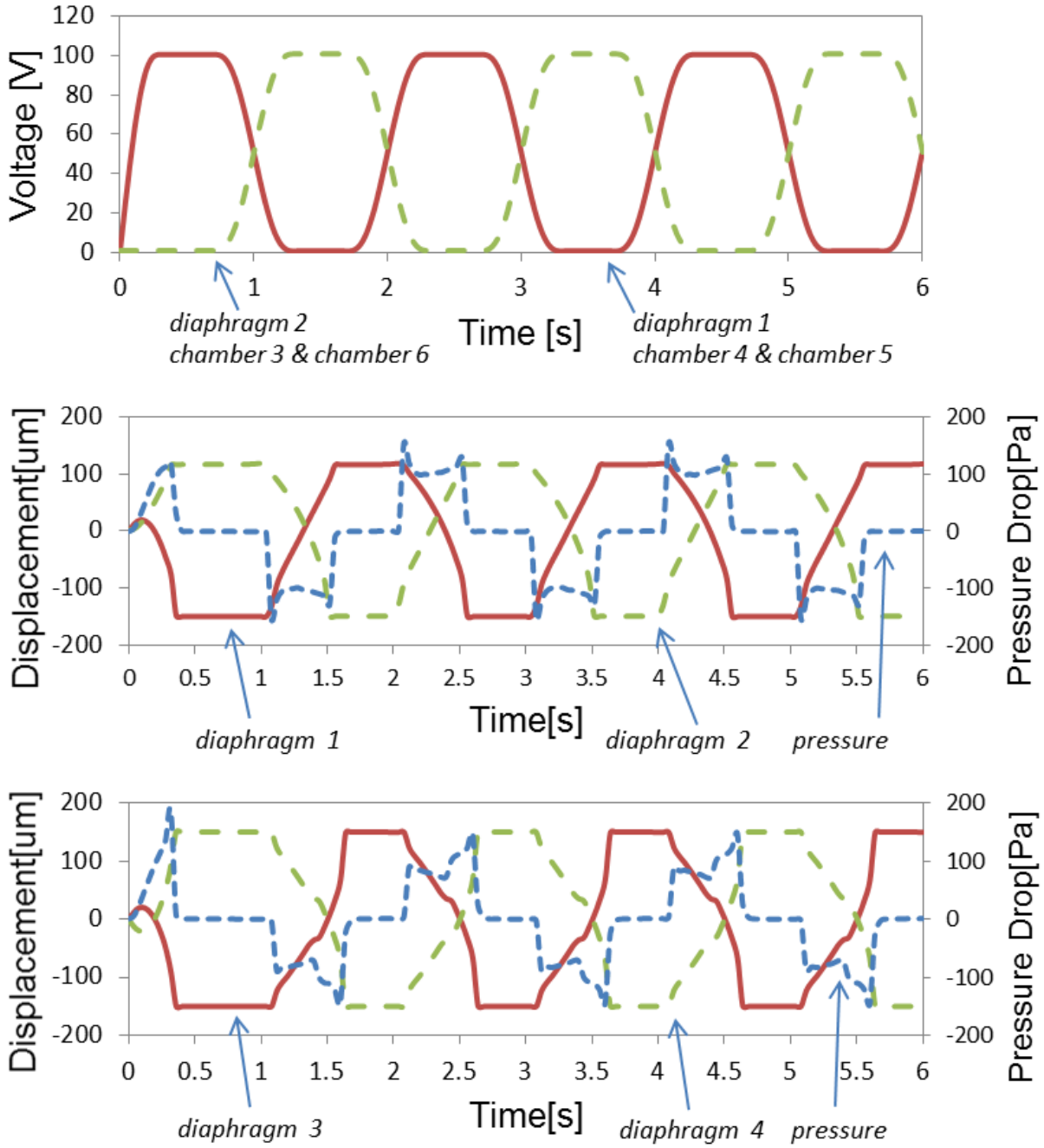

Figure 4.7. Results of the displacement and pressure drop for the multiphysics simulation for (b) single element and (c) stacked double elements under (a) applied voltage. In (b) and (c): Red and green: diaphragm displacement; Blue: pressure drop.

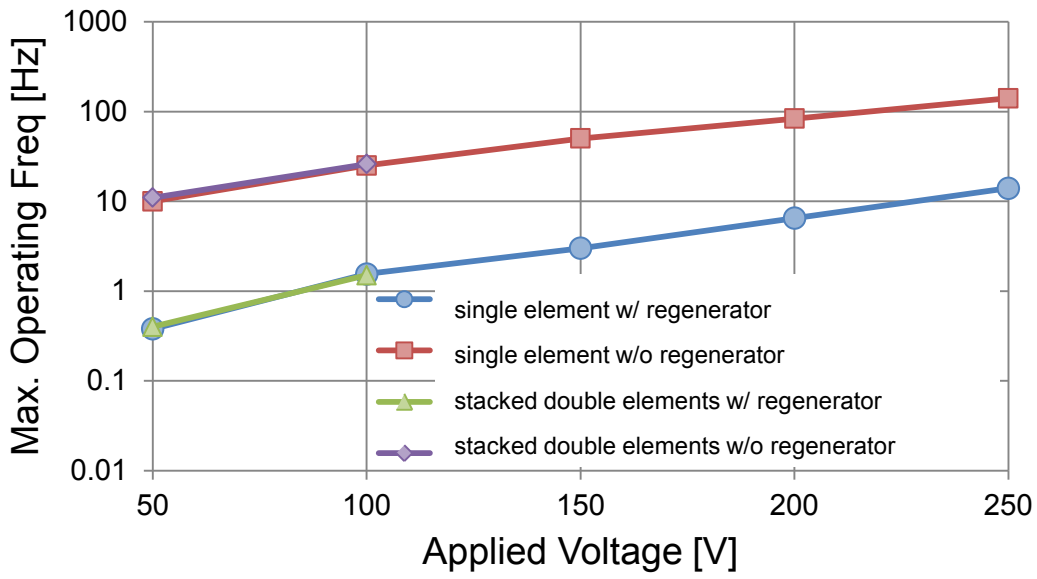

Figure 4.8. Maximum operating frequency for particular applied voltage. Simulations include single stacked cooling element with and without regenerator, and back to back stacked double cooling elements with and without regenerator

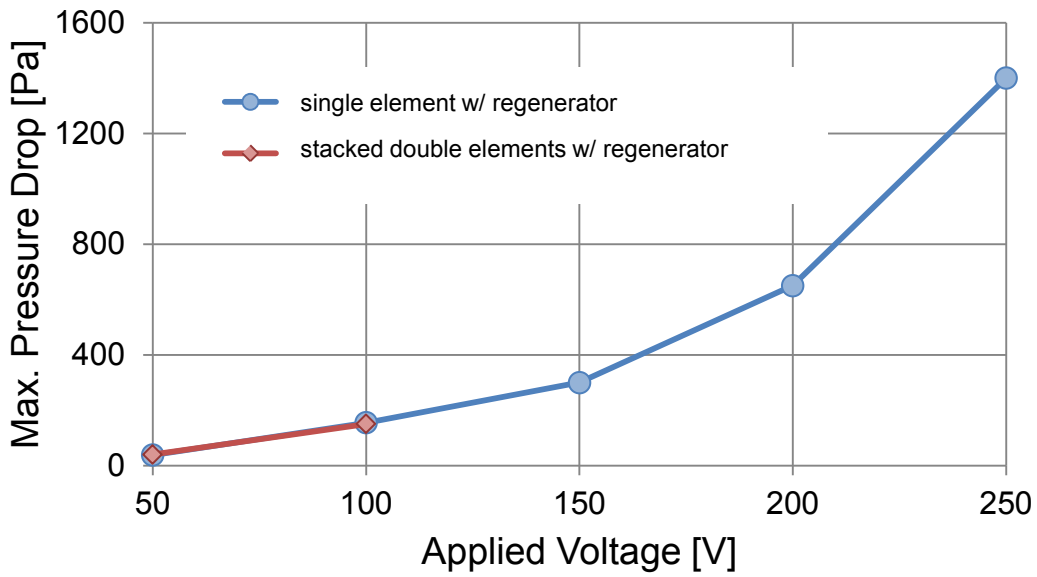

Figure 4.9. Maximum pressure drop for particular applied voltage for single stacked cooling element and back to back stacked elements with regenerator.

4.4 Fabrication of Micro-Pump

4.4.1 Ultra-thin PDMS Diaphragm with Embedded Metal Electrodes

Based on development of a transfer method for ultra-thin PDMS by using gelatin as sacrificial layer in Chapter 2, 11 μm thick PDMS diaphragms with embedded metal electrodes are fabricated and released with minimum feature size of 2 μm. Gelatin powder (250 bloom, Modernist Pantry, Portsmouth, NH) is first dissolved in warm water (33 wt%). The solution is spun on a silicon handle substrate at 1000 rpm for 2 min with infrared heating applied simultaneously to prevent the gelatin from hardening, and then baked in a 40°C oven to form a 10 μm-thick sacrificial gelatin layer. PDMS (Sylgard 184, Dow Corning, Midland, MI) is created by mixing pre-polymer gel and the cross linker in a 10:1 (w/w) ratio. The mixture is spun at 6000 rpm and cured for 12 h in an oven at 70ºC to create a 10 μm-thick PDMS layer. For creating the PDMS membrane with embedded metal electrodes, Cr/Al/Cr metal layers (5 nm/200 nm/5 nm) are then evaporated (deposition rate 1 Å/s), and wet etched in a serpentine mesh pattern to prevent buckling and breakage [47]. A second layer of 2 μm-thick PDMS is spun and cured to seal the metal layer. Access openings to pads connected to the embedded wiring are created by PDMS masking and CF_4/O_2 plasma ashing of the PDMS. Figure 4.10 shows the optical pictures of fabrication diaphragm and bonding pad. The mesh lines in the picture are 4 μm wide. The corresponding pump's structure and its cross section is shown in Figure 4.2.

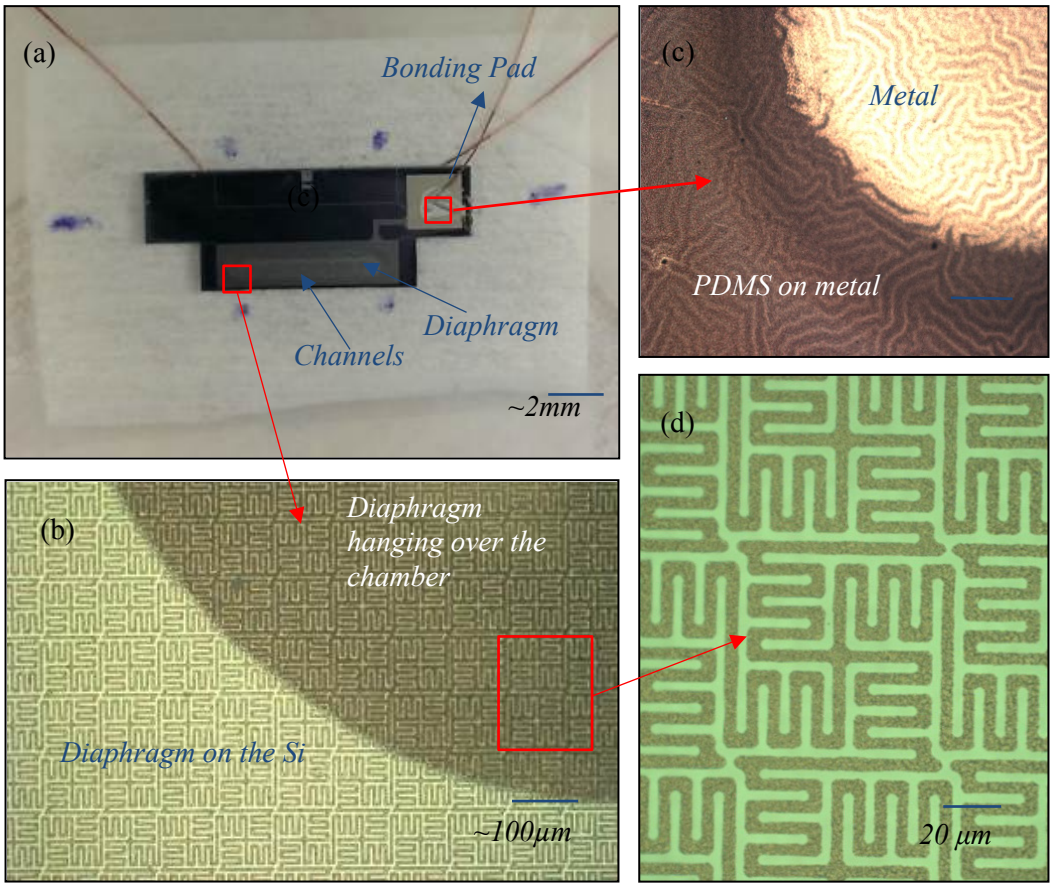

Figure 4.10. Fabricated large stroke electrostatic actuated PDMS-on-Si micro-pump. (a) Assembled micro-pump (b) and (c) Fabricated diaphragm hanging over the chamber. (d) Fabricated bonding pad.

4.4.2 Shaped Silicon Substrate Fabricated by Modified Grayscale Photolithography

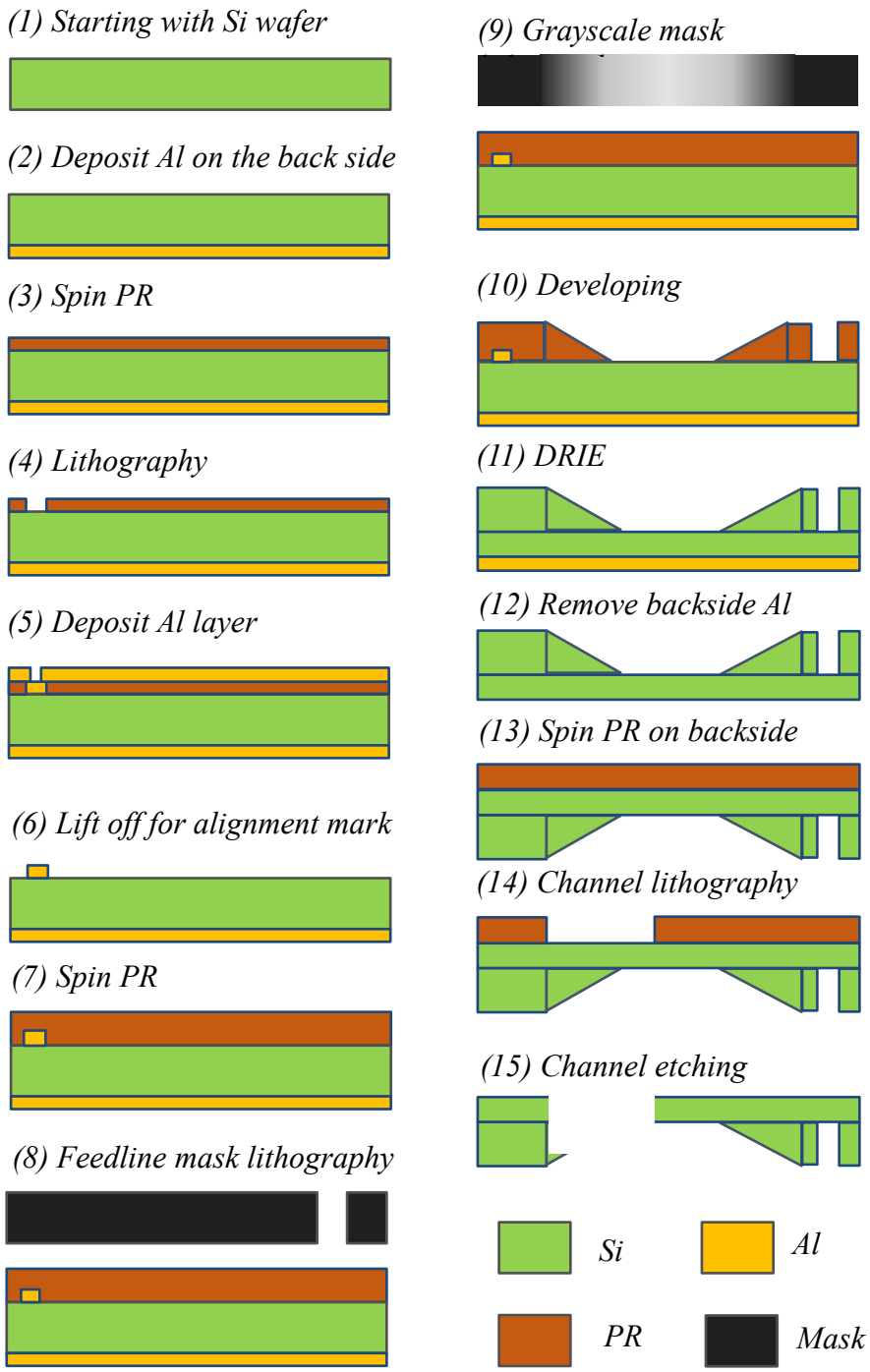

Figure 4.11. Process flow for shaped Si substrate electrode fabrication

Grayscale optical masks are designed and fabricated to produce cubic function spline shaped structures for the Si substrate electrodes based on the calibration of the overexposed, dilute development lithography process discussed in Chapter 3. The feed lines are created by double exposure technique, and the full process flow is shown in Figure 4.11.. In the grayscale photolithography, a Karl Suss MA6 (λ=320 nm, resolution ~ 1 μm) contact aligner and AZ4210 photoresist are used for the lithography process. The AZ4210 photoresist is spun at 2000 rpm on a Si substrate, coated with hexamethyldisilazane (HMDS), to create a 3 μm thick resist layer. The wafer is soft baked at 95°C for 2 min. The sample is over exposed for 380 s at 5 mW/cm^2 intensity under proximity mode. The gap between the sample and the grayscale mask is set to be 150 μm to diffract the UV light. The sample is then soaked horizontally in AZ developer that is over diluted with water (AZ developer to water: 1:2.7). No agitation is used during development. As soon as the 2 μm resist located in the 100% UV transmission regions is dissolved, the development is stopped. This process takes 33 min. The wafer is removed from the developer, rinsed slowly in DI water, and dried with nitrogen. The developed resist profile is then measured by a KLA Tencor P-15 profilometer. The developed resist is then etched in a Surface Technology System (SPTS) inductively coupled plasma Deep Reactive Ion Etching (DRIE) machine to transfer the resist profile to form a Si etch pit having a 100 μm maximum depth. The process conditions are listed in Table 3.1.

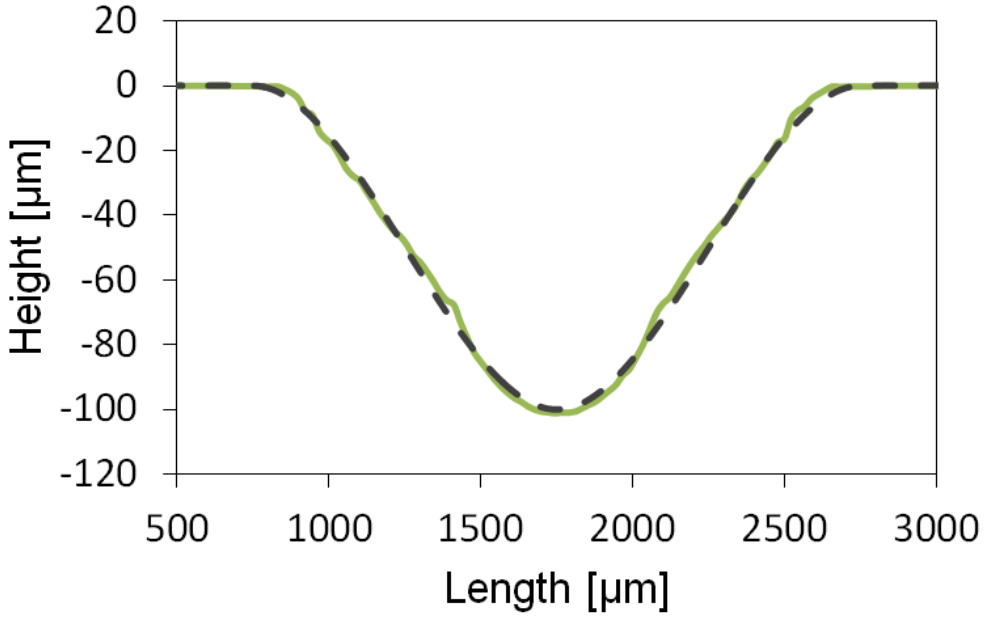

Figure 4.12 Measured Si height after DRIE. The profile is designed as a cubic function shape.

The measured profile is shown in Figure 4.12. A 150 µm deep cavity is also fabricated by using 2 µm photoresist, 50 min development, and same transfer process, which is also shown in Figure 4.12. The measured etch pit shape matches the designed cubic function shape within 10%. Optical and SEM pictures are shown in Figure 4.13. The channels on the Si structure in the SEM are created by a second backside patterned DRIE step. A 2 µm thick PECVD oxide is coated on the top surface of the chamber to prevent potential shoring problem during the actuation.

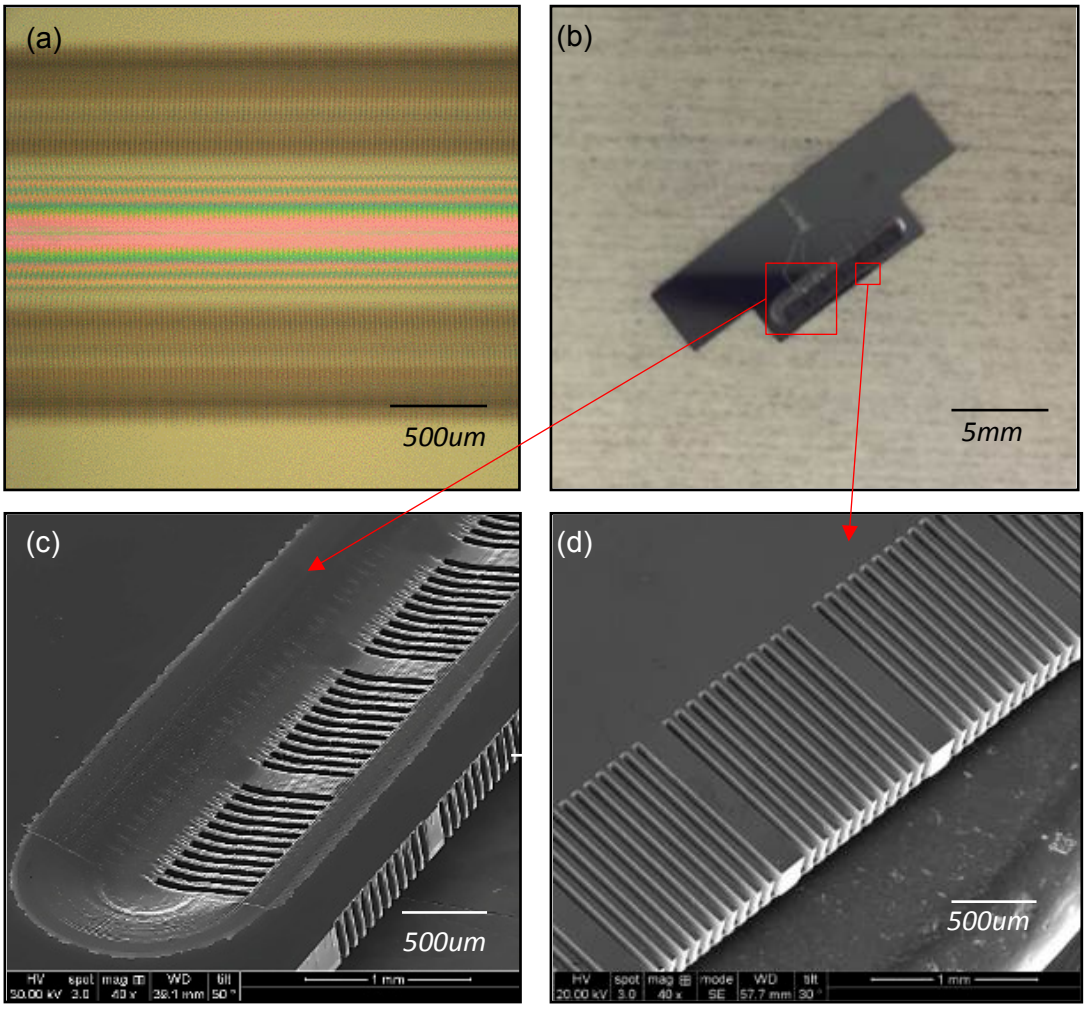

Figure 4.13 Fabricated 100 µm deep curved Si substrate (a) Optical picture of developed photoresist. (b) Full part. (c) Front side SEM of the shaped Si electrode.(d) back side SEM of Si channels.

4.4.3 Micro-Pump Assembly

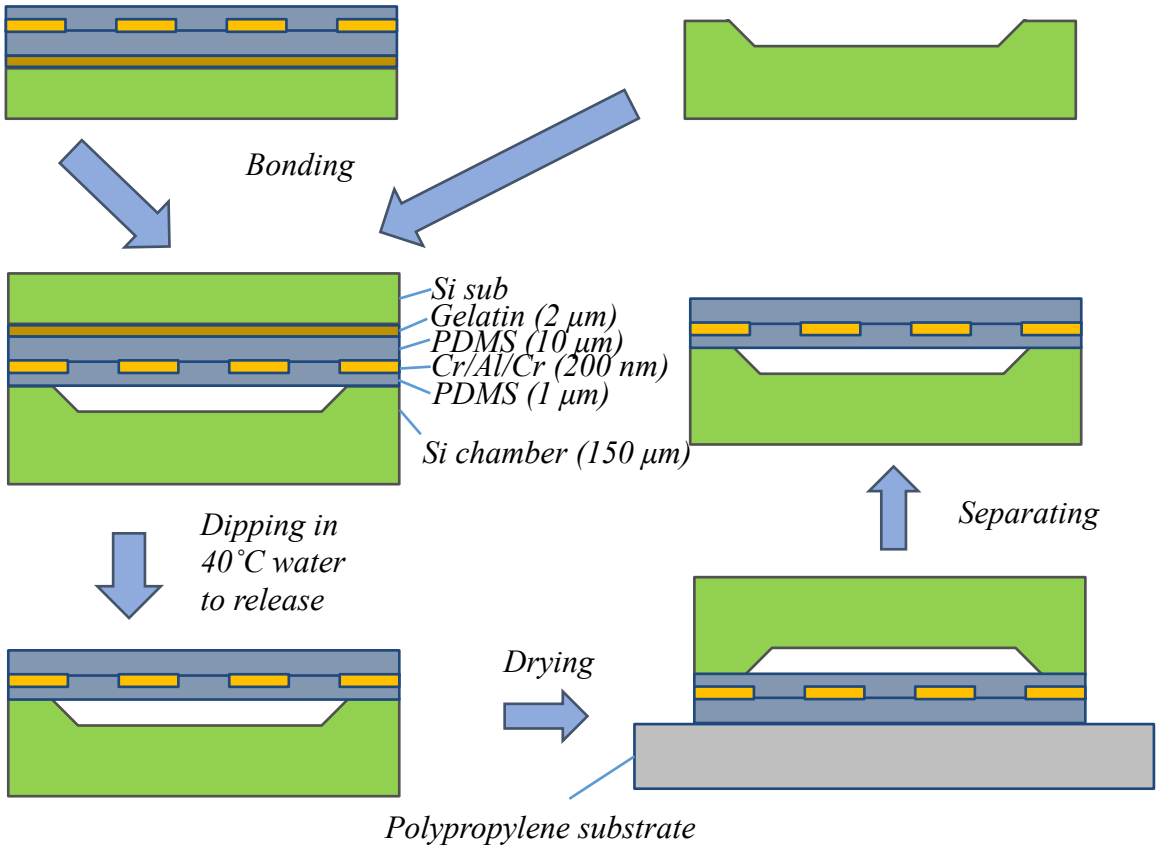

Figure 4.14 Process flow for micro-pump assembly. After bonding, the assembled device is then dipped in 40°C warm water to dissolve gelatin to release the pump. The polypropylene prevents the diaphragm sticking on the Si electrode when drying.

After plasma surface activation treatment of the PDMS diaphragm and of the Si chamber to increase adhesion, the two components are aligned and bonded using a device bonder (Besi/Laurier M9). The assembled device is then dipped in 40°C warm water. The gelatin layer dissolves after about 2 hours, releasing the micro-pump. The device is flipped over and placed on

a polypropylene substrate to dry for 30min. The polypropylene prevents the diaphragm sticking on the Si electrode when drying. The process flow is shown in Figure 4.14, and the final fabricated micro-pump is shown is Figure 4.10 (a).

The micro-pump fabrication suffers low yield. This comes from possibility of failure accumulated from each step. The spinning of PDMS may include particles resulting in uneven surface that could cause bonding issue. It also may result in defect that could cause shorting problem during the actuation. The evaporation has a low possibility to crack the films due to the TCE mismatch. The adhesion between Cr and PDMS is worse than the regular semiconductor materials such as adhesion between Cr and Si. The metal could be peeled off during the lithography and etching process due to the low adhesion. In the lithography, the photoresist could not be spun evenly on the PDMS surface sometimes, and the soft bake may crack the sample due to the TCE mismatch. The dicing process also has the chance to damage the sample. The issues from grayscale lithography presented in Chapter 3 may fail the Si chamber fabrication. The bonding and release process has some failure possibility. A larger bonding area brings a higher possibility of failure. In the bonding process, some of regions are not bonded tightly, resulting in diaphragm peeling off during the release process. In the contrary, some regions do not release even after long time immersion in the warm water. The bonding pad etch rate in RIE etcher sometimes varies. This may cause the bonding pad to be etched through. In summary, the failures mainly come from the incompatibility with traditional semiconductor fabrication techniques and instability of manual process. More exploration needs to be performed to refine and improve the fabrication process to increase the yield in the future.

4.5 Actuation Tests of Micro-Pump

The test bed setup for actuation testing is shown in Figure 4.15. A function generator (HP 33120a) provides the actuation voltage, which is amplified by a high voltage amplifier (Trek 2210; Trek, Inc., Medina, NY). A 1 MΩ resistor is connected in series to protect the amplifier in case the testing pump gets shorted. The current is monitored by a picometer (Keithley 2400; Keithley Instruments, Cleveland, OH). The PDMS diaphragm of the pump in the actuation test is measured as 14 μm thick and the sealing layer is 2 μm thick. The Si substrate electrode is coated with 2 μm thick PECVD oxide. Silver paste is used to connect the bonding pads and the wires. The diaphragm is operated by electrostatic actuation in the air to demonstrate its actuation ability (Figure 4.16 (a) and (b)). The pump chamber is then filled with heat transfer fluid HT-70 (Solvay Solexis, Inc, West Deptford, NJ), and the pump is immersed in the fluid as well (Figure 4.16 (c) and (d)). In Figure 4.16, the diaphragm is hanging over 2 mm x 1 cm x 100 μm pump chamber, with shape parameters *a* equals to 0.5, and *b* equals to 0.15, corresponding to a pumping volume of 1 μL. When the voltage (150 V) turns on, the diaphragm is completely snapped in on the chamber. The optical picture by microscope showing the details of the diaphragm are also shown in the figure.

The center displacement of the diaphragm along with pump volume under different applied voltage are measured and shown in Figure 4.17. The diaphragm is totally snapped in at 150 V, and the stroke is 100 μm, corresponding to a pumping volume of 1 μL/stroke, and a pumping rate of 60 μL/min at 1 Hz. The FEA simulation is performed to compare the measurement result. In the simulation, the effective Young's modulus of the 12 μm diaphragm and 2 μm sealing layer is set to be 6.5 MPa and 12 MPa respectively, according to the characterization in Chapter 2. The

measurement displacement is smaller than the simulations. The reason is possible due to the imperfect etched cubic function shape of Si electrode, such as bump shown in Figure 4.12, and the roughness due to grayscale lithography. The bump is about 8 μm height and 75 μm wide. Simulation including bump structure is firstly performed to explore the effect. However, it failed to converge. When the diaphragm snaps in on the bump, the simulation stops due to the converging error. This leads to explore the bump effect by investigating the sensitivity of profile parameter *a* and *b*. Figure 4.18 shows the variation of *a* and *b* and the corresponding maximum size change in the Si profile.

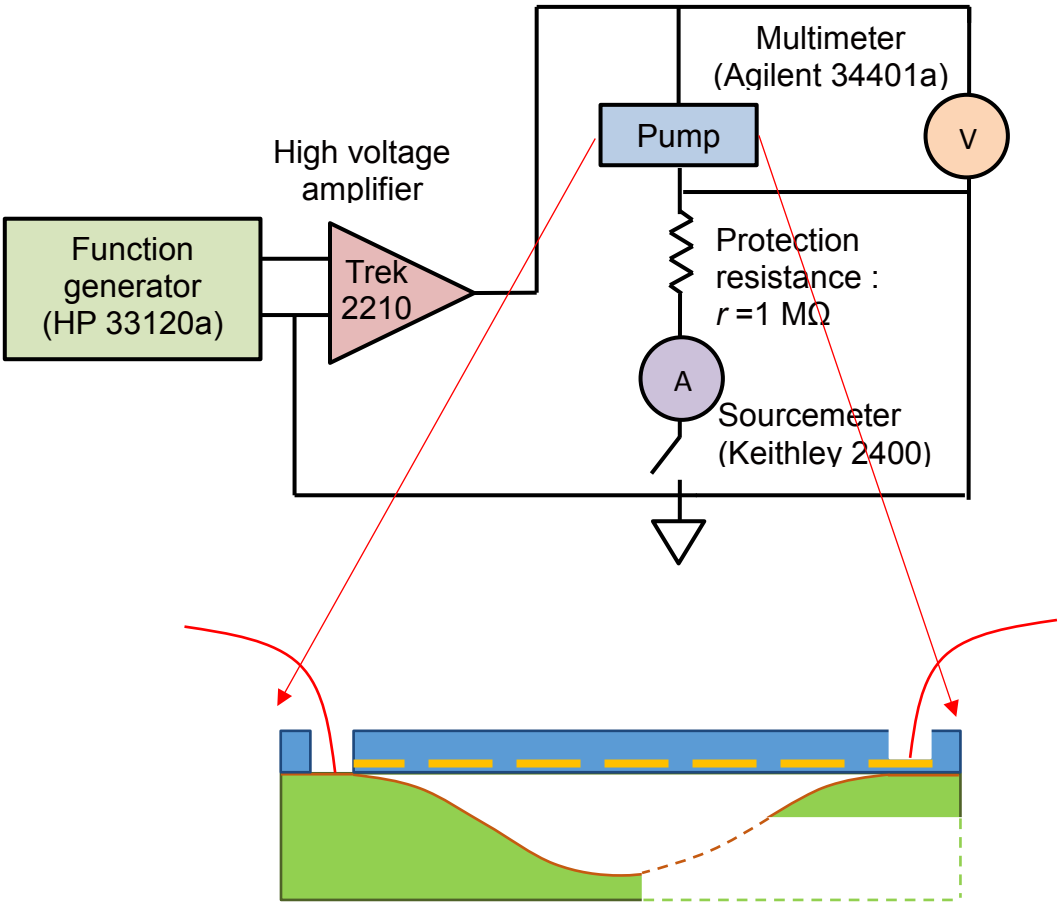

Figure 4.15 Test bed setup for micro-pump electrostatic actuation.

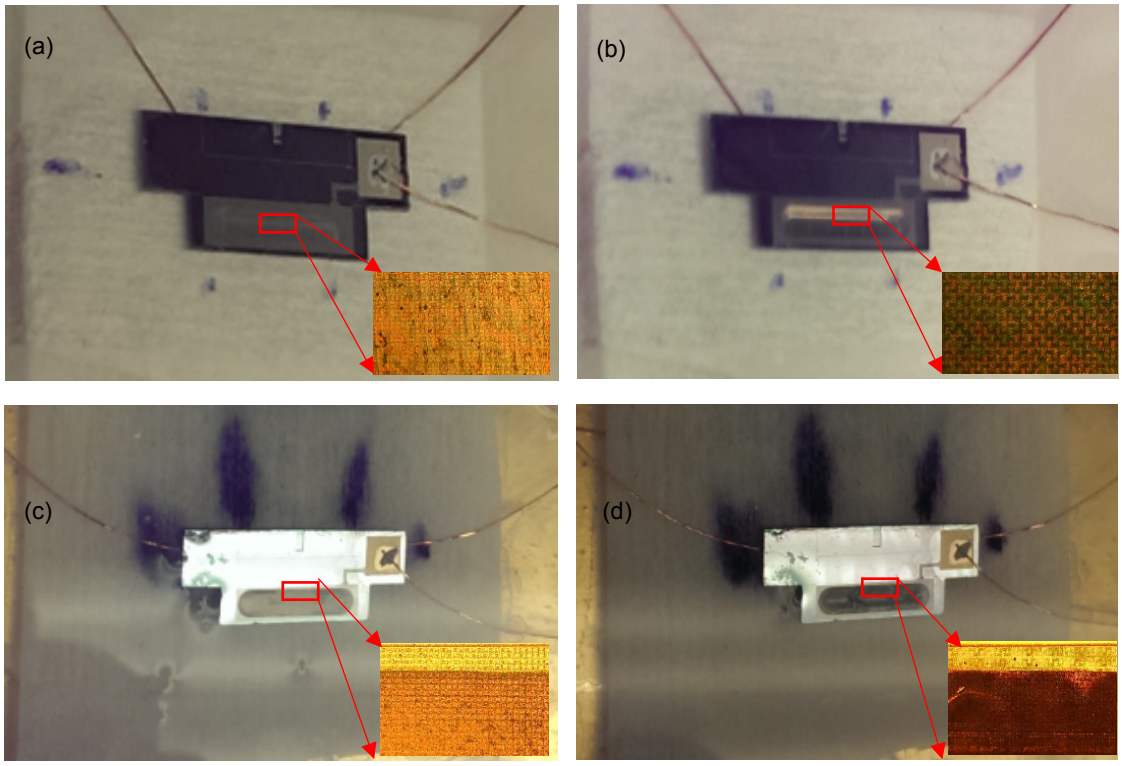

Figure 4.16. Optical images of pump actuation (a) and (b) diaphragm is operated in the air. (c) and (d) diaphragm and pump is operated with filling with the HT-70.

Figure 4.19 shows some examples of corresponding shapes. Simulations are then performed with these shapes. Figure 4.20 shows the simulation results of the diaphragm displacement vs applied voltage for different values of *a* while value of *b* is remained as a constant. Figure 4.21 shows the results for different values of *b* while value of *a* is remained as a constant. The result of the sensitivity of *a* and *b* for the required snap-in voltage is shown in Figure 4.22. From figures, it shows the parameter *b* has a huge impact for require snap-in voltage. For example, when the value of *b* changes from 0.15 to 0.115, corresponding to only 4.5 um change in the profile, the snap-in voltage changes from 127 V to 165 V accordingly. Therefore

the bump appearing in the Si chamber may bring some effect on snap-in voltage, leading the mismatch between the measurement and simulation. The result of sensitivity here and the result from Figure 4.5 show a very complex relationship among the Si profile shape, applied voltage and diaphragm displacement. Therefore, micro-pumps with different Si shaped chambers are fabricated to explore their effect.

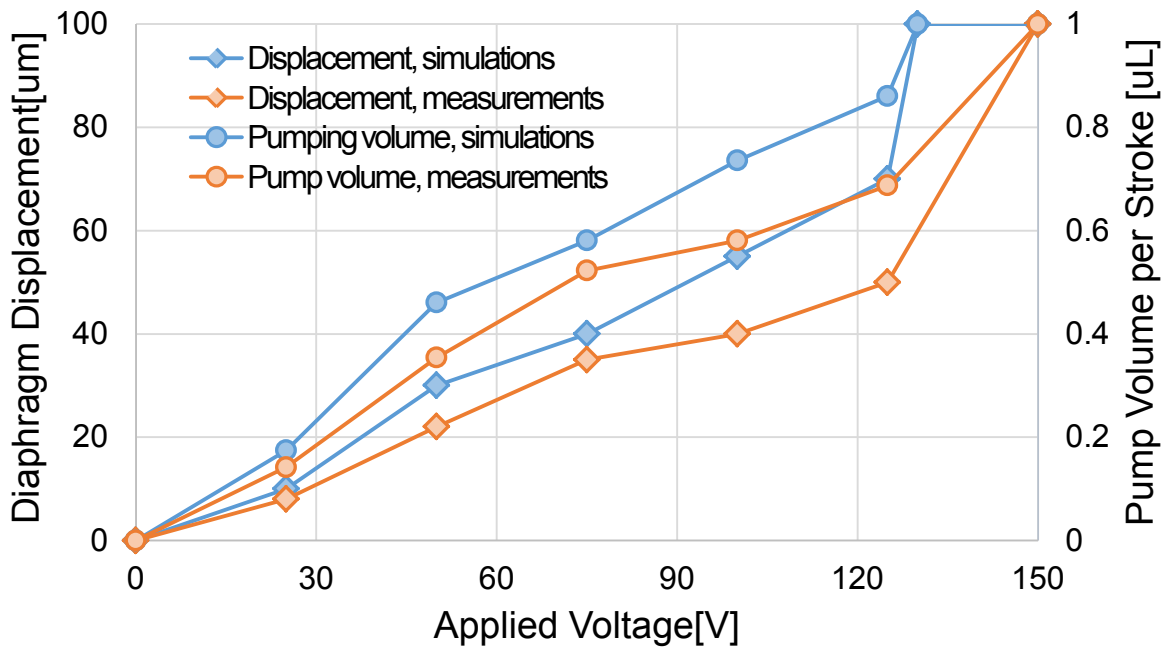

Figure 4.17. Measured vs. simulated displacement of the center of the pump diaphragm and the corresponding displaced volume.

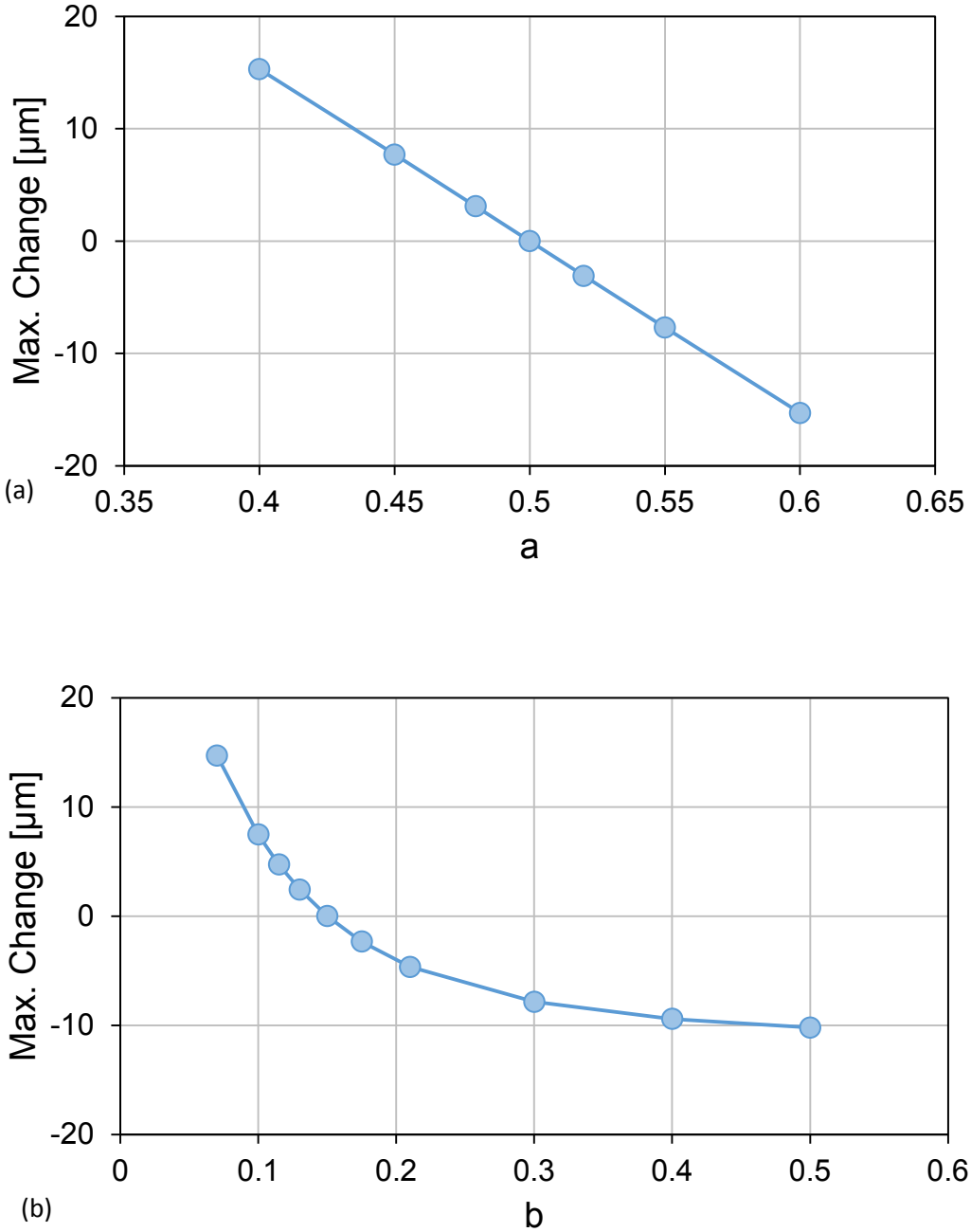

Figure 4.18. Variation of a and b and the corresponding maximum size change in the profile. (a) b is set to be 0.16, and a varies from 0.4 to 0.6. (b) a is set to be 0.5, and b varies from 0.07 to 0.5

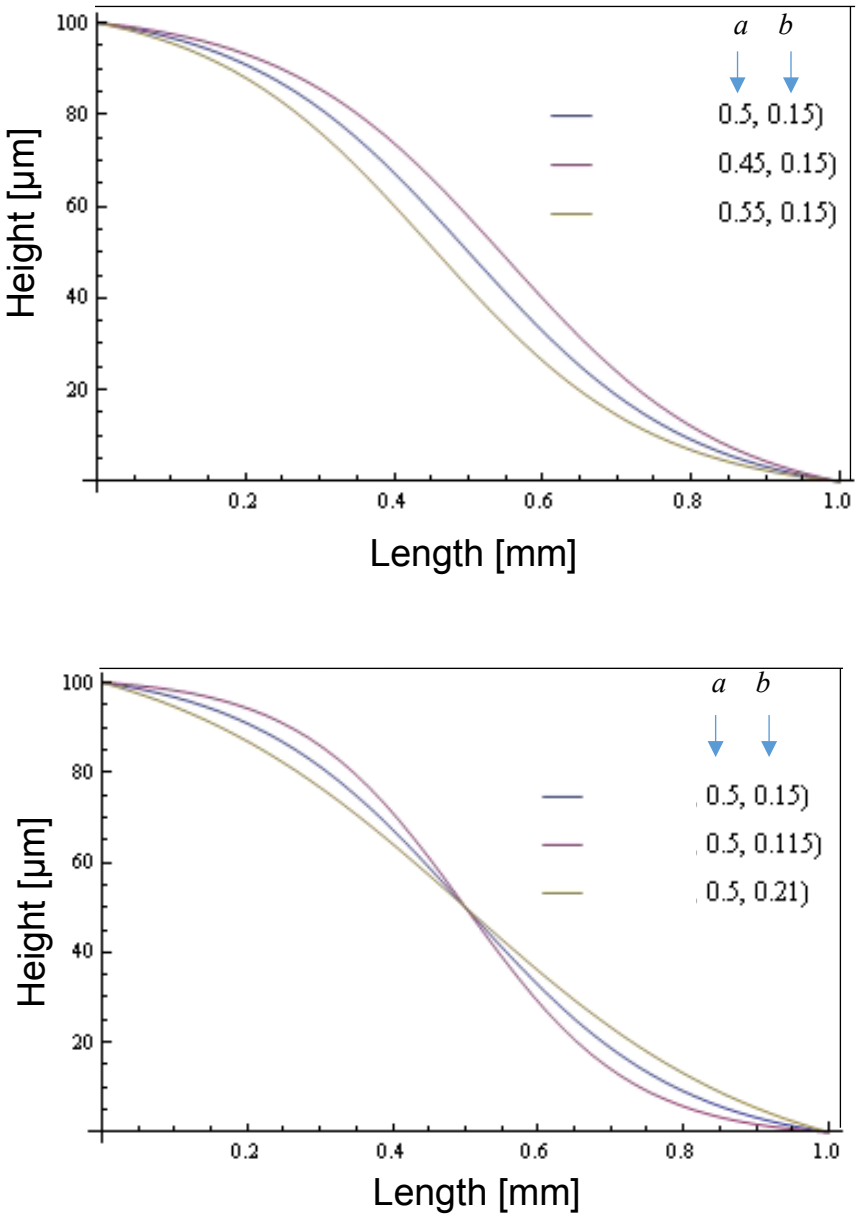

Figure 4.19. Different shapes for different values of a and b.

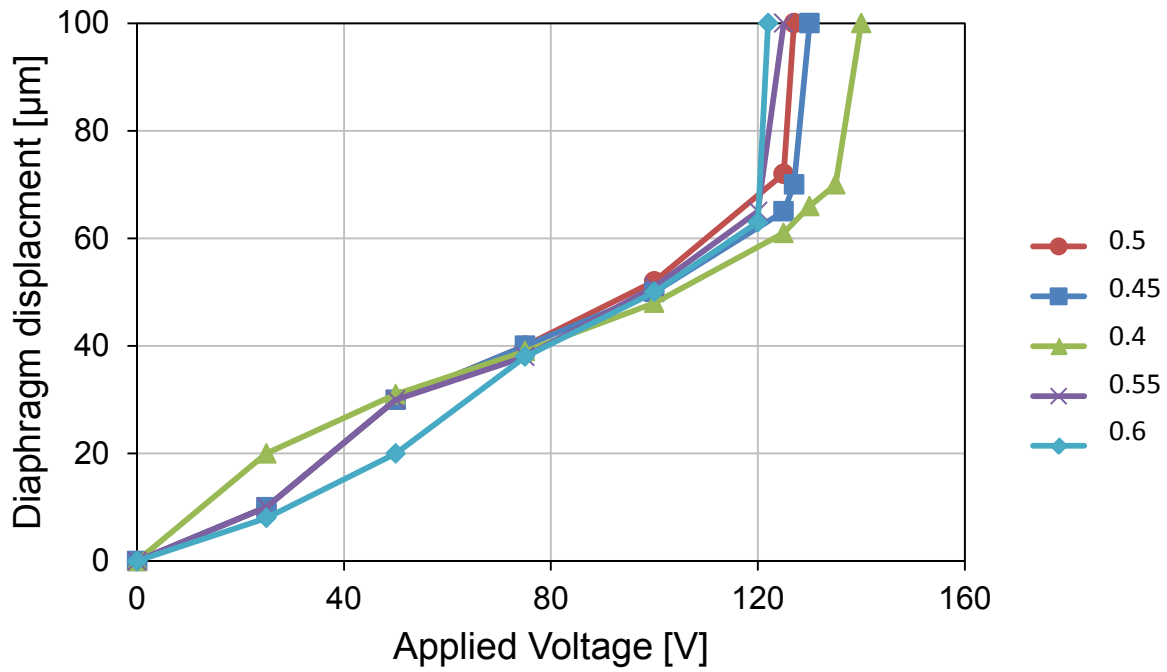

Figure 4.20. Diaphragm displacement vs applied for changing value of a while keeping b as the value of 0.15.

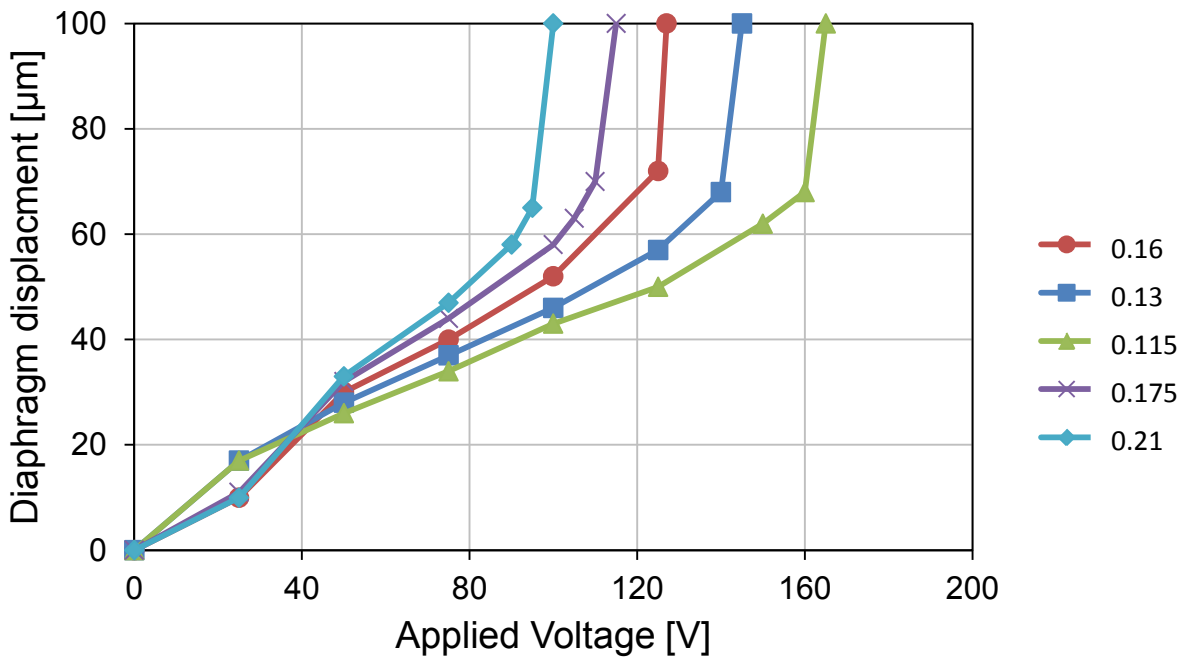

Figure 4.21. Diaphragm displacement vs applied for changing value of b while keeping a as the value of 0.5.

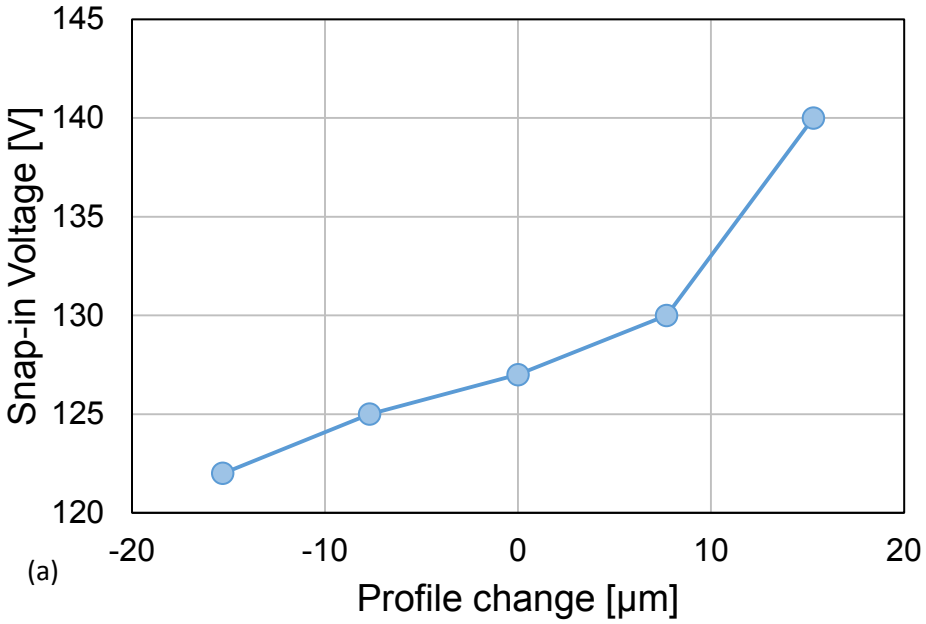

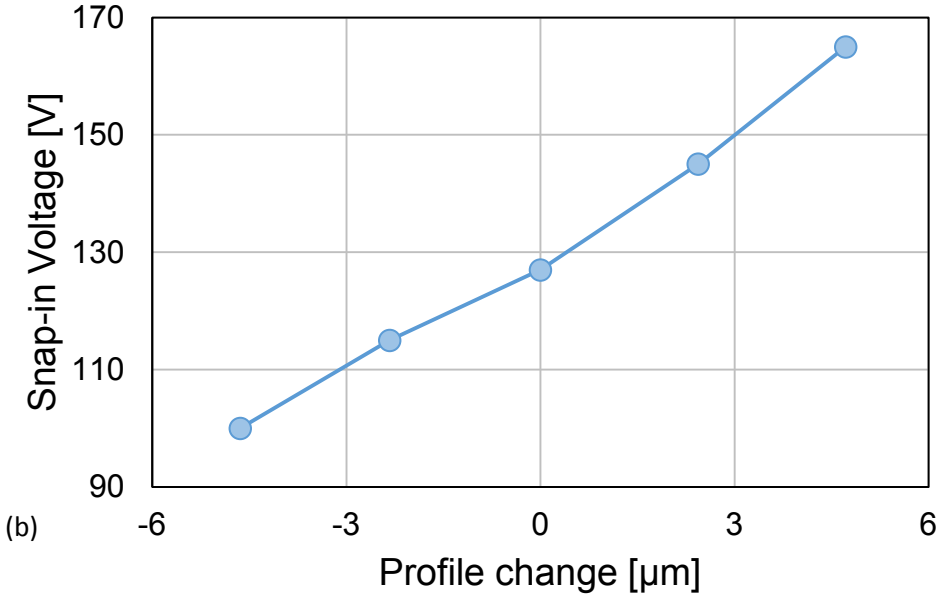

Figure 4.22. Sensitivity of profile height changes from (a) parameter a and (b) parameter b for snap-in voltage

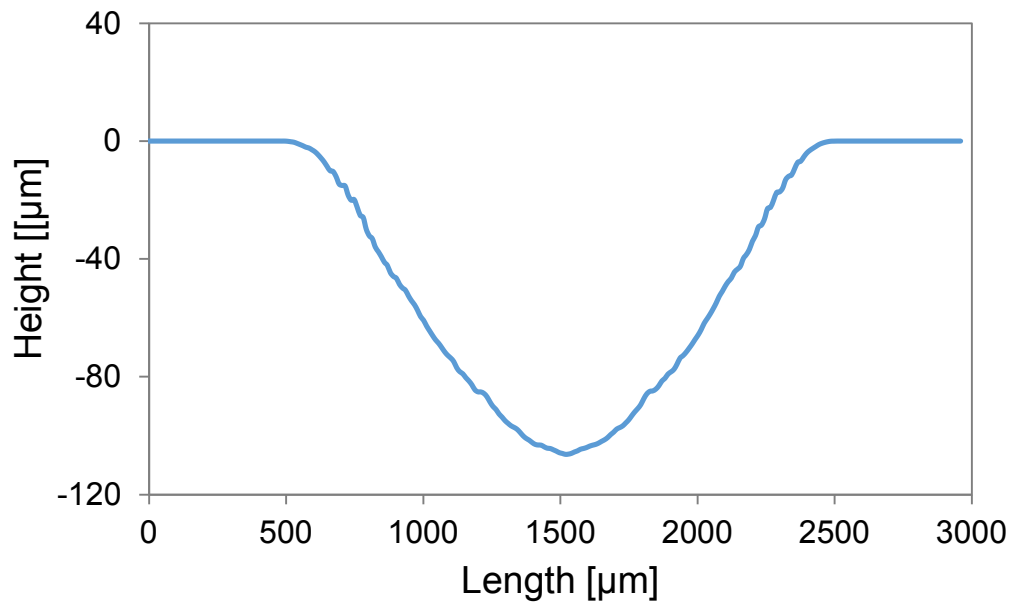

Figure 4.23. Fabricated Si chamber with a = 0.58, b = 0.17.

Based on the profile shapes represented in section 3.6, pumps with different Si chambers are fabricated. Their corresponding parameter *a* and *b* are *a* = 0.45, *b* = 0.11; *a* = 0.48, *b* = 0.145; *a* = 0.44, *b* = 0.18 and *a* = 0.58 , *b* = 0.17. One of examples of fabricated chamber profiles is shown in Figure 4.23. Figure 4.24 shows the result of comparison between the measurement and simulation for the required snap-in voltage. The data reported in Figure 4.17 is also included. It is shown that the measurement result agrees with the trend of the simulations, and they match within 20%. When the value of parameter *b* decreases, the required snap-in voltage increases. This also matches the sensitivity analysis of *b* presented in Figure 4.22. The mismatches from these pumps are smaller than the mismatch presented in Figure 4.22. This is possibly due to lower bumps on the chambers. The preliminary tests show that the maximum operating

frequency the pump is 3 Hz. Higher frequencies could cause the diaphragm not returning its original position after each actuation cycle.

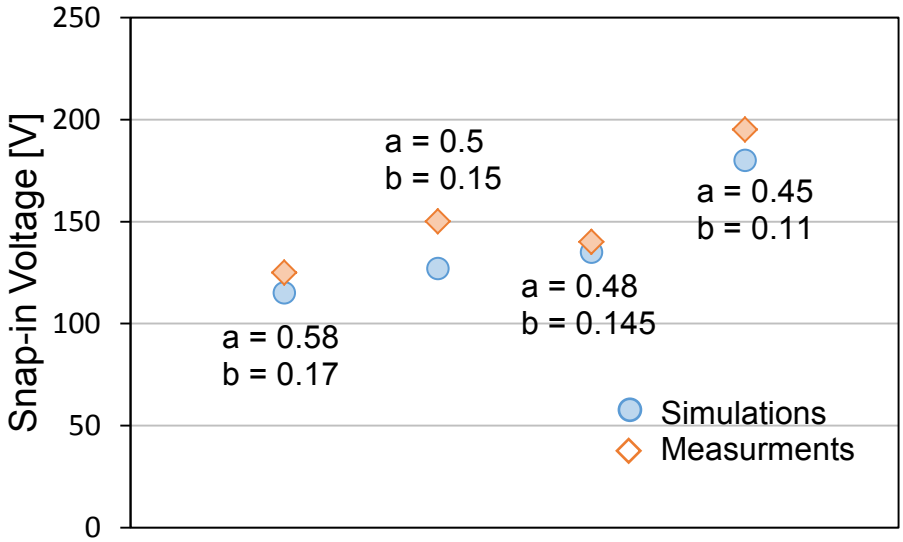

Figure 4.24. Measurement and simulation results for different chamber shapes of micro-pumps. Blue dots: Simulation; and red dots: measurements.

An integrated system of two micro-pump elements based on the micro-cooler design is also fabricated. Figure 4.25 shows the structure of the two-pump system. The two diaphragms are designed on one piece of PDMS, and each diaphragm has two bonding pads to guarantee the electrode connection. The two Si chamber are also connected. The regenerator area in the micro-cooler system is replaced by the channels, which are etched from the backside of chamber by utilizing aspect ratio dependent etching. The fabricated element is shown in Figure 4.26. The bottom of the chamber is then sealed by a 120 μm thick PDMS. The double pump system is firstly operated by electrostatic actuation in the air. When the voltage (250 V) is applied on one of the pumps, the diaphragm of that pump is completely snapped in on the chamber, squeezing

the air through the channels to the other pump, pushing the other pump's diaphragm up (Figure 4.27). The similar process happens when the voltage is applied the other pump. Galden HT-70 fluorinated heat transfer fluid is then injected into pump to test the double pump actuation for the fluid.

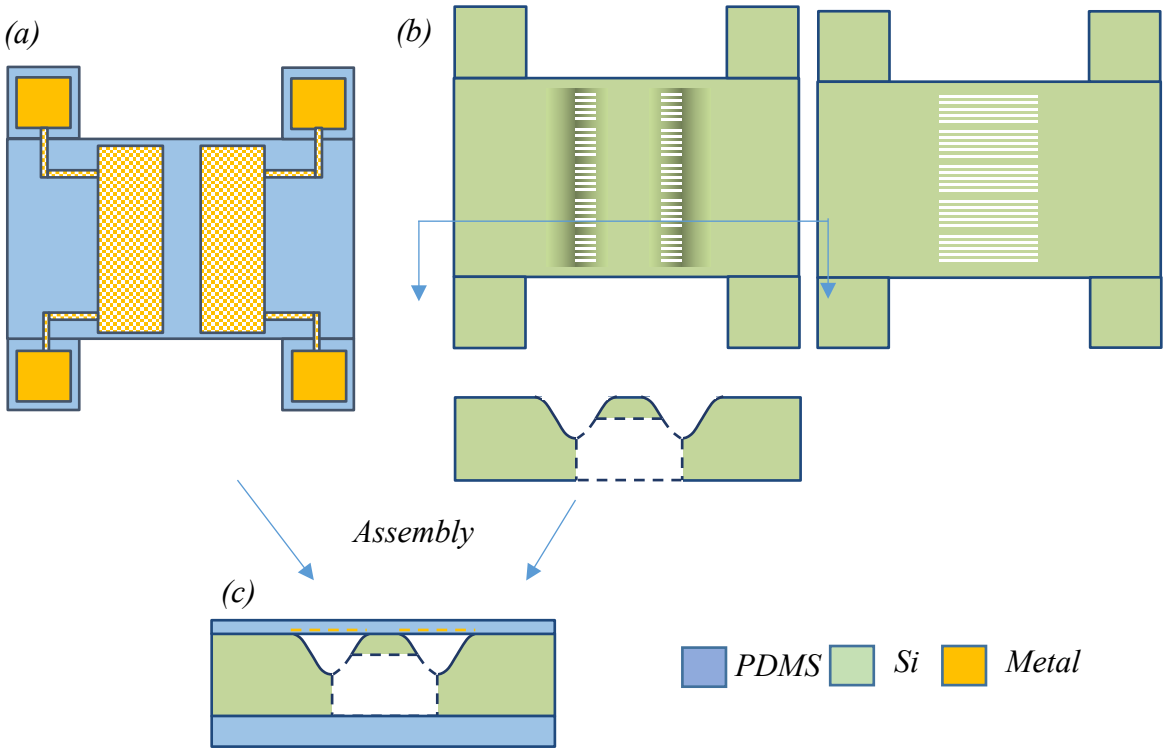

Figure 4.25. Illustration and cross section for double micro-pump element. (a)Top view of diaphragm. (b) Top, bottom, and cross section view of chamber. (c) Cross section of assembly element.

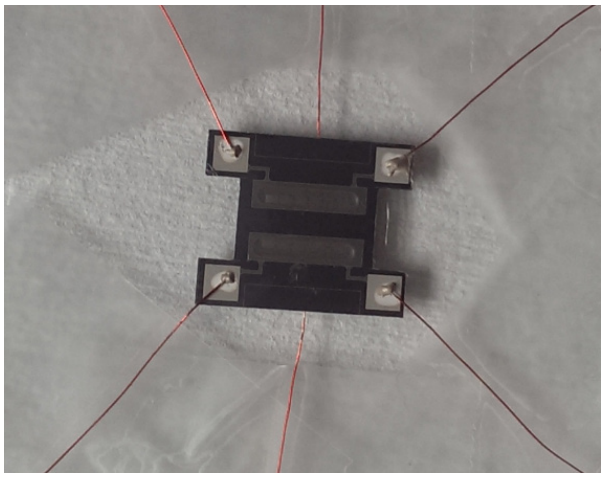

Figure 4.26. Fabricated double pump element.

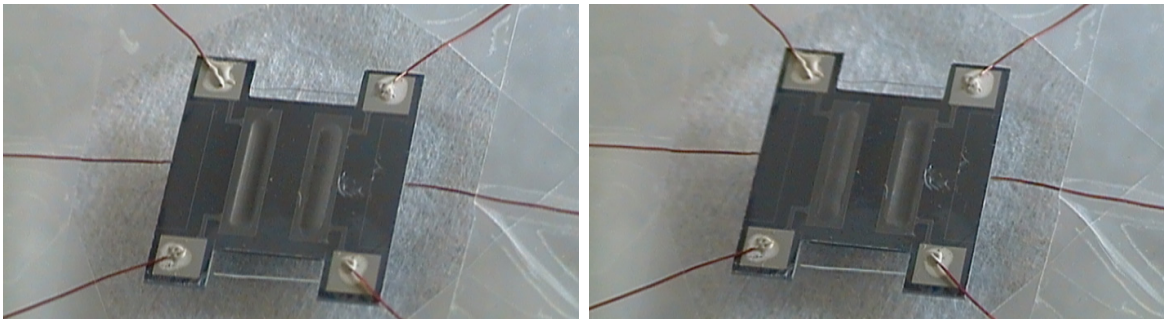

Figure 4.27. The double pump system is operated by electrostatic actuation in the air. When the voltage is applied on one of the pump, the diaphragm of that pump is completely snapped in on the chamber, squeezing the air through the channels to the other pump, and pushing the other pump's diaphragm up.

4.6 Summary and Conclusion

In summary, we introduce a large stroke electrostatic micro-pump made from a compliant thin PDMS diaphragm embedded with metal electrodes and bonded over a smoothly curved Si substrate that acts as the counter electrode. The maximum measured displacement of the diaphragm of the micro-pump was 100 μm, giving a displacement volume of 1 μL/stroke, and a pumping rate of 60 μL/min at 1 Hz. The performance of the pumps may be further improved by increasing actuation voltage, chamber depth, smoothness of the profile, and comparing effects of varying parametric shape of the profile. This ultra-large stroke PDMS micro-pump may open a promising route for fabricating other large electrostatic stroke actuators.

Chapter 5 Electrocaloric Regenerator Sub-Assembly

5.1 Introduction

In the micro-cooling system, the electrocaloric regenerator is placed between the two micro-pumps to store or release thermal energy depending upon the electrical control signal. Recently, a large EC effect was discovered in thin films of $PbZr_{0.95}Ti_{0.05}O_3$ [16],, a poly(vinylidene fluoride-trifluoroethylene) [P(VDF-TrFE)] copolymer [17], and a P(VDF-TrFE-chlorofluoroethylene) [P(VDF-TrFE-CFE)] terpolymer [17]. The P(VDF-TrFE-CFE) terpolymer demonstrates an adiabatic temperature change of 7 K at an electric field of 100 V/μm near room temperature [23] and is easily and economically fabricated, making it favorable for mass production [82]. These findings point to the potential of applying EC cooling in micro-devices using polymer thin films. In this chapter, the P(VDF-TrFE-CFE) terpolymer is fabricated and its thermal and electrical performance tested. Terpolymer layers are then assembled with a set of interspersed photodefinable epoxy spacers to create the EC regenerator for the micro-cooling system.

5.2 Design Concept

As mentioned in Chapter 1, the electrocaloric microcooler cooling element includes two micro-pumps made of cavities and diaphragms with the electrocaloric regenerator placed between the pumps. The electrocaloric terpolymer regenerator includes two kinds of components: electrocaloric terpolymer layers and a set of spacers.

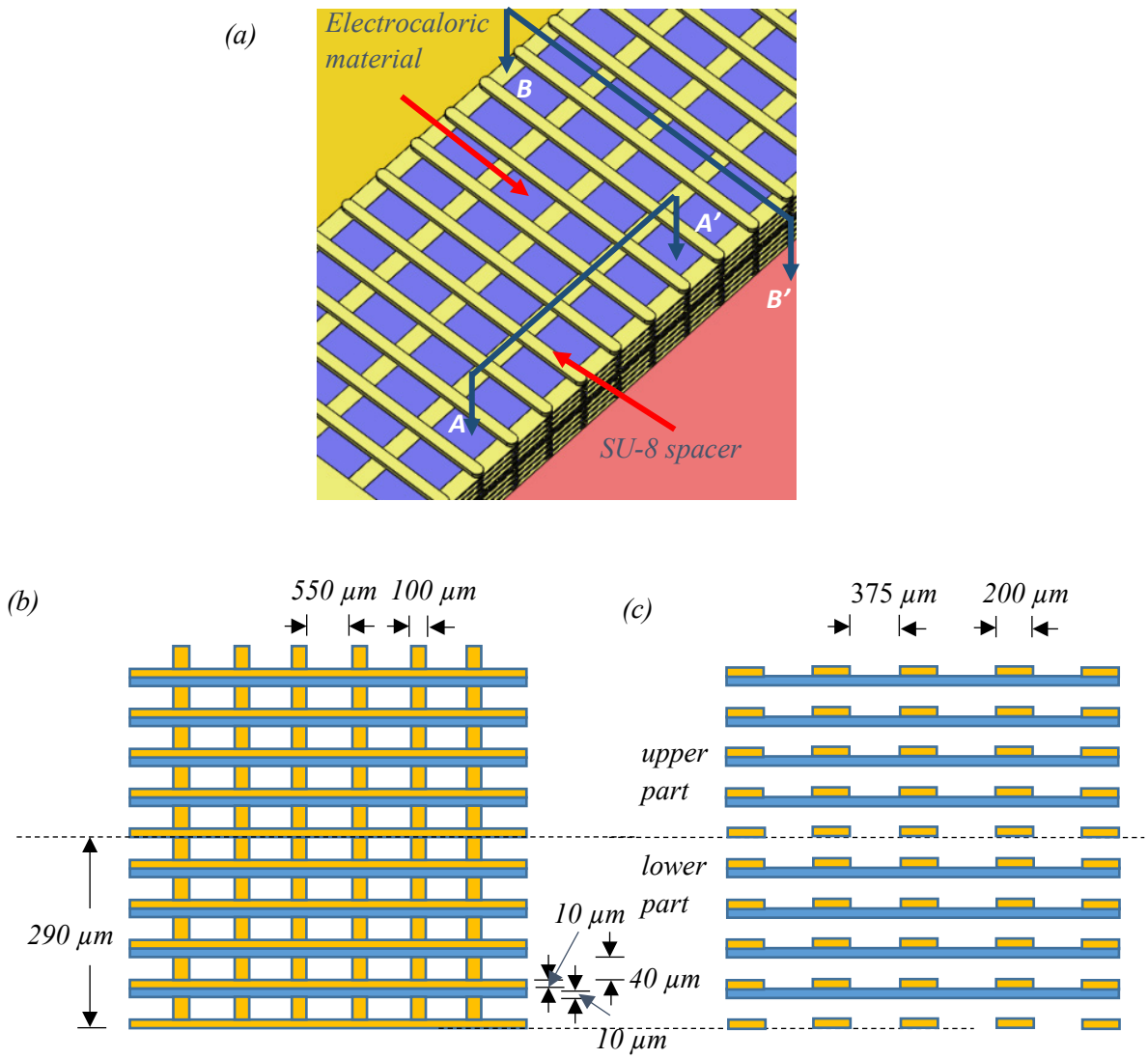

Figure 5.1. (a) Solid model for electrocaloric regenerator. The 1 cm x 2.5 mm x 580 µm regenerator includes 8 layers of electrocaloric polymer and 10 SU-8 spacers. (b) A-A' cross section of the electrocaloric regenerator. (c) B-B' cross section of the electrocaloric regenerator.

As shown in Figure 5.1, the regenerator comprises the electrocaloric terpolymer layers interleaved with spacers patterned from SU-8 photodefinable epoxy (MicroChem Corp., Westborough, MA). Ferroelectric relaxor terpolymer layers are 2 mm wide, 1 cm long and 10 µm thick. Spacers made of SU-8 photodefinable epoxy are placed between the terpolymer

layers to form channels to allow the passage of fluid. The 1 cm x 2.5 mm x 580 μm regenerator includes 8 layers of electrocaloric polymer and 10 SU-8 spacers. The diaphragms of the micro-pump on either side of electrocaloric terpolymer are actuated to drive the working fluid (Galden HT-70, Solvay Solexis, Inc), that transfers heat between the two chambers. The heat is extracted from the cold fluid chamber and released to the hot chamber to achieve cooling. The details of synchronization of the micro-pump and electrocaloric cycle is presented in Chapter 6.

5.3 Fabrication of EC Regenerator

5.3.1 EC Terpolymer Film

The EC terpolymer film was fabricated by Ying-Ju Yu using a solution cast method following instructions from Piezotech S.A.S (Hesingue, France). The polymer powder was first completely dissolved into methyl ethyl ketone and then the solution was cast on a silicon wafer and baked at a temperature of 50˚C overnight to evaporate the solvent. After drying, the film was attached with a 3 inch diameter aluminum ring (shown in Figure 5.3) and immersed in water for two hours and then peeled off the wafer. The film was suspended with the aluminum ring and annealed at a temperature of 100˚C for seven hours to improve crystallinity and remove residual solvent [23, 82]. The gold with a thickness of 100 nm was sputtered on both sides of the EC sample as the electrode by using machined aluminum shadow masks (Figure 5.2) with 1.2 cm by 2 mm rectangular holes, shown in Figure 5.3. Then the film was cut to the shape of electrocaloric regenerator by using a customized cutter designed by Suresh Santhanam (Figure 5.4). The cutter includes a six degree stage and a blade. The film is fixed on the stage with the aluminum ring and an absorbent laboratory countertop paper is placed underneath it when the cutting is performed.

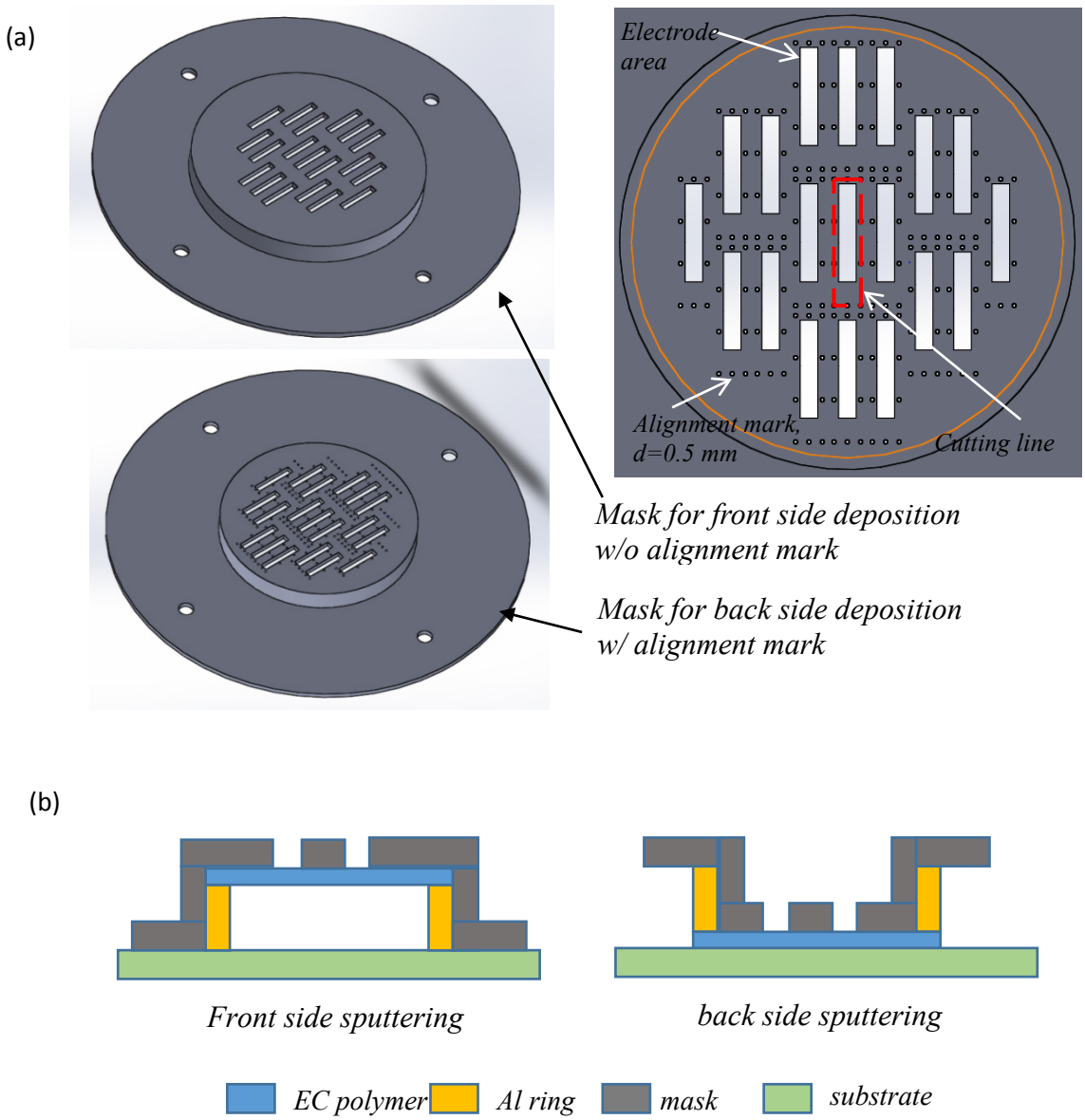

Figure 5.2. (a) Shadow masks for fabricate the EC terpolymer. The masks have 1.2 cm by 2mm rectangular holes. The small circular holes are designed for alignment during the cutting and assembly. (b) Cross section for EC terpolymer setup. The front side mask is used for front side sputtering, and back side mask is used for back side sputtering

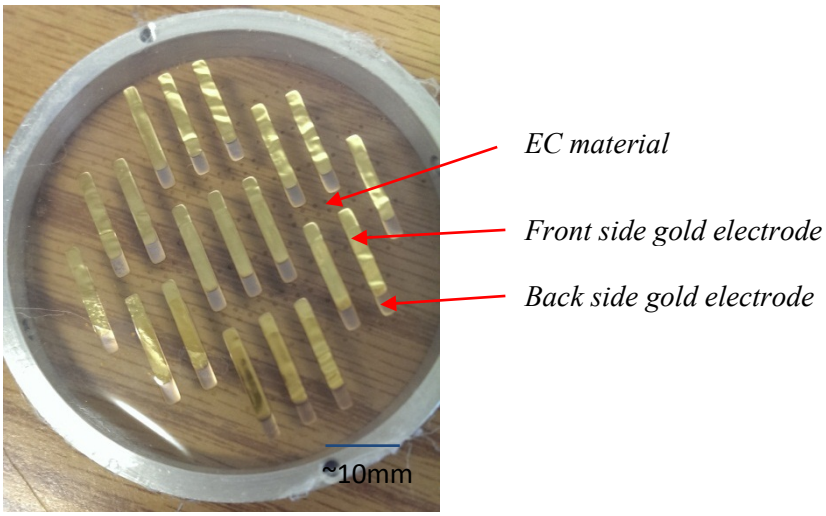

Figure 5.3. Fabricated electrocaloric films with gold electrodes on both sides. The film is suspended on the cylindrical aluminum frame.

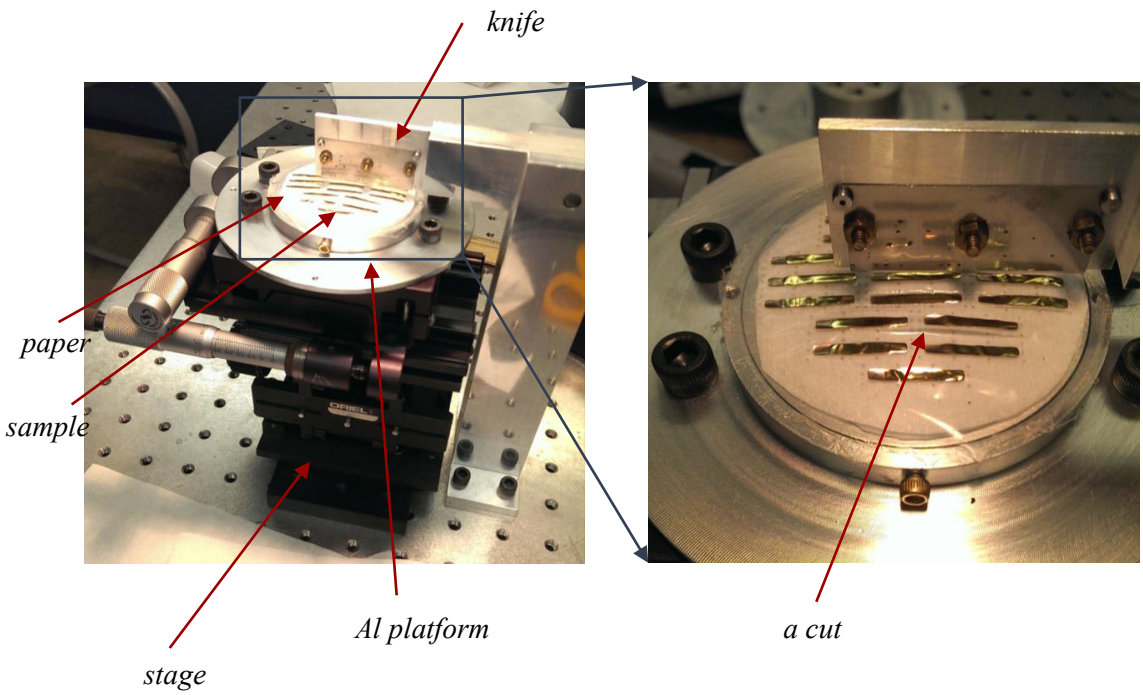

Figure 5.4. Customized cutter for cutting EC terpolymer.

5.3.2 SU-8 Spacer

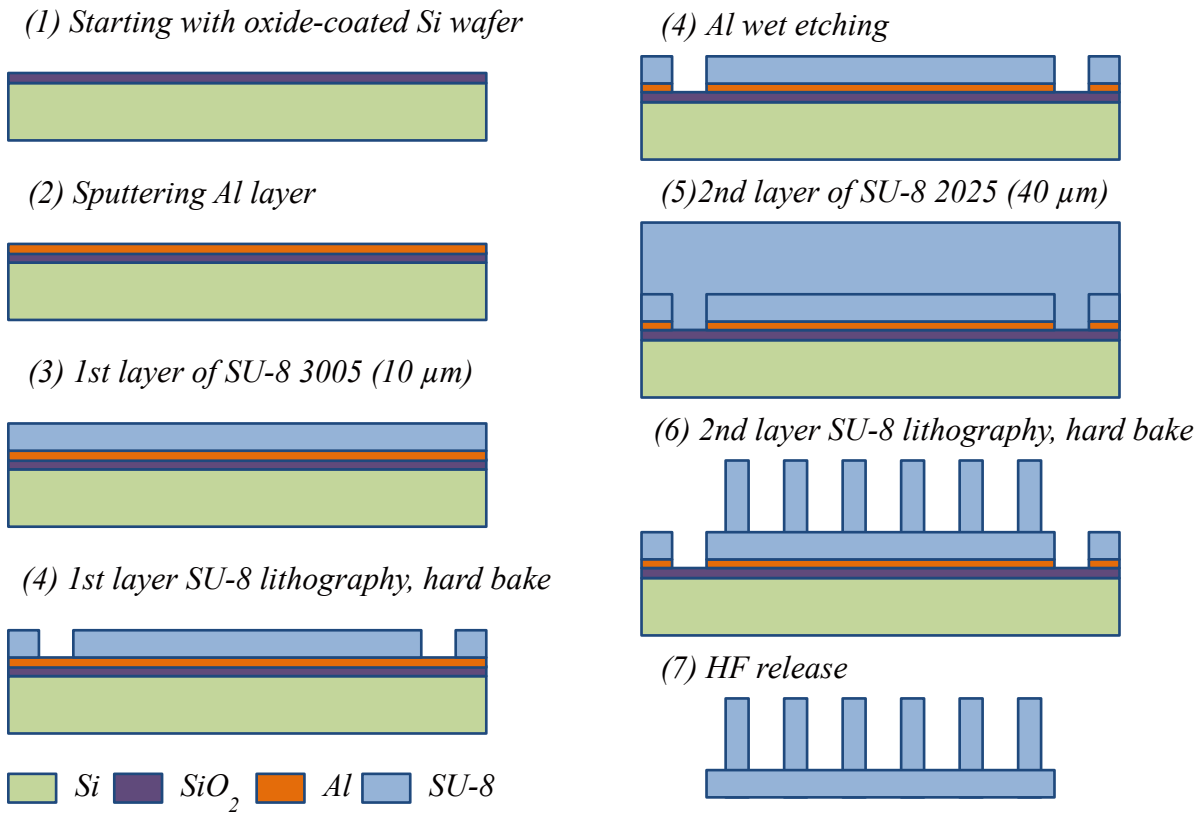

Figure 5.5. Process flow for SU-8 spacer fabrication. The spacers are fabricated by patterning two layers of SU-8 subsequently.

The spacers are fabricated by patterning two layers of SU-8 sequentially, as shown in Figure 5.5. Aluminum alignment marks are first deposited and patterned on a Si wafer covered with a 1 µm oxide layer. The aluminum alignment is needed because regular alignment marks made in the first layer of SU-8 would not be visible after the second SU-8 layer is spun. SU-8 3005 (MicroChem Corp., Westborough, MA) is spun on the wafer to create a 10 µm-thick film. The SU-8 is then patterned and hard baked to form the base layer of the spacer. SU-8 2025 is

spun on the base layer, then patterned, developed and hard baked to create a 40 µm top layer. The wafer is then dipped into HF to remove the oxide and release the structures. After release, the SU-8 spacers curl in *y*-axis direction (defined in Figure 5.6) with a radius of curvature of ~5 cm due the temperature coefficient of expansion mismatch between two SU-8 layers. The spacers are flattened by a device bonder (Besi/Laurier M9; pressure: 20 kPa; temperature: 150˚C; time: 5 min). Figure 5.6 shows the fabricated SU-8 spacer and its corresponding 3D model. This SU-8 spacer has two bars on the base layer instead 5 bars depicted in Figure 5.1.

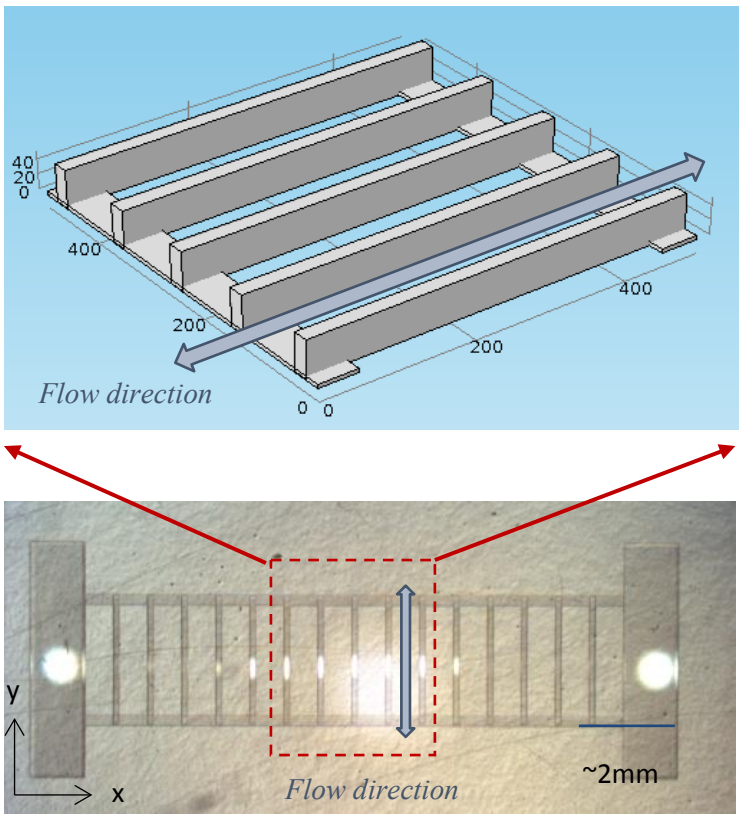

Figure 5.6. Fabricated SU-8 spacer and its illustration of 3D model

5.3.3 EC Regenerator Assembly

The electrocaloric films and SU-8 spacers are assembled into a 3D-printed package to form the electrocaloric regenerator. Four layers of EC polymer (10 µm thick each) and five layers of SU-8 spacers are assembled alternately in the package. The assembly is shown schematically in Figure 5.7. The sputtered electrode on one side of the EC polymer layers is longer than the other side along the polymer's long edge. Neighboring electrodes from two adjacent polymer layers are electrically connected to the same potential. This connection prevents any shorting problems when silver paste is added to the end of the assembly. Having the same potential on neighboring electrodes also eliminates electrical field formation in the heat transfer fluid. The total height of the assembly is 290 µm, which is matched to the 300 µm thick micro-pump located on the two sides of the regenerator. The final assembled regenerator is shown in Figure 5.8.

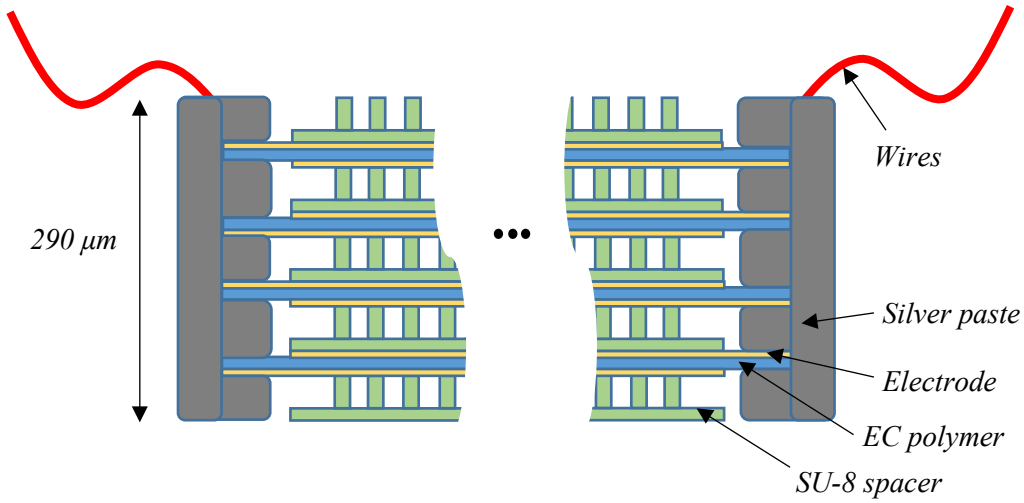

Figure 5.7. Cross section of assembled EC regenerator.

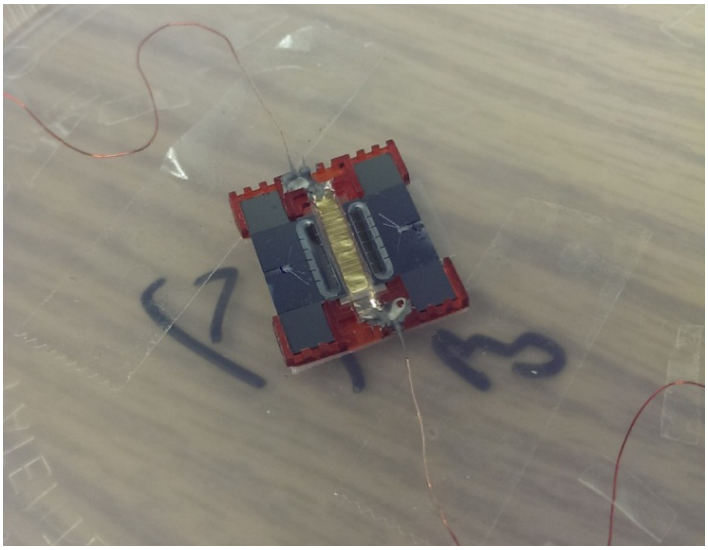

Figure 5.8. Assembled EC regenerator in the 3D printed package.

5.4 Thermal and Electrical Tests of EC Terpolymer

The work in this section is the joint work with Dongzhi Guo [26].

Direct and indirect techniques can be applied to measure the EC effect of the P(VDF-TrFE-CFE) terpolymer. In the indirect measurement, a differential scanning calorimeter is used to measure the heat flow under a high electric field and isothermal conditions [83, 84]. This technique is best suited to bulk materials as the output heat flow signal for a thin film sample is very small. Jia and Ju [85] reported an approach for characterizing the EC effect in a thin film sitting on an insulating substrate. In this approach, the temperature response of a resistance thermometer deposited on the bottom of the EC film is monitored as an electric field is turned on and off. In the reported measurements, the temperature change is less than 10% of that expected because the heat loss from the EC film to the substrate is large. Lu et al. [22] employed a

specially designed calorimeter to measure the EC effect in a thin film. In this approach, the heat generated in the EC film is compared with the heat generated from a standard reference resistor. More recently, an infrared camera [82] was used to measure the temperature change in a 50 μm-thick polymer film under the direct application of an electric field.

In this section, the infrared imaging technique is used to directly measure the transient temperature response of thin films of a P(VDF-TrFE-CFE) terpolymer (11 to 12 μm thick) under varying electric fields near ambient conditions. For such a thin film, the convection heat transfer between the thin film sample and the air is not negligible and must be included in the analysis. A significant percentage of the adiabatic temperature change (about 50%) is still realized, however, and this effect is much larger than that obtained in other techniques [83, 84, 85]. The ramp time of the applied voltage is varied to quantify the heat transfer between the sample and the ambient environment and to obtain the adiabatic temperature change. The frequency dependence of the EC effect is investigated and the film stability is also explored.

5.4.1 Experimental Setup

P(VDF-TrFE-CFE) terpolymer film samples were fabricated by Ying-Ju Yu. Gold electrodes were sputtered on both sides of the sample following the same method presented in Section 5.3.1. To obtain the temperature map accurately, a 2 mm diameter circular area at the center of the electrode surface was coated with a 5 μm layer of carbon ink with to increase its emissivity to 0.7.

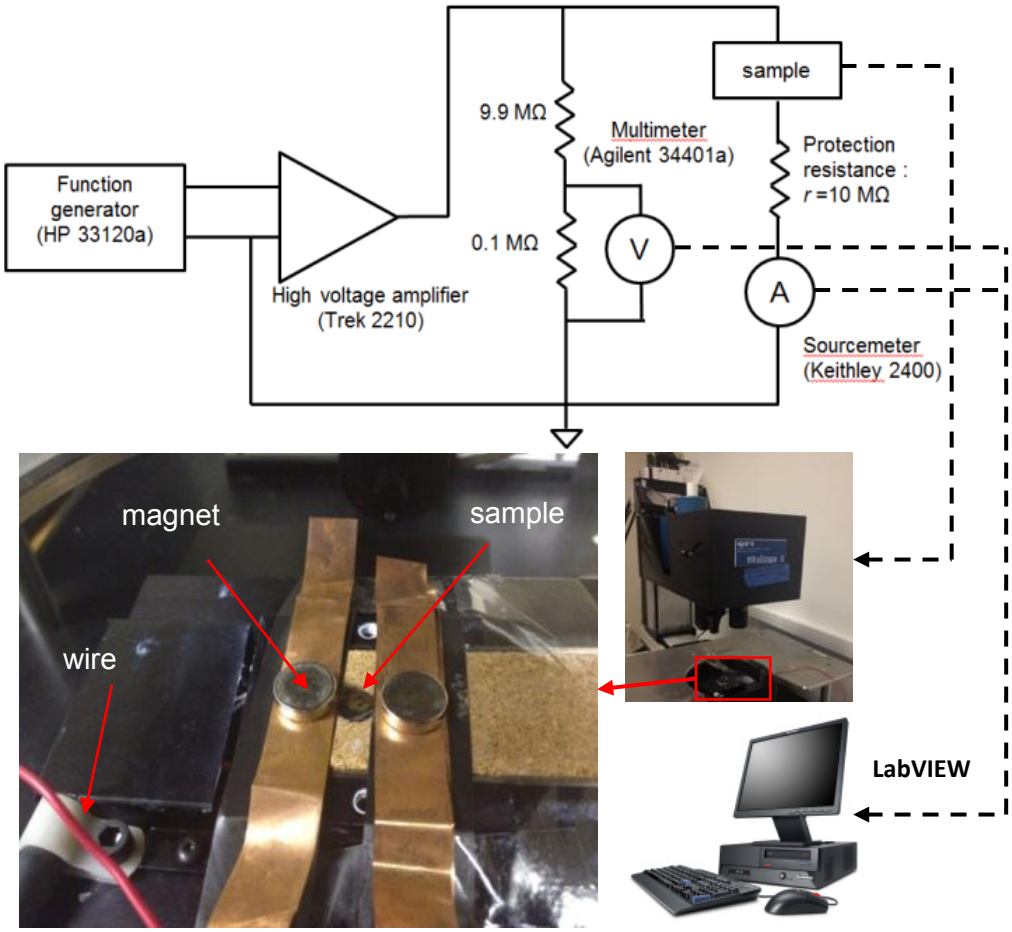

Figure 5.9. Test bed setup for the thermal and electrical test for the EC materials.

The infrared imaging technique is used to directly measure the transient temperature of the electrocaloric film (P(VDF-TrFE-CFE) terpolymer) in the room environment using the test bed shown in Figure 5.9. The film sample is suspended above a thermal stage in the air, and a 1 mm gap is left between the sample and the stage to avoid the fast heat dissipation to the thermal stage. The wires are attached to the electrodes by using magnets to avoid the damage of the films. Voltage pulses are supplied by a function generator (HP 33120a) and amplified by a high voltage amplifier (Trek 2210). The current and the voltage are measured by a source meter (Keithley 2400) and a multimeter (Agilent 34401a) respectively, and are collected by LabVIEW. The temperature images are recorded by the QFI InfraScope II system (Quantum Focus

Instruments Corp., Vista, CA), that has a sample rate of 14 frames per second. For obtaining the temperature map correctly, a thin layer of carbon ink with a thickness of 5 μm is coated on the electrode surface to increase the emissivity (~ 0.7). The temperature error of infrared camera is ±0.1˚C by calibration. The obtained temperature information is averaged on the area coated with the ink.

5.4.2 Measured Results and the Adiabatic Temperature Change

Three samples were tested at a stage temperature of 25˚C for electric field values between 40 and 90 V/μm. For each test, three consecutive trapezoidal pulses with a period of 30 s were applied to check for repeatability. The ramp time of the voltage pulse was varied (0.8 s, 1.2 s, and 1.6 s) to quantify the heat transfer between the sample and the air environment. A typical result of the current and temperature responses are shown in Figure 5.10 (a)-(b). Each sample shows a similar behavior. The current leakage for all samples is very small (10 to 30 nA when the voltage is applied for 15 s). Joule heating in the film is thus negligible, consistent with the temperature data ($T_3 = T_1$) in Figure 5.10(b).

The temperature response induced by the electric field change happens very fast (~milliseconds) [14]. The sample temperature thus rises fast (0.5 s) when the electric field is turned on (event 1 to event 2 in Figure 5.10(a) and 1(b)). With the electric field still on, the temperature decreases exponentially back (time constant: ~1 s) to the initial temperature due to the heat exchange between the air and the sample (event 2 to event 3). When the electric field is turned off, the temperature quickly decreases (0.5 s) below the initial temperature (event 3 to event 4) and then rises exponentially back (time constant: ~1 s) to the initial temperature (event 4 to event 5).

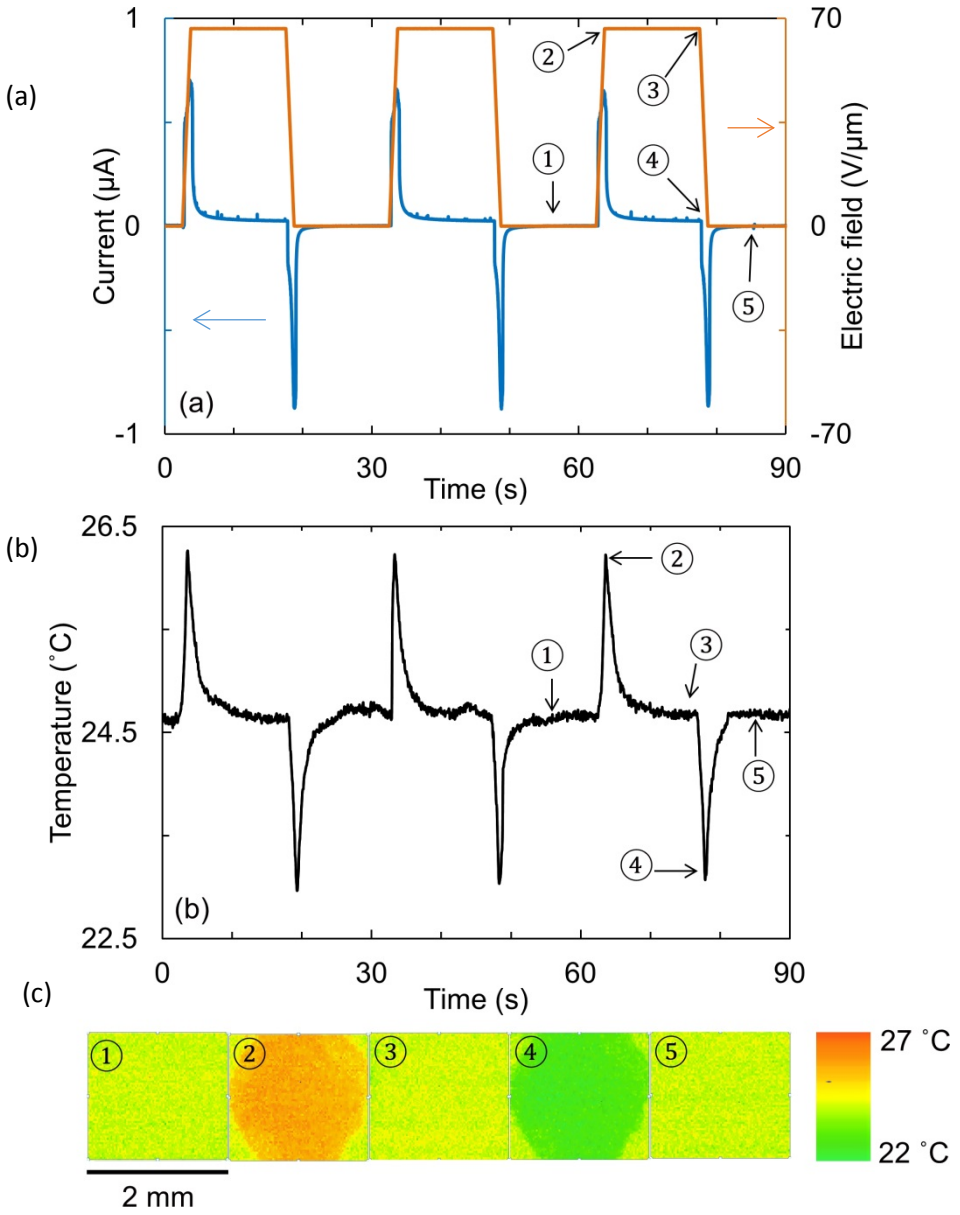

Figure 5.10 (a) Example of a trapezoidal electric field applied to the EC sample and the measured current. The ramp time of the electric field is 1.2 s and its maximum amplitude is 67 V/μm. (b) and (c) Infrascope-measured temperature and images at different time in a cycle and the temperature as a function of time. The temperature changes abruptly when the electric field is ramping up and down (event 2 and event 4, respectively).

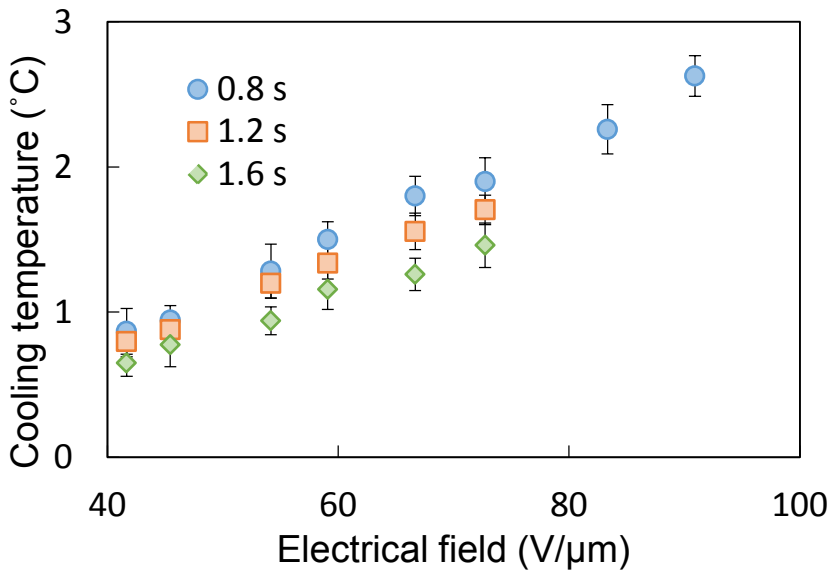

Figure 5.11 Measured cooling temperature as a function of the electric field at different voltage ramp times. The stage temperature is 25 ˚C for all measurements.

The measured cooling temperature induced by the EC effect at different ramp time of the voltages is plotted in Figure 5.11. When the ramp time of the electric field is reduced, the cooling temperature increases as the heat loss due to the air is less in a shorter ramp time. The adiabatic temperature change of the terpolymer was calculated by estimating the heat transfer between the sample and the air. The details of this calculation can be found in Dongzhi Guo's thesis [26].

One example of the comparison between the measured data and the computational results is plotted in Figure 5.12. Then the adiabatic temperature change was obtained and is plotted in Figure 5.13 along with literature results. The adiabatic temperature change over the electric field agrees well with that from Li et al. [23], Jia and Ju [85].

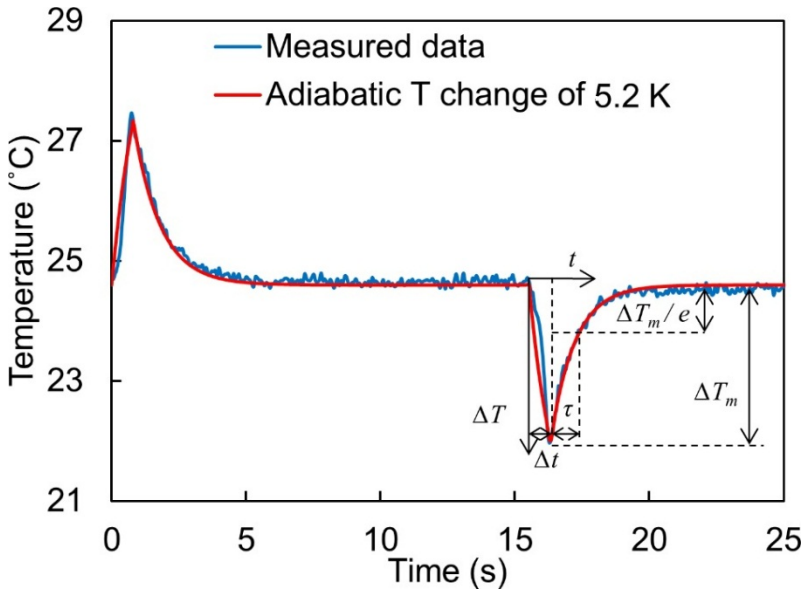

Figure 5.12 The comparison between the measured data and the computational result at an electric field of 90 V/μm. The details of definitions and calculations can be found in [26].

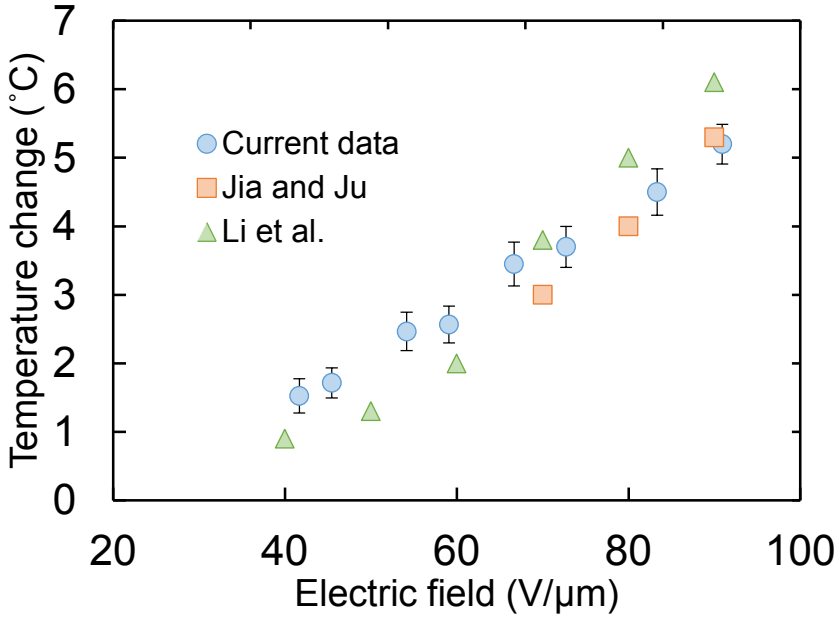

Figure 5.13 Adiabatic temperature change vs. electric field and comparison to literature results.

5.4.3 Effect of Stage Temperature and Operating Frequency

The temperature dependence of the EC effect of the P(VDF-TrFE-CFE) terpolymer is plotted in Figure 5.17 for stage temperatures between 20˚C and 30˚C. When compared with the 25˚C case, the EC effect is increased by 10 to 20 % at a temperature of 30˚C, which is consistent with the results reported in [23].

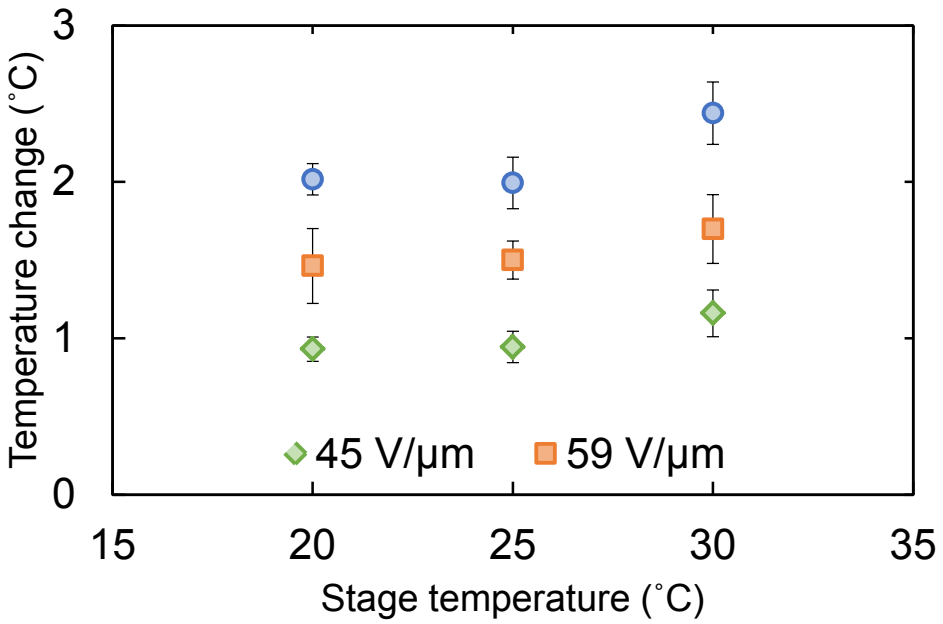

Figure 5.14 Measured cooling temperature at different stage temperatures. The ramp time of the voltage is 0.8 s.

The effect of the electric field frequency on the temperature change is shown in Figure 5.15 (a) and Figure 5.15 (b) for frequencies between 0.03 and 0.3 Hz. As shown in Figure 5.15 (a), the minimum temperature (i.e., location 4 in Figure 5.10) increases with increasing frequency as the thermal time constant (~1 s) becomes larger than the period of the operating frequencies.

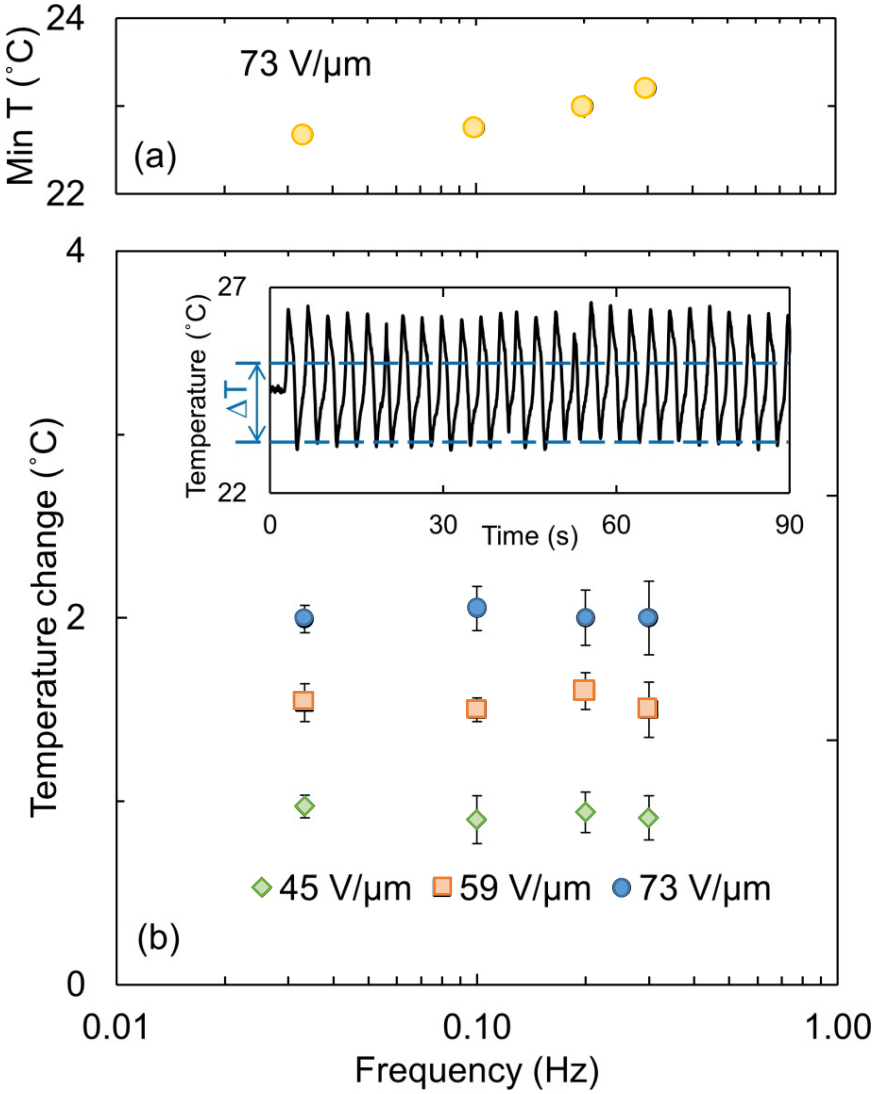

Figure 5.15 (a) Measured minimum temperature as a function of the operating frequency for an electric field of 73 V/ μm. (b) Measured temperature change when switching off the electric field with the operating frequency. A ramp time of 0.8 s is fixed at different frequencies for a fair comparison. The stage temperature is 25˚C. The inset is a plot of measured temperature when the operating frequency is 0.3 Hz and the electric field amplitude is 73 V/μm. ΔT is the temperature change when switching off the electric field.

The inset in Figure 5.15 (b) shows the temperature-time history for a frequency of 0.3 Hz. Note that the temperature does not return to the initial value during the air cooling/heating stages and that an offset average temperature is realized. Thus, the maximum and the minimum temperatures decrease compared to lower-frequency operation. The measured cooling temperature (ΔT) induced by EC effect when switching the electric field off is indicated in the inset figure, and this temperature change as a function of the frequency is plotted in Figure 5.15(b). We find that the measured temperature change does not change in the operating frequency range of 0.03 ~ 0.3 Hz, demonstrating that the EC effect in the P(VDF-TrFE-CFE) terpolymer is frequency-independent. The current result is promising, in that a practical device will operate in a frequency range of 1 to 10 Hz. For example, Gu et al. [24] fabricated a solid-state chip-scale electrocaloric cooler using a P(VDF-TrFE) polymer and tested it at 1 Hz.

5.4.4 EC Terpolymer Stability

The stability of the material was assessed by conducting a 30 minute test of a sample. The operating frequency was 0.2 Hz and the amplitude of the electric field was 54 V/μm. The temperature history is plotted in Figure 5.16. The temperature data was not measured continuously due to the limitation of the infrascope. The time spacing between adjacent data collection periods is 2 minutes. No failure was observed within 30 minutes. The maximum and the minimum temperature measured by the infrared camera are 25.6˚C and 23.7˚C. The performance is stable and demonstrates the potential of applying the P(VDF-TrFE-CFE) polymer in a microcooler application.

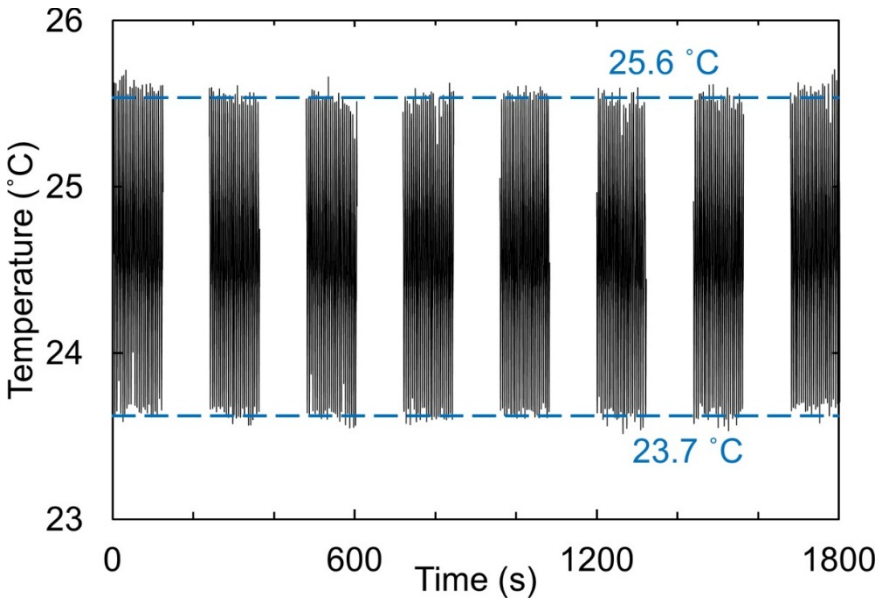

Figure 5.16 Temperature history of a sample for 30 minutes at a stage temperature of 25°C. The ramp time of the voltage is 0.8 s. The frequency is 0.2 Hz and the electric field amplitude is 54 V/µm. Gaps in the data are due to limitations of the infrascope. The electric field was modulated at all times.

5.4.5 Breakdown of EC Terpolymer

During the electrical tests, it is found the higher voltage (greater than 80V/µm) leads to larger probability to breakdown the P(VDF-TrFE-CFE) terpolymer. Figure 5.17. shows the comparison of leakage current between applied voltages of 54V/µm and 88 V/µm. From the previous section, the experiments show the current is stable and consistent at 54V/µm even for very long testing periods. When 88 V/µm voltage is applied, the P(VDF-TrFE-CFE) terpolymer starts to breakdown at some points in the polymer usually after dozens to hundreds of cycles. More breakdown points arise with time. It is believed that the breakdown is due to flaws in the

films. The solution cast creates voids, resulting in early breakdown because the thicknesses of polymer at voids are thinner than other places, or generates defects (e.g., particle defects).

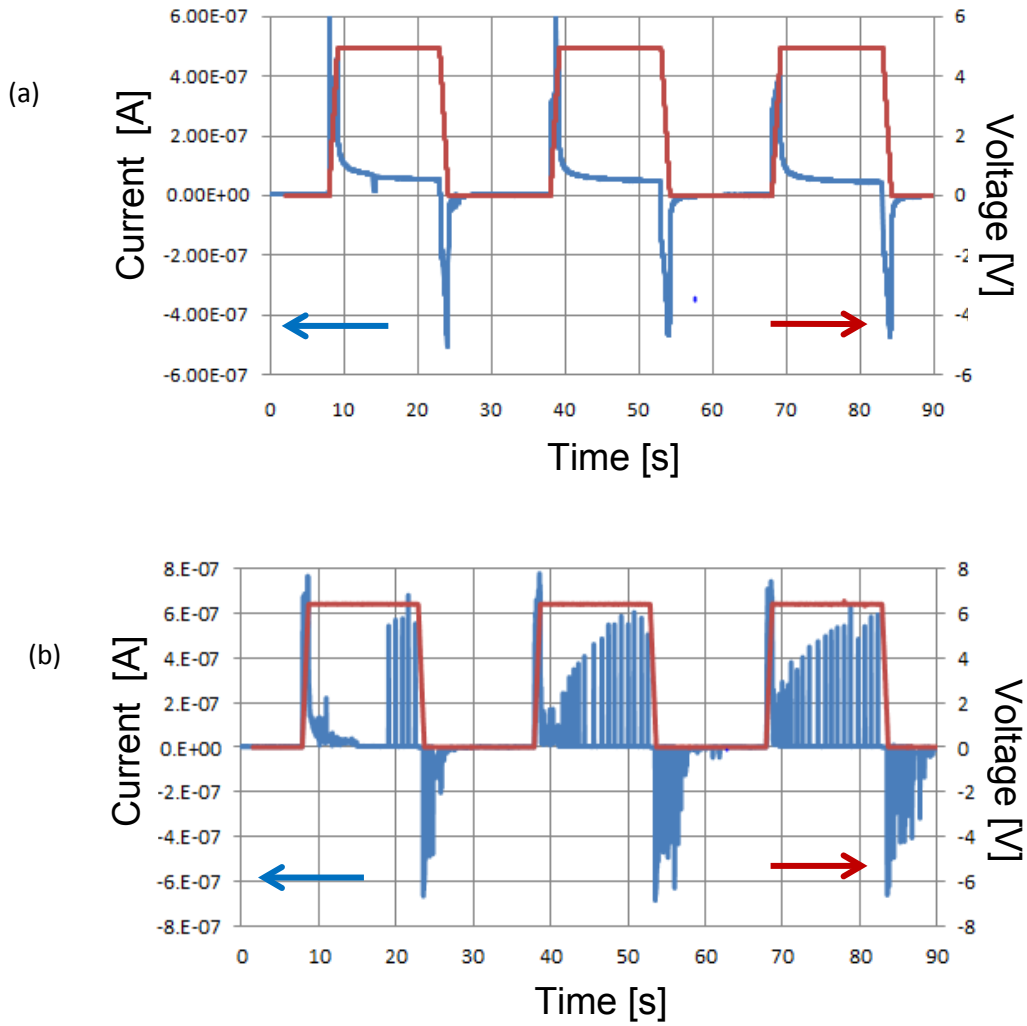

Figure 5.17. Leakage current at applied voltage (a) 54V/µm and (b) 88 V/µm. When 88 V/µm voltage is applied, the P(VDF-TrFE-CFE) terpolymer starts to breakdown usually after dozens of cycles.

Figure 5.18 gives the 3D images of a polymer film surface after breakdown collected by an optical profilometer (Veeco/Wyco NT 3300; Veeco Instruments, Inc., Plainview, NY). The

picture clearly shows the uneven surface of terpolymer (orange and red) and the through hole (blue) caused by the breakdown.

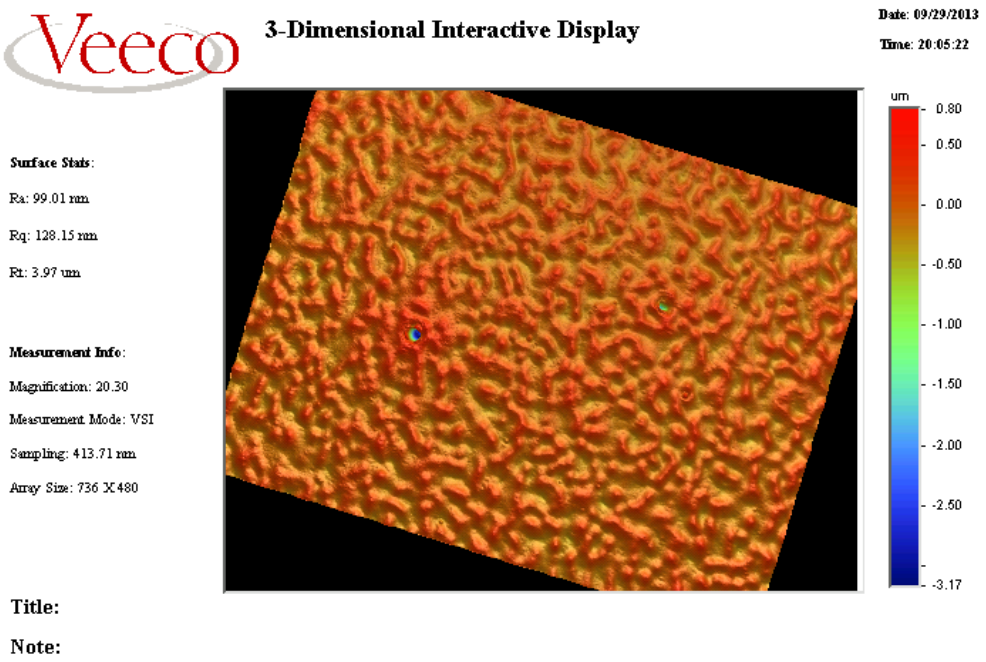

Figure 5.18 3D images of polymer after breakdown collected by optical profilometry. The picture shows the uneven surface of terpolymer and the through hole caused by breakdown.

5.5 Structural Tests of EC Terpolymer

The work in this section is the joint work with Dongzhi Guo.

Crystal orientations in the P(VDF-TrFE-CFE) terpolymer film were first investigated by Yang et al., [86] and the temperature-induced RFE-FE [86] phase transition was explored by a 2D wide-angle X-ray diffraction (WAXD). In this section, X-ray diffraction (XRD) is employed

for the first time to study the structural behavior of relaxor ferroelectric (RFE)-ferroelectric (FE) phase transition in a P(VDF-TrFE-CFE) terpolymer thin film when an electric field is applied.

X-ray diffraction is a powerful non-destructive technique for characterizing crystalline materials. It provides information on structure, phase, preferred crystal orientation, and other structural parameters, such as average lattice parameter, strain, and crystal defects. X-ray diffraction peaks are produced by constructive interference of a monochromatic beam scattered from each set of lattice planes at specific angles. The peak intensity of a given reflection (*h, k, l*) is proportional to the number of *h*, *k*, *l* planes in the reflecting condition (Bragg's law). Consequently, the X-ray diffraction pattern is the fingerprint of periodic atomic arrangements in a given material.

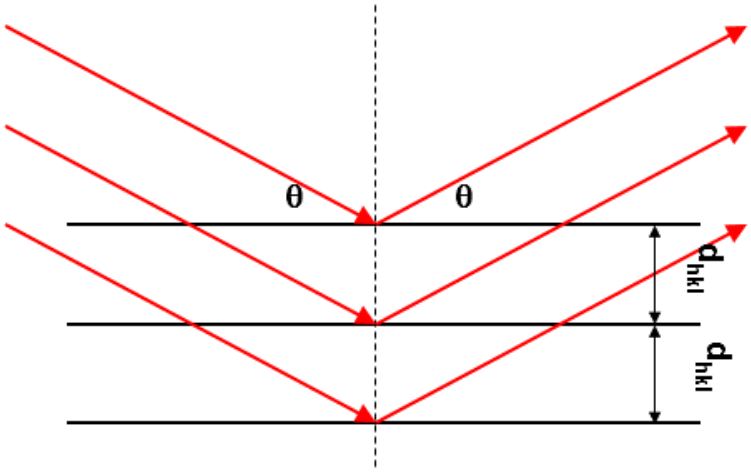

Figure 5.19 Illustration for XRD peaks generation and calculation of d-spacing in crystals.

To extract the lattice parameter, let us consider an X-ray beam incident on a pair of parallel planes P1 and P2, separated by an interplanar spacing d illustrated in Figure 5.19. The two parallel incident rays 1 and 2 make an angle (Theta, θ) with these planes. A reflected beam

of maximum intensity will result if the waves represented by 1' and 2' are in phase. The difference in the path length between 1 to 1' and 2 to 2' must then be an integral number of wavelengths, (λ). This relationship is expressed mathematically in terms of Bragg's law:

$$2d\sin\theta = n\lambda \Rightarrow d = \frac{n\lambda}{2\sin\theta}. \tag{5.1}$$

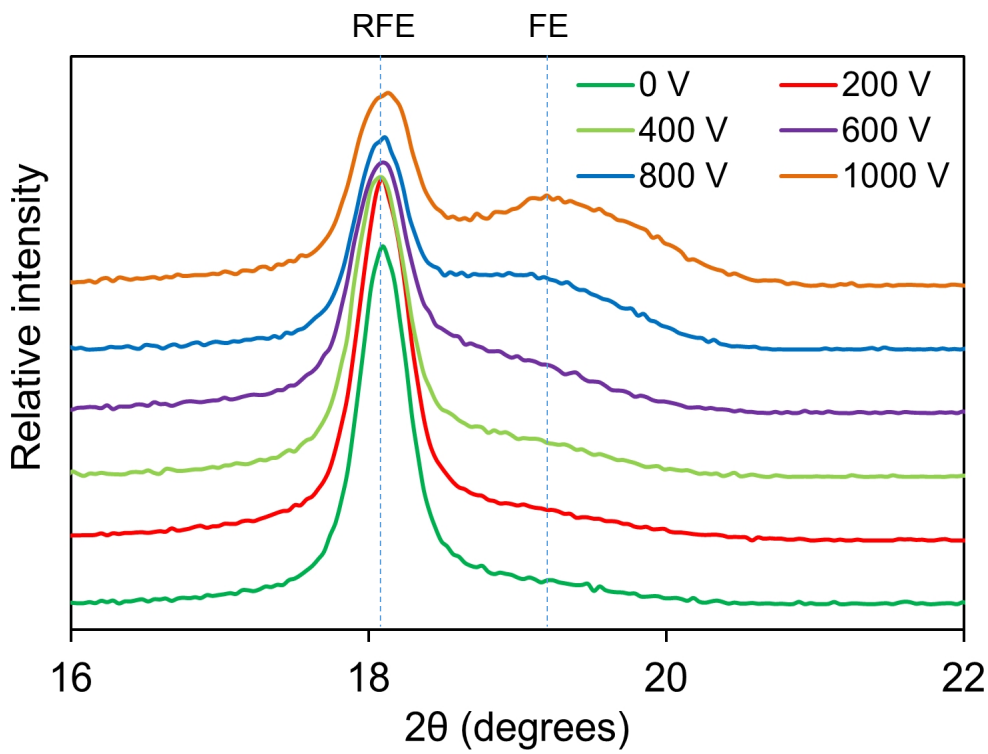

Figure 5.20. XRD data for an 11 μm-thick P(VDF-TrFE-CFE) terpolymer film with different voltages at a temperature of 25˚C. The ferroelectric phase peak gradually grows and the relaxor ferroelectric phase peak reduces with the increase of the electric field.

The electric field-dependent θ-2θ XRD measurements for a P(VDF-TrFE-CFE) terpolymer were conducted at a temperature of 25˚C and the results are plotted in Figure 5.20. Without electric field, only the RFE phase exists for the terpolymer and the RFE phase peak occurs at 2θ = 18.1˚, corresponding to a (110) *d*-spacing of 4.9 Å. When the voltage applied to the terpolymer is 200 V, no obvious change of the XRD profile is found. While increasing the voltage further (above 400 V), the FE phase appears and the RFE phase reduces. The FE phase occurs at 2θ = 19.2˚ (d = 4.62 Å) and grows with the increase of the voltage. The RFE phase shifts to slightly higher θ values as increasing the voltage and the *d*-spacing is reduced to 4.88 Å at 1000 V where the 2θ value is 18.14˚. Conversely, the material is converted from the FE phase to the RFE phase when removing the electric field. The reversible electric field-induced RFE-FE phase transition is critical to the EC effect of the terpolymer and its application in the micro-coolers.

5.6 Electrical Tests of EC Regenerator

The assembled regenerator is tested electrically to prove the feasibility of the assembly process. Before assembly, the capacitance and leaking current of each individual sample of four EC layers are examined, and their dielectric constant are determined. After assembly, the capacitance and the leakage current of the entire regenerator are measured. The results are shown in Table 5.1 and Figure 5.21. The regenerator's capacitance and leakage current approximately equal to the total value of four EC layers, demonstrating that the assembled regenerator is not damaged during assembly.

Table 5.1 Capacitance measurements for individual EC layer and assembled regenerator

	Thickness (μm)	Capacitance (nF)	Dielectric constant
EC layer 1	10	0.737	38
EC layer 2	9	0.780	36
EC layer 3	8	0.965	40
EC layer 4	8	0.935	38
Regenerator	-	3.502	-

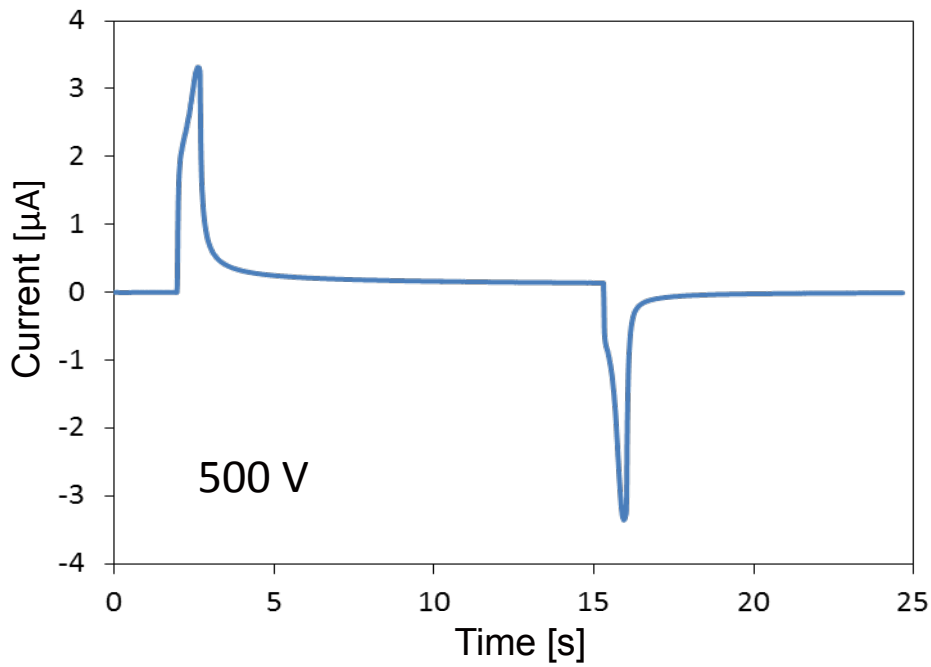

Figure 5.21 Leakage current measurement for the assembled regenerator with 500 V, 0.8 s ramp pulse applied.

5.7 Summary and Conclusion

The EC regenerator is designed and fabricated by assembling the P(VDF-TrFE-CFE) terpolymer layers and SU-8 spacers. In the micro-cooling system, it functions to store or release thermal energy depending upon the electrical control signal. Preliminary electrical tests are performed, which validate the proper assembly.

The EC characterization of the P(VDF-TrFE-CFE) terpolymer was characterized by infrared imaging is convenient and economical method. The heat dissipation of the sample in the air was modeled and used to estimate the adiabatic temperature change at different electric field magnitudes. At an electric field of 90 V/μm, an adiabatic temperature change of 5.2˚C is obtained in this work. In an operating frequency range of 0.03 to 0.3 Hz, the EC effect was observed to be independent of frequency. The stability of the material was validated by a long time testing. All results suggest that this polymer is a promising material for the micro-scale cooling application.

Chapter 6 Micro-Cooler Assembly

6.1 Introduction

The two micro-pumps and EC regenerator are assembled into the 3D printed box to create the micro-cooling system. The details of design and analysis of micro-cooler can be found in Dongzhi Guo's thesis [26].

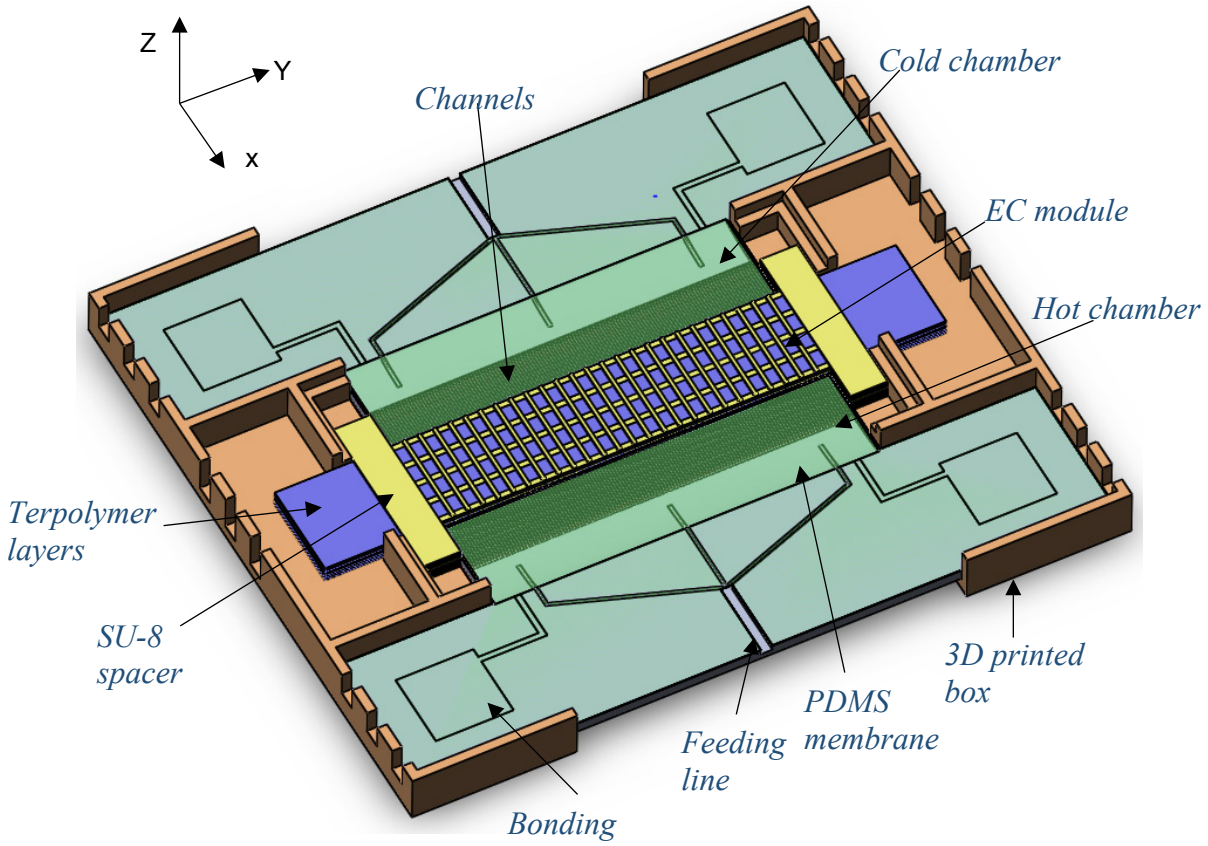

Figure 6.1 Solid-model view of the EC cooler element. The two diaphragm actuators are driven electro-statically. The EC module, which includes multiple terpolymer layers, is located between two diaphragm actuators. The fluid flow is within the plane of the wafer (Courtesy of Andrew Slippey, Advanced Cooling Technologies, Inc.).

Intended operation of the system is as follows. The micro-pumps are actuated electrostatically to drive the working fluid. Timing of diaphragm actuation and voltage applied on electrocaloric materials is shown in Figure 6.2. Δt_1 is the ramp time and Δt_2 is designed as 90° phase lag to maximize the heat transfer. Through synchronization of the electrical and mechanical cycling, the heat is extracted from the cold chamber and released to the hot chamber to achieve cooling.

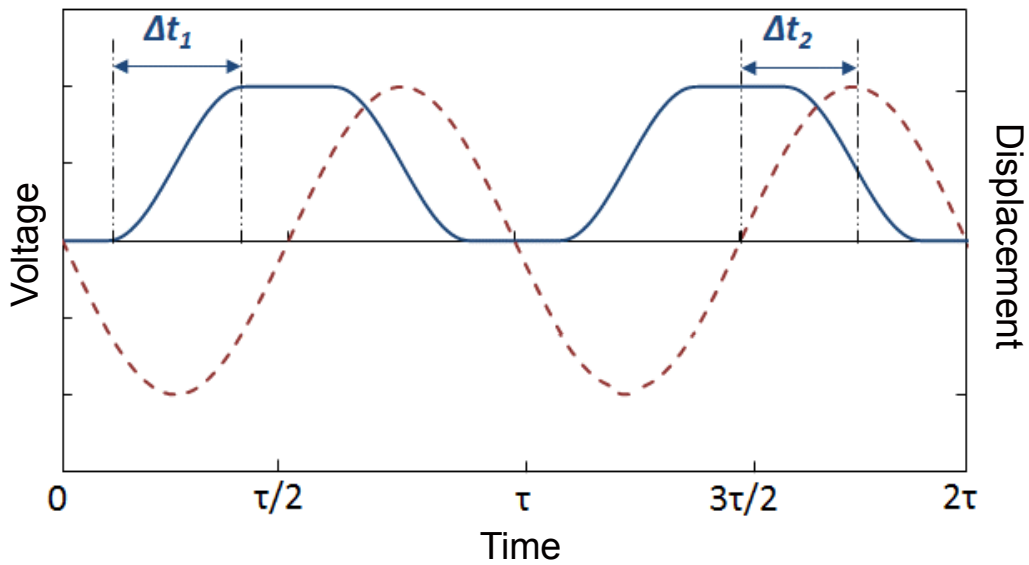

Figure 6.2. (Dash line) Timing of a micro-pump diaphragm actuation and (solid line) voltage applied on electrocaloric regenerator.

6.2 Finite Element Simulation of Micro-Cooler

The content in this section is a joint work with Dongzhi Guo [26].

Chapter 4 presented finite element simulations of micro-pump. The full simulation for the cooling system using COMSOL Multiphysics includes the micro-pumps, and the regenerator.

The heat transfer module employed along with mechanical, electrostatic and fluid modules. The fluid flow is incompressible and described by the Navier-Stokes equations. The energy equation within the EC material is

$$\rho c \frac{\partial T}{\partial t} = k\nabla^2 T - \dot{Q}, \tag{6.1}$$

where T is the temperature and t is time. $\dot{Q}$ is the heat source term due to the EC effect of the material, which is described by

$$\dot{Q} = \rho T (\frac{\partial S}{\partial E})_T \frac{\partial E}{\partial t}, \tag{6.2}$$

where S is the entropy and E is the applied electric field [87]. The relationship between the entropy change and the electric field can be obtained from experimental data [23]. For the P(VDF-TrFE-CFE) terpolymer, the entropy in Equation (6.2) can be modeled as

$$S = C_1 E^2 + C_2 E, \tag{6.3}$$

where $C_1 = -2.71\times10^{-15}$ J·m^2/(kg·K·V^2) and $C_2 = -6.85\times10^{-8}$ J·m/(kg·K·V) [23]. While the relationship between entropy and electric field is generally temperature-dependent, the EC effect of this terpolymer does not demonstrate a large deviation when the temperature changes from 270 K to 320 K (−3 ºC to 47 ºC) [23]. Therefore, the entropy change is assumed to be temperature independent for simplicity within this temperature range. It is reported that dielectric loss of the terpolymer is small and can be ignored [23].

Thermal evaluation of the micro-cooler system is performed by Dongzhi Guo [26, 27]. The evaluations show that when the system is operated at a temperature difference of 5 K, a

cooling power density of ~3 W/cm^2 is achieved at 20 Hz [26, 27]. The full system simulation results are compared with the thermal evaluations in this section.

6.2.1 Computation Setup

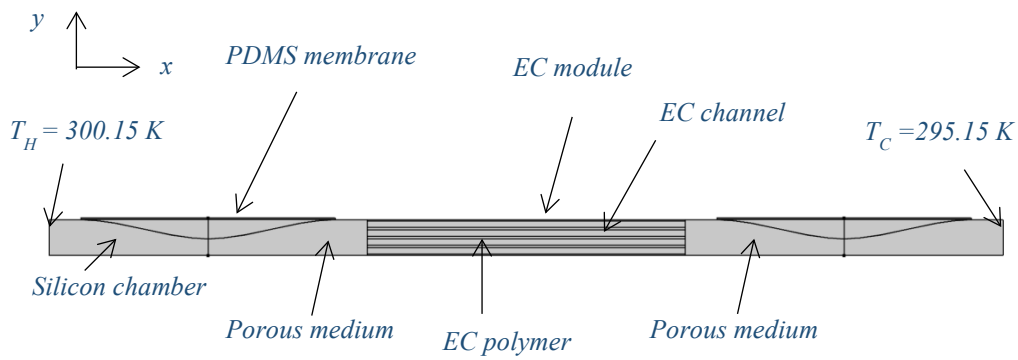

Figure 6.3 2D computational region of the EC cooling device coupled with multiple physics phenomena.

The computational region is shown in Figure 6.2. The multiphysics modeling is coupled with electrostatics, solid mechanics (Mooney Rivlin model), contact model, fluid-solid interaction, porous medium, heat transfer models and moving mesh technique. The substrate shape is a cubic curve, and the maximum height is 150 µm. The diaphragm length is 2 mm, and the thickness is 13 µm. The material constants used for the present Mooney Rivlin model of PDMS membrane are C_1 = 321 kPa, C_2 = 0 kPa, and the Young's modulus is 2 MPa. The diaphragms are driven electrostatically. The insulating layer thickness between the electrodes and the diaphragm contact surface is 2 µm. The EC module length is 2.5 mm, including 5 layers of terpolymer. For the middle terpolymers, the thickness is 20 µm. The thickness of top and bottom layers is 10 µm. The channel width between EC layers is 50 µm. The electric field

amplitude applied to the EC material is 100 V/ μm. The thermal boundary conditions and modeling are described in [26, 27]. The temperature at the hot end of the element is constant and is T_H = 300.15 K. The cold end has a constant temperature of T_C = 295.15 K. The remaining surfaces are thermally insulated. The initial temperature for the whole system is a linear profile in the x-direction. The no-slip condition is applied to the solid-liquid interfaces.

6.2.2 Results and Discussion

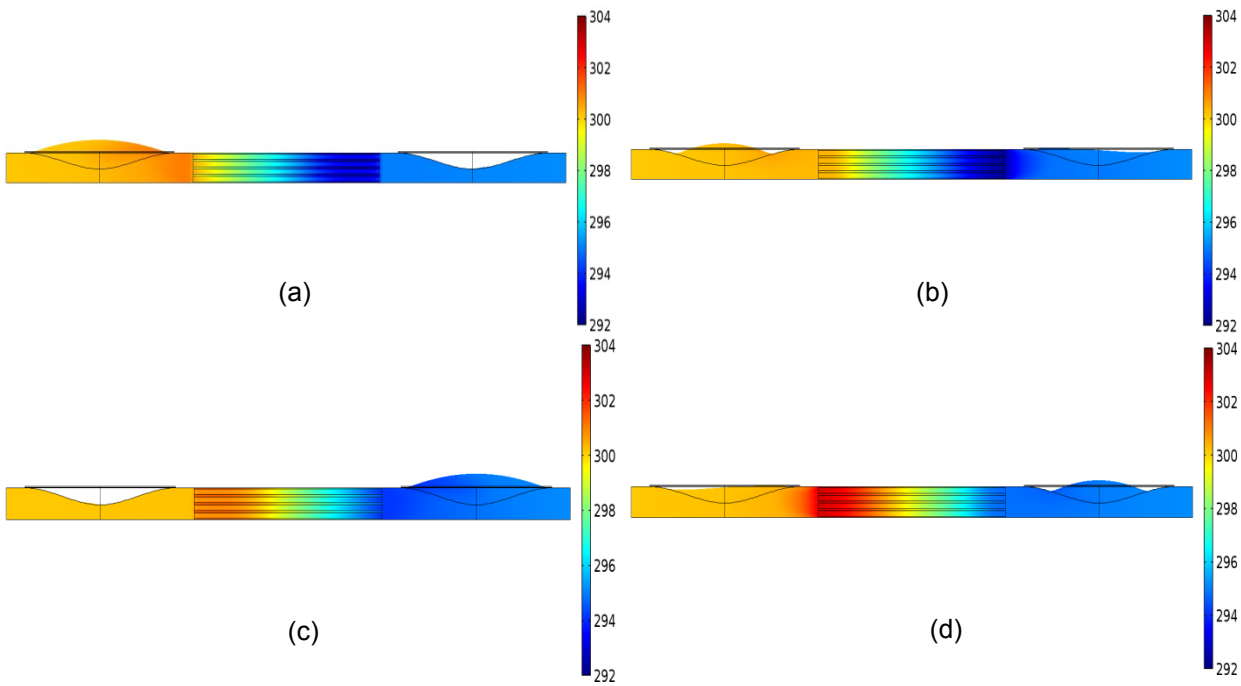

Figure 6.4 Temperature contours at different time when the diaphragm is driven electrostatically at an operating frequency of 5 Hz. (a) t = 1 s (b) t = 1.05 s (c) t = 1.1 s (d) t = 1.15 s.

When the voltage is applied to PDMS membrane, the membrane starts to snap in. The fluid in the chamber is pumped out and passes the EC channels. One example of the time-dependent temperature distribution of the system is shown in Figure 6.4. The diaphragm motion and deformation are also displayed in these figures.

The voltage applied to the PDMS membrane in this case is 170 V and the operating frequency is 5 Hz. The spring constant k_c for the contact force is 5×10^{10} Pa/m. The volume variations of hot and cold chambers and the electric field applied to EC materials are plotted in Figure 6.5. A 90˚ phase lag is maintained between the chamber volume variations and the EC electric field. The volume variations of hot and cold chambers, corresponding to the driven voltage of hot and cold diaphragms, are plotted in Figure 6.6. A phase lag of 270˚ is observed between them.

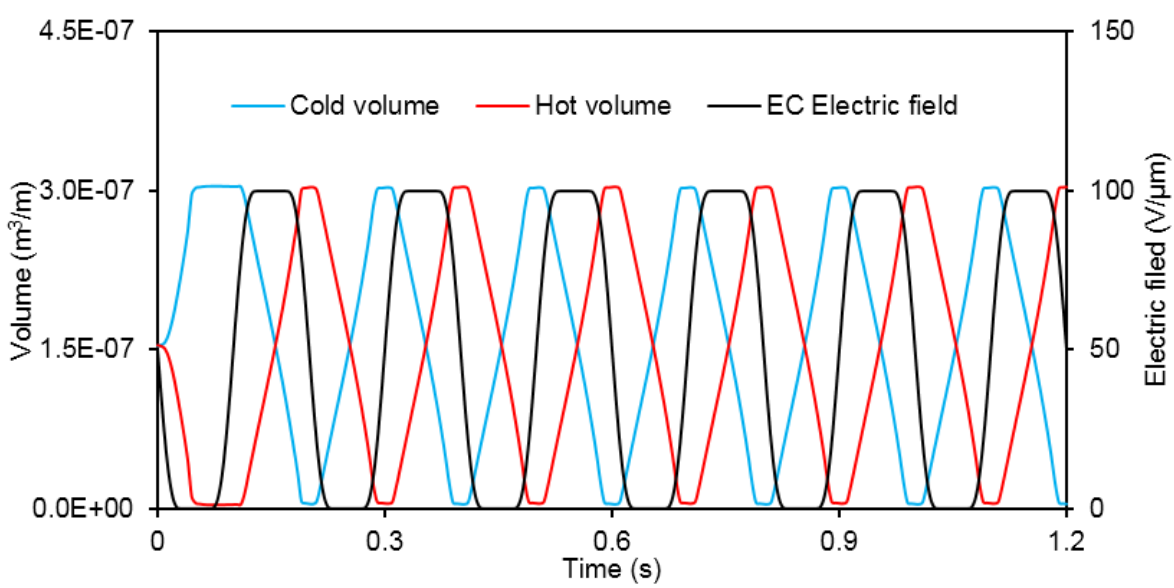

Figure 6.5 The volume variations of hot and cold chambers and the electric filed applied to EC materials.

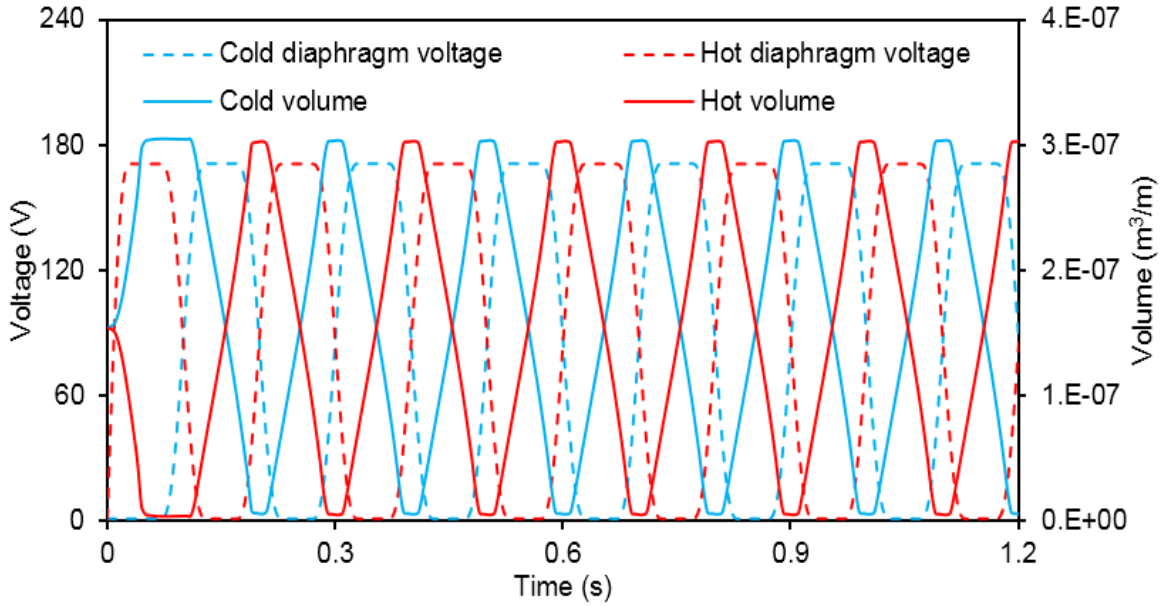

Figure 6.6 The volume variations of hot and cold chambers, corresponding to the driven voltage of hot and cold diaphragms.

The cooling power densities and the maximum pressure drop in the element in a frequency range of 1 to 10 Hz are plotted in Figure 6.7. A comparison between the system modeling and the thermal evaluation [26, 27] is also displayed and a good agreement is indicated between them.

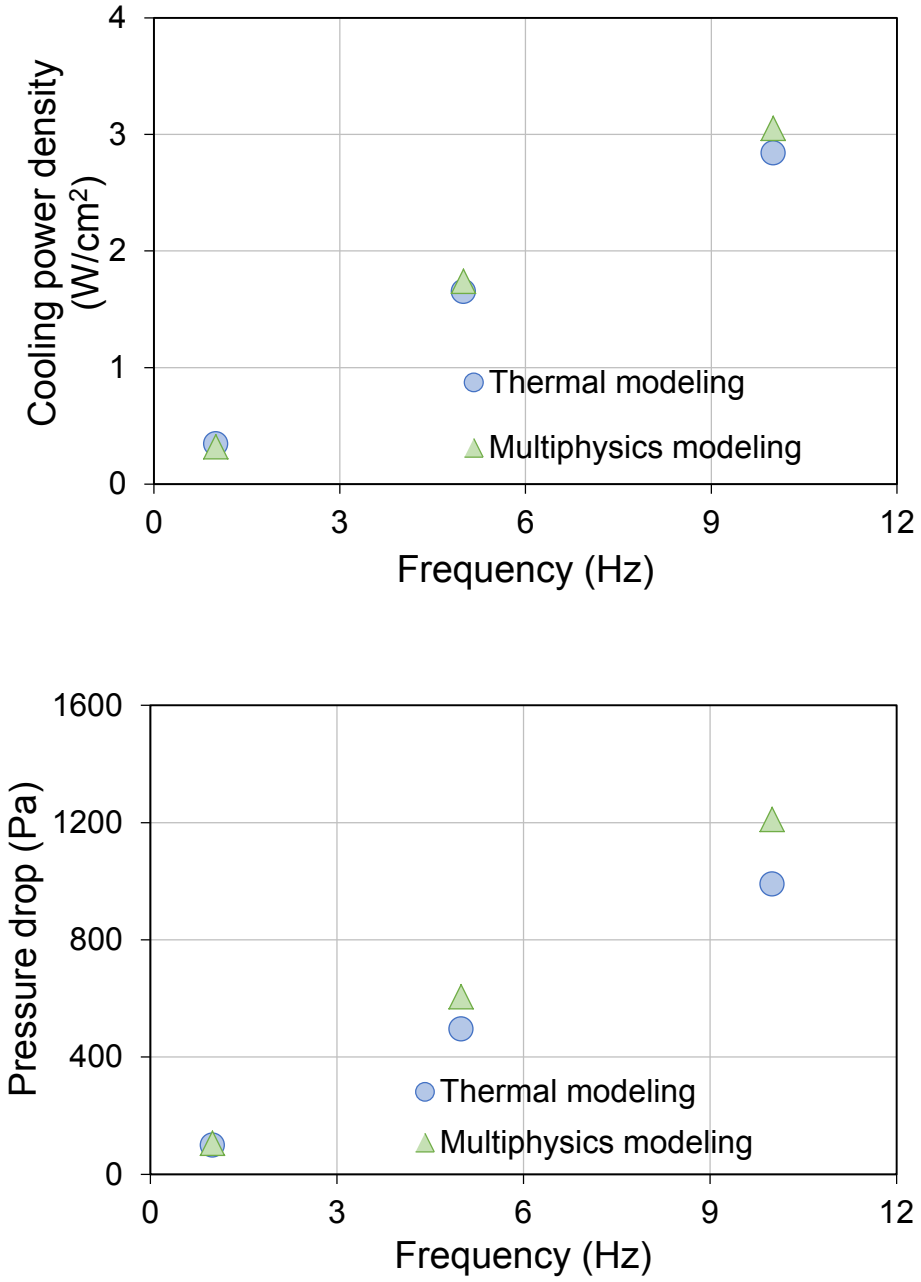

Figure 6.7 Comparisons of (a) the cooling power density and (b) pressure drop in a frequency range of 1 to 10 Hz between the thermal modeling results [26] and multiphysics modeling results.

6.3 Assembly of Micro-Cooler

The electrostatic micro-pumps and the electrocaloric regenerator are assembled in the 3D printed package. The first version of assembly (Figure 6.8 (a)) includes pumps without the embedded electrodes in the PDMS diaphragms. The assembly is designed for the thermal performance evaluation by using external mechanical pumps. The envisioned ultimate version of assembly (Figure 6.8 (b)) includes stacked double micro-pumps for push-pull electrostatic operation.

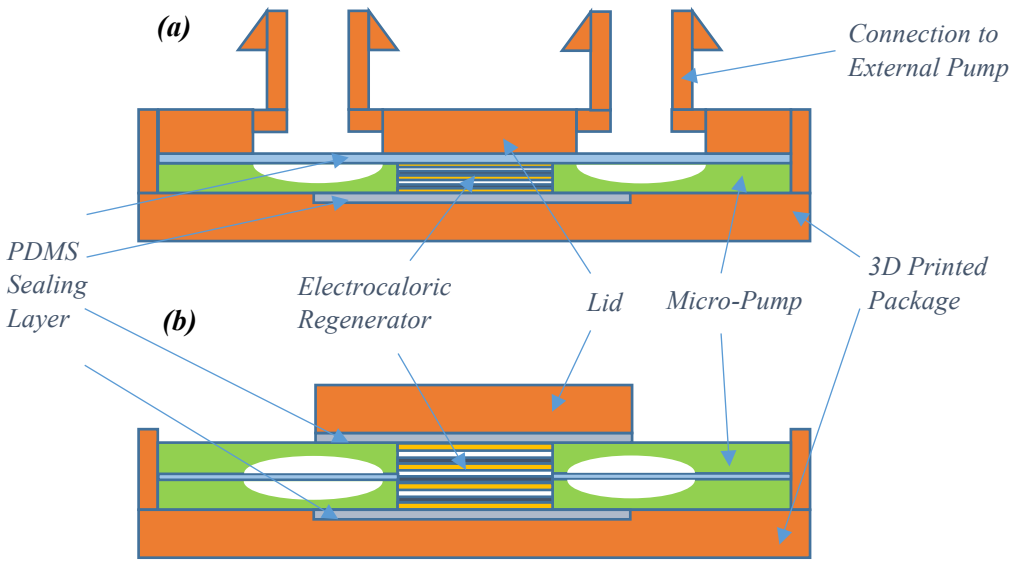

Figure 6.8. (a) Cross section of assembly for single element for thermal performance evaluation using external mechanical pumps. (b) Envisioned assembly for micro-cooler with stacked push-pull elements.

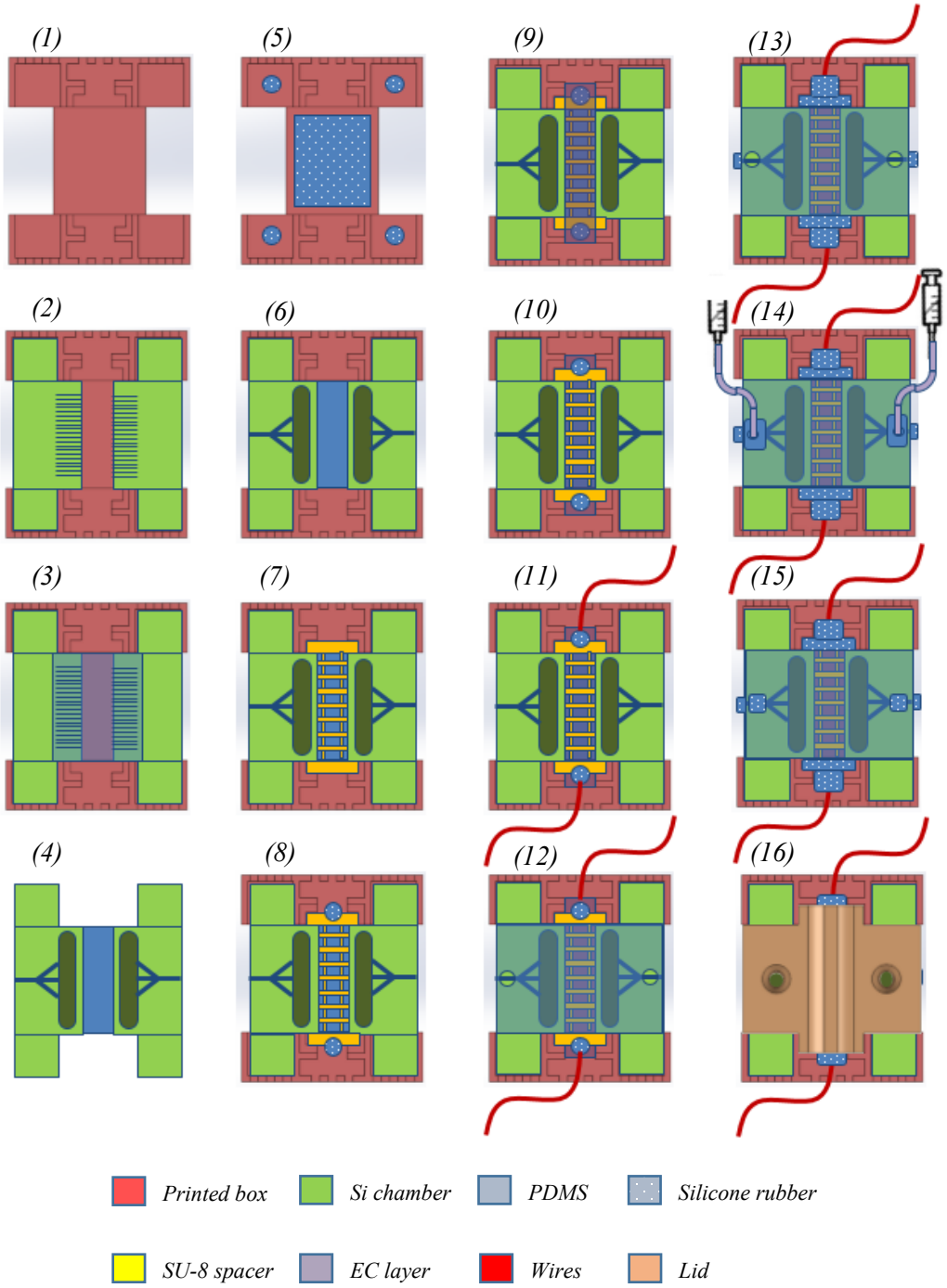
(1)
(5)
(9)
(13)
(2)
(6)
(10)
(14)
(3)
(7)
(11)
(15)
(4)
(8)
(12)
(16)
Printed box
Si chamber
PDMS
Silicone rubber
SU-8 spacer
EC layer
Wires
Lid

Figure 6.9 Micro-cooler assembly process flow. (1) 3D-printed package. (2) Place two chambers upside down in the package. (3) Attach bottom PDMS sealing layer on the bottom of two chambers. (4) Take two chambers with PDMS layer out of package. (5) Drop liquid PDMS in the package (center and four corners). (6) Put chambers back in the package. (7) Place SU-8 spacer in the package. (8) Drop liquid PDMS to fix SU-8 spacer. (9) Place EC polymer on the SU-8 spacer. (10) Use liquid PDMS to fix the EC polymer. Repeat (7) and (10). (11) Connect the wires. (12) Attach the top sealing PDMS layer with feeding holes. (13) Drop liquid PDMS and silicone rubber to seal the chambers except for the feeding holes. (14) Inject liquid into the chamber through the feeding holes. (15) Seal the feeding holes with liquid PDMS. (16) Attach lid.

The assembly process flow is shown in Figure 6.9. A thick PDMS layer is first attached on the bottom of two chambers in the 3D printed box. The chambers with attached bottom PDMS are then flipped over. The regenerator is then assembled by following the procedure developed in Chapter 5. The top PDMS layer with two injection holes is placed to cover the entire chamber area and regenerator area. After the device is sealed by a liquid PDMS (Sylgard 184, Dow Corning) and silicone rubber (Dap Products, Inc., Baltimore, MD), working fluid (HT-70) is injected into the chamber, and the lid with external pump connection is attached to the device. Figure 6.10 and Figure 6.11 shows some pictures of devices during the assembly, including the cooler before lid is attached, after lid is attached and after connection tube for external pump is attached.

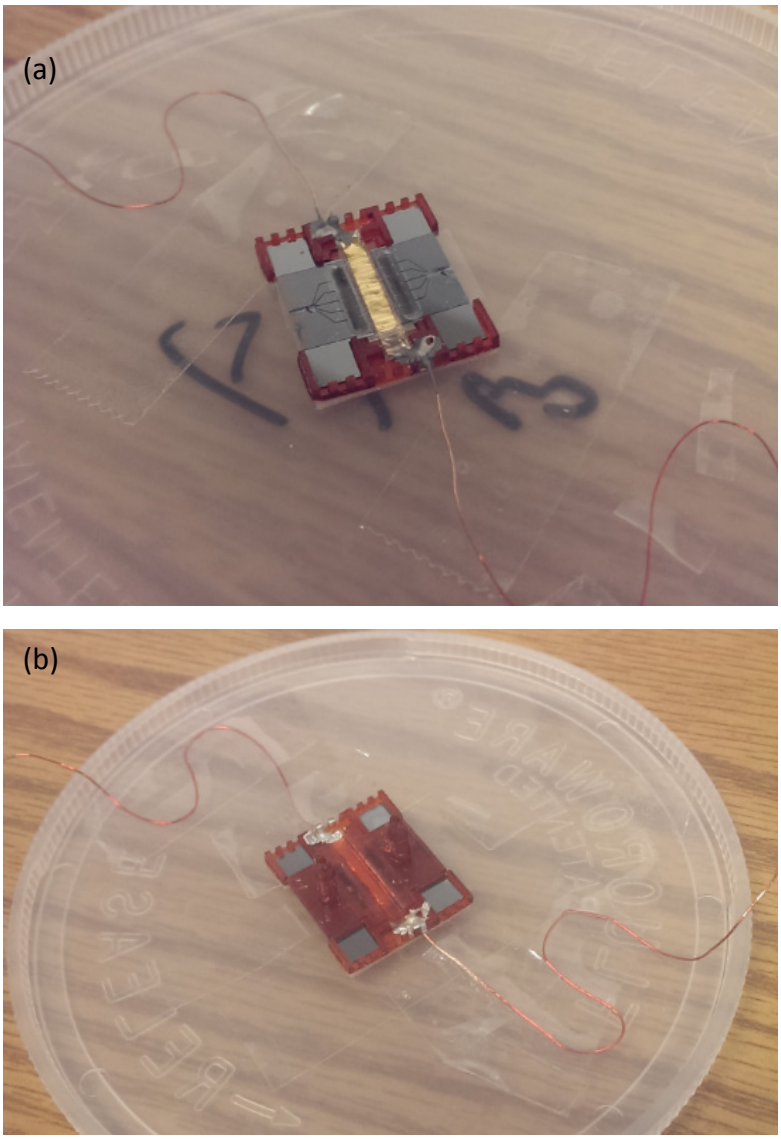

Figure 6.10 (a) Assembled micro-cooler after working fluid injection, but before the lid is attached. (b)After lid is attached.

Three of these prototypes were assembled and made ready for testing near the end of the project. Unfortunately, the prototypes broke at various points after assembly. The first prototype sample was damaged during shipping to Advanced Cooling Technologies, Inc. (ACT). The wires to the electrocaloric subsystem de-bonded from the sample and the working fluid leaked. Two

additional prototype system samples were hand delivered to ACT. One sample was installed into the test bed; however, one of the wires to the electrocaloric regenerator became disconnected and could not be successfully reconnected. The last sample suffered from leakage of the fluid from the electrocaloric region, the precise cause was not able to be determined.

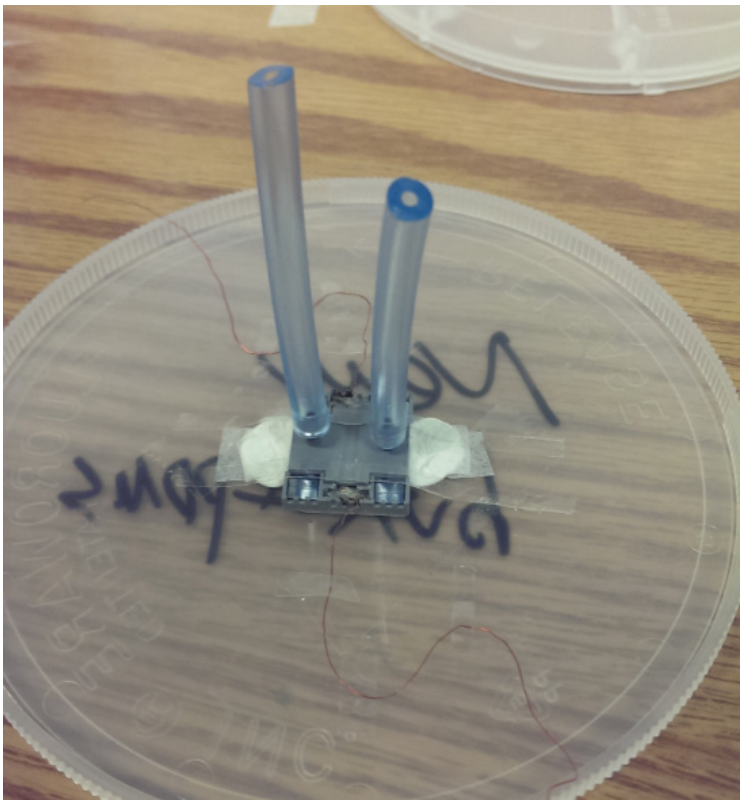

Figure 6.11 Assembled micro-cooler after testing tube is attached. The cooler is ready to test with external pump.

6.4 Summary and Conclusion

The multiphysics modeling for the micro-cooler including heat transfer module, mechanical, electrostatic and fluid modules was successfully performed, and it is validated by

the thermal modeling done before. The two micro-pumps and EC regenerator were assembled into the 3D printed package to create the micro-cooling system. Three assembled micro-coolers were delivered to Advanced Cooling Technologies, Inc., for testing their thermal performance. However, the samples were either damaged during the shipping or partially broken during the testing. The feasibility of the micro-cooler needs to be validated in the future.

Chapter 7 Summary and Future Work

7.1 Thesis Conclusion

In this thesis, a new micro refrigeration system based on MEMS techniques and EC effect was designed, fabricated, and partially tested to meet the increasing demand on thermal engineering and cooling technologies [27].

The innovative processing methods demonstrated in this thesis can successfully fabricate, pattern, release and transfer large area (> 5 cm) ultra-thin (down to 1 μm) PDMS film embedded metal electrodes having critical dimension down to 2 μm [30, 31]. The fabrication and transfer of ultra-thin PDMS thin films with or without embedded electrodes enables moving electrode fabrication for the micro-pumps and it also opens a new possibility for creating other soft electronics devices.

The mechanical properties of the PDMS thin film are characterized [31], and the effective Young's modulus follows a consistent power law as a function of PDMS thickness, having a value of 9 MPa for 1 μm-thick films, which is ten times that of bulk PDMS (0.9 MPa). The mechanical properties of PDMS films thinner than 20 μm is reported for the first time. Additional fabrication, such as metal evaporation and reactive ion etching increases PDMS stiffness by 20 to 70% due to enhancement of cross links and hardening of the surface, and this effect is greater when films become thinner. The characterization of mechanical properties for these very thin films is critical for the micro-pumps design and it is also very meaningful for designing and modeling other MEMS elastomer actuators.

A modified grayscale photolithography process is developed for fabricating the shaped Si substrate electrode. The photoresist is overexposed through the grayscale mask and very dilute AZ developer is used for a timed etch of the resist. Compared to prior grayscale lithography processes, the modified process enables the use of almost the entire dosage region (~100 to 1800 mJ/cm^2; traditional grayscale lithography: ~90 to 450 mJ/cm^2), giving more grayscale levels, resulting in a smoother resist profile (RMS: 0.05 μm to 0.1 μm compared to 0.4 μm to 0.5 μm in traditional grayscale lithography [64]). Relatively slow development allows repeatable timed control of the designed photoresist shape and it can also compensate for variations from other steps in the lithography process. This modified grayscale process enables fabricating of predicable and smooth 2.5D microstructures in MEMS devices and other systems.

The maximum measured displacement of the diaphragm of the micro-pump was 100 μm, giving a displacement volume of 1 μL/stroke, and a pumping rate of 60 μL/min at 1 Hz [28]. This ultra-large stroke PDMS micro-pump provides large pump volume for the micro-cooler. It may also open a promising route for fabricating other large electrostatic stroke actuators.

The EC effect of a P(VDF-TrFE-CFE) terpolymer was characterized by infrared imaging (joint work with Dongzhi Guo) that can be conducted conveniently and economically [32]. The heat dissipation of the sample in the air was modeled and used to estimate the adiabatic temperature change at different electric field magnitudes. At an electric field of 90 V/μm, an adiabatic temperature change of 5.2°C was obtained. In an operating frequency range of 0.03 to 0.3 Hz, the EC effect was observed to be independent of frequency. The stability of the material was validated by a long time testing. All results suggest that this polymer is a promising material for micro-scale cooling application.

Finite element multiphysics modeling (joint work with Dongzhi Guo) coupled with the Mooney Rivlin hyperplastic model, fluid-solid interaction, heat transfer, porous medium, contact model, electrostatics, and moving mesh technique, was conducted to evaluate the full system thermal performance. The system may enlighten other researchers to explore more possibilities to fulfill the requirement for today's increasing demand of electronics cooling.

7.2 Future Work

One issue with the current fabrication process for the micro-cooler is low yield. As mentioned in Chapter 4, this mainly comes from possibility of failures accumulated from each step. Several fabrication processes needs to be improved or refined to acquire better control of the quality then enhancing the yield. A cleanroom environment may be used for PDMS spinning to reduce the particulates. Different evaporation recipes could be explored to reduce the stress causing the films cracking. Work has already been done before by several researchers to characterize the relationship between film stress, chamber pressure, and deposition rate [88]. It shows lower chamber pressure and slower deposition rate can reduce the stress. Alternative combinations of metal layers instead of Cr/Al, (such as Ti, Au) could be evaporated to improve the adhesion between the metal and PDMS. The adhesion could be also enhanced by involving 2 kV Ar^+ ion bombardment on the PDMS surface before deposition [89]. The bonding and release process can be explored and modified in efforts to increase the yield. For example, the effect of different power, temperature, and time of oxygen plasma activation and the effect of different bonding time, temperature, and pressure could be optimized. Preliminary work has been done by other researchers [90, 91]. The mix ratio of gelation with water and the thickness of gelatin release layer may also bring improvements to the release process. In addition, the process

duration of the micro-pump also needs to be shortened. Currently, it takes a month to fabricate a micro-pump under the entire fabrication process. This is majorly due to multiple and complex process flows caused by the incompatibility of processing the special materials (PDMS, gelatin) by using traditional semiconductor fabrication tools. For reducing the fabrication time, customized fabrication machines may be needed in the future.

Significant work remains to be done for the modified grayscale lithography to obtain a more stable and repeatable method. The mechanism of grayscale lithography needs to be explored more in detail. For example, the effect of environmental factors, such as temperature and humidity, and the aging effect of resist and developer are of interest. Studies suggest the aging effect of photoresist may bring huge impact for its reaction kinetics [92]. The impact of the elliptical mirror (newly installed in our exposure system) should be found out. The mechanism behind the bump formation at certain grayscale levels also should be addressed. The reconstruction of UV light under a proximity mode may be a complex problem and it can be simulated through optical lithography modeling [93].

Another topic that is not fully explored is the shape effect of the Si chamber for the pump diaphragm displacement and its required snap-in voltage. Although preliminary work has be done in Chapter 4, more work needs to be accomplished. More measurement data is needed to validate the sensitivity of the profiles from the simulations. And the shape needs to be further optimized for the minimum snap-in voltage. For the pump actuation, the dynamic behaviors of the diaphragm should be tested, such as amplitude and phase lag under different AC driving voltage. These measurements need characterizing tools that can detect large and fast movements in the relatively large diaphragm region. Due to compliant PDMS diaphragm, the maximum

operating frequency is low compared to other reported electrostatic micro-pumps that often can operate at several dozens to several hundred Hz, although their diaphragm movement is only several microns [70, 94, 95]. The operating frequency of the micro-pump may be increased by making its diaphragm stiffer (e.g., by mixing with a different PDMS cure and base ratio, or possibly by embedding with an SU-8 skeletal structure), and by minimizing the depth of the chamber. The pumping rate is displacement volume times operating frequency. Although the stiffer diaphragm and shallower chamber decrease the stroke, the pumping rate should be optimized. By decreasing the chamber depth, the actuation voltage could also be reduced. In addition, more types of fluid needs to be tested in the micro-pump besides HT-70. The effects from the fluid on the micro-pumps, such as viscosity, wetting property, surface force, need to be explored in the future. The design of the pump can also be adapted to other future applications instead of the micro-cooler, such as a micro total analysis system (μTAS) and for biological sampling [71, 96]. For example, the dimension of the pump could be modified or scaled; valves could be added; the channels could be open at different places and the pump could be cascaded to make it more flexible to more applications.

The assembly that includes stacked double micro-pumps for push-pull electrostatic operation may be warranted to be accomplished in the future. The feasibility of the micro-cooler system also needs to be validated.

Appendix

Appendix 1. Process Flows and Recipes

Process flow for micro-pump fabrication

1. Process flow and recipes for PDMS diaphragm with embedded metal electrode.

1). Gelatin solution preparation.

   a. Gelatin power (250 bloom, Modernist Pantry) is mixed with DI water (gelatin: water 1:9 w/w). The powder and water is placed alternatively (repeating 1 g powder and 9 g water) to prevent lumping.

   b. The mixture is then heated in the oven at 60 ºC for 1 hour to dissolve.

2). PDMS solution preparation.

   a. PDMS solution (Sylgard 184, Dow Corning) is created by mixing pre-polymer gel and the cross linker in a 10:1 (w/w) ratio.

   b. The solution is agitated for 5 min for better mixing.

   c. The solution is placed in a vacuum chamber (Gast vacuum pump) for 2 hours to remove bubbles.

3). Spinning gelatin sacrificial layer.

   a. 4’’ Si wafer is cleaned with acetone and IPA.

   b. The heated gelatin mixture is spun at 1000 rpm for 2 min (Laurell WS-650Mz). The infrared heating is applied simultaneously to prevent the gelatin from hardening.

   c. The sample is then baked in a 40°C oven to form a 200nm-thick sacrificial gelatin layer.

4). Spinning the first layer of PDMS.

a. The PDMS solution is spun on the gelatin at 500 rpm for 30 s, accelerated to 3000 rpm for 30 s, spun at 6000 rpm speed for 150 s, and then decelerated slowly at 170 rpm/s^2 to form 10 μm thick PDMS layer.

b. The sample is then cured for 12 h in an oven at 70°C.

5). Metal evaporation.

a. 5 nm Cr is first evaporated on the PDMS (Ultek E-Beam Evaporator) as an adhesion layer. The recipe is:

Voltage (V)	Current (mA)	Pressure (T)	Deposition Rate (Å/s)
6000	40-50	1e-6 to 2e-6	1

b. 200 nm Al is then evaporated on the Cr as the diaphragm electrode. The recipe is

Voltage (V)	Current (mA)	Pressure (T)	Deposition Rate (Å/s)
6000	60-100	1e-6 to 2e-6	1

c. Another 5 nm Cr is evaporated on the Al to create the sandwich structure.

6). Sample dicing.

a. HDMS is spun (CEE 100CB Table Top Spinner) on the deposited sample at 4000 rpm for 30 s as adhesion layer.

b. AZ 4210 photoresist is then spun at 4000 rpm for 30 s to create 2.1 μm thick protection layer.

c. The film is heated on the hot plate at 80 ºC for 5 min. The initial temperate is 20 ºC and the ramping rate is 5 ºC/min. Faster ramping rate may cause film cracking.

d. The resist is flood exposed (Karl Suss MA6) at 5 mW/cm^2 for 200 s. This is for photoresist removal after dicing. The acetone is not applicable for the removal because it swells PDMS.

e. The sample is diced into 22 mm by 15 mm rectangular dies (Kulicke & Soffa 782-6 Dicing Saw).

f. The die is immersed in AZ developer for 2 min to remove the photoresist.

g. After developing, it is rinsed with DI water and dried.

7). Lithography.

a. HDMS is spun on the die at 4000 rpm for 30 s as adhesion layer.

b. AZ 4210 photoresist is then spun at 4000 rpm for 30 s to create 2.1 μm thick layer.

c. It is then heated on the hot plate at 80 ºC for 5 min. The initial temperate is 20 ºC and the ramping rate is 5 ºC/min.

d. The photoresist is exposed (Karl Suss MA6) at 5 mW/cm^2 for 120 s with diaphragm electrode mask.

e. The exposed sample is developed in AZ developer (AZ developer: water 1:1) for 2 min.

f. After developing, it is rinsed with DI water and dried.

g. The developed resist is flood exposed at 5 mW/cm^2 for 200 s. This is for photoresist removal after wet etching.

h. It is treated in oxygen plasma (IPC Barrel Etcher) at 50 W for 2 min for descum.

8). Wet etching.

a. The sample is placed on a 50 ºC hot place for 10 min to increase the adhesion between the resist and film.

b. After baking, it is first immersed in Cr etchant for 20 s to pattern the top Cr layer.

c. After etching, the film is rinsed with DI water and dried. It is then placed back on the 50 ºC hot place for 10 min.

d. The sample is immersed in the Al etchant for 300 s to pattern the Al layer.

e. The film is rinsed with DI water and dried. It is then placed back on the 50 ºC hot place for 10 min.

f. The sample is then immersed in the Cr etchant for 20 s to pattern the bottom Cr layer.

g. The film is rinsed with DI water and dried. It is then placed back on the 50 ºC hot place for 10 min.

h. The sample is immersed in AZ developer for 2 min to remove the photoresist.

i. The sample is rinsed with DI water and dried.

9). Spinning the second layer of PDMS.

a. To achieve 1 μm films, the PDMS solution is created by first mixing pre-polymer gel and the cross linker in a 10:1 (w/w) ratio and then diluted with hexane (ACS grade, Fisher Scientific) (PDMS: Hexane 1:9 w/w).

b. The mixture is filtered by 0.2 μm syringe filter (PALL Acrodisc Syringe Filters).

c. The mixture is spun on patterned sample at 6000 rpm for 150 s to create 1 μm thick PDMS layer.

d. The sample is then cured for 12 h in an oven at 70°C.

2. Process flow and recipes for shaped Si chamber.

1). Depositing back side protection layer.

a. 4'', double polished Si wafer is cleaned with acetone and IPA.

b. The backside is deposit with 1 μm PECVD silicon oxide (Trion Orion PECVD System). The recipe is:

Power (W)	N_2O (sccm)	SiH_4 (sccm)	Pressure (mT)	Temprature (ºC)	Rate (μm/min)
60	70	75	900	375	0.1

Or the backside is sputtered with 300 nm Al layer (CVC Connexion 6-Target Sputtering System). The recipe is:

Power (W)	Ar flow (sccm)	Pressure (mT)	Rate (μm/min)
250	50	5	0.018

2). Alignment mark fabrication.

a. HDMS is spun on the front side of the sample at 4000 rpm for 30 s for an adhesion layer.

b. AZ 4210 photoresist is then spun at 4000 rpm for 30 s to create 2.1 μm thick resist layer.

c. It is then heated on the hot plate at 95 ºC for 1 min.

d. The resist is exposed (Karl Suss MA6) at 5 mW/cm^2 for 120 s with alignment mask.

e. The resist is developed in AZ developer (AZ developer: water 1:1) for 2 min.

f. It is then rinsed with DI water and dried.

g. The sample is placed in oxygen plasma (IPC Barrel Etcher) at 100 W for 2 min for descum.

h. 50 nm Al layer is sputtered on the resist (CVC Connexion 6-Target Sputtering System). The recipe is:

Power (W)	Ar flow (sccm)	Pressure (mT)	Rate (μm/min)
250	50	5	0.018

i. The sample is immersed in acetone for 4 hours for a lift-off process.

j. It is then rinsed with DI water and dried.

3). Grayscale lithography

a. HDMS is spun on the front side at 4000 rpm for 30 s for an adhesion layer.

b. AZ 4210 photoresist is then spun at 2000 rpm for 45 s to create 3.1 μm thick resist layer.

c. It is then heated on the hot plate at 95 ºC for 2 min.

d. The resist is exposed (Karl Suss MA6) at 5 mW/cm^2 for 120 s under contact mode with feed line mask.

e. The resist is exposed (Karl Suss MA6) at 5 mW/cm^2 for 380 s under proximity mode with grayscale mask. The gap between the sample and the grayscale mask is set to be 150 μm to diffract the UV light.

f. The AZ developer is over diluted with water (AZ developer to water: 1:2.7). The mixing process is completed by using measuring cylinders.

g. The exposed sample is then soaked horizontally in diluted AZ developer. No agitation is used during development. As soon as the 2 μm resist located in the 100% UV transmission regions is dissolved, the development is stopped. This process takes 30 min.

h. The sample is rinsed with DI water and dried.

4). Deep reactive ion etching

a. The developed sample is mounted on a carrier wafer with 120 ºC heat release tape.

b. Anisotropic DRIE is first performed (Surface Technology System) for 75 min. The recipe is:

Etch	SF_6 flow (sccm)	O_2 flow (sccm)	Cycle time (s)	Pressure (mT)	Coil power (W)	Platen Power (W)	Temperature (ºC)
	130	13	12	20	600	12	19
Passivation	C_4F_8 flow (sccm)	O_2 flow (sccm)	Cycle time (s)	Pressure (mT)	Coil power (W)	Platen Power (W)	Temperature (ºC)
	85	0	8	10	600	0	19

c. The etched sample is then followed by 2 min isotropic etching. The recipe is:

Etch	SF_6 flow (sccm)	O_2 flow (sccm)	Cycle time (s)	Pressure (mT)	Coil power (W)	Platen Power (W)	Temperature (ºC)
	130	0	n/a	50	600	12	19

d. It is then heated at 130 ºC to release from the carrier wafer.

5). Back side lithography

a. The sample is first immersed in buffered HF for 5 min to remove the backside SiO_2 protection layer. (or immersed in Al etchant to remove Al protection layer.)

b. HDMS is spun on the back side of the sample at 4000 rpm for 30 s for an adhesion layer.

c. AZ 4260 photoresist is then spun at 3000 rpm for 30 s to create 7 μm thick resist layer.

d. It is then heated on the hot plate at 95 ºC for 5 min.

e. The resist is exposed (Karl Suss MA6) at 5 mW/cm^2 for 600 s with the channel mask by using back side alignment.

f. The resist is developed in AZ 400k developer (AZ developer: water 1:4) for 2 min.

g. It is then rinsed with DI water and dried.

h. The sample is placed in oxygen plasma (IPC Barrel Etcher) at 100 W for 2 min for descum.

6). Back side channel etching

a. The developed sample is mounted on a carrier wafer with 120 ºC heat release tape.

b. DRIE is first performed for 150 min to create the backside channels and separate each chamber by utilizing aspect ratio dependent etching. The recipe is:

Etch	SF_6 flow (sccm)	O_2 flow (sccm)	Cycle time (s)	Pressure (mT)	Coil power (W)	Platen Power (W)	Temperature (ºC)
	130	13	12	20	600	12	19
Passivation	C_4F_8 flow (sccm)	O_2 flow (sccm)	Cycle time (s)	Pressure (mT)	Coil power (W)	Platen Power (W)	Temperature (ºC)
	85	0	8	10	600	0	19

c. The etched sample is heated at 130 ºC to release from the carrier wafer.

d. The sample is immersed in piranha solution (sulfuric acid: peroxide 2:1) to remove the resist.

e. It is then rinsed with DI water and dried.

3. Process flow and recipes for pump assembly.

1). Bonding diaphragm and chamber.

a. The fabricated diaphragm and chamber are treated with oxygen plasma at 50 W for 1 min to increase the bonding adhesion.

b. The two components are aligned and bonded using a device bonder (Besi/Laurier M9). The recipe is:

Weight (g)	Temperature (ºC)	Time (min)
2000	20	3

c. The bonded device is then placed at room temperature for 2 days before release to increase the adhesion.

2). Release and transfer.

a. The PDMS is cut by a scalpel along the chamber edge for the release. The PDMS in the exposed area is removed.

b. The sample is immersed in a 40 ºC warm water for 2 - 3 hours. The water is replaced every 1 hour to lower the gelatin concentration.

c. The released pump is immersed in 50 ºC warm water for 30 min to remove the gelatin residue.

d. The device is flipped over and placed on a polypropylene substrate with a water droplet, then is dried in a 40 ºC oven for 30 min. The polypropylene prevents the diaphragm sticking on the Si chamber when drying.

e. The released pump is picked up by tweezer from polypropylene substrate.

4. Process flow and recipes for bonding pad fabrication.

1). PDMS mask molding.

a. 300 μm thick Si substrate is DRIE into 80 mm by 200 mm rectangular piece.

b. The prepared PDMS solution is poured on a Si substrate with the Si piece on it to form 1 mm thick PDMS mask.

e. The sample is then cured for 12 h in an oven at 70°C.

c. The mask is peeled off from the substrate.

d. A 2 mm diameter circular opening is cut by a No. 15 gauge needle.

e. The C_4F_8 polymer film is deposit (Surface Technology System) on the back side of mask to avoid PDMS-PDMS sticking during the etching process. The recipe is:

C_4F_8 flow (sccm)	Pressure (mT)	Coil power (W)	Platen Power (W)	Temperature (ºC)
85	10	600	0	19

2). Bonding pad etching and wire connection

a. The pump is covered with PDMS mask and placed in a reactive ion etch system (Trion Phantom III RIE etcher). The etching recipe is:

CF_4 flow (sccm)	O_2 flow (sccm)	Power (W)	Pressure (mT)	Etching Rate (μm/min)
30	10	100	60	0.25

b. The connecting wires are attached on the bonding pads with silver paste (Ted Pella PELCO High Performance Silver Paste).

Appendix 2. FEA Simulation Settings

Setting of multiphysics modeling of micro-cooler by COMSOL 4.3b

1. Parameters

	Parameters	*Values*
Frequency	f	5[Hz]
Diaphragm voltage/2	Vin0	85[V]
Contact coefficient	cfc	5e10[Pa/m]
Substrate height	H	280[um]
Chamber corner height	H_c	10[um]
Chamber height	H_ch	150[um]
Chamber gap height	H_g	2[um]
Base height	H_b	H-H_ch
EC length	L_ec	2500[um]
Chamber length	L	2000[um]
Total length	LL	2500[um]
Diaphragm height	H_d	13[um]
EC layer number	n_ec	6
Insulating layer height	H_i	2[um]

HT-70 viscosity	vis_70	0.00084[Pa*s]
HT-70 porosity	por_70	0.66666
HT-70 permeability	per_70	3.5e-11[m^2]
EC thickness	t_ec	20[um]
EC channel height	h_ch	50[um]
HT-70 heat transfer coefficient	k_70	0.065[W/m/K]
HT-70 heat capacity	cp_70	970[J/kg/K]
EC electrical field	E0	100[MV/m]
EC density	den_ec	1800[kg/m^3]
EC permittivity	epss	0.5
EC heat transfer coefficient	h_fs	NU*k_70/w_ch
EC area	A_wet	1/2/w_ch
EC channel width	w_ch	50[um]
Si heat transfer coefficient	k_si	163[W/m/K]

Mesh element number settings	M_H_g	15
	M_L	50
	M_H_i	2
	M_H_d	4
	M_L_r	40
	M_H_r	10
	M_ch_e	12
Mooney Rivlin C_1	C1	321[kPa]
Mooney Rivlin C_2	C2	0[kPa]
Chamber half length	L_d	L/2
Substrate corner length	L_ch_e	(LL-L)/2
HT-70 density	den_70	1680[kg/m^3]

2. Variables

	Variables	*Equations*
Gap of left part of diaphragm 1	gap1	H_ch*(3*((x-L_ch_e)/L_d)^2-2*((x-L_ch_e)/L_d)^3)+v_solid
Gap of right part of diaphragm 1	gap2	H_ch*(1-3*((x-LL/2)/L_d)^2+2*((x-LL/2)/L_d)^3)+v_solid
Gap of left part of diaphragm 2	gap3	H_ch*(3*((x-L_ch_e-LL-L_ec)/L_d)^2-2*((x-L_ch_e-LL-L_ec)/L_d)^3)+v_solid
Gap of right part of diaphragm 2	gap4	H_ch*(1-3*((x-LL/2-LL-L_ec)/L_d)^2+2*((x-LL/2-LL-L_ec)/L_d)^3)+v_solid
Test voltage on diaphragm 1	Vin1e	2*Vin0+1[V]
Test voltage on diaphragm 2	Vin2e	1[V]
Contact force of left part of diaphragm 1	Fc1	(gap1<0)*(-cfc)*gap1
Contact force of right part of diaphragm 1	Fc2	(gap2<0)*(-cfc)*gap2
Contact force of left part of diaphragm 2	Fc3	(gap3<0)*(-cfc)*gap3
Contact force of right part of diaphragm 2	Fc4	(gap4<0)*(-cfc)*gap4
Test voltage on diaphragm 1	Vin1d	Vin0*wv1(t)+Vin0+1[v]
Applied voltage on diaphragm 2	Vin2	(t<0.2/f)*1[V]+(t>=0.2/f)*(Vin0*wv2(t)+Vin0+1[V])
Test voltage on diaphragm 1	Vin1c	(t<0.3/f)*(Vin0*wv1(t)+Vin0+1[v])+(t>=0.3/f)*(2*Vin0+1[V])
Applied voltage on diaphragm 1	Vin1	(t<0.2/f)*(2*Vin0*wv1(t)+1[V])+(t>=0.2/f)*(Vin0*wv1(t)+Vin0+1[v])
Relationship of electrical field vs entropy	dsde	-(6.85e-8)-2*(2.71e-15)*V_ec
Applied voltage on EC	V_ec	E0*(wv1(t+0.5/f)+1)/2

3. Geometry & Materials

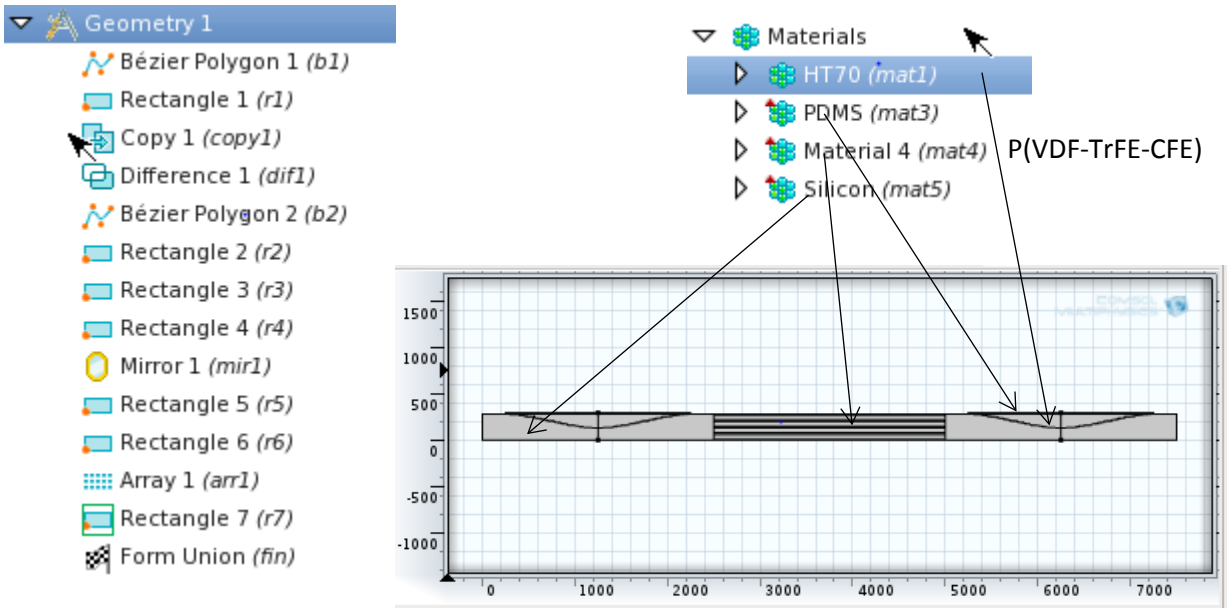

4. Physics

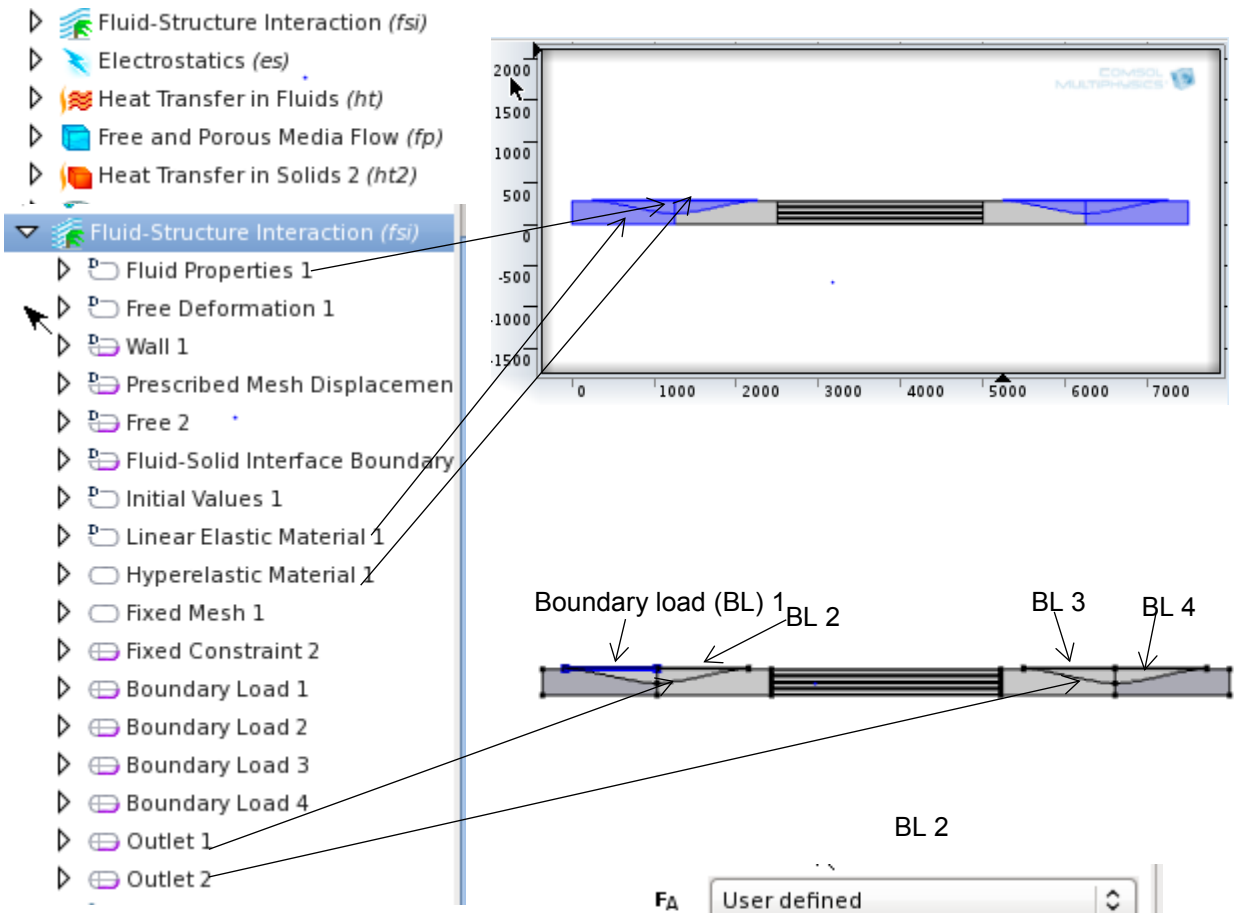

BL 2

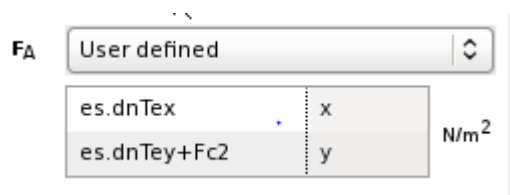

Boundary load 1

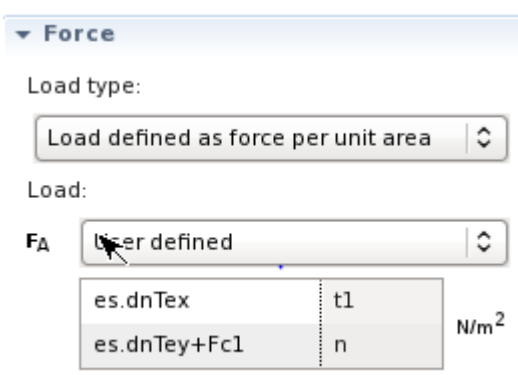

BL 3

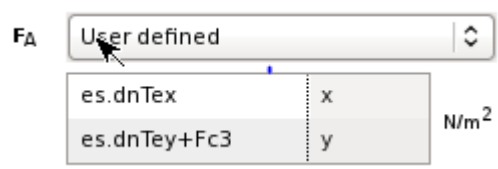

BL 4

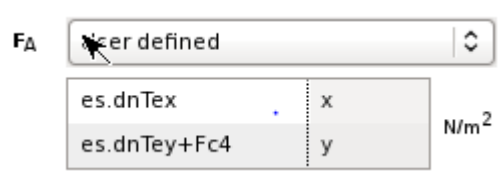

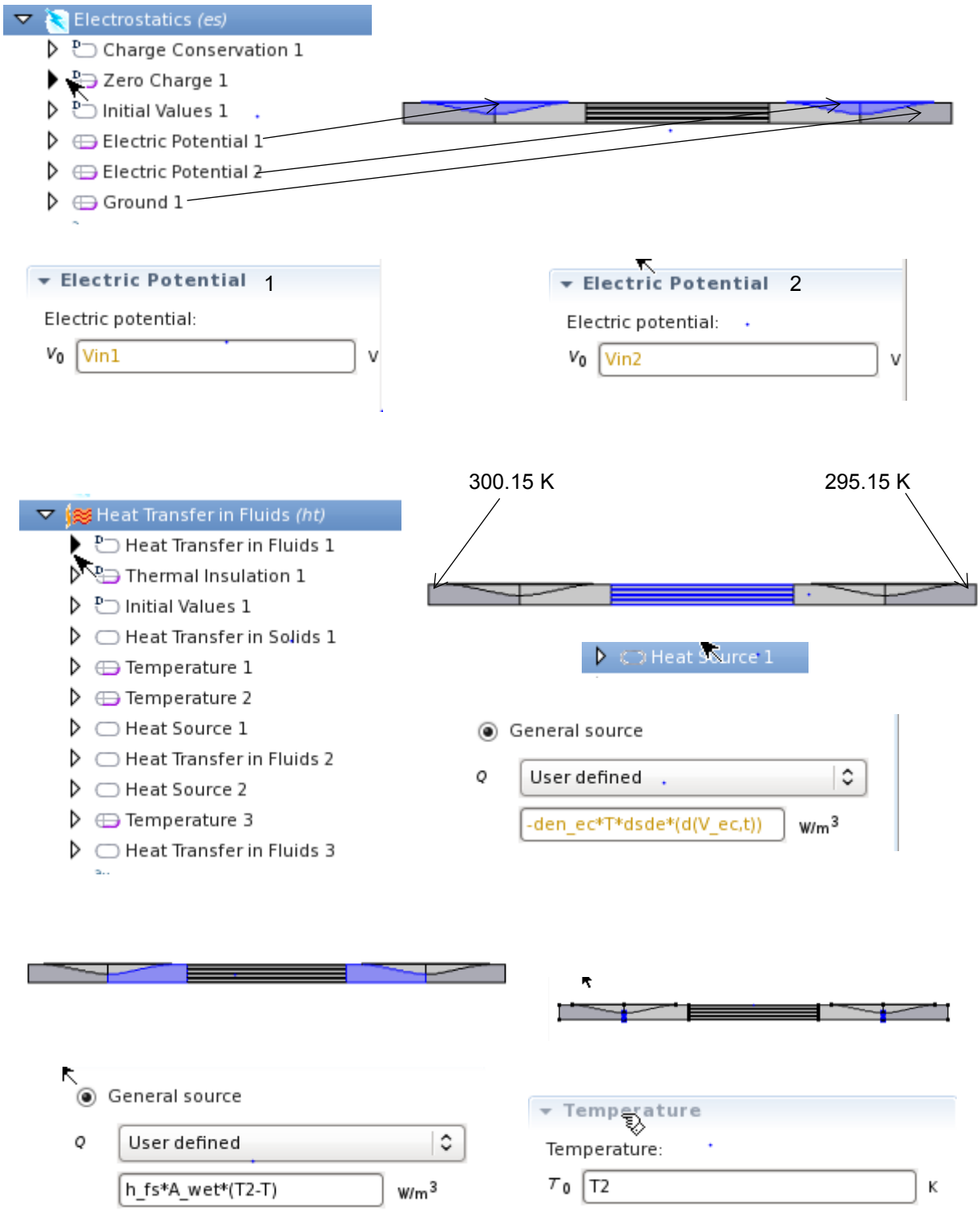
Electrostatics (es)
Charge Conservation 1
Zero Charge 1
Initial Values 1
Electric Potential 1
Electric Potential 2
Ground 1
Electric Potential 1
Electric potential:
V0 Vin1 V
Electric Potential 2
Electric potential:
V0 Vin2 V
300.15 K
295.15 K
Heat Transfer in Fluids (ht)
Heat Transfer in Fluids 1
Thermal Insulation 1
Initial Values 1
Heat Transfer in Solids 1
Temperature 1
Temperature 2
Heat Source 1
Heat Transfer in Fluids 2
Heat Source 2
Temperature 3
Heat Transfer in Fluids 3
Heat Source 1
General source
Q User defined
-den_ec*T*dsde*(d(V_ec,t)) W/m3
General source
Q User defined
h_fs*A_wet*(T2-T) W/m3
Temperature
Temperature:
T0 T2 K

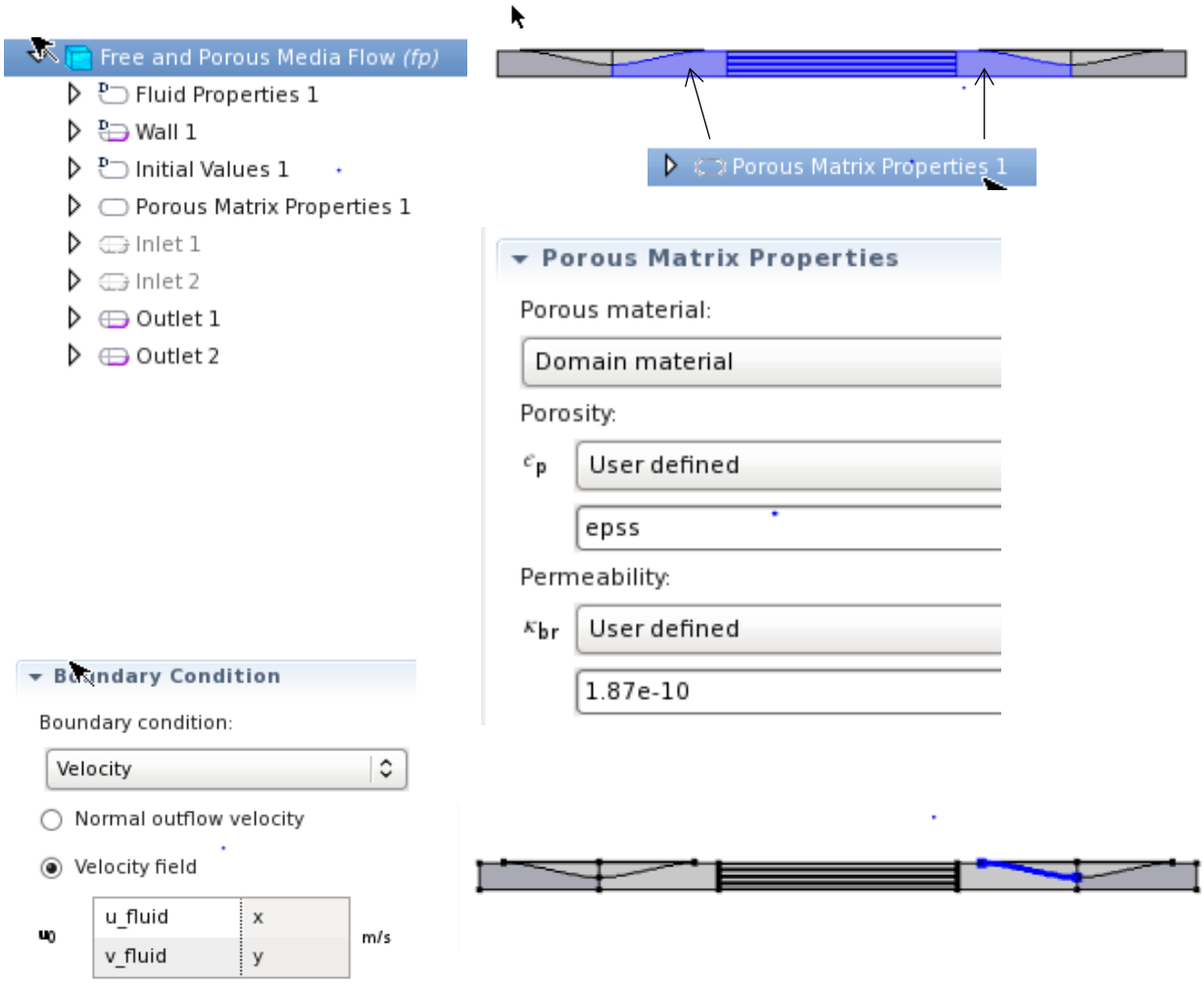
Free and Porous Media Flow (fp)
Fluid Properties 1
Wall 1
Initial Values 1
Porous Matrix Properties 1
Inlet 1
Inlet 2
Outlet 1
Outlet 2
Porous Matrix Properties 1
Porous Matrix Properties
Porous material:
Domain material
Porosity:
User defined
epss
Permeability:
User defined
1.87e-10
Boundary Condition
Boundary condition:
Velocity
Normal outflow velocity
Velocity field
u_fluid
v_fluid
x
y
m/s

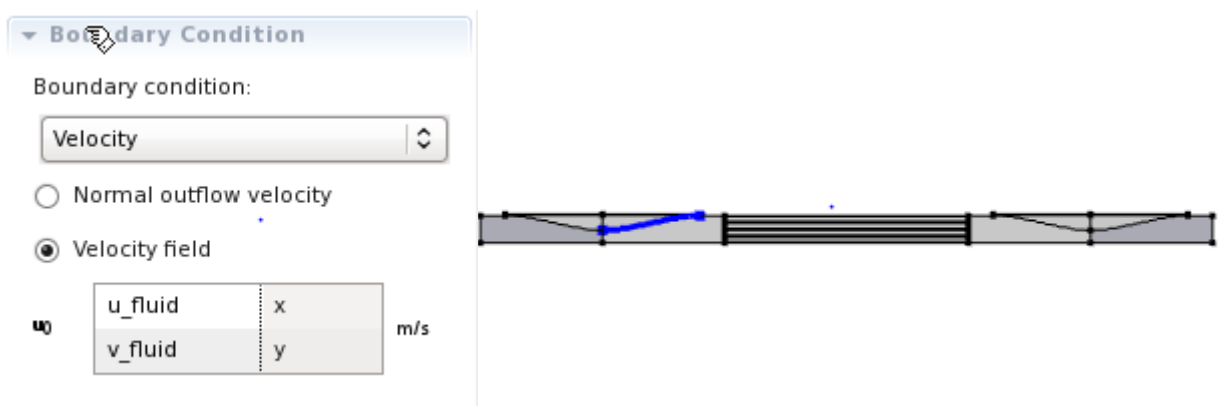
Boundary Condition
Boundary condition:
Velocity
Normal outflow velocity
Velocity field
u_fluid
v_fluid
x
y
m/s

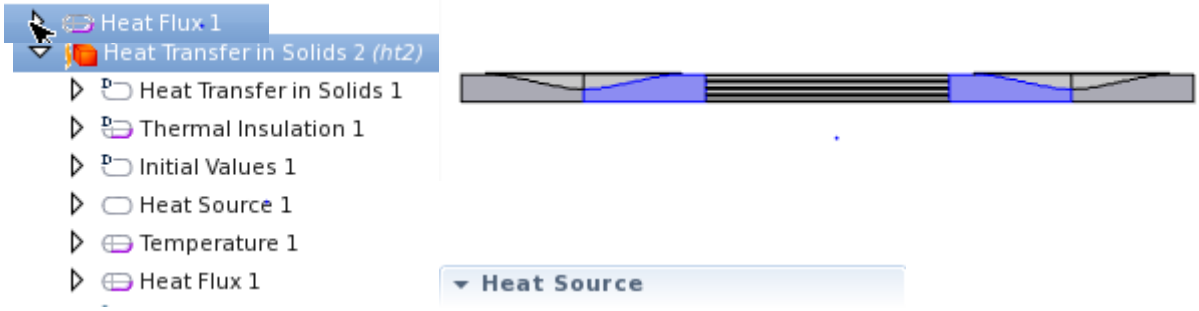
Heat Flux 1
Heat Transfer in Solids 2 (ht2)
Heat Transfer in Solids 1
Thermal Insulation 1
Initial Values 1
Heat Source 1
Temperature 1
Heat Flux 1

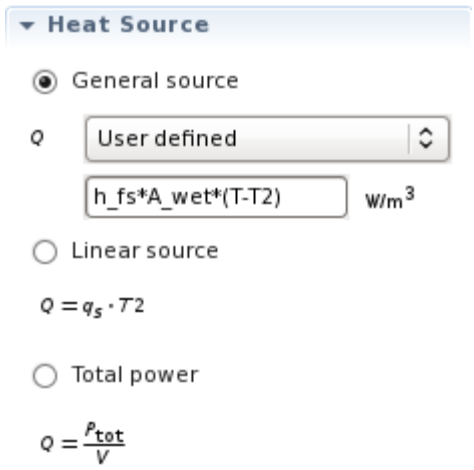
Heat Source
General source
Q
User defined
h_fs*A_wet*(T-T2)
W/m3
Linear source
Q = qs · T2
Total power
Q = Ptot / V

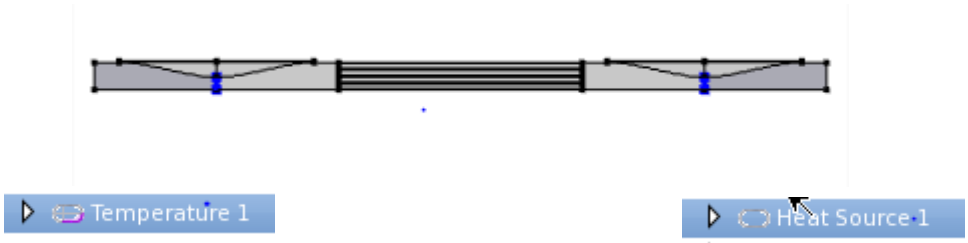
Temperature 1
Heat Source 1

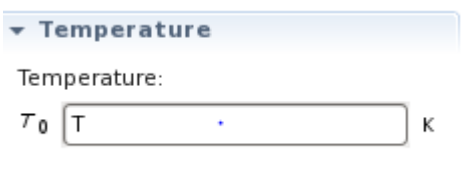
Temperature
Temperature:
T0
T
K

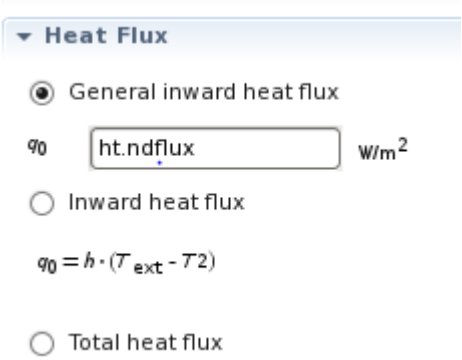
Heat Flux
General inward heat flux
q0
ht.ndflux
W/m2
Inward heat flux
q0 = h · (T ext - T2)
Total heat flux

5. Mesh

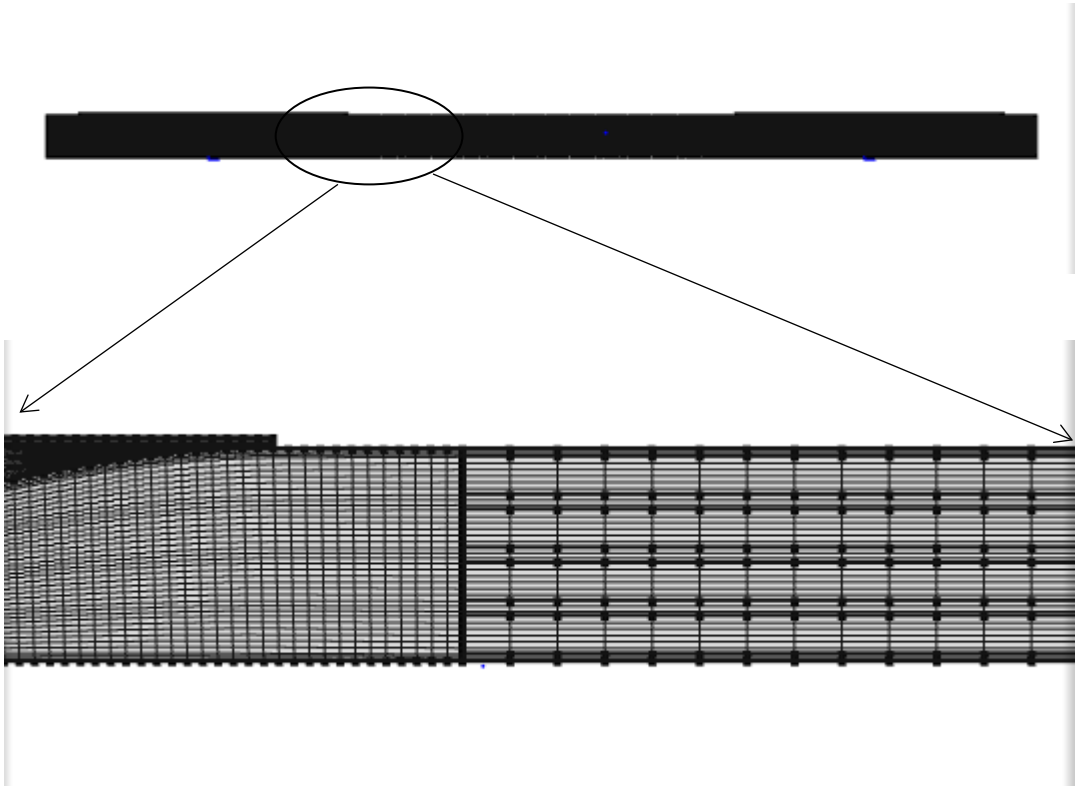

6. Study

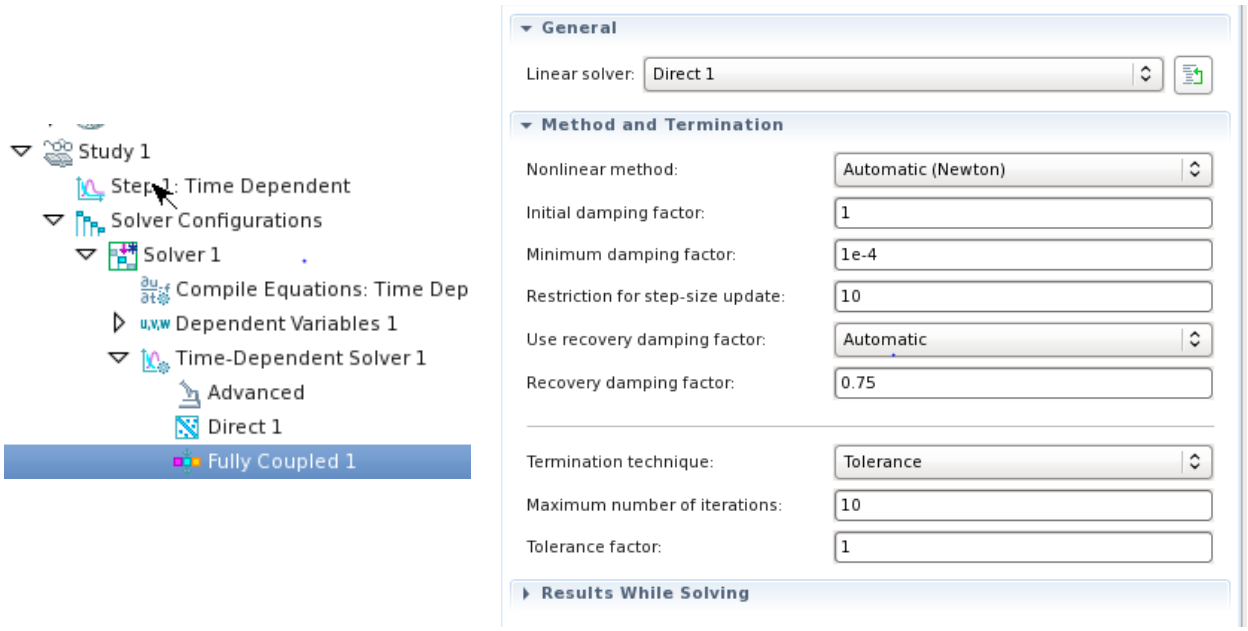

Appendix 3. Scripts and Codes

1. Mathematica Code for the model of circular PDMS membrane:

```
ClearAll["Global`*"];

ϵ=10^-4;

SolveBalloon[λ0_?NumberQ,κ0_,ζ0_]:=Module[{},


Clear[r,λ1,λ2,κ1,κ2,ρ,ζ,θ,T1,T2,equation1,equation2,equation3,equation4,equation5,equation6,
equation7,bc1,bc2,bc3,bc4,bc5,bc6,bc7];

 λ1[0]=λ0;λ2[0]=λ0;

 κ1[0]=κ0;κ2[0]=κ0;

 ρ[0]=0;ζ[0]=ζ0;θ[0]=0;

 λ1'[0]=0;λ2'[0]=0;

 κ1'[0]=0;κ2'[0]=0;

 ρ'[0]=λ1[0];ζ'[0]=0;θ'[0]=κ1[0]λ1[0];

 λ1''[0]=-((κ1[0]^2 λ1[0]^3 (2λ1[0]^6-3))/(4(3+λ1[0]^6)));

 λ2''[0]=-((κ1[0]^2 λ1[0]^3 (2λ1[0]^6+3))/(4(3+λ1[0]^6)));

 T1[0]=(1/(λ1[0]λ2[0]))(λ1[0]^2-1/(λ1[0]^2 λ2[0]^2));

 T1''[0]=1/λ1[0]^10 (3λ1[0]^3 λ1''[0]+λ1[0]^9 λ1''[0]+3λ1[0]^3 λ2''[0]-λ1[0]^9 λ2''[0]);

 κ2''[0]=-(κ1[0]/T1[0])T1''[0];κ1''[0]=3κ2''[0];

 ρ''[0]=0;ζ''[0]=-κ1[0] λ1[0]^2;θ''[0]=0;

 bc1=λ1[ϵ]==λ1[0]+λ1'[0]ϵ+1/2 λ1''[0]ϵ2;

 bc2=λ2[ϵ]==λ2[0]+λ2'[0]ϵ+1/2 λ2''[0]ϵ2;

 bc3=κ1[ϵ]==κ1[0]+κ1'[0]ϵ+1/2 κ1''[0]ϵ2;
```

```
bc4=κ2[ϵ]==κ2[0]+κ2'[0]ϵ+1/2 κ2''[0]ϵ2;

bc5=ρ[ϵ]==ρ[0]+ρ'[0]ϵ+1/2 ρ''[0]ϵ2;

bc6=ζ[ϵ]==ζ[0]+ζ'[0]ϵ+1/2 ζ''[0]ϵ2;

bc7=θ[ϵ]==θ[0]+θ'[0]ϵ+1/2 θ''[0]ϵ2;

T1[r]=(1/(λ1[r]λ2[r]))(λ1[r]^2-1/(λ1[r]^2 λ2[r]^2));

T2[r]=(1/(λ1[r]λ2[r]))(λ2[r]^2-1/(λ1[r]^2 λ2[r]^2));

T1'[r]=-(1/ρ[r])ρ'[r](T1[r]-T2[r]);

T2'[r]=(3 λ2[r] λ1’[r]-λ1[r]^2 λ2[r]^5 λ1’[r]+3 λ1[r] λ2’[r]+λ1[r]^3 λ2[r]^4 λ2’[r])/(λ1[r]^4 λ2[r]^4);

equation1=ρ'[r]==λ1[r]Cos[θ[r]];

equation2=λ2'[r]==1/r (ρ'[r]-λ2[r]);

equation3=λ1'[r]==1/(λ2[r](λ1[r]^4 λ2[r]^2+3)) (λ1[r]^4 λ2[r]^4 T1'[r]+λ1[r]λ2'[r](λ2[r]^2 λ1[r]^4-3));

equation4=θ'[r]==κ1[r]λ1[r];

equation5=κ2'[r]==1/(r λ2[r]) ρ'[r](κ1[r]-κ2[r]);

equation6=κ1'[r]==-(1/T1[r])(κ1[r] T1'[r]+κ2[r] T2'[r]+T2[r] κ2'[r]);

equation7=ζ'[r]==-λ1[r]Sin[θ[r]];


{ρ,ζ,θ,λ1,λ2,κ1,κ2}/.NDSolve[{equation1,equation2,equation3,equation4,equation5,equation6,e
quation7,bc1,bc2,bc3,bc4,bc5,bc6,bc7},{ρ,ζ,θ,λ1,λ2,κ1,κ2},{r,ϵ,1},Method-
>Automatic,AccuracyGoal->7,PrecisionGoal->7,MaxSteps->100000][[1]]

]


λ21[λ0_?NumberQ,κ0_?NumberQ,ζ0_?NumberQ]:=SolveBalloon[λ0,κ0,ζ0][[5]][x]/.x->1;

ζ1[λ0_?NumberQ,κ0_?NumberQ,ζ0_?NumberQ]:=SolveBalloon[λ0,κ0,ζ0][[2]][x]/.x->1;

Findκ0ζ0[λ0_?NumberQ]:=Module[{},
```

```
  Clear[k0,z0,k1,z1,k2,z2];
  If[λ0==1,{k1=0,k2=0.0000001;},
   {k1=((2^(√(λ0- 1)) )/λ0)-(0.3 (2^(√(λ0- 1)) )/λ0);
    k2=((2^(√(λ0- 1)) )/λ0)-(0.2 (2^(√(λ0- 1)) )/λ0)}];
  If[λ0==1,{z1=0;z2=0.0000001},
   {z1=0,z2=0.1}];
  {k0,z0}/.FindRoot[{λ21[λ0,k0,z0]==1,ζ1[λ0,k0,z0]==0},{k0,k1,k2},{z0,z1,z2}]
  ]
SolveFinal[λ0_]:=Module[{},
  s=SolveBalloon[λ0,Findκ0ζ0[λ0][[1]],Findκ0ζ0[λ0][[2]]];
  κ1N=s[[6]][r];
  κ2N=s[[7]][r];
  λ1N=s[[4]][r];
  λ2N=s[[5]][r];
  T1N=(1/(λ1N λ2N))(λ1N^2-1/(λ1N^2 λ2N^2));
  T2N=(1/(λ1N λ2N))(λ2N^2-1/(λ1N^2 λ2N^2));
  pN=κ1N T1N+κ2N T2N;
  {ParametricPlot[{s[[1]][r],s[[2]][r]},{r,ϵ,1}],
   s[[2]][r]/.r->ϵ,
   pN/.r->ϵ  }
  ]
SolveP[a_,h_,YE_,λ0_?NumberQ]:=Module[{},
```

```
  C1=YE*3.33*^5/2;

  s=SolveBalloon[λ0,Findκ0ζ0[λ0][[1]],Findκ0ζ0[λ0][[2]]];

  κ1N=s[[6]][r];

  κ2N=s[[7]][r];

  λ1N=s[[4]][r];

  λ2N=s[[5]][r];

  T1N=(1/(λ1N λ2N))(λ1N^2-1/(λ1N^2 λ2N^2));

  T2N=(1/(λ1N λ2N))(λ2N^2-1/(λ1N^2 λ2N^2));

  pN=κ1N T1N+κ2N T2N;

  pNa=pN/.r->ϵ

  ]

Balloonλ[a_,h_,YE_,λ0_]:=Module[{},

  C1=YE*3.33*^5/2;

  s=SolveBalloon[λ0,Findκ0ζ0[λ0][[1]],Findκ0ζ0[λ0][[2]]];

  κ1N=s[[6]][r];

  κ2N=s[[7]][r];

  λ1N=s[[4]][r];

  λ2N=s[[5]][r];

  T1N=(1/(λ1N λ2N))(λ1N^2-1/(λ1N^2 λ2N^2));

  T2N=(1/(λ1N λ2N))(λ2N^2-1/(λ1N^2 λ2N^2));

  pN=κ1N T1N+κ2N T2N;

  pNa=pN/.r->ϵ  ;

  ρR=s[[1]][r]a/.r->rR/ a;
```

```
  ζR=s[[2]][r]a/.r->rR/ a;

  pR=2pNa C1 h/a;

  ParametricPlot[{ρR,ζR},{rR,ϵ a  ,a},PlotRange->All,AspectRatio->Automatic]

  ]

Solveλ0[a_,h_,YE_,p_?NumberQ]:=Module[{},

  Clear[λ0,pNN,l0];


s=Interpolation[{{0.000851801,1.001},{0.234941,1.05},{0.527781,1.1},{0.999251,1.2},{1.30987,
1.3},{1.51122,1.4},{1.64358,1.5},{1.73175,1.6},{1.82968,1.8},{1.86955,2},{1.87917,2.2}},Interpol
ationOrder->1];

  pNN=p a/(YE 3.33*^5 h);

  If[pNN<1.88,

   l0=s[x]/.x->pNN,

   Print["Beyond stable point"];

   ];

  λ0/.FindRoot[SolveP[a,h,YE,λ0]==pNN,{λ0,l0}]

  ]

Balloonp[a_,h_,YE_,p_]:=Module[{},

  Balloonλ[a,h,YE,Solveλ0[a,h,YE,p]]

  ]

Solveλ0[1*^-3,53*^-6,3.5,50000]

1.155

Pr=Array[pp,10]

{pp[1],pp[2],pp[3],pp[4],pp[5],pp[6],pp[7],pp[8],pp[9],pp[10]}
```

```
Fig=Array[ff,10]

{ff[1],ff[2],ff[3],ff[4],ff[5],ff[6],ff[7],ff[8],ff[9],ff[10]}

pp[1]=50;pp[2]=500;pp[3]=2000;pp[4]=5000;pp[5]=10000;pp[6]=20000;pp[7]=30000;pp[8]=400
00;pp[9]=50000;

For[i=1,i<=9,i++,ff[i]=Balloonp[1*^-3,56*^-6,1.8,pp[i]]]

Show[{ff[1],ff[2],ff[3],ff[4],ff[5],ff[6],ff[7],ff[8],ff[9]},Frame->True,PlotRange-
>{{0,.001},{0,0.00072}},BaseStyle->{FontWeight->"Bold",FontSize->25},GridLines->Automatic]
```

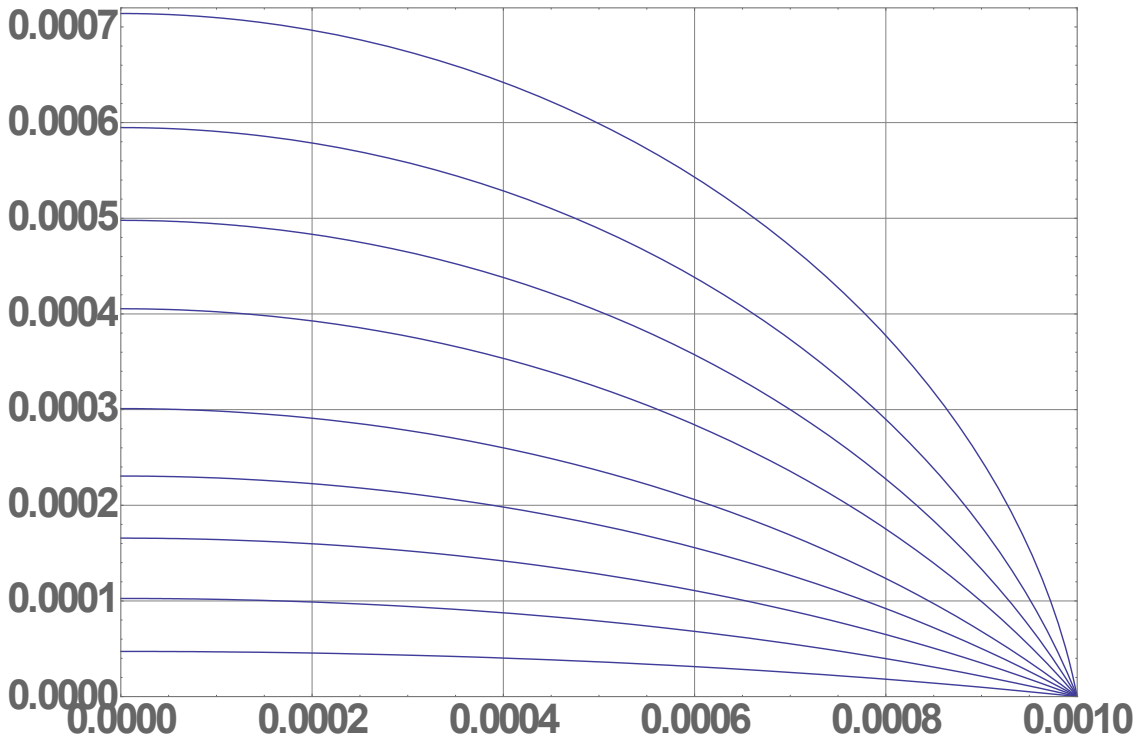

2. Mathematica Code for grayscale lithography calculation:

```
Clear["Global`*"]

f[br_]:=h1(Exp[(1-br)/bf]-1)

h1=0.1;

bf=0.274;

Plot[f[br],{br,0,1}]
```

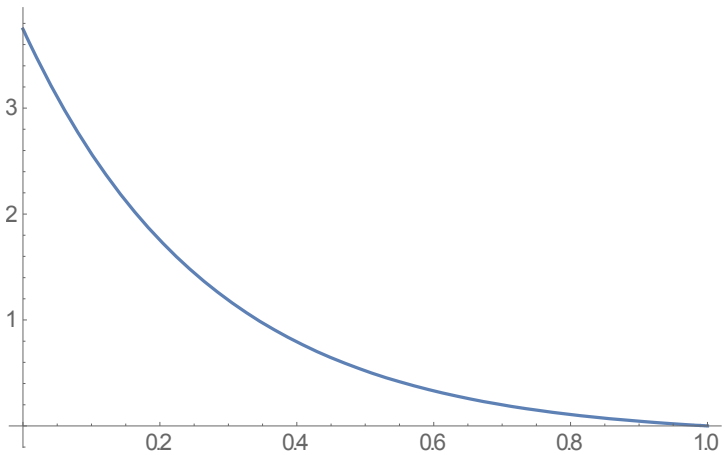


```
cu[r_]:=1+2r^3-3 r^2

li[r_]:=1-r

f[x_,a_,b_]:=1/(E^(-(x-(1-a))/b)+1)

fd[x_,a_,b_]:=1-(f[x,a,b]-f[0,a,b])/(f[1,a,b]-f[0,a,b])

Plot[{fd[r,0.5,0.16],fd[r,0.4,0.3],fd[r,0.6,0.3],fd[r,0.6,0.16],fd[r,0.6,0.5],fd[r,0.8,0.3],li[r]},{r,0,1},P
lotLegends->"Expressions"]

{
```

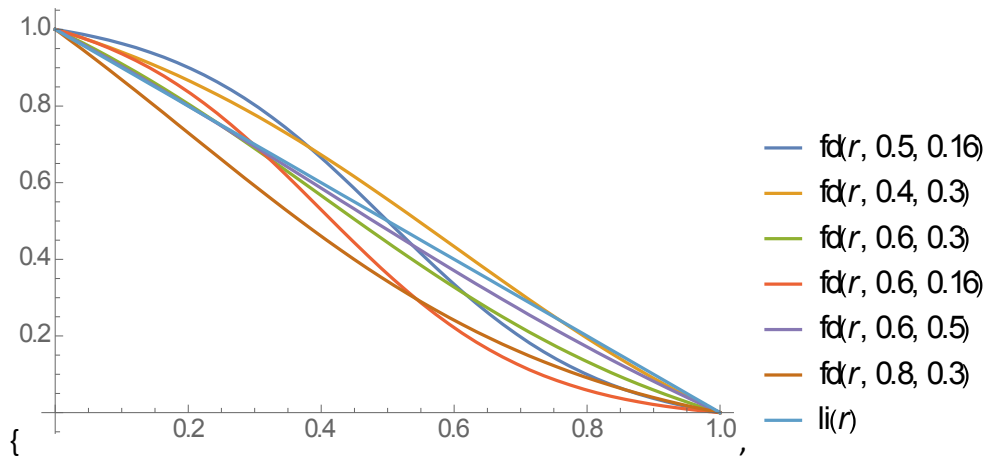


```
{                                                                    }
}

tcu=(x/.Solve[3cu[r]==f[x],x])[[1]]

-0.274 Log[0.260006 (3.1 -9. r^2+6. r^3)]

t516=(x/.Solve[3fd[r,0.5,0.16]==f[x],x])[[1]]

-0.274 Log[0.260006 (3.23787 -3.27574/(1. +22.7599 E^(-6.25 r)))]

a516=Array[b516,126];

For[i=0,i<=125,i++,a516[[i+1]]=Round[64t516/.r->(i/125)]]

y516[x_]:=a516[[(126-x/8)]]

t43=(x/.Solve[3fd[r,0.4,0.3]==f[x],x])[[1]]

-0.274 Log[0.260006 (3.63201 -4.46303/(1. +7.38906 E^(-3.33333 r)))]

a43=Array[b43,126];

For[i=0,i<=125,i++,a43[[i+1]]=Round[64t43/.r->(i/125)]]

t63=(x/.Solve[3fd[r,0.6,0.3]==f[x],x])[[1]]

-0.274 Log[0.260006 (4.03103 -4.46303/(1. +3.79367 E^(-3.33333 r)))]

a63=Array[b63,126];

For[i=0,i<=125,i++,a63[[i+1]]=Round[64t63/.r->(i/125)]]
```

```
y63[x_]:=a63[[(126-x/8)]]

t616=(x/.Solve[3fd[r,0.6,0.16]==f[x],x])[[1]]

-0.274 Log[0.260006 (3.35253 -3.32903/(1. +12.1825 E^(-6.25 r)))]

a616=Array[b616,126];

For[i=0,i<=125,i++,a616[[i+1]]=Round[64t616/.r->(i/125)]]

y616[x_]:=a616[[(126-x/8)]]

t65=(x/.Solve[3fd[r,0.6,0.5]==f[x],x])[[1]]

-0.274 Log[0.260006 (5.12852 -6.54309/(1. +2.22554 E^(-2. r)))]

a65=Array[b65,126];

For[i=0,i<=125,i++,a65[[i+1]]=Round[64t65/.r->(i/125)]]

y65[x_]:=a65[[(126-x/8)]]

t83=(x/.Solve[3fd[r,0.8,0.3]==f[x],x])[[1]]

-0.274 Log[0.260006 (4.80821 -5.03535/(1. +1.94773 E^(-3.33333 r)))]

a83=Array[b83,126];

For[i=0,i<=125,i++,a83[[i+1]]=Round[64t83/.r->(i/125)]]

y83[x_]:=a83[[(126-x/8)]]

tli=(x/.Solve[3li[r]==f[x],x])[[1]]

-0.274 Log[0.260006 (3.1 -3. r)]

ali=Array[bli,126];

For[i=0,i<=125,i++,ali[[i+1]]=Round[64tli/.r->(i/125)]]

yli[x_]:=ali[[(126-x/8)]]

aorg=Array[borg,126];

For[i=0,i<=125,i++,aorg[[i+1]]=Round[i/125*64]]
```

```
yorg[x_]:=aorg[[(126-x/8)]]

ListPlot[{a516,a43,a63,a616,a65,a83,ali,aorg}/64,Joined->True,InterpolationOrder->0,PlotLegends->Automatic,DataRange->{0,1}]
```

{

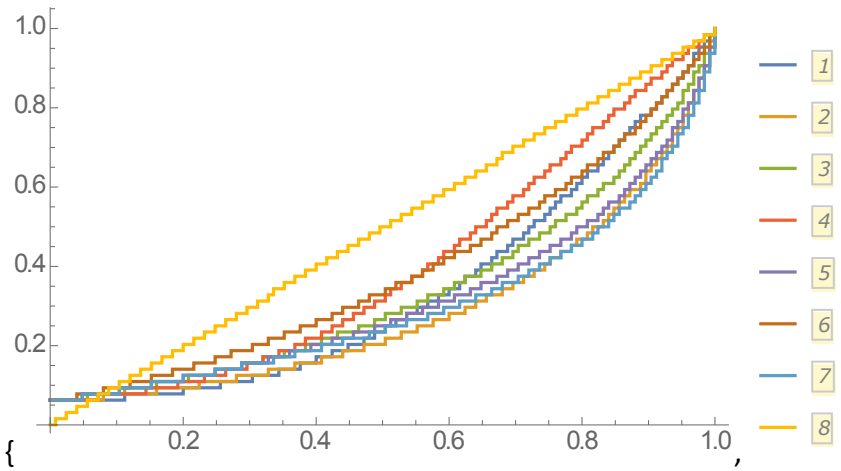

{ , }

}

References

[1] International Technology Fkoadmap for Semiconductors Web Site (http://public.itrs.net/)

[2] G. Walker, *Stirling cycle machines*, 1976, Clarendon Press, Oxford.

[3] A. Bar-Cohen, J. D. Albrecht and J. J. Maurer, "Near-junction thermal management for wide bandgap devices." *Compound Semiconductor Integrated Circuit Symposium (CSICS), IEEE*, Oct.16-19, 2011, Waikoloa, HI.

[4] R. Venkatasubramanian, E. Siivola, T. Colpitts, and B. O'Quinn, *Nature* **413**, 597–602 (2001).

[5] C. LaBounty, A. Shakouri, and J. E. Bowers, *J. Appl. Phys*. **89**, 4059–4064 (2001).

[6] A. Majumdar, *Science* **303,** 777-778 (2004).

[7] W. Kim, J. Zide, A. Gossard, D. Klenov, S. Stemmer, A. Shakouri, and A. Majumdar, *Phys. Rev. Lett*. **96**, 045901 (2006).

[8] http://searchnetworking.techtarget.com/definition/Peltier-effect

[9] http://chemecar.wikispaces.asu.edu/Propose+Propulsion+Methods

[10] J. Sharp, J. Bierschenk and H.B. Lyon, Jr., "Overview of solid-state thermoelectric refrigerators and possible applications to on-chip thermal management," *Proc. IEEE*, v.94, no.8, Aug.2006, pp.1602-12.

[11] Moran, M.E., et al., "Micro-Scale Regenerative Heat Exchanger", *AIAA Canada Europe-USA-Asia (CANEUS) 2004 Conference on Micro-Nano-Technologies for Aerospace Applications,* Monterey, CA, Nov. 1-5, 2004.

[12] Moran, M.E., "Micro-Scalable Thermal Control Device", *US Patent* No. 6,385,973 B1, May 14, 2002.

[13] Y.S. Ju, "Solid-State Refrigeration Based on the Electrocaloric Effect for Electronics Cooling", *J. Electron. Packag*. **132,** 041004 (2010).

[14] T. Furukawa, "Piezoelectricity and pyroelectricity in polymers", *IEEE Trans. Electr. Insul.* **24** (3) (1989) 375–394.

[15] P. Kobeco, and I.V. Kurtchatov, "Dielectric properties of rochelle salt crystal." *Z Phys* **66** (1930) 192–205.

[16] Mischenko, A.S., Zhang, Q., Scott, J.F., Whatmore, R.W. and Mathur, N.D., "Giant Electrocaloric Effect in Thin-Film PbZr0.95Ti0.05O3", *Science*, 2006, **311**, pp. 1270-1.

[17] Neese, B., Chu, B., Lu, S.G., Wang, Y., Furman, E. and Zhang, Q.M., "Large Electrocaloric Effect in Ferroelectric Polymers Near Room Temperature", *Science*, 2008, **321**, pp. 821-823.

[18] Y.S. Ju, "Solid-state refrigeration based on the electrocaloric effect for electronics cooling." *Journal of Electronic Packaging* **132** (2010) 041004.

[19] G.G. Wiseman and J.K. Kuebler, "Electrocaloric effect in ferroelectric rochelle salt." *Physical Review* **131** (5) (1963) 2023-2027.

[20] W.N. Lawless and A.J. Morrow, “Specific heat and electrocaloric properties of a SrTiO3 ceramic at low temperatures.” *Ferroelectrics* **15** (1) (1977) 159-165.

[21] B. A. Tuttle and D. A. Payne, “The effects of microstructure on the electrocaloric properties of Pb(Zr,Sn,Ti)O3 ceramics.” *Ferroelectrics* **37** (1) (1981) 603-606.

[22] S. G. Lu, B. Rožic, Q. M. Zhang, Z. Kutnjak, X. Li, E. Furman, L. J. Gorny, M. R. Lin, B. Malic, M. Kosec, R. Blinc and R. Pirc, “Organic and inorganic relaxor ferroelectrics with giant electrocaloric effect.” *Applied Physics Letters* **97** (2010) 162904.

[23] X. Li, X.S. Qian, S.G. Lu, J. Cheng, Z. Fang and Q.M. Zhang, “Tunable temperature dependence of electrocaloric effect in ferroelectric relaxor poly(vinylidene fluoride-trifluoroethylene - chlorofluoroethylene) terpolymer.” *Applied Physics Letters* **99** (2011) 052907.

[24] H. Gu, X. Qian, X. Li, B. Craven, W. Zhu, A. Cheng, S. C. Yao, and Q. M. Zhang, “A chip scale electrocaloric effect based cooling device.” *Applied Physics Letters* **102** (2013) 122904.

[25] H. Gu, B. Craven, X. Qian, X. Li, A. Cheng, and Q. M. Zhang, “Simulation of chip-size electrocaloric refrigerator with high cooling-power density.” *Applied Physics Letters* **102** (2013) 112901.

[26] D. Guo, “Design, Analysis, Modeling and Testing of a Micro-scale Refrigeration System”, Ph. D. thesis (2014).

[27] D. Guo, J. Gao, Y.J. Yu, S. Santhanam, A. Slippey, G. K. Fedder, A. J. H. McGaughey and S. C. Yao, “Design and modeling of a fluid-based micro-scale electrocaloric refrigeration system.” *International Journal of Heat and Mass Transfer* **72** (2014) 559-564.

[28] J. Gao, D. Guo, S. Santhanam, G.K. Fedder, “Large stroke electrostatic actuated PDMS-on-silicon micro-pump”, in: *Proceedings of the 18th IEEE International Conference on Solid-State Sensors, Actuators and Microsystems (TRANSDUCERS)*, 2015, pp 117 - 120

[29] B. Morgan, C. Waits, J. Krizmanic, and R. Ghodssi, “Development of a deep silicon phase Fresnel lens using gray-scale technology and deep reactive ion etching,” *J. Microelectromech. Syst.*, vol. 13, no. 1, pp. 113–120, Feb. 2004.

[30] J. Gao, D. Guo, S. Santhanam, Y. Yu, A.J.H. McGaughey, S.C. Yao, G.K. Fedder, "Release and transfer of large-area ultra-thin PDMS",in: *Proceedings of IEEE 27th International Conference on the Micro Electro Mechanical Systems (MEMS),* 2014, pp 544-547

[31] J. Gao, D. Guo, S. Santhanam, G.K. Fedder, "Material Characterization and Transfer of Large-Area Ultra-Thin Polydimethylsiloxane Membranes", *J. Microelectromech. Syst.,* in print

[32] D. Guo, J. Gao, Y.J. Yu, S. Santhanam, G.K. Fedder, A.J.H. McGaughey, S.C. Yao, "Electrocaloric characterization of a poly(vinylidene fluoride-trifluoroethylene-chlorofluoroethylene) terpolymer by infrared imaging", *Applied Physics Letters* **105**, 031906 (2014)

[33] T. Sekitani, Y. Noguchi, T. Fukushima, T. Aida and T, Someya, “A rubberlike stretchable active matrix using elastic conductors”, *Science* **321** 1468 (2008).

[34] T. Sekitani, H. Nakajima, H. Maeda, T. Fukushima, T. Aida, K, Hata and T, Someya, "Stretchable active-matrix organic light-emitting diode display using printable elastic conductors", *Nat. Mater*. **8** 494–9 (2009).

[35] S. Lacour, D. Chan, S. Wagner, T. Li and Z. Suo, "Mechanisms of reversible stretchability of thin metal films on elastomeric substrates", *Appl. Phys. Lett*. **88** 204103 (2006).

[36] S. Rosset, M. Samuel, P. Dubois and H. Shea, "Metal ion implantation for the fabrication of stretchable electrodes on elastomers", *Adv. Funct. Mater*. **19** 470–8 (2009).

[37] H. Takao, K, Miyamura, H. Ebi, M. Ashiki, K. Sawada, M. Ishida, "A MEMS microvalve with PDMS diaphragm and two-chamber configuration of thermo-pneumatic actuator for integrated blood test system on silicon", *Sensors and Actuators A* **119** (2005) 468–475.

[38] O. Jeong and S. Konishi, "Fabrication and drive test of pneumatic PDMS micro pump", *Sensors and Actuators A* **135** (2007) 849–856.

[39] D-H Kim, N. Lu, R. Ma, Y-S. Kim, J. A. Rogers, et al, "Epidermal Electronics", *Science* **333**, 838 (2011)

[40] M. Liu, J. Sun, Y. Sun, C. Bock and Q. Chen, "Thickness-dependent mechanical properties of polydimethylsiloxane membranes", *J. Micromech. Microeng*. **19** (2009) 035028.

[41] F. Carrillo, S. Gupta, M. Balooch, S. Marshall, G. Marshall, L. Pruitt and C. Puttlitz "Nanoindentation of polydimethylsiloxane elastomers: effect of crosslinking, work of adhesion, and fluid environment on elastic modulus", *J. Mater. Res.* **20** (2005) 2820–30.

[42] F. Schneider, T. Fellner, J. Wilde and U. Wallrabe, “Mechanical properties of silicones for MEMS”, *J. Micromech. Microeng.* **18** (2008) 065008.

[43] I. Johnston, D. McCluskey, C. Tan and M. Tracey, “Mechanical characterization of bulk Sylgard 184 for microfluidics and microengineering”, *J. Micromech. Microeng*. **24** (2014) 035017.

[44] S. Yoon, V. Reyes-Ortiz, H. Kim, H. Seo and M. Mofrad, “Analysis of circular PDMS microballoons with ultralarge deflection for MEMS design”, *J. Microelectromech*. Syst. **19** (2010) 854–64.

[45] A. Gerratt, I. Penskiy and S. Bergbreiter, “In situ characterization of PDMS in SOI-MEMS”, *J. Micromech. Microeng*. **23** (2013) 045003.

[46] Dow Corning, Product data sheet of Sylgard 184 silicone elastomer, available from http://www.dowcorning.com.

[47] J. Neumann, et al., “CMOS-MEMS membrane for audio-frequency acoustic actuation”, *Sensors and Actuators A* ***95*** *(2002) 175-182*

[48] https://en.wikipedia.org/wiki/Berkovich_tip

[49] R.W. Ogden, 1984, *Non-Linear Elastic Deformations*, ISBN 0-486-69648-0, Dover

[50] M. Mooney, “A theory of large elastic deformation,” Journal of Applied Physics **11**(9), pp. 582-592. (1940).

[51] R. Rivlin, “Large elastic deformations of isotropic materials”, *Philosophical Transactions of the Royal Society of London. Series A, Mathematical and Physical Sciences*, **241**(835) (1948).

[52] J. Selby and M. Shannon, “Inflation of a circular elastomeric membrane into a horizontally semi-infinite liquid reservoir of finite vertical depth: Quasi-static deformation model”, *International Journal of Engineering Science* **47** (2009) 700–717.

[53] S. Granick, Z. Lin and S. Bae, “Materials science: Molecules squeezed and stroked”, *Nature* **425**, 467-468 (2003).

[54] N. Bowden, S. Brittain, A. Evans, J. Hutchinson and G. Whitesides, “Spontaneous formation of ordered structures in thin films of metals supported on an elastomeric polymer”, *Nature* **393**, 146-149 (1998).

[55] D. Cristea, P. Obreja, M. Kusko, E. Manea and R. Rebigan, “Polymer micromachining for micro- and nanophotonics” *Mater. Sci. Eng. C* **26** 1049–55 (2006).

[56] H. Hillborg, J. Ankner, U. Gedde, G. Smith, H. Yasuda and K. Wikstrom, “Crosslinked polydimethylsiloxane exposed to oxygen plasma studied by neutron reflectometry and other surface specific techniques” *Polymer* **41**, 6851 (2000).

[57] M. Liu, J. Sun and Q. Chen, “Influences of heating temperature on mechanical properties of polydimethylsiloxane”, *Sensors and Actuators A* **151** (2009) 42–45.

[58] C. Beuret, G.-A. Racine, J. Gobet, R. Luthier, N.F. de Rooij, "Microfabrication of 3D multidirectional inclined structures by UV lithography and electroplating", in*: Proceedings of the IEEE International Conference on Micro Electro Mechanical Systems,* 1994, pp. 81–85.

[59] T.-K.A. Chou, K. Najafi, "Fabrication of out-of-plane curved surfaces in Si by utilizing RIE lag", in: *Proceedings of the IEEE International Conference on Micro Electro Mechanical Systems,* 2002, pp. 145–148.

[60] A.A. Ayón, S. Nagle, L. Fréchette, R. Ghodssi, A. Epstein, M.A. Schmidt, "Tailoring etch directionality in a deep reactive ion etching tool", *in: Proceedings of the Transducers'99*, 1999, pp. 854–857.

[61] A. Bertsh, H. Lorenz, P. Renaud, "Combining microstereolithography and thick resist UB lithography for 3D microfabrication", in: *Proceedings of the IEEE International Conference on Micro Electro Mechanical Systems,* 1998, pp. 18–23.

[62] Y. Opplinger, P. Sixt, J.M. Stauffer, J.M. Mayor, P. Regnault, G. Voirin, "One-step 3D shaping using a gray-tone mask for optical and microelectronic applications", *Microelectron. Eng.* **23** (1994) 449–454.

[63] T.J. Suleski, D.C. O'Shea, "Gray-scale masks for diffractive-optics fabrication. I. Commercial slide images", *Appl. Opt.* **34** (1995) 7507– 7517.

[64] D.C. O'Shea, W.S. Rockward, "Gray-scale masks for diffractive-optics fabrication. II. Spatially filtered halftone screens", *Appl. Opt*. **34** (1995) 7518–7526.

[65] C.M. Waits, B. Morgan, M. Kastantin, R. Ghodssi, “Microfabrication of 3D silicon MEMS structures using gray-scale lithography and deep reactive ion etching”, *Sensors and Actuators A* **119** (2005) 245–253

[66] P. Yao, G. J. Schneider, and D. Prather, “Three-dimensional lithographical fabrication of microchannels,” *J. Microelectromech. Syst*., vol. 14, no. 4, pp. 799–805, Aug. 2005.

[67] P. Yao, G. J. Schneider, D. Prather, E. Wetzel, and D. O’Brien,“Fabrication of three-dimensional photonic crystals with multilayer photolithography,” *Opt. Express*, vol. 13, no. 7, pp. 2370–2376, Apr. 2005.

[68] Christopher M Waits, Alireza Modafe and Reza Ghodssi, “Investigation of gray-scale technology for large area 3D silicon MEMS structures”, *J. Micromech. Microeng*. **13** (2003) 170–177

[69] Lance Mosher, Christopher M. Waits, "Double-Exposure Grayscale Photolithography", *Microelectromech. Syst*., vol. 18, no. 2, pp. 1308–315, Apr. 2009.

[70] Stephen A. Campbell, “The science and engineering of microelectronic fabrication”, 2nd edition, *Oxford Press*, 2001

[71] Taylor M T, Nguyen P, Ching J and Petersen K E, “Simulation of microfluidic pumping in a genomic DNA blood-processing cassette” *J. Micromech. Microeng.* **13** 201–8 (2003)

[72] Zhang L et al, “Measurements and modeling of two-phase flow in microchannels with nearly constant heat flux boundary conditions” *J. Microelectromech. Syst.* **11** 12–9 (2002)

[73] Johari, J.; Yunas, J.; Yeopmajlis, B. “Piezoeletric Micropump for Drug Delivery System Fabricated Using Two Optical Masks.” *.Adv. Mat. Res.* 2009, **74**, 279-282.

[74] Yamahata, C; Lotto, C; Al Assaf, E.; Gijs, M.A.M. “A PMMA valveless micropump using electromagnetic actuation”. *Microfluid. Nanofluid*. 2005, **1**, 197-207.

[75] O.C. Jeong, S.S.Yang, “Fabrication and test of a thermopneumatic micropump with a corrugated p+diaphragm”, *Sens. Actuators A: Phys*. **83** (2000)249-25

[76] William R. Herb, et al., “Dual Diaphragm, Single chamber Mesopump”, *US Patent* No. 6,179,586, B1, Jan. 30, 2001.

[77] J. Gao, et al., “Stirling Microcooler Array with Elemental In-Plane Flow”, *37th GOMACTech Conf., Las Vegas, 2012*

[78] D. Guo, A. J. H. McGaughey, J. Gao, G. K. Fedder, M. Lee and S. C. Yao, “Multiphysics modeling of a micro-scale Stirling refrigeration system.” *International Journal of Thermal Sciences* **74** (2013) 44-52.

[79] O.C. Jeong, S.S.Yang, “Fabrication and test of a thermopneumatic micropump with a corrugated p+diaphragm”, *Sens. Actuators A: Phys*. **83** (2000)249-25

[80] http://www.ulet.co.kr/product/Vacuum%20Fluids/heat/galden.htm.

[81] D. Guo, J. Gao, Y.J. Yu, S. Santhanam, A. Slippey, G. K. Fedder, A. J. H. McGaughey and S. C. Yao, “Design of a Fluid-Based Micro-scale Electocaloric Refrigeration system”, *ASME 2013 Summer Heat Transfer Conference, Minneapolis, MN,* (2013)

[82] G. Sebald, L. Seveyrat, J.F. Capsal, P.J. Cottinet and D. Guyomar, "Differential scanning calorimeter and infrared imaging for electrocaloric characterization of poly(vinylidene fluoride-trifluoroethylenechlorofluoroethylene) terpolymer." *Applied Physics Letters* **101** (2012) 022907.

[83] G. Sebald, L. Seveyrat, D. Guyomar, L. Lebrun, B. Guiffard and S. Pruvost, "Electrocaloric and pyroelectric properties of 0.75Pb(Mg1/3Nb2/3)O3-0.25PbTiO3 single crystals." *Journal of Applied Physics* **100** (12) (2006) 124112.

[84] Y. Bai, G. Zheng and S. Shi, "Direct measurement of giant electrocaloric effect in BaTiO3 multilayer thick film structure beyond theoretical prediction." *Applied Physics Letters* **96** (2010) 192902.

[85]Y. Jia and Y. S. Ju, "Direct characterization of the electrocaloric effects in thin films supported on substrates." *Applied Physics Letters* **103** (2013) 042903.

[86] L. Yang, X. Li, E. Allahyarov, P. L. Taylor, Q.M. Zhang, and L. Zhu*, Polymer* **54**, 1709-1728 (2013).

[87] S.G. Lu, Q. M. Zhang, "Electrocaloric materials for solid-state refrigeration." *Advanced Materials* **21** (2009) 1-5.

[88] G. Guisbiers, S. Strehle, M. Wautelet, "Modeling of residual stresses in thin films deposited by electron beam evaporation", *Microelectronic Engineering* **82** (2005) 665–669

[89] A. Delcorte, S. Befahy, C. Poleunis, M. Troosters and P. Bertrand, "Improvement of metal adhesion to silicone films: a ToF-SIMS study", *Adhesion Aspects of Thin Films*, Vol. 2, pp. 1–12

[90] M. A Eddings, M. A. Johnson and B. K. Gale, “Determining the optimal PDMS–PDMS bonding technique for microfluidic devices”, *J. Micromech. Microeng.* **18** (2008) 067001

[91] K. C. Tang, E Liao, W. L. Ong, J. D. S. Wong, A. Agarwal, R. Nagarajan and L. Yobas, “Evaluation of bonding between oxygen plasma treated polydimethyl siloxane and passivated silicon”, *Journal of Physics: Conference Series* **34** (2006) 155–161

[92] T. Perera, M. P. C. Watts, “Study Of The Reaction Kinetics Of The Photoresist Aging Process”, *Advances in Resist Technology and Processing V*, Vol. 0920

[93] Chris Mack, “Fundamental Principles of Optical Lithography: The Science of Microfabrication”, *John Wiley & Sons Inc*, 2007

[94] R. M, Linnemann and P. Woias, “Robust design of gas and liquid micropumps”, *Sensors Actuators A* **68** 480–6, 1998

[95] R. Zengerle, K. Ulrich, M. Richter A. Richter, "A bidirectional silicon micropump", *Sensors Actuators* A **50** 81–6 1995

[96] M.A. Unger, H. Chou, T. Thorsen, A. Scherer, S.R. Quake, “Monolithic microfabricated valves and pumps by multilayer soft lithography”, *Science* **288** (2000) 113–116.